Background-free detection and mixed-species crystals in micro- and macroscopic ion-traps for scalable QIP

A thesis submitted for the degree of
Doctor of Philosophy

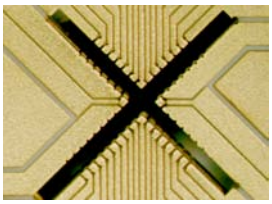

Norbert Matthias Linke

Michaelmas Term
2012

New College
Oxford

Abstract

Background-free detection and mixed-species crystals in micro- and macroscopic ion-traps for scalable QIP

A thesis submitted for the degree of Doctor of Philosophy

Michaelmas Term 2012

Norbert M. Linke

New College, Oxford

Scalability and the implementation of fault tolerant quantum gates are the two main challenges which must be overcome in order to unlock the vast potential of quantum computing. This thesis describes work with calcium ions trapped in both microscopic and macroscopic linear Paul traps addressing both of these issues.

We describe the assembly of a microstructured multi-zone ion trap which forms part of our group's contribution to the European "Microtrap" collaboration. We report the successful trapping of ions and characterization of the trap as well as a measurement of the heating rate. In miniaturized trap structures such as this one, background scattered light from the cooling beam causes difficulties. We introduce and demonstrate experimentally two techniques to overcome this problem. The first achieves background-free detection of ions using different repumping methods to enable the filtering out of the excitation wavelength. The second makes possible background-free readout of trapped ion qubits by separating in time the excitation and detection steps.

The second half of the thesis describes our experimental efforts towards implementing a two-qubit entangling gate with a mixed-species crystal. We describe the setup and characterization of a new macroscopic trap including the trapping and coherent manipulation of the internal states of both $^{40}Ca^{+}$ and $^{43}Ca^{+}$ ions. We accomplish the simultaneous independent readout of two qubits implemented in a $^{40}Ca^{+}-^{43}Ca^{+}$ ion pair. We also present the setup and characterization of two injection-locked frequency-doubled Raman lasers and demonstrate coherent manipulation as well as a measurement of the off-resonant photon scattering error they introduce. Finally, we use them to achieve sideband cooling to the motional ground state of a mixed species ion crystal.

Acknowledgments

I am extremely grateful to my supervisor, Dr. David Lucas, for giving me the opportunity to be part of his extraordinary research group and for all his fantastic support over the past four years, both in and out of the lab. His attention to detail, scientific rigor and approachable character are phenomenal. I also want to thank him for his patient proof-reading of this thesis which has been tremendously helpful. Moreover, he deserves great credit for bringing our group into the Microtrap collaboration.

I want to give very warm thanks to Prof. Derek Stacey for his enthusiasm for understanding any scientific data I presented him with. His support and encouragement throughout my time here has been pivotal. He has also generously shared his hoard of teaching experience which has proved very useful during my last two years.

A huge thank-you goes to my fellow D.Phil. student Chris Ballance whose thoroughness, expertise and infectious eagerness have made rebuilding the "old lab" a success and working together a joy. He was also a big help finding and correcting errors in this thesis.

I owe a large debt of gratitude to Dr. David Szwer who was my fellow student, and post-doc. He has taught me a great deal about ion trapping and worked with me on the Raman system and the scattering experiments. He was also a keen boardgame buddy[1] and much fun was had. I would like to very much thank Dr. David Allcock for his ideas and experimental support on the background-free detection experiment as well as for general lab and ion-trapping wisdom. Additionally, Prof. Jonathan Home and other former members of our group whose work on two-qubit gates still leads us on.

A big "Microtrap-slap" for all their effort on the project goes to Robert Stockill, the most successful summer student any lab could have wished for, my fellow D.Phil. students Chris Ballance and Microtrap pioneer Dr. Alice "senior student" Burrell who made the "serious Microtrap business" an enjoyable experience and especially to Dr. Jeff Sherman, post-doc extraordinaire, whose knowledge of atomic physics, repertoire of puns, vacuum system baking enthusiasm, scientific presentation skills, appreciation of the absurdity of politics and resourceful spouse are unparalleled. It was sad to see him leave for the US during my second year[2].

I would like to thank Hugo Janacek for taking up atomic physics modeling problems including analyzing my "banana island" data[3] and other scans with great success.

[1] together with A. Burrell, S. Webster and H. Janacek

[2] where his bike was stereotypically abandoned in favo*u*r of a planet-warming SUV...

[3] see chapter 8

Special thanks go to Prof. Andrew Steane for helpful discussions and establishing Oxford in the world of ion trapping. Dr. Luca Guidoni of Université Paris Diderot who visited our lab for a year gave valuable advice for getting both traps presented in this thesis up and running and somehow managed to even further improve the excellent working atmosphere in our group. I also want to thank Dr. Simon Webster for designing the new trap, his work on assembling the vacuum system and his help with the initial trap characterization; Thomas Harty for proof-reading and vital input on the toroidal resonators; Diana Prado Lopes Aude Craik for being a delightful office-mate and for making me think about density matrices.

This work would not have been possible without the amazing technical support available at the Oxford Physics department. I owe many thanks to Matt Newport, Simon Moulder and Rob Harris for making mechanical work a highlight of being a graduate student here. Paul Pattinson, Martin Scott and Peter Clack for their help with etching, wirebonding and ultrasonic cutting respectively; Phil Prior for carpentry; Alan Francis for simply handing me everything I needed with a smile and Graham Quelch for general technical assistance on many occasions. Additionally, I would like to express my appreciation for the work of Graham Silman and Tony Applewhaite during the remodeling process of the "new old lab". I am also grateful to Sue Gardner for administrative support.

I would furthermore like to thank Magali, my parents, and all the great friends I have made in Oxford for their support, love and encouragement.

I thankfully acknowledge funding by the EPSRC and by New College through their Wykeham scholarship.

Finally, I would like to thank Prof. Henry Snaith for having a cacophonous liquid-nitrogen valve installed outside my office window which kept me awake and focused during my write-up period.

Contents

Chapter 1

Introduction

Quantum mechanics has been the basis for an incredible leap in computing technology in the 20th century. Until the 1950s computers were based on vacuum tubes which were unreliable, large in size, high in power consumption and forbiddingly expensive. Put simply, the approach wasn't scalable. The breakthrough came with the invention of the transistor which was founded on the quantum theory of semiconductor contacts developed by John Bardeen [1]. It has made possible the astonishing development of (classical) computing over the last half century.

Today, quantum computing faces similar challenges. First conceived in the 1980s, in theory, its computational power widely surpasses that of a classical computer. It relies on quantum mechanical two-level systems and their superposition states as qubits and on entanglement between different qubits as its main resource. The technical overhead involved in realizing even a couple of qubits is very high. Scaling quantum computing up to hundreds of qubits will require innovation in several areas. Gate operations must be performed with high enough fidelity to become fault-tolerant which means the remaining errors can be eliminated by using quantum error correction methods. Architectures providing the physical qubits need to develop the capability to control them reliably in large numbers. The work presented in this thesis addresses both of these critical issues.

1.1 The quantum computer

Based on the ideas of R. P. Feynman [2] and D. Deutsch [3], a series of demands has been laid out by D. DiVincenzo that a set of quantum systems and operations need to fulfill in order to be considered a candidate for a universal quantum information processor [4]:

1. A scalable physical system with well characterized qubits
2. The ability to initialize the state of the qubits to a simple fiducial state, such as $|000...\rangle$
3. Long relevant decoherence times, much longer than the gate operation time
4. A "universal" set of quantum gates
5. A qubit specific measurement capability.

The list is extended by two "Desiderata for Quantum Communication" which are the "ability to interconvert stationary and flying qubits" and to "faithfully transmit flying qubits between specified locations". These are not just important in the context of quantum communication experiments such as quantum key distribution for secure encryption protocols and fundamental tests of non-locality in quantum mechanics [5], but also play a role for improving scalability by interconnecting quantum systems (see section 1.3.2).

A large number of candidate systems are in the race to fulfill these requirements [6]. Apart from trapped ions which this thesis is concerned with, qubits are currently being implemented in the collective spin states of NMR systems, in the polarization states of single photons, the electronic energy levels of quantum dots and NV-centres, on neutral atoms trapped in atom chips and optical lattices and in quantized currents across Josephson junctions in superconducting circuits. Further efforts aim to use the spin states of single trapped electrons [7].

At this stage, there is no clear single approach that can be identified as the optimum choice for a quantum computing architecture since the different systems offer different advantages and drawbacks. Photons allow the transport of quantum information over distances but are easily lost due to absorption. They also do not stay in one place long enough for use as a quantum memory, though new EIT-based schemes for storing single photons in an atomic vapour (for $\sim 100\,\mu$s) are being investigated [8]. NMR systems, while offering robust quantum operations are not scalable to a large number of qubits since the spin ensembles are initialized in a mixed (thermal equilibrium) state [9]. Quantum dots and NV-centres implanted in a host crystal on the other hand are an intrinsically scalable technology but limited control over the strong influence of the crystal environment restricts the coherence time [10, 11]. Superconducting qubits used to be similarly limited but have made substantial advances over the last few years [12, 13, 14]. In the future, a combination of several technologies might be found to be favourable.

For the moment however, the most advanced system in terms of fulfilling the DiVincenzo criteria are trapped ion qubits. The following gives a short overview of quantum operations performed with trapped ions.

1.2 Realization with ion traps

Ions held in traps consisting of a combination of static electric fields and either radiofrequency electric (Paul traps) or static magnetic fields (Penning traps) for confinement provide a stable, theoretically well understood and highly controllable quantum system which is well isolated from the environment. Most quantum computing experiments are done in linear Paul traps which have a weak axial trap direction realized with a DC field and a stronger radial confinement provided by a radiofrequency quadrupole field. Combined with laser cooling, this setup provides linear crystals of ions at fixed positions in

space which form the basis for the concept of ion trap quantum computing. A comprehensive overview of the subject can be found in [15]. The review does not include the recent advances using microwave gates and surface electrode traps. Please refer to [16] and references therein.

Ions offer a choice of qubit states between either ground state qubits using the Zeeman or (if a nuclear spin is present) hyperfine substates as $|0\rangle$ and $|1\rangle$, or optical qubits using the ground state and a metastable state (e.g. the $3D_{5/2}$ state in Ca^+) as qubit states. Our group uses the former and more details are given in chapter 6 of this thesis.

The qubits can be initialized with good fidelity ($\geq 99\,\%$) by optical pumping or in case of the optical qubit with frequency-selective excitation [17]. Coherence times for optical qubits are limited by the lifetime of the metastable state (~ 1 s in Ca^+). For ground state qubits, coherence times of tens of seconds have been measured [18]. They are limited by energy shifts of the qubit states due to magnetic field fluctuations. Ions with a hyperfine structure allow the use of magnetic field insensitive "clock states" which have coherence times of up to 1 min [19]. These times are long compared to the two-qubit gate times which are typically on the order of 10-100 μs. Readout of the ion state can be achieved by state-dependent excitation of fluorescence. More details can be found in chapter 6. Our group has reported readout fidelities of 99.99% in $^{40}Ca^+$ [20] and $99.77(3)\%$ in $^{43}Ca^+$ [21].

Realizing single qubit gates is straightforwardly achieved by driving transitions between the qubit states. This is done directly with laser light for optical qubits or via a Raman transition for ground state qubits. The latter can also be driven with radio- or microwaves at the respective qubit frequency. The biggest complication in this context is individual addressing of ions in a linear crystal avoiding cross-talk with neighboring ions. Strategies to overcome this are discussed below.

Two-qubit gates rely on the shared motional modes of a crystal of trapped ions as a quantum bus to transfer information between ions. Lasers can be used to excite the motional mode conditionally on the initial state of one ion which corresponds to a classical CNOT gate. If that ion is prepared in a superposition state to begin with, an entangling gate can be realized. This concept was developed by I. Cirac and P. Zoller [22] and first implemented by the group of R. Blatt in Innsbruck [23]. A further development is the gate suggested by K. Mølmer and A. Sørensen [24, 25] which overcomes the Cirac-Zoller gate's strict requirement for ground state cooling and ion addressing by using the interfering excitation paths of bichromatic pulses. It was first demonstrated at NIST [26] by creating entanglement between four ions. This preceded the experimental realization of the Cirac-Zoller gate. A third type of gate which is a variant of the Mølmer - Sørensen gate is the "wobble" gate using state dependent forces to excite and de-excite the ions motion during a gate pulse causing it to pick up a phase. The gate was first described and implemented by the NIST group using $^9Be^+$ hyperfine qubits [27] and the highest fidelity to date ($99.3(1)\%$) was reported by the Innsbruck group [28]. Our group has performed this

gate in the past [29] between two $^{40}Ca^{+}$ ions and it forms the basis for future experiments in our laboratory, the development of which are described in this thesis. An overview of the gate is given in [21] and a more detailed description can be found in [30].

By employing these gates, several quantum algorithms have been demonstrated on a small number of qubits over the last decade. Among them are the teleportation of a quantum state [31, 32], entanglement swapping [33], the Deutsch-Josza algorithm [34], the quantum Fourier transform [35] and Grover's search algorithm [36]. A quantum error correction protocol consisting of three correction cycles has also been implemented [37]. It uses quantum control to feed back on the qubits rather than the single-step realization previously shown [38] which employed classical feedback.

Apart from these algorithms, trapped ions have been used for quantum simulations. These correspond to "analogue" quantum computing where the quantum states used for the simulations are analogues for other quantum states which allows predictions about the system of interest based on outcome of measurements on the analogue. Systems investigated include spin-chains with up to nine ions investigating magnetic phase transitions [39], the Dirac equation [40] and recently the implementation of a universal six-qubit digital simulation [41].

Trapped ions also form the basis of the best atomic clocks built to date [42]. Additionally, the control over individual quantum systems they provide, especially for generating entanglement, has been a resource seminal to a large body of work in metrology [17, 43, 44, 45, 46].

1.3 The challenges

Many of the requirements for a universal quantum processor have been shown individually in trapped ions, but in order to combine them into a universal processor, there are important challenges to overcome. In a recent review article [47], R. Blatt and D. J. Wineland summarize them in the following way: "...two main issues must be dealt with: improving gate fidelity, and overcoming the additional problems associated with large numbers of ions (...) to reach fault tolerant operation".

1.3.1 Fault tolerance

The range of computational operations performed in trapped ions so far is limited by the fidelity of the individual gates. For longer sequences, the errors multiply and limit the overall fidelity achievable. Increasing the fidelity of one- and two-qubit gates directly increases of the number of computations possible but it also brings the use of quantum error correction protocols within reach [48].

Quantum error correction is of course a quantum computation operation in itself requiring an overhead of additional qubits and gate operations. Therefore, in order to be able to overcome the errors in quantum gates by perpetual correction, they have to be below a certain level in the first place. This so called fault-tolerance threshold has been estimated as $\leq 10^{-4}$ errors per gate [49] and gives a benchmark for quantum gate performance below which they could be usefully applied as part of an error-corrected quantum algorithm. An introduction reviewing protocols for quantum error correction has recently been published by R. Raussendorf [50].

There are different kinds of effects constraining entangling gate fidelities to $\sim 10^{-2}$ at the moment. Firstly, there are technical limitations on how precisely the different fields the ions interact with can be controlled. The laser, microwave and radiofrequency fields used to drive transitions are subject to errors both in frequency and intensity. Laser beams additionally suffer from polarization impurity which limits the quality of state preparation when initializing the qubits by optical pumping as well as readout if ion shelving is required [51]. The same is true for the radiofrequency potentials used to trap the ions. Instabilities here cause fluctuations in trap strength which introduce errors when addressing the motional states of the ions. Stray fields and trap anharmonicities can heat up the ions which again limits the length of computing operations that can be performed in a fault-tolerant way since even so called "warm" gates like the Mølmer-Sørensen gate, while not having a stringent requirement for the ions being in the ground state of motion, still perform worse with rising temperature. Another problem is fluctuations in the applied and the background magnetic field which shift the ionic energy levels causing decoherence by dephasing.

These challenges are being addressed by optimization of the control systems, trap geometries and gate methods. Transitions with far-detuned pairs of Raman laser beams report fidelities of up to 99.5% [52] limited by scattering error. Higher intensities and further detunings can push this beyond the fault tolerant threshold. This thesis contains a Raman laser setup to this end. An alternative way to drive Raman transitions uses a frequency comb [53]. Improved control electronics combined with new trap designs featuring additional control, e.g. with optimized microwave fields [54, 19] form futher efforts to address the problems listed above. Currently, motional gates driven with microwaves are being pursued at Oxford and in other groups following the success of single-qubit gates in ground state qubits using rf and microwave fields which have reported error rates of $2 \cdot 10^{-5}$ per gate [55] for experiments performed at NIST and as small as $1 \cdot 10^{-6}$ per gate at Oxford [19]. One of the issues with typical microwave and rf driven gates (see chapter 6) is the gate speed which is typically an order of magnitude smaller than for laser gates. For this reason state-of-the-art surface traps include microwave resonators and place the ions in the evanescent field of a microwave guide [16]. The group of C. Monroe at the university of Maryland is pioneering a new kind of laser gate driven faster than the motional

period of the the trapped ions using shaped ultrafast laser pulses [56] and has recently reported motional entanglement with 91 % fidelity [57] in 15 ns.

The second kind of restrictions on the overall fidelity are limitations fundamental to the ion species or qubit state used. For example, qubits implemented in metastable states are limited in their lifetime and qubits in Zeeman states (e.g. the $^{40}Ca^{+}$ ground state qubit) are particularly sensitive to magnetic field fluctuations as described above. Here, new ways of realizing qubits, for example in superposition states forming a so-called decoherence free subspace [58] or employing schemes to keep them coherent for longer with tailored series of pulses [59] are avenues being pursued. The choice of ion or qubit state for a particular operation is clearly important. Making use of a field insensitive pair of states as qubits, our group has recently demonstrated a coherence time of 48 ± 10 s in $^{43}Ca^{+}$ without additional rephasing pulses [19].

An experiment towards implementing a high-fidelity laser gate between two different isotopes is described in this thesis which is addressing both these issues, firstly by optimizing control with the Raman pulses as mentioned above and secondly by combining different ion species ($^{40}Ca^{+}$ and $^{43}Ca^{+}$) in an entangling gate to gather the advantages of both (see section 1.4 below for details). Performing gates like this has a number of experimental prerequisites which I will briefly list here. We need to be able to reliably trap and stably hold mixed species crystals for extended periods of time (see chapter 4). In order to couple the internal and motional state of the ions, a set of mutually coherent Raman beams must be available (see chapter 5). Since the motion is the bus through which information is transferred between the internal state qubits, good motional coherence will have to be verified. For this reason, the crystal needs to be cooled near the motional ground state (chapter 7). Additionally, simultaneous readout of both isotopes in a mixed crystal, simultaneous individual addressing and coherent manipulation with microwaves and radiofrequency respectively must be demonstrated (see chapter 6). Successful provision of these experimental capabilities is reported in this work.

1.3.2 Scalability

Apart from further improving the implementation of quantum gates, ion trap quantum computing experiments need to be scaled up to a larger number of qubits. The Innsbruck group has demonstrated an entangled state between up to 14 ions [60]. Coherently controlling an increasing number of ions in a single linear trap poses significant difficulties. Adding more and more ions to the crystal causes the motional modes to bunch in frequency which increases cross-coupling and makes it harder to selectively excite a single one. This is known as spectral crowding [61] and has itself been suggested for use in a quantum computing scheme for a large ion crystal in an anharmonic potential [62].

Addressing individual ions is usually done by tightly focusing a laser beam [34] or

more recently by spectral addressing using a magnetic field gradient along the trap axis [63, 64]. At a constant trap strength, the ion-distance is reduced with rising ion number which increases unwanted cross-talk during addressing. Adding more ions also means having to increase the ratio between radial and axial trap strength to avoid two- or three dimensional crystals. Overcoming the last two difficulties by reducing the axial trap strength comes at the cost of slowing down the motional gate speed which then limits the number of gates that can be performed before decoherence destroys the quantum state.

Several strategies to overcome these problems are being pursued. One is to share quantum information between ions localized in different traps. This idea was included as an addendum in DiVincenzo's list of criteria as "Desiderata for Quantum Communication" [4]. Creating entanglement between ions in traps a metre apart using photons has been demonstrated [65]. However, the low collection efficiency of single photons emitted from a single ion severely limits the speed of this approach at the moment. Efforts to increase this by specialized collection optics [66] or the use of optical cavities [67, 68, 69, 70] are underway. The short-range coupling between closely spaced ($54\ \mu$m) ion traps using the dipole-dipole interaction has also been shown [71].

The second strategy is to move the ions themselves and generate entanglement between pairs of them locally avoiding any cross-coupling issues during addressing. This requires the separation, shuttling, reordering and recombination of ion crystals [72, 73, 74, 75]. A complete set of methods for two-qubit computation using these techniques has been experimentally implemented at NIST [76]. One problem during these processes is heating of the ions. Avoiding this by adiabatically moving the ions would severely delay the process. Instead, sympathetic cooling with a second ion species has been used in the NIST experiments. Recently, so called fast transport on timescales on the order of a motional cycle has been realized at Mainz as well as NIST [77, 78]. It features optimized potential shifts for accelerating and decelerating the ion wave packet in order to minimize heating.

Architectures implementing many traps in a single device and allowing the necessary operations naturally lead to a miniaturization and microfabrication of trap geometries [68]. One avenue are surface traps [79, 80, 81, 82] where structures with hundreds of trapping zones have been tested [83]. Another are microfabricated three-dimensional traps [84, 73, 85] one of which will be presented in this thesis.

Miniaturization brings with it a smaller distance d between the ions and the surrounding trap structure. One issue that becomes more prevalent under these conditions is heating by fluctuating electric fields which has been found to scale unfavorably as $\sim d^{-4}$ [86]. This is being addressed in the ion-trapping community by testing different materials, surface cleaning [87, 88] and the use of cryogenically cooled traps [89, 90].

Another major issue that arises with miniaturized geometries, particularly surface traps but also any experiment where ions are held in close proximity to surfaces is scat-

tered laser light from the cooling beams. This light is picked up by the imaging system and causes large background on the ion signals. New strategies to tackle this problem are described and their implementation demonstrated in this thesis.

1.4 The calcium ion

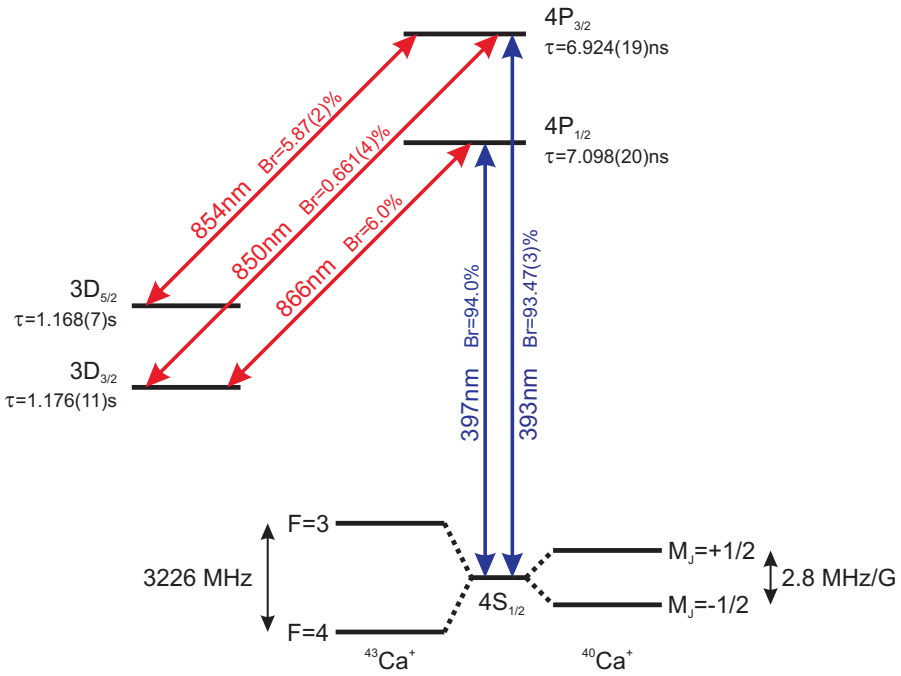

Figure 1.1: Ca^+ level structure showing the levels used in our experiments. Their lifetimes (τ) and the branching ratios for spontaneous emission (Br) are indicated. The ground state $S_{1/2}$ shows the splitting used to implement the qubit in the two different isotopes, the Zeeman qubit in $^{40}Ca^+$ and the hyperfine qubit in $^{43}Ca^+$ (see chapter 6 for details). The wavelengths of the five transitions we use are labeled (compare section 4.2.8). Figure modified from [21].

The chemical element of choice for the ion trapping experiments in our group is calcium which is stripped of one electron by photo-ionization and trapped in Paul traps of various designs. Apart from the most abundant isotope $^{40}Ca^+$, we use $^{43}Ca^+$ which is the only naturally-occurring odd-numbered isotope. Its nuclear spin ($I = 7/2$) gives rise to a hyperfine structure. Since calcium is an alkaline earth metal, its singly charged cation only has one valence electron.

Figure 1.1 shows a level diagram with the five transitions used in our experiment and the ground state sublevels we use as our qubits in the two isotopes. The isotope shifts for all the transitions can be found in appendix D. The short-lived $P_{1/2}$ transition allows Doppler cooling during which the low-lying $D_{3/2}$-state needs to be repumped. The $D_{5/2}$ state is used for electron shelving during readout (see chapter 6). All wavelengths shown as well as the ones needed for photo-ionization are available in commercial diode lasers.

$^{40}Ca^+$ is an easier ion to work with than $^{43}Ca^+$ due to the simpler atomic structure. Its ground state qubit avoids any population leakage from the qubit states which means the isotope might be a better choice for some quantum operations. However, $^{43}Ca^+$ presents several distinct advantages that make it attractive for quantum computing experiments. The hyperfine qubit which can be implemented in its ground state allows direct high-fidelity readout (see chapter 6). Most importantly, $^{43}Ca^+$ offers the possibility to store information in magnetic field insensitive "clock" states which are very robust against decoherence [91, 19]. Entangling gates between the two isotopes will therefore allow the transfer of quantum information from $^{40}Ca^+$ into such a clock state qubit making these states accessible as a "quantum main memory" in a larger quantum computing architecture.

A mixed species crystal allows individual addressing of the two ions without the need to individually focus laser beams onto a single ion because their internal transition frequencies differ, in our case by the isotope shift on the order a few GHz (see appendix D). The ground state qubit splittings are also different which means that single qubit gates can be driven on each of them selectively with oscillating magnetic fields (microwaves in $^{43}Ca^+$ and radiofrequency in $^{40}Ca^+$). Crucially, each of the qubits implemented in the two ions can be read-out independently. In the gate previously implemented in our group using a a $^{40}Ca^+ - ^{40}Ca^+$ crystal, the states $|\uparrow\downarrow\rangle$ and $|\downarrow\uparrow\rangle$ could not be distinguished. With the mixed species gate, full state tomography [92] will be possible.

While these advantages hold for crystals containing different atomic species generally, using two isotopes of calcium to form a same-species mixed crystal, presents a distinct advantage. The isotope shifts between them while large enough for reliable addressing can still be spanned with frequency shifts provided by EOMs, so that only one set of lasers is needed. This is also true for generating the ions by photoionization (see chapter 4, section 4.2.8.1) and simplifies the experimental overhead significantly.

1.5 Thesis overview

This section briefly summarizes the content of each of the following chapters. The first half is dedicated to experiments concerned with scalability of ion trap quantum computing and miniaturization of trapped ion experiments generally while the second half focuses on experimental work towards high fidelity laser-driven quantum logic gates.

Chapter 2 describes the assembly, modeling and operation of a microstructured ion trap. Characterization of this trap forms part of our group's contribution to the European Microtrap project. The measured heating rate is compared to similar traps from the collaboration.

A problem not just in our Microtrap but universal to miniaturized trap geometries is scatter from the cooling beam causing large background on the ion signal. The work in

chapter 3 addresses this by demonstrating background-free detection of trapped ions as well as the background-free readout of the qubit implemented in a trapped ion.

Apart from scalability, fault-tolerant quantum gates are another major effort in quantum computing. Chapter 4 describes the new trap built for the mixed species experiment and the experimental apparatus provided for its operation. It also presents data characterizing the trap.

Entangling gates require coupling the internal and motional states of the ions which we accomplish with a pair of Raman lasers. The laser system consisting of two injection-locked frequency-doubled diode lasers is detailed in chapter 5. The chapter also includes a study of off-resonant photon scattering as a possible error source for laser-driven gates introduced by the Raman beams.

The qubits realized in the two isotopes of calcium are characterized in chapter 6 together with their readout schemes. The chapter includes experiments showing single-qubit addressing and coherent manipulation with oscillating magnetic fields as well as simultaneous independent readout of both qubits. Finally, it demonstrates the coherent driving of Raman transitions in both isotopes with the laser system described in chapter 5.

In chapter 7 we present ion cooling experiments as a next step towards the gate including pulsed sideband cooling of a two-ion crystal of $^{40}Ca^{+}$ and $^{43}Ca^{+}$ close to the motional ground state.

To conclude, chapter 8 summarizes and gives an outlook at the future of the projects presented.

Chapter 2

Microtrap

2.1 Motivation

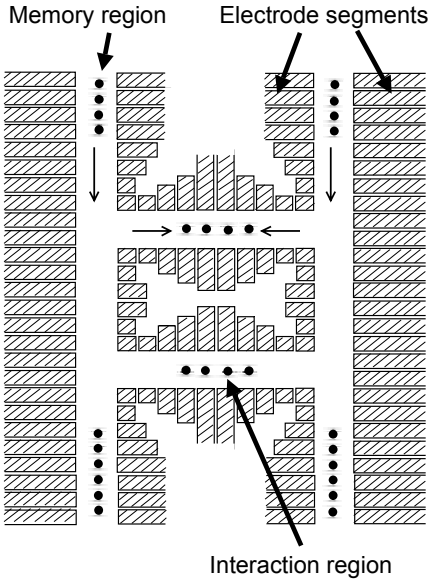

Figure 2.1: Suggested ion trap architecture for quantum computing (figure from [93]).

As described in chapter 1, a major challenge facing experimental quantum computing is scalability. In order to involve many qubits in computing operations, the quantum systems they are based upon need to be available and controllable in sufficient number. For trapped ions an architecture to meet these requirements has been suggested [93, 94] (see figure 2.1). It consists of an ensemble of loading, storage and processing zones as well as junctions to reorder ions in order to facilitate two-qubit gates between any two of them. The aim of the European Microtrap project[1] is to develop, implement and test miniaturized trap geometries based on this concept and share knowledge and experience across a number of different research groups. A primary goal is the development of fabrication capabilities for microstructured ion traps in Europe, which had previously only been realized in the US [95, 96].

[1] http://www.microtrap.eu/

To this end, a number of similar trap geometries were designed, most of them featuring linear trap arrangements. At the time of the start of the project (early 2006) surface-electrode traps were only just emerging and so a three-dimensional design was chosen. While surface traps now offer easier fabrication employing standard methods of photolithography and do not require any assembly post-fabrication, there are still strong arguments in favour of 3D-traps. Using a three-dimensional geometry has the advantage that the electrode structure surrounds the ions. As a result, higher trap-strengths are achieved for the same applied voltages since a larger proportion of the applied voltage contributes to confinement[2]. This is advantageous, since the applied voltages are technically limited, e.g. by arcing in miniaturized geometries. It also minimizes non-linearities in the ions' motion since the region in which the trap can be considered harmonic is larger.

The specific design choice made by the consortium for the trap geometry closely follows the Kielpinski proposal (figure 2.1) and the scale of the trap was determined by the manufacturing techniques available which limit feature-size to tens of μm (see 2.2 for details). The goal of the efforts described in this chapter is to assemble and characterize the trap our group received so that this assessment together with information gathered by other groups in the consortium can be used for the next generation of ion-traps.

Apart from microtraps similar to the one presented here, the project also includes the development and fabrication of a monolithic segmented ion trap at NPL [85].

2.2 Trap description

The trap described here was received by our group as part of the Microtrap collaboration. It is therefore being referred to as the "Microtrap". The chip material is a microstructured gold electrode pattern on alumina wafer. The wafers were manufactured by Micreon[3] and electroplated by MicroGan[4]. The fabrication process involved three stages. First, a laser-machining step to cut the alumina wafers and generate the electrode pattern. This was followed by an electroplating stage to generate a gold layer of $3-5$ μm thickness. Finally, further laser-machining electrically isolated adjacent electrodes and generated tracks leading to the edge of the chip.

The trap consists of three layers, two trap chips and an alumina spacer. Each of these layers is 125 μm thick (see fig. 2.3). It is a multi-zone design with four individual trap arms on a single chip each of which constitutes a segmented linear Paul trap (designated "orange", "purple", "pink", "green"; see figure 2.2). The arms are arranged in a cross-shape and connected by a central junction.

[2] this can be quantified by the "trap efficiency" (see [85])
[3] http://www.micreon.de
[4] http://www.microgan.com

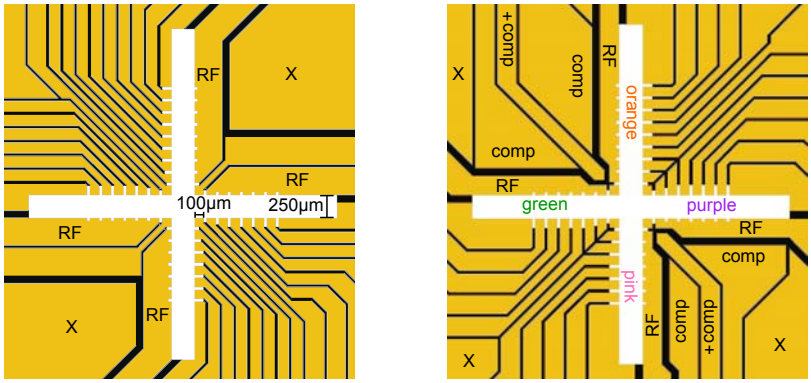

Figure 2.2: Scale drawing of the trapping region of the Microtrap with the bottom wafer (right) and the top wafer (left). Compensation (comp), RF and corner compensation (+comp) electrodes are indicated. Other electrodes carry DC for axial confinement. Floating regions (see section 2.3.1.5) are marked with "X". Trap and electrode dimensions are shown on the left, the colour code for the different traps on the right. See appendix A.2 for complete drawings of the wafers.

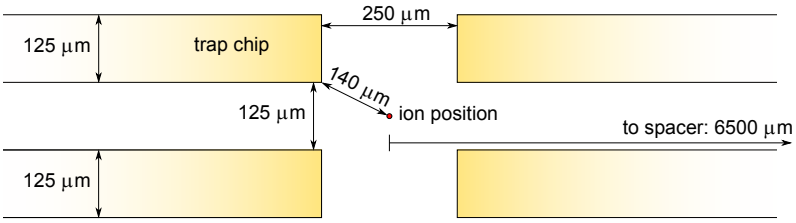

Figure 2.3: Scale cross section drawing of the trap centre showing dimensions. The ion is located at a distance of $140\ \mu$m from the electrodes and 6.5 mm from the insulating spacer.

Figure 2.2 shows the electrode structure on the top side of each of the two wafers. Each electrode is connected to the edge of the chip by a track. When the wafers are arranged on top of each other, each trap arm has a pair of RF electrodes for radial confinement and two sets of DC electrodes for axial confinement. This allows the trapping of ions between the two wafers which are separated by the insulating spacer. The DC electrodes are $100\ \mu$m wide with $30\ \mu$m gaps. Each arm has a pair of compensation electrodes provided on the wafer side facing the ion (top wafer bottom side and bottom wafer top side, see fig. 2.2 "comp" and appendix A.2). In addition the corner electrodes have their own recessed compensation electrodes located between the compensation electrodes for neighbouring trap arms (fig. 2.2 "+comp"). These allow the application of additional compensation voltages in the central junction region. The chips also contain unconnected patches (marked "X"), an issue which is addressed in section 2.3.1.5.

The electrodes wrap around inside the edge of the cross-shaped slit and end on the other side. This can be seen in figure 2.2 on the bottom wafer where the five central DC electrodes end just off the trap slot. The tracks connecting them are on the underside of the wafer.

Figure A.1 in appendix A.2 shows the full schematics of both wafers and the spacer. In order to shield the dielectric as much as possible from the ion, the spacer has a wide clearance around the trap slots. All tracks lead to bond pads at the edge of the top side of the chip to allow the connection to the chip carrier by wirebonding. The top wafer has recesses where the pads on the bottom wafer are located to allow all pads to be arranged along the edge. These recesses are also duplicated on the structure of the spacer. Since the chip will be attached to the chip carrier on the bottom, all bond pads must lie on the top sides of the wafers. For this reason, most via tracks are designed to be on the top sides and the remaining ones lead to bond pads which wrap around at the edges to a set of pads on the top.

The chip is assembled by gluing the two wafers to both sides of the spacer. In order to introduce glue between the layers, each wafer has a set of five small glue holes with a radius of $125\ \mu$m. The three layers must be aligned precisely with respect to each other. As reference points, all three layers have three alignment holes in corresponding locations with a diameter of $375\ \mu$m.

2.3 Trap assembly

Before the three layers of the trap chip could be glued together as mentioned above, the wafers had to go through several preparation steps to rectify faults. Following this procedure, the chip was assembled and attached to the chip carrier which itself had gone through several modification steps to make it fit for purpose. Finally, the bond pads were wire bonded to the contacts on the chip carrier. This section documents these stages constituting the assembly of the trap package.

2.3.1 Trap chip preparation

2.3.1.1 Problems

Six issues were discovered upon the initial inspection of the trap wafers by the Innsbruck group. Firstly, the gold coating had produced an uneven surface finish with a number of bumps and depressions (see fig. 2.4c and b). Secondly, the machining process had left a number of gold "nuggets" protruding from the surface on the DC electrodes. There are six larger nuggets ($\sim 10\,\mu$m) on the top wafer (see fig. 2.4 red dots) and one on the bottom one (see fig. 2.4d and blue dot). Both these and the low surface quality can cause problems with trapped ions since they constitute sharp features on charged surfaces which can be a point for arcing and lead to local variations and inhomogeneities in the electric field. This can cause heating of ion crystals due to a distorted quadrupole RF-field. Local extrema in the DC potential can also make transport of the ions along the trap axis more difficult since they break the site-to-site symmetry from one DC electrode to the next.

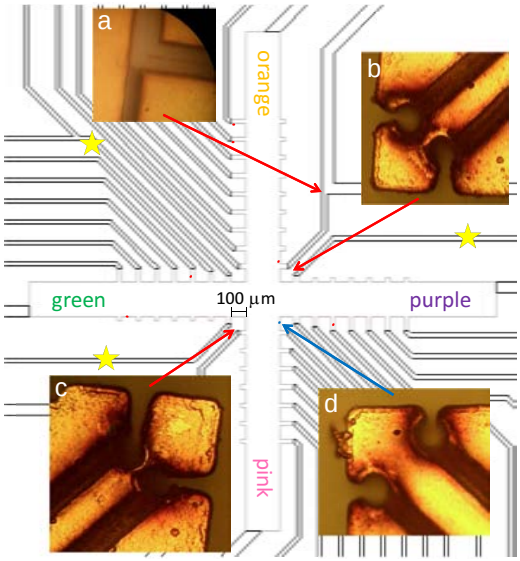

Figure 2.4: Summary of the technical faults discovered on the wafers. The schematic in the background shows the top wafer. Yellow stars indicate electrodes which are shorted together. Red dots indicate nuggets on the top wafer, blue on the bottom (corresponding position). Insets: a) gold dust in the insulating tracks. b) and c) Thin vias connecting two (out of a total eight) corner electrodes. Rough surface finish. d) Nugget on the corner electrode of the bottom wafer. Also, the intact corner electrode via can be seen for comparison with b and c.

The third problem is a layer of gold dust left from the laser machining process in the insulating gaps between the electrodes. Conductive material in these gaps creates the risk of shorting neighbouring electrodes together either through a direct link or through increasing the chance of surface flash-over to occur when voltages are applied to the electrodes.

The fourth issue is a result of imprecisions in the laser machining. On two of the corner electrodes on the top wafer the laser machining holes either side are placed such that the remaining conducting vias are very narrow (~ 5 μm). Upon close optical inspection (see fig. 2.4c) these also look contorted due to the proximity to the machining either side. They therefore might not provide a sound connection to the electrodes. If this is the case, however, it can not be remedied. The bottom wafer fortunately does not present this issue.

Additionally, three shorts have been discovered between corner electrodes and one of their respective neighbouring electrodes (see star markings on fig. 2.4 for positions). This was measured on the bond pads. The bottom wafer presented no shorts.

Finally, a design flaw came to light when we made the voltage assignment plan for the trap. There is a number of conducting regions on the wafers which are not connected to any bond pad and are therefore left floating. These are the patches that are not used for trapping but contain the mounting and glue holes (see appendix A.2). From a trapping standpoint, this is still undesirable since charge can accumulate on them and create uncontrollable fields in the trapping region. The following sections describe our attempts to tackle these problems, where possible.

2.3.1.2 Assembly work stage setup

To facilitate the necessary manipulations on the trap we constructed a manipulation and observation work stage. Two holders for hypodermic needles were mounted on a pair of x-y-z translation stages with micrometre adjustment. The needles were electrically grounded to avoid charging effects that might cause the light wafers to stick to them. The translation stages were attached around the base of an optical microscope[5]. In the centre, either a block for the chip carrier or a base for microscope slides was placed. In order to hold the wafers in place on the microscope slide we glued bits of practice spacer in a square shape onto it (see figure 2.11b). This allowed the manipulation of the wafers with micron precision using the needles. The entire setup was attached to an optical breadboard to move it to the clean room and the wirebonding laboratory which is located in a different building. To pick up the wafers without damaging them we used a suction pen with a rubber tip as well as a pair of tweezers with Kapton coating.

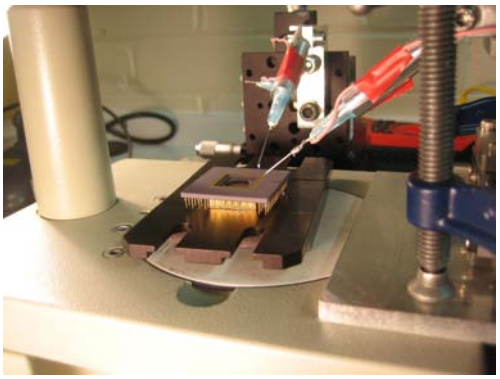

Figure 2.5: Manipulation setup, here with chip carrier

2.3.1.3 Nugget removal attempt

In order to remove the nuggets from the trap wafers, the Innsbruck group had tested two mechanical procedures [97]. For the dislodging of nuggets from the top of electrodes, a needle tip was used. The nuggets in between the electrodes proved to be a bigger problem since the small gap requires an object thin and yet strong enough to be inserted. The two approaches attempted were a thin foil which proved not to be rigid enough and a thin wire which was inserted between the DC electrodes (or "teeth") and pulled out in an effort to detach the nuggets. The fatal result can be seen in figure 2.6. One of the electrodes has broken and is leaning against its neighbour. One of the problems stated by the Innsbruck group was the fact that their particular trap had three laser machining holes at the stem of the electrodes making them thinner and more likely to break (see fig. 2.6).

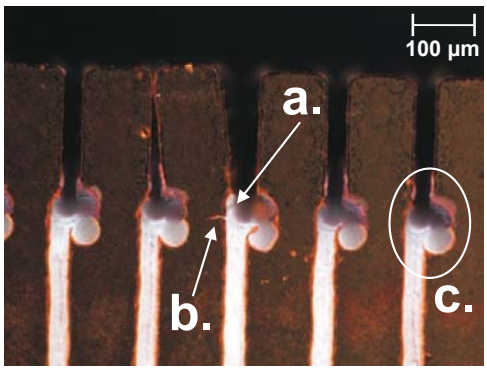

Figure 2.6: Damage caused by "flossing" in a trap used in Innsbruck [97]. The Alumina wafer was cracked (a). The gold coating is torn partly but still holding the electrode on (b). The three laser machining holes (c) at the base are a structural weakness on this particular trap.

[5]MEC-10, 4-50x magnification

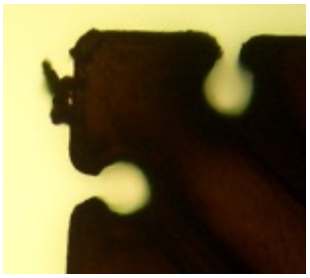

Figure 2.7: Corner electrode nugget.

The electrodes on our own trap are very similar in dimension to the one shown here and the material is identical. Our trap has only one machining hole at each side of the electrode stem but these holes are closer together on the corner electrode leaving the stem to be similar in size ($\sim 50\ \mu$m). There are only four nuggets between electrodes in our trap (see fig. 2.4) and so we had to weigh the risk of damaging our trap against the benefits of removing these. With the voltage differences between neighbouring electrodes likely to be on the order of a few volts only, we deemed the risk of arcing to be low. Three of the nuggets are located on the front of electrodes where they could be more critical for trapping. On the top wafer there is one very small nugget ($< 10\ \mu$m) on the RF electrode in the "orange" trap near the junction and one on the "green" trap RF electrode near the end which is quite large ($\sim 30\ \mu$m) but can be avoided when trapping in this arm. The third is on the bottom wafer on the corner electrode between "pink" and "purple" trap. It too is large ($\sim 40\ \mu$m) but one of the images taken at Innsbruck shows it to be apparently only partly attached (see fig. 2.7).

Additionally it is protruding $\sim 20\ \mu$m into the trapping region. Rather than being an oval lump like the other two, it also seems to have a more spiky structure. It therefore seemed less solid to us and combined with the fact that it appears be the easiest to remove and the most likely to cause problems, we decided to attempt to dislodge it using the sharp edge of the tip of a hypodermic needle.

We placed the needle above the wafer with the edge aligned between nugget and electrode. We then carefully lowered the needle in an effort to dislodge it. The nugget didn't seem to move or bend and when we increased the force, the wafer snapped loose and jumped about $100\ \mu$m to the side. Upon inspection, all the electrodes were intact but unfortunately the nugget seemed unchanged. Rather than exert more force on it, we decided to not risk any further trap damage. None of the nuggets are detrimental to trapping in any one arm and the large flaky nugget we failed to remove will most likely only be a problem for ion transfer between the "pink" and the "purple" trap arm.

2.3.1.4 Etching

With the goal of improving the surface quality, removing shorts and small nuggets as well as dissolving the gold dust, a gold etching step was performed on the trap chips. The etch used was Königswasser (aqua regia), a mixture of hydrochloric acid (HCl) and nitric acid (HNO_3) in a volume ratio of 1:3. Neither of the constituent acids has an effect on gold on its own, but they react to produce gaseous nitrosyl chloride (NOCl) and nascent chloride which are able to oxidize gold and platinum:

$$HNO_3(aq) + 3\,HCl(aq) \rightarrow NOCl(g) + 2\,Cl(g) + 2\,H_2O(l)$$

The gold ions (Au^{3+}) formed in this way are removed by a reaction with the Chlorine ions provided by the hydrochloric acid to give chlorauric acid ($HAuCl_4$). Since both the reagents and the reactants of the mixture are used in the process of dissolving gold, the potency of Königswasser varies over time.

Following a procedure tested by the Innsbruck group [97], we prepared a fresh solution of Königswasser by mixing 120 ml of 32% HCl and 20 ml of 65% HNO_3. After leaving it for 15 minutes, we added 0.5 ml of the surfactant "Triton-X 100". This reduces the surface tension in order to ensure that the insides of the small laser-machined trenches are wetted by the solution. The wafers were then in turn held by a corner with PTFE tweezers, stirred in the solution for 40 seconds and rinsed thoroughly with deionized water. The wafers were then left to dry. The whole procedure was performed in the department's "Class 10000" clean room to reduce the risk of introducing contaminants on the wafers while being able to operate in a fume cupboard during the handling of the acid mixture.

An inspection of the wafer after etching revealed that all the gold dust was gone from the tracks and from between the electrodes. The gold surface had a cleaner, more reflective finish suggestive of an improvement in surface quality. The smaller spikier nuggets on the stems of some of the electrodes were reduced in size, however the larger nuggets described above remained unchanged. This is not surprising since their size is comparable to the gold layer thickness. The three shorts on the top wafer were still present after the etching which means they were not due to gold dust but caused by a fault in the fabrication process. They are not detrimental to trapping in any of the arms and so we did not investigate them further.

Our handling of the trap wafers in the clean room had left a few dust particles on them which we were able to remove with a clean-air duster. We decided subsequently to perform the remaining steps in our own laboratory.

2.3.1.5 Connecting floating sites

As mentioned in section 2.3.1.1, there are a number of conducting patches on the wafers which are not connected to any of the bond pads. During the experiment they can charge up and cause stray fields in the trapping region. Figure 2.8 illustrates the situation with the bottom side of the bottom wafer as an example.

To define their potential we used electrically conductive silver epoxy[6] to connect them to a DC electrode. In order not to influence the trap, we preferably choose the last (elongated) DC electrode wherever possible since it is not necessary for trapping. In the case of patches lying further away, a corner electrode or a compensation electrode was used. The connections had to be made close to the trapping region to make sure the epoxy patches lay inside the clearance region of the spacer (see figure 2.11a).

[6] EPO-TEK H20E

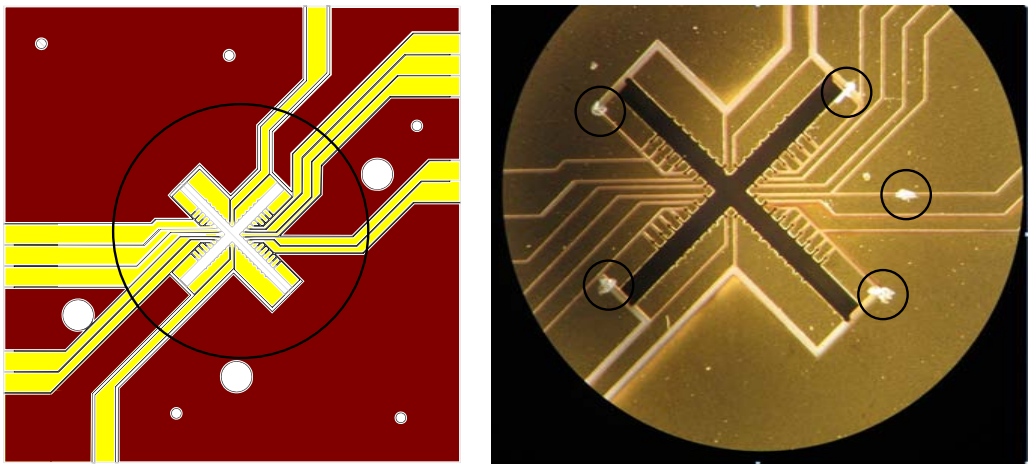

Figure 2.8: Connecting floating sites on the chip. Left: Schematic of the bottom side of the bottom wafer with connected electrodes (yellow) and unconnected sites (red). Right: The circled area on the left is shown in a microscope image. The silver patches (circled) are conductive epoxy painted on to connect floating sites. The chip is aligned with the "orange" trap on the bottom right.

To reliably make the connection between the intended electrodes only, the conductive epoxy had to be applied with a precision of about $100\,\mu$m. In order to facilitate this, we employed a "painting" technique. An organic monofilament donated by one of the scientists involved was cleaned thoroughly[7] in Neutracon and then glued to the tip of a hypodermic needle. With a small drop of conductive epoxy at its tip, this "brush" was moved with one of the x-y-z translation stages under microscope to paint on the epoxy at the required sites. All connections were electrically tested by touching the respective electrodes with a pair of needles and measuring the conductivity. For a map of all the connections made see appendix A.2.

2.3.2 Gluing

The trap is assembled by gluing the two wafers to either side of the alumina spacer. The first step is placing the chip onto the spacer and aligning it carefully using the two mounted needles as manipulation tools and the three alignment holes as a reference. All holes need to overlap with their spacer counterparts so that the spacer surface cannot be seen through the alignment hole any more. This was achieved to $\sim 1\,\mu$m precision. After the alignment, the glue is introduced through a set of five glue holes on each wafer $250\,\mu$m in diameter and subsequently cured. After that, the structure is flipped over so that the spacer is on top and the second wafer can be attached.

Before attempting assembly, extensive tests and practice runs were carried out on spare wafers and spacers to find the optimum procedure.

[7] a method known as "shampooing"

2.3.2.1 Glue choice

The efforts described here built on previous work carried out by Alice Burrell in our group in coordination with Delia Kaufmann from the University of Siegen which had identified two possible choices for the glue, Epotek 353ND (*a*) and Epotek OG142-14 (*b*). The glue has to fulfill a number of requirements for our specific application:

1. A low outgassing rate to make it usable in ultra-high vacuum.

2. The right viscosity both to stick to a needle tip and to run down the glue holes.

3. Reliably curable without danger to the trap.

4. Electrically insulating.

Both glues in question are specified to fulfill requirement 1 and both were found to be workable concerning 2 (see 2.3.2.2). Looking at point 3, glue *a* is heat curing which seemed to us more reliable than the UV-curing glue *b* since we could not be sure that the UV light applied would reach the glue between the trap chips. Uncured glue is a problem not only for reduced adhesion but also for an increase in outgassing.

To evaluate point 4, the glues' electrical conductivity was tested. Two wires were glued to a microscope slide and their distance d measured under the microscope using the travel of one of the needles mounted on a micrometre translation stage. The data and the setup are shown in figure 2.9. Voltages U_1 between 0 and $1000\,\mathrm{V}$ were applied and U_2 recorded. A straight line fit yields a slope m which gives a value for the resistance in the following way: $R = m^{-1} \cdot \frac{1\mathrm{V}}{1\mathrm{mV}} \cdot 1\mathrm{G}\Omega$. To account for the fact that d was $70\ \mu$m for *b* and $40\ \mu$m for *a*, the U_2 values for *b* were scaled up by the factor $7/4$. The results show that the resistances are on the same order of magnitude with b about 30% higher. Also, no arcing occured even at $U_1 = 1\,\mathrm{kV}$. With the DC voltages applied to the trap expected to be on the order of a few volts and the RF peak amplitude a few hundred volts, both glues can be expected to perform without problems. For our higher confidence in the heat-curing process, we settled on using glue *a*, Epotek 353ND, to assemble the Microtrap.

A separate test with UV curing Epoxy (*b*) was carried out with a small air bubble between the glued wires. Arcing occurred at $U_1 = 1000\,\mathrm{V}$ which makes clear the importance of applying glue free of bubbles. The creation of bubbles is unavoidable when mixing the two glue components. A test showed that these can be removed by centrifuging the glue after mixing. However, we found that vigorous shaking of the glue packaging for about 5 minutes gave a layer of glue at the bottom of the pack equally free of bubbles.

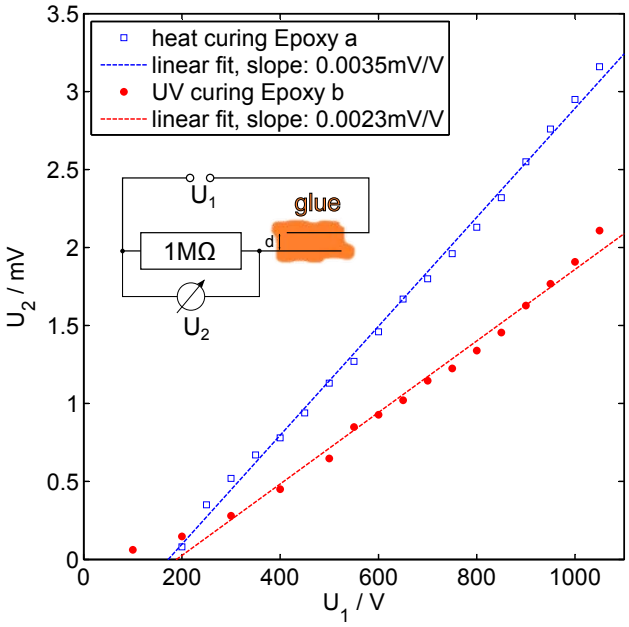

Figure 2.9: Electrical conductivity test data for heat curing (*a*, blue) and UV curing (*b*, red) Epoxy. The data for *b* (red) has been scaled up to represent the fact that the data was taken at $d = 70\ \mu$m as opposed to $d = 40\ \mu$m for *a* (blue). Straight line fits are shown which give the resistances $R_a = 286\,\text{G}\Omega$ and $R_b = 435\,\text{G}\Omega$. The inset shows a schematic measurement setup.

2.3.2.2 Glue application and curing

The application method for the glue was developed using a number of practice wafers and spacers[8] which have the same dimensions as the actual trap chips and are gold coated. They lack the trap slot and electrode structure but have glue and alignment holes identical to those found on the trap.

The application principle is as follows: A small drop of glue is brought in contact with the inside wall of the glue hole which it subsequently runs down. Reaching the bottom it is pulled into the thin gap between the wafers by surface tension. The main obstacle is surface tension on the top of the chip which makes the glue spread out on the top surface rather than run down the hole. Also, contact with a section of the top edge of the glue hole was often found to have enough surface tension to prevent the drop from running down. Instead, the wetted section of the hole edge would grow to a full circle creating a closed layer of glue bridging the hole. Our practice runs produced the following technique which was found reliably to avoid these problems (see figure 2.10). A hypodermic needle mounted on one of the translation stages is modified by bending the very tip downwards around halfway along the tapered section. Using a second handheld needle, a small drop of glue taken from a bubble-free section of the mixed glue packaging is placed on the inside edge of the bent tip. The tip is then introduced into the glue hole so that the drop

[8] bought from Reinhardt Microtech AG, Germany

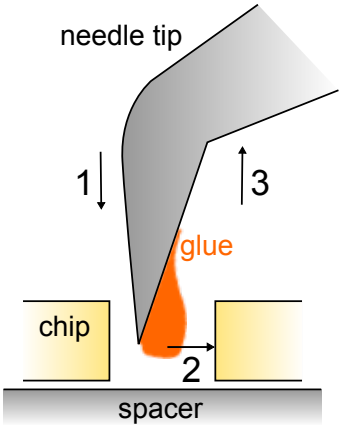

Figure 2.10: Cross-section view: Application of glue using the bent tip of a hypodermic needle. A small drop of bubble-free glue is applied to the side of the tip which is then lowered into the hole using the translation stage (step 1). It is then moved across until the glue drop touches the hole wall (step 2). The needle is then raised leaving the drop sticking to the hole wall (step 3) sinking down and wetting the walls all around the hole. Reaching the bottom, it is pulled by surface tension into the small gap between trap chip and spacer.

is below the top rim. It is then moved across until the drop of glue touches the inside wall which can be observed through the microscope as it starts spreading out along the wall. The needle is subsequently raised up leaving the drop behind on the wall, spreading out around it and running down. When it reaches the bottom it is visibly pulled into the gap between chip and spacer. Observing this process is the criterion for a successful application.

Figure 2.11 shows two microscope images of the trap chip at different stages of the assembly process. In 2.11a the spacer has been attached to the bottom chip and in 2.11b, the top chip is also in place.

To cure the glue, the microscope slide with the chip was placed on a hot plate and covered with an insulated metal enclosure. The chip was then heated up slowly to 100°C and held at that temperature for 15 mins, exceeding the specified minimum curing schedule of 10 mins at this temperature.

The finished trap was wirebonded to the chip carrier which is detailed in appendix A.3. The preparation of the chip carrier prior to this is described in the following section.

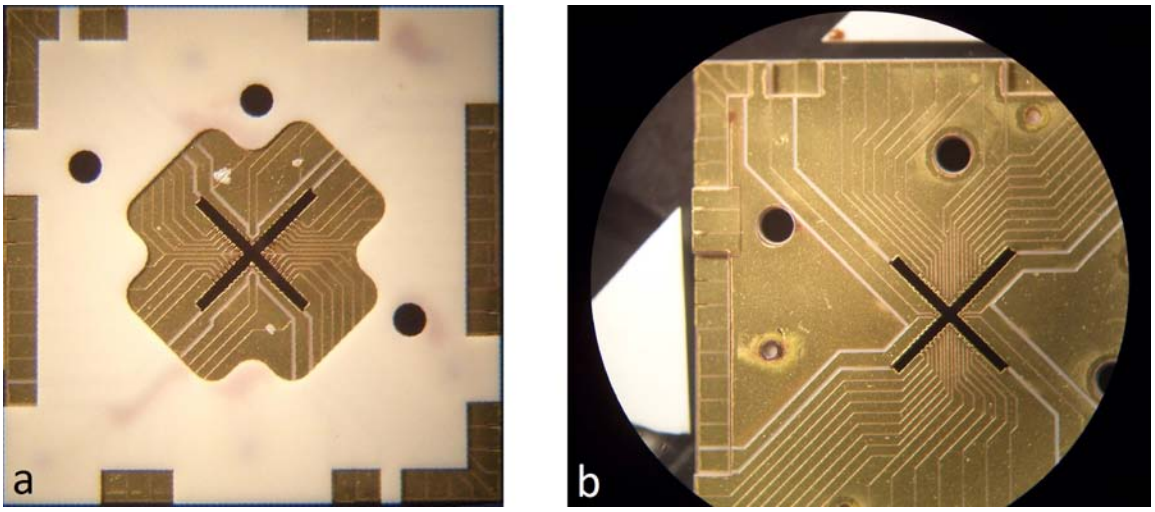

Figure 2.11: a: Trap chip after gluing the first wafer to the spacer. Several silver patches of conducting epoxy (see section 2.3.1.5) can be seen (compare figure A.1). b: Trap after gluing. The alignment holes show that the three layers are well aligned with each other. In the background, the assembly stage consisting of bits of practice wafer glued to a microscope slide is visible. The images are aligned such that the "orange" trap is on the top right.

2.3.3 Chip carrier preparation

The second constituent part of the trap package is the 100-pin chip carrier[9]. It consists of a black alumina ceramic body with a central recess around which 100 gold-coated bond pads are arranged. Each of these is connected to a pin on the back side arranged in a grid pattern forming a ceramic pin grid array (CPGA). Two modifications are required before the carrier can receive the chip. First, the central metalization in the recess needs to be removed without damaging the bond pads. This allows the trap chip to be placed without shorting the different electrode tracks together. Then, a hole has to be cut in the centre to allow optical access to the back side of the chip.

A series of etches was employed to strip the central region of the chip carrier of its metalization. The top metal layer is gold which was removed using an MDF iodine-iodide etch revealing a nickel layer. After removing it with ferric chloride ($FeCl_3$) a third layer came to light unexpectedly[10]. We identified it as tungsten and removed it using a solution of 30% hydrogen peroxide at 70°C. To protect the bond pads on the side of the recess from the various etching agents applied, they were covered by a strip of Kapton tape.

After the successful removal of the metalization, we had a hole of 1 cm diameter cut in the centre of the chip carrier. Chipping prevents the use of a rotational drill on ceramics so an ultrasonic cutter was used. It consists of a metal cylinder which vibrates at an ultrasonic frequency. It is placed on the ceramic using a carbon particle paste as the abrasive. The process takes several hours to cut through the 2 mm thick ceramic body. The subsequent removal of the carbon abrasive proved difficult since it would not yield to any organic solvents in an ultrasonic bath. Subsequently, a mechanical method was employed using a mild dental abrasive and an electric polishing tool[11] which successfully got rid of all the deposited carbon.

Finally, the trap chip was glued into the central recess of the chip carrier (figure 2.12).

[9] Kyocera drawing number IPKX0F1-8180AB
[10] this was not mentioned in the manufacturer's data sheet
[11] Braun 2150

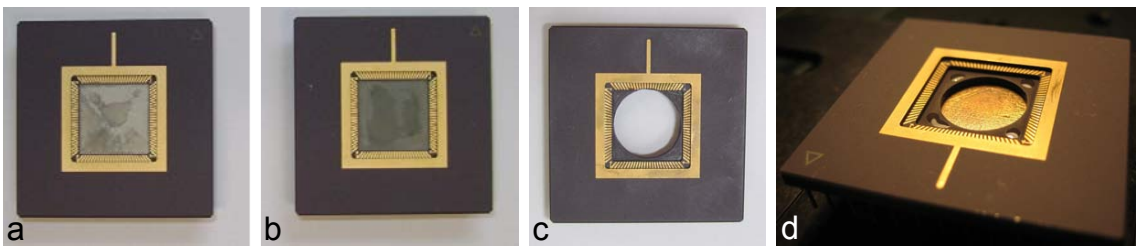

Figure 2.12: a: Chip carrier after the removal of the gold layer, the nickel layer is visible. b: The tungsten layer after the removal of the nickel. c: The stripped chip carrier after the cutting of the central hole (test piece, hole not placed centrally). The residual carbon abrasive can be seen. d: The chip carrier during package assembly. Four glue patches are visible.

2.4 Experimental setup

This section describes the experimental setup surrounding the trap. It consists of the vacuum chamber housing the trap, the voltage supplies for the trap DC and RF as well as the calcium ovens, the optical setup to provide the cooling and photo-ionization lasers and the imaging optics to collect and to observe the fluorescence.

2.4.1 Vacuum system

2.4.1.1 UHV chamber and feedthroughs

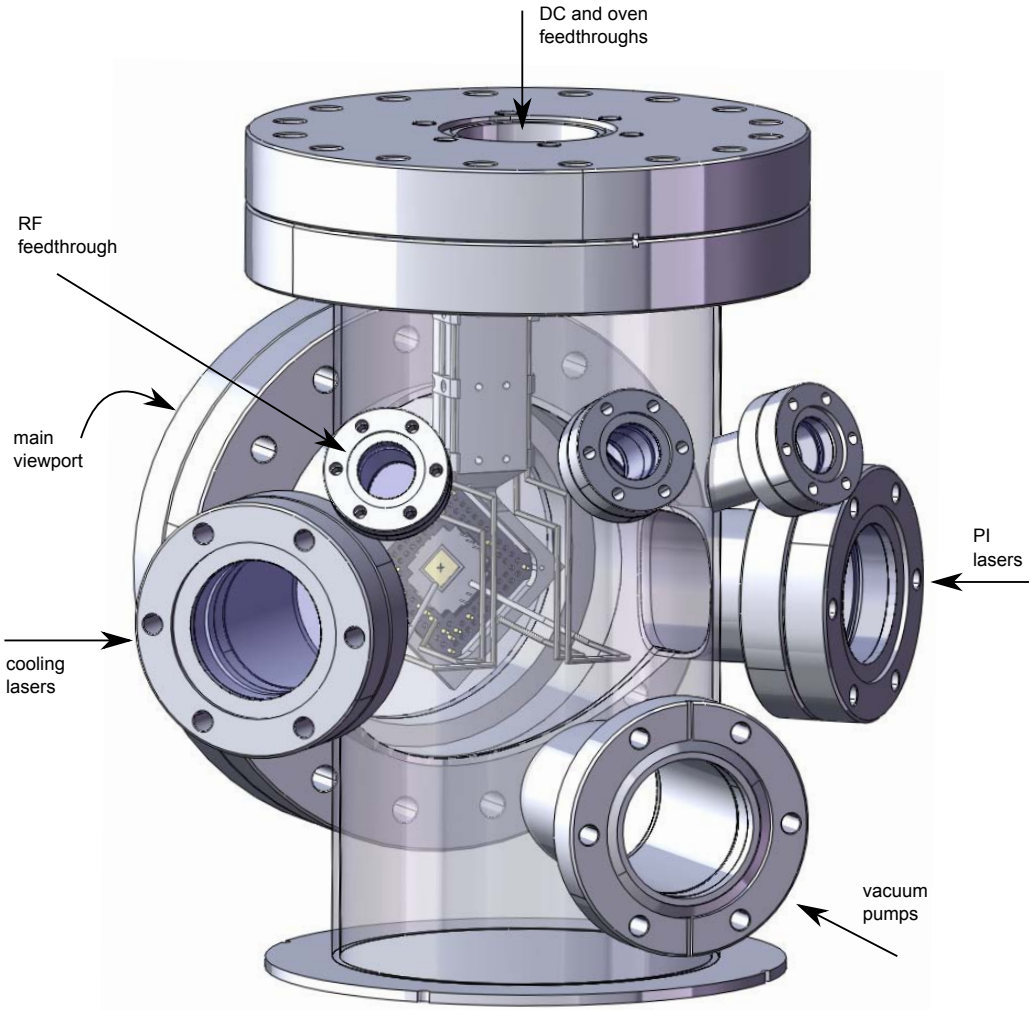

Figure 2.13: 3D drawing showing the vacuum chamber housing the trap. The model was created to scale in SolidWorks. The walls of the main tube are shown transparently so that the chip arm holding the trap, the pin receptacles in the vespel sockets and the ovens can be seen. The eight flanges connecting to the chamber are shown (see text for description). RF feedthrough and CF35/CF63 cross on the top not shown.

The trap is housed in a custom-built[12] vacuum chamber with eight CF flanges of varying size[13]. A 3D construction drawing can be seen in figure 2.13. The chamber has two CF100 flanges, one on the front for the main view port and one on the top. The latter holds an CF100-to-CF35 adapter on which the trap arm is mounted. The main chamber also has three CF35 flanges, one on each side aligned at $45°$ to the main viewport to provide access for laser beams and one on the back through which the pumping is performed. Finally, there are three CF16 flanges on the back, all at an angle of $20°$ to the horizontal facing down towards the centre of the main flange. The two outer ones are aligned at an angle of $15°$ to the centre. The central and left one have view ports on them to introduce laser beams with a vertical component while the third holds the feedthrough for the RF supply.

The CF100-to-CF35 adapter on the top has a CF35/CF63 cross attached (not shown in fig. 2.13), the top of which holds a 4-way feedthrough for the oven supply. The voltages for the 76 different DC electrodes are supplied through four 25-way ribbon cables[14], one for each trap arm, which are plugged into 2x25pin SubD feedthroughs[15] in CF63 flanges mounted on either side of the cross. Due to the high individual failure rate for each of the 50 sealed pins during the bakeout process, these feedthroughs both developed leaks and had to be replaced.

The ultra-high vacuum in the chamber with a pressure of $1.0 \cdot 10^{-10}$ Torr is maintained by three pumps: an ion pump[16], a titanium-sublimation pump housed in a tube of $400\,\mathrm{cm}^2$ internal surface area which is water-coolable through a double-helix of copper-tubing[17] wound around the outside, and a chemical sorption pump[18]. In order to monitor the pressure, an ion gauge[19] is used. The chamber is shut off using an all-metal valve[20]. The chamber went through a number of baking stages: First, a hard bake at 400°C with only the steel components, ion-gauge and Ti-sub pump. Then a medium bake with the feedthroughs, cables, ion and sorption pumps as well as the ovens installed (250°C) and a final soft bake (150°C) with the trap and the viewports in place. The final pressure achieved is about an order of magnitude higher than in other systems in our laboratory. We believe this is due to the large amount of adhesives such as Kapton tape and glue used inside the system.

Mounted on the trap arm is a chip socket consisting of two UHV-compatible Vespel SP-3 plates between which pin receptacles[21] are held. Into these receptacles are crimped either the individual strands of 25-way ribbon cables for the DC supply or Kapton-dipped

[12] VACOM ref. SPE-2008106040

[13] hence its nickname "Octoflange"

[14] Kurt J Lesker part FTAK2512P, 28AWG Kapton-coated silver-plated copper wires with monofilament PEEK weaving and a PEEK D-sub connector

[15] Kurt J Lesker IFDGG251056X

[16] Varian Valcon Plus 20 Diode, 27l/s

[17] thermal contact provided with heat paste (Electrolube HTS Silicone Heat Transfer Compound)

[18] SAES Getter GP50 Mk2

[19] Varian UHV-24P with x-ray limit of $5 \cdot 10^{-12}$ Torr

[20] Kurt J Lesker part VZCR40R

[21] MILL-MAX 0672-4-15-15-30-27-10-0, gold-plated brass shells, gold-plated beryllium copper contacts

copper wire[22] to supply the RF. This socket will hold any CPGA package and therefore the vacuum system is able to accommodate any 3D trap packaged in this way.

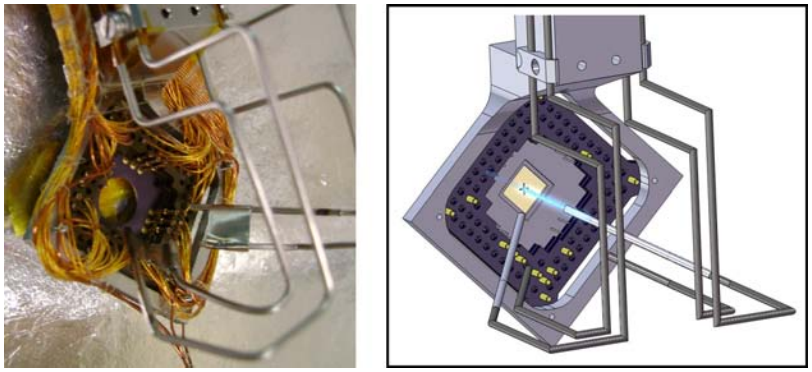

Figure 2.14: Right: A 3D construction drawing (SolidWorks) of the trap arm with ovens. The stream of neutral calcium from the right oven is indicated in light blue. Left: A photograph of the assembled trap arm. The vespel sockets connected to the wires can be seen. Each wire is part of a 25-way ribbon cable (see text). A test chip carrier is plugged in on which a Kapton tape cross marks the trap location. The calcium ovens can be seen either side (see section 2.4.1.2).

2.4.1.2 Calcium ovens

The calcium ovens are bolted to the side of the trap arm. They are mounted directly on their supply wires and are insulated against the trap arm with Kapton tape. Following the design developed in [98], they consist of a steel tube of 2 mm outer diameter stuck firmly onto a 1 mm steel wire and fixed by a spot-weld. Around the base of the tube tantalum foil is wound which is used to connect it to a second steel rod. The foil is again attached to both wires with a number of spot-welds. The tube is filled with small pieces of calcium immediately before the system is pumped down to avoid oxidation. Running current through the wires will predominantly heat the bottom end of the tube surrounded by the Ta foil where the calcium is located. Evaporating calcium escapes through the long tube creating a collimated stream of neutral calcium (see figure 2.14).

The oven design was tested using a prototype in a small separate setup using a CF35 T-piece. The oven was mounted to point at a microscope slide placed in front of a view port. After pumping the T-piece down to $5 \cdot 10^{-6}$ mbar, we slowly increased the current until at 7 A a grey shading of the glass slide from the deposited calcium became visible. We left the oven on for 20 mins to get a distinct calcium layer. The glass slide showed a central spot where most of the material had been deposited, surrounded by a grey disk of lower density. From the sizes of these and the distance between oven tip and glass slide, we estimated the full exit angle of the core calcium beam to be $12°$ and the maximum scattering angle $40°$.

[22] 311K-KAP-060

In the experiment, the ovens are placed below the trap chip either side pointing upwards at its centre at a distance of 1 cm so that the core beam covers the entire cross area. They are aligned to be $\sim 80°$ from the photo-ionization beam direction through their corresponding side viewport to allow loading with only a small Doppler shift. During the experiment, our typical oven current[23] for loading ions was 3 A.

2.4.1.3 B field coil

Right in front of the main viewport, a single B-field coil is placed. It has 132 turns and a resistance of $2\ \Omega$. The nominal magnetic flux density at the position of the ion is $B = 6.6$ G/A. It provides a magnetic field perpendicular to the chip surface. To provide laser light which is nominally $\sigma^{\pm}$-polarized, the beams coming through the two view ports either side must be vertically polarized. In the experiments described below the coil was run[24] at 0.7 A (4.6 G).

2.4.2 Voltage supplies

We decided to use the "orange" trap for initial trapping since it has the most DC electrodes and therefore would allow trapping even if some had become disconnected or shorted. This section describes the provision of voltages for radial and axial confinement in this trap arm.

2.4.2.1 RF resonator

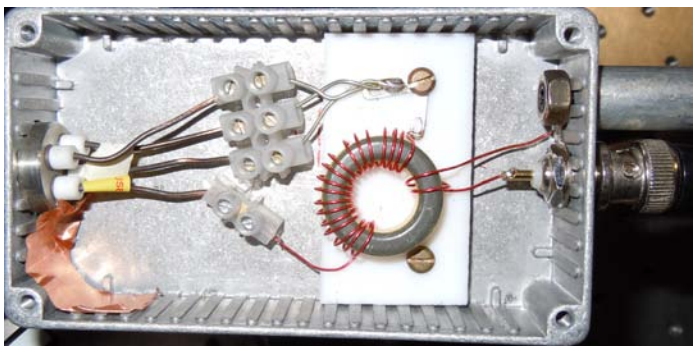

Figure 2.15: Photograph of the RF-resonator. The high voltage side of the toroid is connected to the "orange" trap RF wire on the feedthrough (left), the wires for the other traps are tied to ground.

The radio frequency for the radial confinement in the trap is generated by a synthesized function generator[25] and then amplified by a toroidal transformer. The toroid[26] has an outer diameter of 23 mm and 18 turns on the high and 1.5 on the low voltage side. The

[23] Power supply used: TTi TSX 3510
[24] Power supply used: TENMA 72-6152
[25] SRS DS345
[26] Micrometals T94-6

loaded resonator quality factor Q is about 150. A direct measurement on the high voltage side by coupling through a low capacitance (1pF) gave a step-up factor of $Q_{stepup} = 15$ which is reasonable given that it is just above $\sqrt{Q}$. The centre resonance frequency is $\omega_{RF} = 2\pi \cdot 20.18\,\text{MHz}$. Figure 2.15 shows the connected resonator. For the work presented here, the RF voltage was only applied to the "orange" trap RF electrodes.

2.4.2.2 DC voltages

The DC voltages for the "orange" trap are provided by a 24-channel DAC evaluation board[27] controlled by a LabView[28] program. Each of the trap electrodes can be addressed individually (see Appendix A.4.1 for a wiring plan of the trap). The program also allows adjustment of the offsets on the two sets of DC electrodes (top and bottom wafer) by entering values for their sum and difference. This is used to compensate the ion by changing its position while maintaining the axial trapping potential. To reduce pick-up of the RF

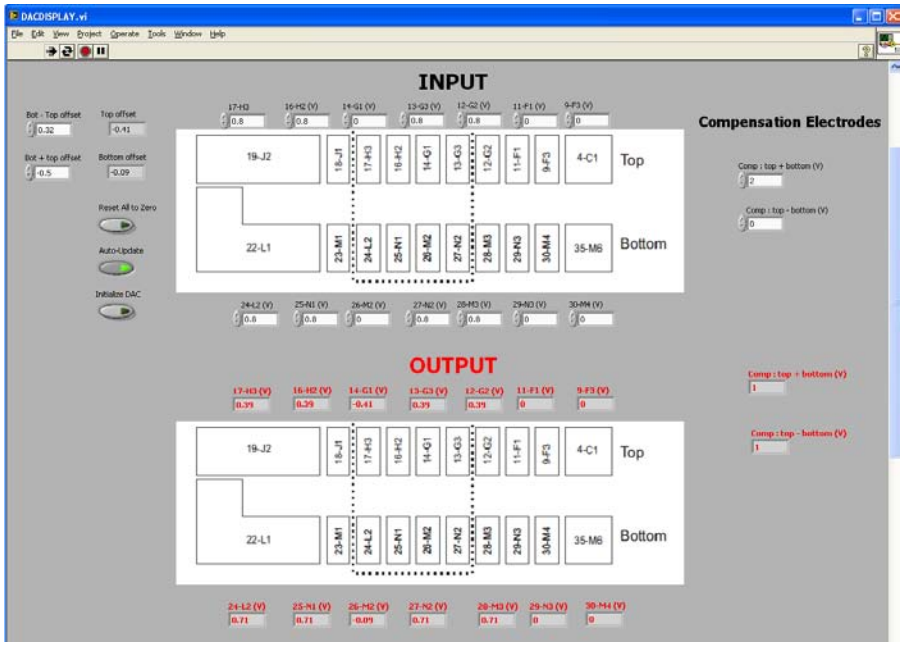

Figure 2.16: Screenshot of the LabView program to control the DAC evaluation board used to apply the trap DC voltages. Each electrode can be addressed separately. For compensation, an offset (sum and difference) can be applied to both the bottom and top set of DC electrodes. The settings show typical values used for trapping. The compensation electrode values (right) were not connected to the trap (see section 2.4.2.3).

voltage on the DC electrodes, a filter board is connected directly to the 25-pin SubD plug in the DC feedthrough. It contains a PCB with an RC filter for each electrode with $R = 10\,\text{k}\Omega$ and $C = 1.8$ nF which corresponds to a cut-off frequency of $f_c = 1/(2\pi RC) = 8.8$ kHz.

[27] Analog Devices EVAL-AD5370/72/73BZ
[28] National Instruments LabView 2009

2.4.2.3 External HV supply and "tickle"

After trapping we found that one of the compensation electrodes (8-E1) was shorted to ground (see appendix A.4.1). The second compensation electrode therefore needed a higher voltage than the 10 V provided by the DAC. Two pairs of breakout connectors were subsequently added to the DAC box one of which allows an external voltage to be applied to the compensation electrodes. The other pair allows access to the output voltage on the compensation electrode pins of the DAC so that the arrangement can still be used to apply DAC voltages to the compensation electrodes by connecting the corresponding breakout plugs. A high voltage supply [29] was used to provide the compensation voltage on the second compensation electrode (32-M5).

Since this electrode was now easily accessible, we also used it to apply the "tickle" voltage used to measure the trap frequencies. The tickle voltage was provided by an arbitrary waveform generator[30] and capacitively added to the DC of the compensation voltage.

2.4.3 Optical setup

Figure 2.17 shows a drawing of the optical setup around the vacuum chamber. The lasers are located on a separate experimental table and brought to the experiment through single-mode optical fibres. The cooling laser at 397 nm is split between the main beam and a diagnostic beam which is sent onto a photodiode. The photodiode signal is used to stabilize the intensity of the experimental beam (to $\leq 1\%$). The red repumper lasers at 866 nm, 850 nm and 854 nm are superimposed on the laser table and sent through the same fibre. Both the cooling and the repumping beams pass half-wave plates to set their polarization to vertical which makes them nominally $\sigma^{\pm}$-polarized at the ion. The two beams are superimposed at a mirror coated for the UV to form the cooling beam. The beam is focused down using a dichroic lens[31] and then sent through the trap slit via a dichroic mirror[32]. Before entering the side viewport a small portion of the beam is split off and sent onto a beam profiler[33] at the same distance from the beam splitter[34] as the trap centre in order to measure the beam spot sizes at the ion and to ensure superposition of the red and blue beams. The spot sizes (beam diameter at $1/e^2$ peak intensity) are 63 μm for the 397 nm beam and 105 μm for the red beams.

The red beam can alternatively be sent onto the ion via a path through the front window at $60°$ to the vertical. The beam is expanded threefold using a telescope and then focused down with a convex lens ($f = 500$ mm). This makes it possible to place the lens

[29] SRS PS310
[30] Agilent 33220A
[31] ThorLabs AC 254-250-A1
[32] UFM 10R
[33] Thorlabs BP:104
[34] ThorLabs BSF-10-A

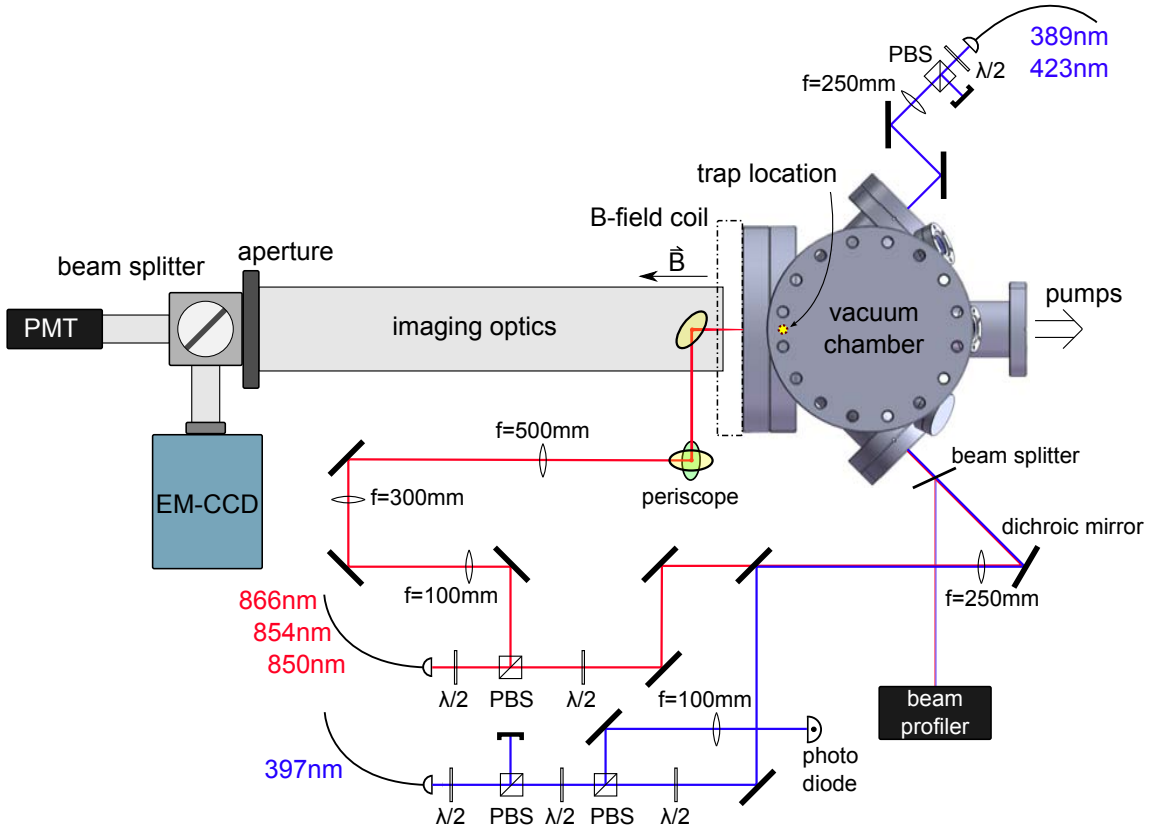

Figure 2.17: Schematic of the optical setup. The trap location inside the vacuum system is indicated by a yellow and red circle. The beam paths for cooling (397, 866, 850, 854 nm) and photo-ionization (423 and 389 nm) are shown as well as the imaging optics and magnetic field coil (see text).

before the periscope and still achieve a spot size of $\sim 80\ \mu$m. This beam is used for micro-motion compensation in the vertical direction (see section 2.6.2).

The photo-ionization beams at 423 nm and 389 nm (see section 4.2.8.1 for details) are superimposed on the laser table and sent through the same fibre. They are focused down and sent through the side viewport at 90° to the cooling beam. The oven under the cooling beam (at $\sim 80°$ to the photo-ionization beams) was used for loading. In front of the main view port the position of the magnetic field coil is indicated by a dotted line. Beyond that, the imaging optics (see section 2.4.4) is shown.

2.4.4 Imaging system

The imaging system was originally constructed by Alice Burrell (née Myerson) and is used on the experiment with minor modifications. It is depicted in figure 2.18. Fluorescence from the ion is collected using a Nikon objective lens[35] with a focal length of 66.75 mm and a large numerical aperture of $\sin(\theta) = 0.29$. Mounted on an xyz-translation stage it

[35] Nikon WD 45

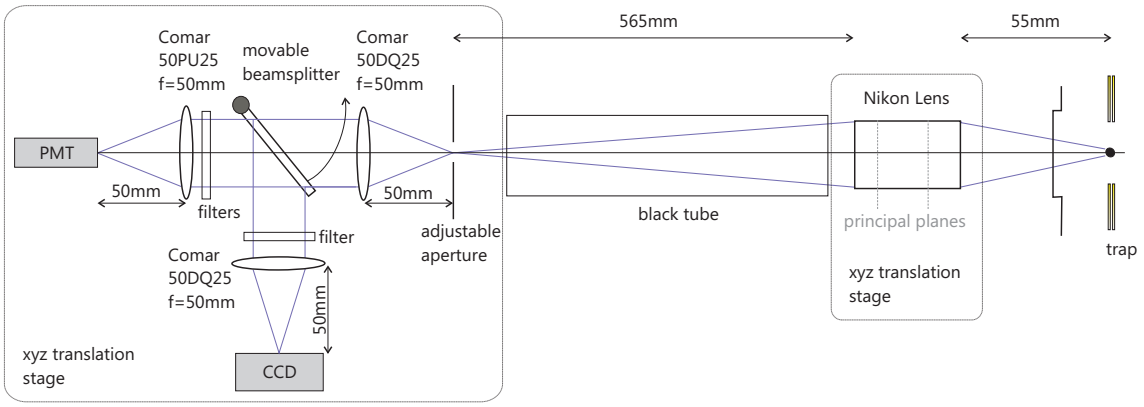

Figure 2.18: Schematic drawing of the imaging system. Light from the ion is collected using a lens system and imaged on either the PMT or the CCD camera (see text). Figure modified from [99].

images the ion with $7.7\times$ magnification onto a set of adjustable shutters. They allow the stopping down of the field of view. This is important when collecting light on the PMT in order to block out light scattered from the electrodes. Typically, the shutters are closed to a square aperture of $200\ \mu$m (corresponding to $25\ \mu$m at the ion's location). Using a pair of lenses with a focal length of 50 mm, the shutter plane is re-imaged on the PMT with $1\times$ magnification. A movable beam splitter with reflectivity $R = 90\%$ can be placed in the beam path to alternatively send most of the light onto a CCD camera[36] instead which gives a live image of the trapped ion(s). With opened shutters, this arrangement is used to find the focus of the objective by imaging the trap electrodes and to align the laser beams with respect to the trap structure.

To cut down further the background light on the PMT, a set of two interference filters[37] is used to block room lights and scatter from the photo-ionization beams at 423 and 389nm. There is no background from the infra-red laser since the PMT is only sensitive in the visible and ultra-violet. The camera does however detect infra-red which is why a glass filter[38] is placed in front of it. There are no other filters in front of the camera, since room lights and the PI beams need to be visible for alignment.

In order to align the imaging system, a small camera[39] was mounted with its CCD in the position of the PMT window. The system was then aligned such that the trap centre was imaged onto the centre of the camera chip. To find the right z-position, the top of the trap chip was brought into focus. Then the objective lens was moved the correct distance[40] towards the trap.

The overall detection efficiency of the system was measured using a pulsed method [100] to be $\eta = 0.248\% \pm 0.003\%$. This includes the PMT quantum efficiency.

[36] Andor Luca DV 437/BU7
[37] Semrock FF01-377/50-25 and FF01-406/15-25 with a combined transmission of 86% at 397 nm
[38] Schott BG38
[39] PULNiX PE 2015
[40] The width of the top wafer $+\ 0.5$ times the width of the spacer: $190\ \mu$m.

2.5 Trap modeling

This section describes the computer simulations of the trapping fields carried out to determine a good set of voltage parametres as a starting point for trapping. As trapping has since been achieved (see section 2.6.1), the model can be compared to experimental data to evaluate the quality of the representation (see section 2.6.3). It can also be used to obtain additional information about the trap which are not easily accessible experimentally, such as an estimate of the trap depth (see section 2.5.3). To make this comparison straightforward, the simulations presented here show a DC voltage configuration typically used in the experiment. It consists of a positive voltage on two electrode pairs either side of a grounded centre electrode pair between which the ion is trapped. The two outermost electrode pairs are also grounded (we write this configuration $0 + +0 + +0$).

2.5.1 Simplified trap model

Paul traps only allow trapping in a certain voltage parameter regime, known as the stability region. To trap for the first time, an estimate of the geometric factors[41] is needed. These translate the voltages applied to the electrodes into the electric potential at the ion's location in the trap centre. To achieve this, a simple computer model was constructed approximating the electrode structure in any one arm of our trap. The model is shown in figure 2.19. It consists of seven pairs of DC electrodes and two simplified RF electrodes on which the small grooves opposite the DC electrode gaps are omitted. Using the boundary element program CPO[42], the potential in the centre resulting from applying a voltage to one or more of the electrodes can be calculated on a spatial grid. Fitting harmonic potential curves to these results yields the geometric factors.

2.5.2 Trap parameters and geometric factors

The ion moves in a potential of the following form [101]:

$$\begin{aligned}\Phi(x,y,z,t) &= \Phi_{\mathrm{stat}}(x,y,z) + \Phi_{\mathrm{RF}}(x,y,t) \\ &= Q_z\,[z^2 - \frac{1}{2}(x^2+y^2)] + Q_r\,\cos(\omega_{\mathrm{RF}}\,t)\,(x^2-y^2)\end{aligned} \tag{2.1}$$

with the quadrupole amplitudes

$$Q_z = \frac{\alpha_z\,V_{DC}}{z_0^2} \tag{2.2}$$

$$Q_r = \frac{\alpha_r\,V_{rf}}{\rho_0^2} \tag{2.3}$$

[41] also known as "shielding factors"

[42] Charged Particle Optics Program 3D, Version 5.6 (2004)

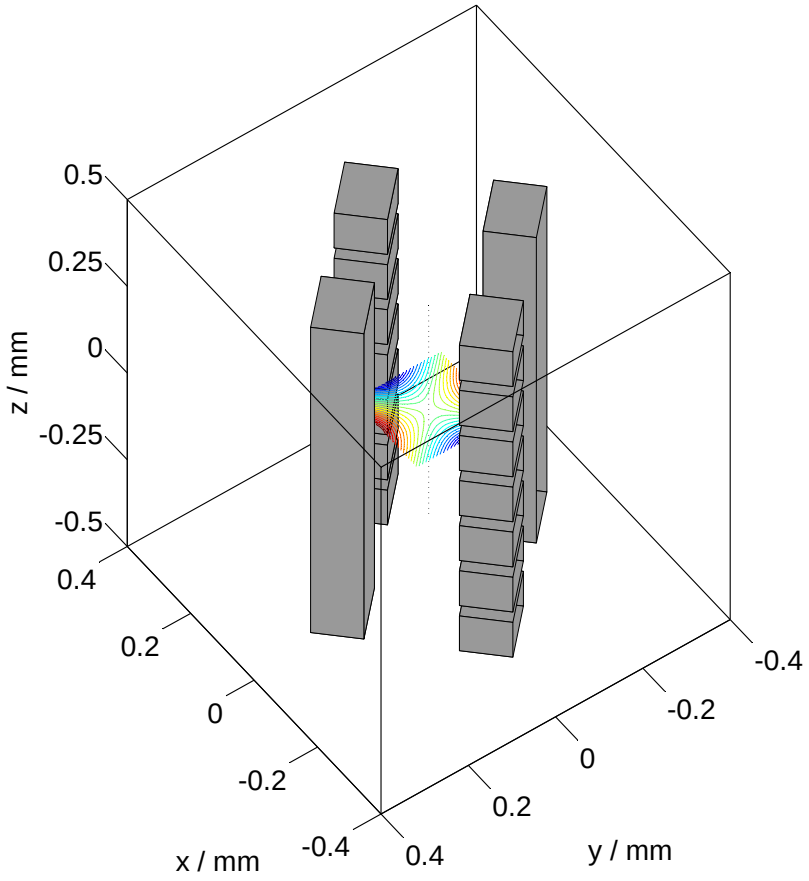

Figure 2.19: Simplified trap model used for the CPO simulations. The electrodes (two elongated RF and seven pairs of DC electrodes) are shown in gray. The trap axis is indicated by a dotted black line. In the centre, a surface plot of the quadrupole potential obtained by applying voltage to both RF electrodes is shown.

Here, z_0 and ρ_0 are the distances to the DC and RF electrodes respectively and $\alpha_{z/r}$ are the axial and radial geometric factors. With the charge $+e$ and mass m of the ion, the axial and radial trap frequencies are

$$\omega_r = \frac{\omega_{\mathrm{RF}}}{2}\sqrt{-a + \frac{q^2}{2}} \tag{2.4}$$

$$\omega_z = \sqrt{\frac{2eQ_z}{m}} \tag{2.5}$$

with the axial and radial trap parameters a and q given by

$$a = \frac{4e}{m\omega_{\mathrm{RF}}^2}Q_z = 2\frac{\omega_z^2}{\omega_{\mathrm{RF}}^2} \tag{2.6}$$

$$q = \frac{4e}{m\omega_{\mathrm{RF}}^2}Q_r \tag{2.7}$$

Implicit in expression 2.4 is the criterion for a stable trap: $a < q^2/2$.

By applying 1 V to the RF electrodes in the CPO simulation, we get the radial quadrupole potential (see fig.2.19, central surface plot). By fitting a second order polyno-

mial along the x- and y- directions to this potential, the factor α_r/ρ_0^2 can be obtained (see eq. 2.1). This factor yields the quadrupole amplitudes at any applied voltage by multiplication (see eq. 2.3). The fits are shown in figure 2.20. The result is $Q_r/V_{rf} = 2.34 \cdot 10^7\ \mathrm{m}^{-2}$.

Using the same procedure with 1 V on four pairs of DC electrodes leaving the central and outermost pairs grounded, we estimate the potential in the axial direction. The quadratic fit results in a quadrupole amplitude $Q_z/V_{DC} = 8.88 \cdot 10^6\ \mathrm{m}^{-2}$ as presented in figure 2.21. This corresponds to an axial trap parameter of $a/V_{DC} = -0.0053$.

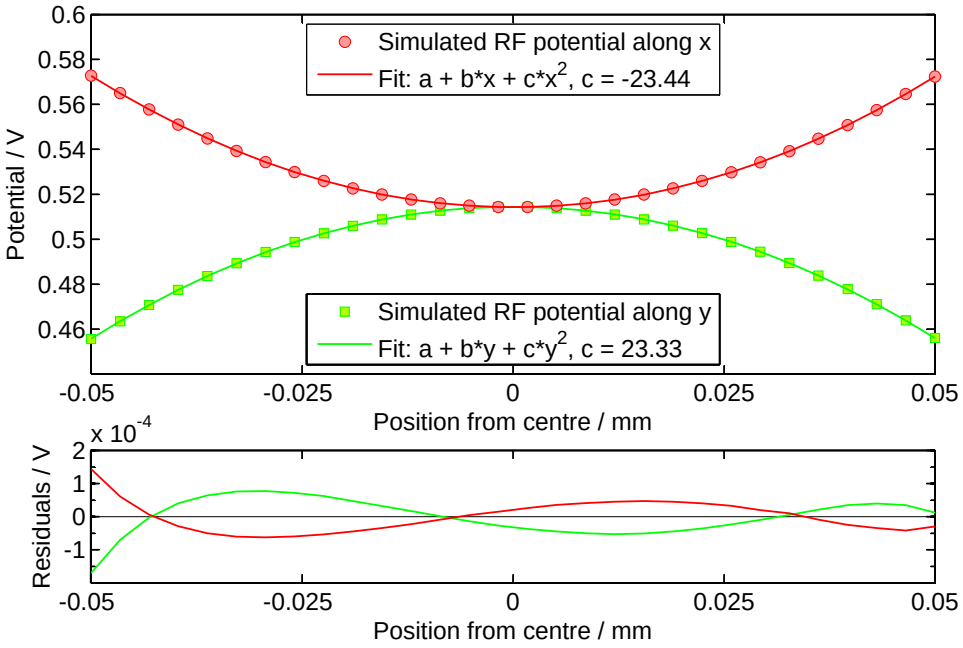

Figure 2.20: Quadratic fit along the two radial directions of the simulated RF potential to obtain Q_r. The factors $c = 23.33$ and -23.44 match closely in magnitude indicating a symmetric field along the trap centre. The other fit parameters are $b_x = 0.0033$, $b_y = -0.0029$ and $a_x = a_y = 0.514$. We believe the asymmetry visible in the residuals to be a numerical artifact in the simulation (e.g. caused by meshing).

The DC potential not only creates a potential well along the trap axis. It also creates a field that pushes the ion radially away from the centre. This has to be overcompensated by the radial pseudo potential in order to create a stable trap (compare equation 2.4). To get an estimate of the antitrapping potential we investigate the DC potential along the y axis which is perpendicular to the alignment direction of the DC electrodes (x axis, see figure 2.19). Figure 2.22 shows the simulated potential including a second order polynomial fit. From the second order parameter, we get $Q_z^{anti}/V_{DC} = -11.4 \cdot 10^6\ \mathrm{m}^{-2}$. This corresponds to an axial anti-trapping parameter of $a/V_{DC} = +0.00682$. This value is larger than the trapping a parameter which is owed to the fact that the DC electrodes are placed off-axis and are therefore giving a large radial contribution to the overall potential. Along the x-axis, the antitrapping is practically flat as expected from the electrode arrangement.

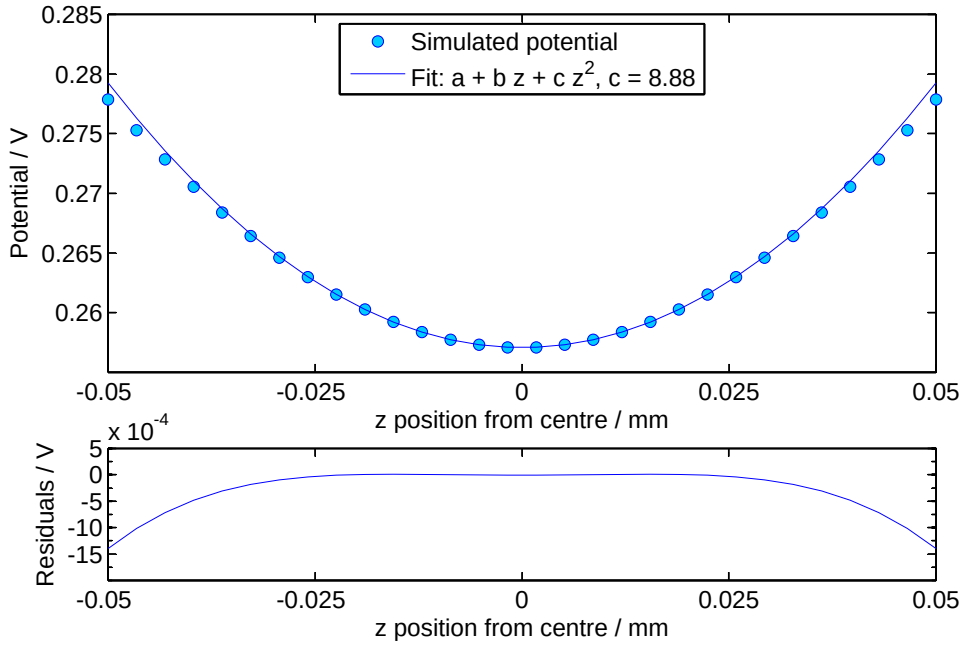

Figure 2.21: Quadratic fit along the axial direction of the simulated DC potential to obtain Q_z. Given the DC electrode size of 0.1 mm, the potential is only expected to be harmonic in the centre of the region shown. Therefore only the central points up to $z = 0.025$ mm were used for the fit. $c = 8.88$ is used to obtain $Q_z/V_{DC} = 8.88 \cdot 10^6\ \mathrm{m}^{-2}$ and the other fit parameters are $b = 0.00001$ and $a = 0.257$.

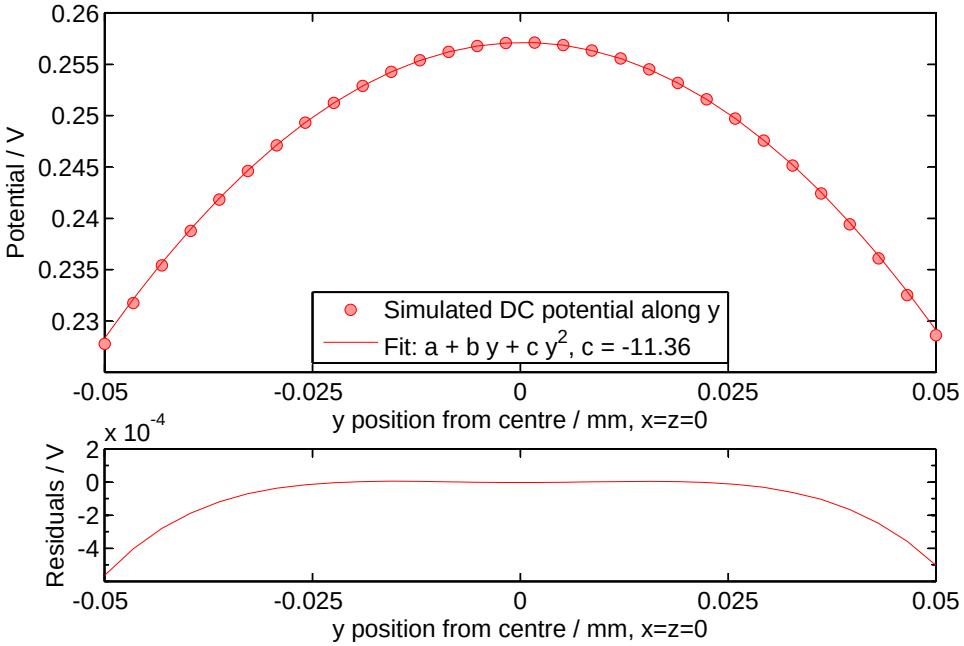

Figure 2.22: Quadratic fit along one of the radial directions (y) of the simulated DC potential. The fit parameters are $a = 0.257$, $b = 0.0078$ and $c = -11.36$ from which we get get $Q_z^{anti}/V_{DC} = -11.4 \cdot 10^6\ \mathrm{m}^{-2}$. As above, only the central points up to $z = 0.025$ mm were used for the fit.

2.5.3 Trap depth estimate

The trap depth is the lowest possible potential difference a trapped ion has to overcome to escape the trap. In our case, this is along the axial direction where the ion can leave the trap without approaching any of the electrodes carrying the RF potential of around $100\mathrm{V}_{pp}$. The DC voltages are not applied by endcaps as in a classical Paul trap and from their off-axis position only create a potential barrier which is low compared to the applied DC voltage. Figure 2.23 illustrates the potential along the z axis. On top of the barrier, the DC electrodes either side let the potential rise further in the radial direction to create a saddle point. For a singly charged ion, the difference between the potential at the bottom of the well and at this saddle point corresponds to the trap depth. In our case, the simulation shows it to be $0.108\,\mathrm{eV}/V_{DC}$.

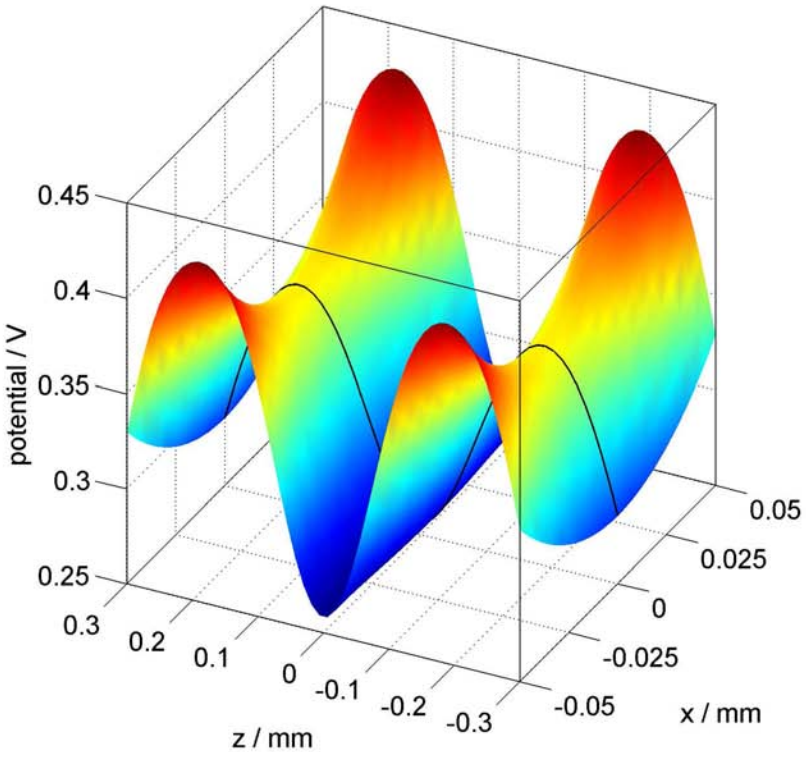

Figure 2.23: DC potential with marked ion escape route (black line) along the trap axis (z-direction). The potential difference from the bottom to the saddle point is $\Delta\Phi = 0.108\ \mathrm{V}/\mathrm{V}_{DC}$. At a typical DC voltage of 0.8 V the trap depth is therefore 0.088eV.

2.6 Results

2.6.1 Trapping ions

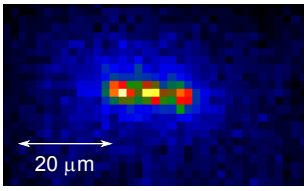

Figure 2.24: Camera image of a three-ion crystal.

To trap ions initially, the imaging system was aligned as described in section 2.4.4. The beam splitter was then put in place to image the trap onto the CCD camera. Firing the ovens, we observed neutral fluorescence along the path of the 423nm beam. This made it possible to steer the beam into the trap centre. The superimposed cooling beams were aligned by observing the scatter along the electrodes on the camera. The pick-off beam on the beam profiler was used to confirm that the beam's focus was at the trap by employing a knife-edge technique. Measuring the power of the beam leaving the trap at the far end, the beam is moved vertically until its power drops to 90% due to cut-off. The position on the beam profiler is recorded. The beam is then moved further until its power drops to 10%. The distance between these two points as measured on the beam profiler can be converted into a beam width (full width w at $1/e^2$ maximum intensity) by evaluating $w = 0.78\,\Delta x_{10-90}$.

Ions were trapped initially using two electrode pairs at 0.5 V and a central pair at 0 V. Optimizing empirically the parameters we found the trap to be most stable and loading reliably at a configuration consisting of two pairs of electrodes at 0.8 V either side of the central pair at 0 V. It was also discovered that several electrodes including one compensation electrode were shorted to ground (see appendix A.4.1 for a details). We found the ion lifetime to be 15 mins which is consistent with the results from the surface traps used in our group which have a similar trap depth. We believe that the main loss process is collision with a background gas atom.

At moderate saturation of the 397 nm Doppler cooling beam (3 μW corresponding to $2I_{sat}$) and using the lasers at 850 and 854 nm as repumpers we typically collect 41000 counts/s on the PMT on a background of 900 counts/s. This corresponds to a signal to background ratio of 45. The background scatter from the trap electrodes is relatively high since the alignment of the beam with respect to the angle of observation made it hard to reduce the scattered light. For trapping we typically close the imaging system aperture to a square of around 200 μm which corresponds to 25 μm at the ion's location. A further reduction of the beam width, aperture size and/or employing a discriminating filter as described in chapter 3 could be used to reduce further the scatter.

2.6.2 Micromotion compensation

To detect and to compensate the ion's micromotion, we used photon arrival time RF correlation measurements [102]. The amplitude of the RF correlation scans is minimized when

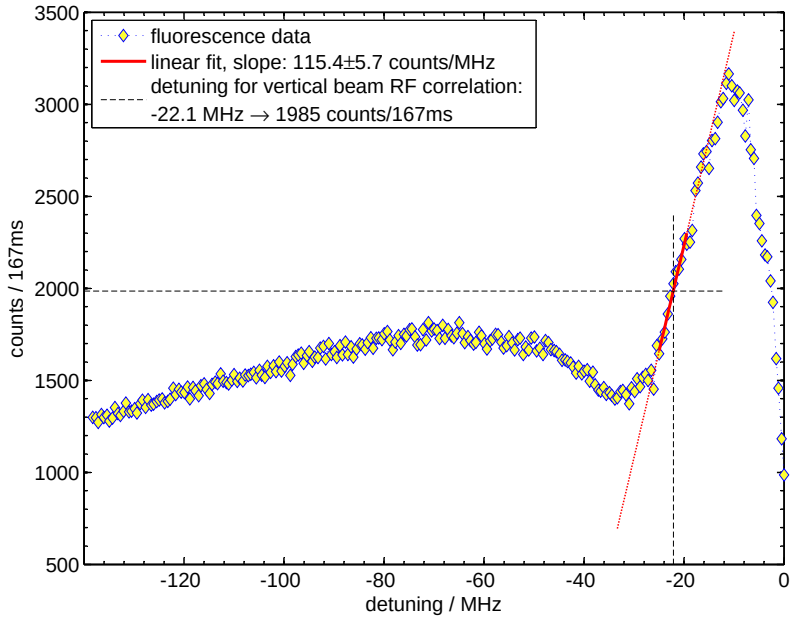

Figure 2.25: Fluorescence data from a scan of the 397nm laser ($I = 17\,I_{sat}$) using the vertical 866nm laser red-detuned as the repumper ($I = 65\,I_{sat}$). For the RF correlation, the 397nm laser is detuned to the flank of the dark resonance (dotted lines), the slope of which is estimated by a linear fit.

the ion is moved into the centre of the RF potential by adjusting the compensation voltages. In our case, with one compensation voltage shorted, there are three degrees of freedom to do this. They are the sum and difference of the offsets on the top and bottom set of DC electrodes V_{b+t} and V_{b-t} as well as the remaining compensation electrode V_{ext}, so named because it required a high voltage ($\sim 100\,\mathrm{V}$) supplied by an external power supply (see section 2.4.2.3).

The micromotion could be minimized with the standard beam setup (397nm cooling laser and repumper through the same side viewport, see fig. 2.17) by setting V_{b-t} roughly and then fine-adjusting the other two voltages (mainly V_{ext}). At the minimum position, a small oscillation at twice the RF frequency could be seen which is indicative of micromotion perpendicular to the beam direction, i.e. vertical. To detect and compensate for this micromotion, we first tried to send in a second $397\,\mathrm{nm}$ beam through the small central rear viewport (at $70°$ to the vertical) but this gave forbiddingly large forward scatter of laser light into the imaging optics. To get around this problem, we introduced the repumping laser at 866 nm through the main viewport at $60°$ to the vertical (see figure 2.17). In contrast to the UV cooling laser, the scattered infrared light is not detected by the PMT. The beams at $397\,\mathrm{nm}$ and $866\,\mathrm{nm}$ form a Λ-system in calcium which at negative $866\,\mathrm{nm}$ detuning produces a dark resonance feature in the $397\,\mathrm{nm}$ fluorescence curve. Since the position of this feature depends on the detuning of the 866 nm laser, it is subject to Doppler shifts along the direction of the beam. This can be exploited to detect micromotion as described in [82].

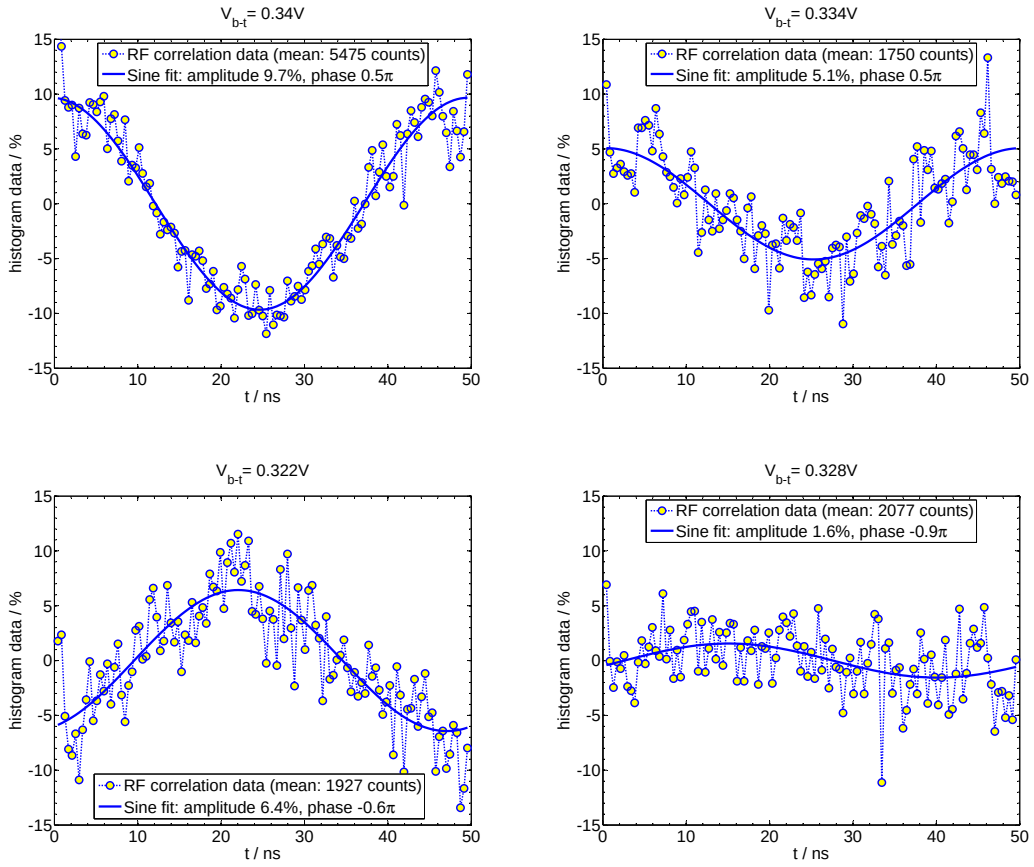

Figure 2.26: Four RF correlation histograms at different compensation voltages V_{b-t}. The histogram counts are normalized and shown as a percentage of the average count rate (which depends on the acquisition time which was different for each data set). Sine curves are fitted to the data with fixed period and offset. The resulting amplitude and phase are shown. The phase flip of π between both sides of the minimum can be seen.

Figure 2.25 shows a scan of the 397 nm cooling laser with a dark resonance introduced by the vertical 866 nm repumper. A detuning is chosen at the flank of the dark resonance (see dotted black line in fig. 2.25) and an RF correlation histogram recorded. Varying the compensation voltage V_{b-t}, the signal was nulled. Figure 2.26 documents this process showing four correlation histograms for different compensation voltages with fitted sine curves. For the fits, the period of the sine curve was fixed. The phase flip from one side of the optimum voltage to the other is clearly observed. At the optimum voltage, the signal is nearly flat. Floating the phase of the sine curve gives an upper bound on the remaining amplitude. Using the slope of the fluorescence curve obtained by a linear fit in figure 2.25 the change in fluorescence of 1.6% due to micromotion can be converted into a Doppler shift of $\Delta f = 275.2\,\mathrm{kHz}$. With the radial trap frequency $f_r = 2.535\,\mathrm{MHz}$, this corresponds to an oscillation amplitude of $x = \sin(60°)\,\Delta f \lambda_{866}/2\pi f_r = 30\,\mathrm{nm}$. The equivalent residual field pushing the ion from the trap centre is only $E = \omega_r^2 mx/q = 3.2\mathrm{V/m}$ which indicates a well compensated trap (compare [103]).

Going back to the vertical repumping beam after optimizing V_{b-t}, we find the previously observed small oscillation at double the RF frequency nulled, confirming the trap to be well compensated in both radial directions. Typical compensation values are $V_{b+t} = 0.50$ V, $V_{b-t} = 0.32$ V and $V_{ext} = 115$ V. From day to day, we found V_{b+t} could be left constant, V_{ext} would change by a few volts, and V_{b-t} needed changes of around 5% for good compensation.

2.6.3 Trap frequencies

By adding an AC voltage to one of the compensation electrodes (see section 2.4.2.3), we are able to measure the axial and radial trap frequencies. This method is know as "tickling" and consists of scanning the frequency of the applied AC voltage until the drive field is in resonance with the ion's secular motion. On resonance, the ion is heated and a drop in fluorescence is observed. This method yields the trap frequencies to within a few kHz. The measurements were repeated for a range of different values of the trap frequencies V_{RF} and V_{DC}.

2.6.3.1 Axial trap frequency

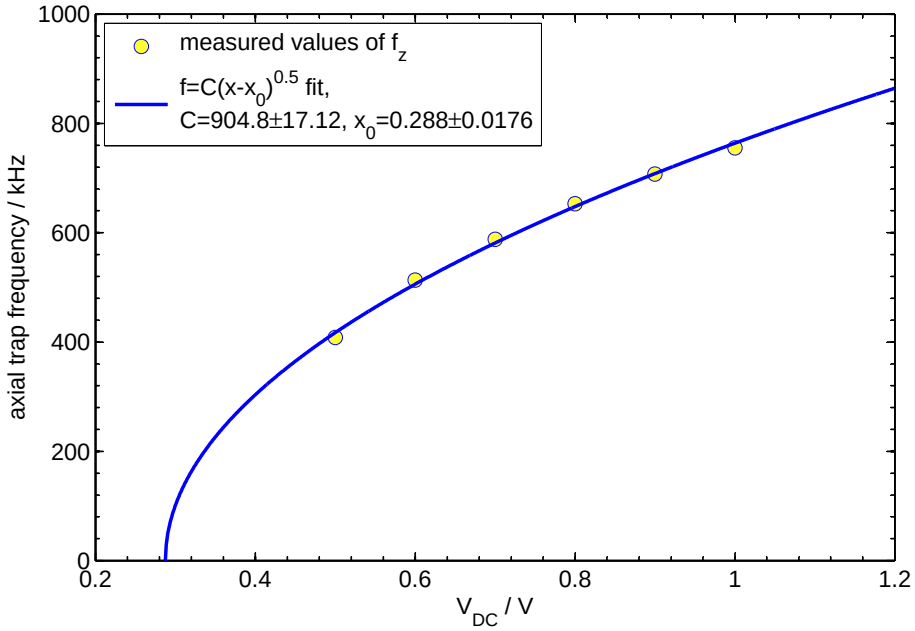

Figure 2.27: Axial trap frequency for different DC voltages. A square-root curve is fitted to the data yielding the parameter $C = 904.8\text{kHz}/\sqrt{\text{V}}$ from which the trap parameter can be calculated (see text). The error in C comes from the fit and assumes an error of ± 5 kHz on the data points.

Figure 2.27 shows the axial frequency for a range of different DC voltages. To determine the quadrupole amplitude for comparison with the model (see section 2.5.2), a square-root curve was fitted to the data. The parameter x_0 allows for an offset on the DC

field experienced by the ion while the parameter C yields the quadrupole amplitude in the following way:

Rewriting equation 2.5 in section 2.5.2 gives

$$\begin{aligned} 2\pi\, f_z &= \sqrt{\frac{-2e}{m}\,\frac{Q_z}{V_{DC}}}\sqrt{V_{DC}} \\ \Rightarrow \frac{Q_z}{V_{DC}} &= (2\pi\, C)^2\,\frac{m}{-2e} \end{aligned} \tag{2.8}$$

For our fitted value of $C = 904.8\text{kHz}/\sqrt{\text{V}}$, this gives $Q_z/V_{DC} = 6.70 \cdot 10^6\ \text{m}^{-2}$ which equates to a trap parameter a of 0.00321 at our typical value of $0.8\ \text{V}_{DC}$. Comparing this value to our simulation in section 2.5.2 ($Q_z/V_{DC} = 8.88 \cdot 10^6\ \text{m}^{-2}$), we find agreement at the $25\,\%$ level which is reasonable because firstly the model presented is rather crude and secondly the actual trap was assembled by hand and is subject to errors in alignment of the electrodes.

The offset value x_0 allows for a field when 0 V is applied. In our case, it indicates that we don't have a stable trap at $V_{DC} < 0.288$ V. A possible explanation for the offset is the fact that the compensation voltage applied by adding an offset to the DC electrode voltages (see 2.6.2) cannot be applied to all electrodes due to the shorts mentioned in 2.6.1. Therefore, there is an axial field gradient between these electrodes and the trap centre which could impede trapping at low DC voltages.

As a test of consistency, we also studied how the axial frequency changes when V_{RF} is varied and found it to be constant except at low values where it drops by a few percent.

2.6.3.2 Radial trap frequency

Figure 2.28 shows measurements of the radial frequency for different V_{pp} settings on the trap RF source. Following equation 2.4, a square root curve is fitted to the data. In an ideal Paul trap as is assumed in the equations in 2.5.2, the a parameter for axial trapping (eq. 2.6) is the same as the one in eq. 2.4 where it describes radial anti-trapping. In our trap, the axial confinement is provided by off-axis DC electrodes which will have a stronger radial effect than the ideal endcaps assumed in the equations. This is confirmed by the model as explained in the text accompanying figure 2.22. For this reason, when fitting the data in figure 2.28, we include a as a second floating parameter in the fit. The result is $a = -0.00684$. The simulation predicted $a/V_{DC} = -0.00682$. At $0.8\ V_{DC}$, this gives $a = -0.00546$ which lies within 20% of the fitted data. Fixing a at a value of -0.00546 while resulting in a slightly worse fit only causes a $2\,\%$ change in the fitted value of q/V_{pp}.

The main result of the fit is the value for q/V_{pp}. To convert this into a quadrupole amplitude we need the applied voltage which is only known precisely before the resonator. The value at the trap depends on the RF resonator's step-up factor which was measured in 2.4.2.1 to be approximately $Q_{stepup} = 15$. We rearrange eq. 2.7 taking into account that

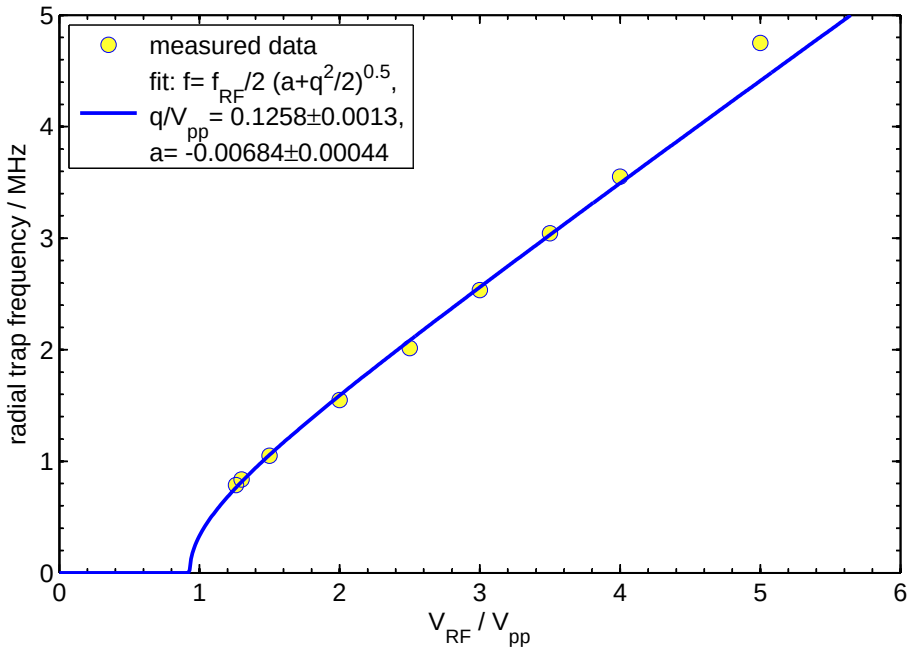

Figure 2.28: Radial trap frequencies for different RF voltages. A square root curve is fitted to the data following eq. 2.4. The a parameter was also allowed to float during the fit (see text). The errors come from the fit and assume an error of ± 5 kHz on the data points. The last data point was not included in the fit.

$V_{pp} = 2V_{RF}$:

$$q/V_{pp} = \frac{4e}{m\omega_{\mathrm{RF}}^2}\frac{Q_r\, Q_{stepup}}{2V_{RF}}$$
$$\Rightarrow \frac{Q_r}{V_{RF}} = \frac{q}{V_{pp}}\frac{m\omega_{\mathrm{RF}}^2}{2e\, Q_{stepup}} \tag{2.9}$$

With $q/V_{pp} = 0.13$, we get $Q_r/V_{RF} = 2.80{\cdot}10^7\,\mathrm{V/m^2}$ which given the previous comparisons and the uncertainty in the measurement of Q_{stepup}, agrees well with our expected value of $2.34 \cdot 10^7\ \mathrm{m}^{-2}$ from the simulations in section 2.5.2.

2.6.4 Heating rate

As an evaluation of the trap's performance, measurements of the heating rate were performed using the Doppler recool method. Doppler recool measurements are a technique to determine the ion's temperature after a heating period and are easy to implement. The principle, as developed in [104], is based on turning off the laser-cooling for a period of time and then recording the fluorescence during re-cooling of the ion in a time-resolved way. The shape of this fluorescence trajectory depends on the ion's motional energy at the time of the turn-on. Repeating this many times and adding the data accumulates these curves into a histogram. The distribution of motional energies after the heating period corresponds to a temperature. To fit the data, a set of fluorescence trajectories for the given

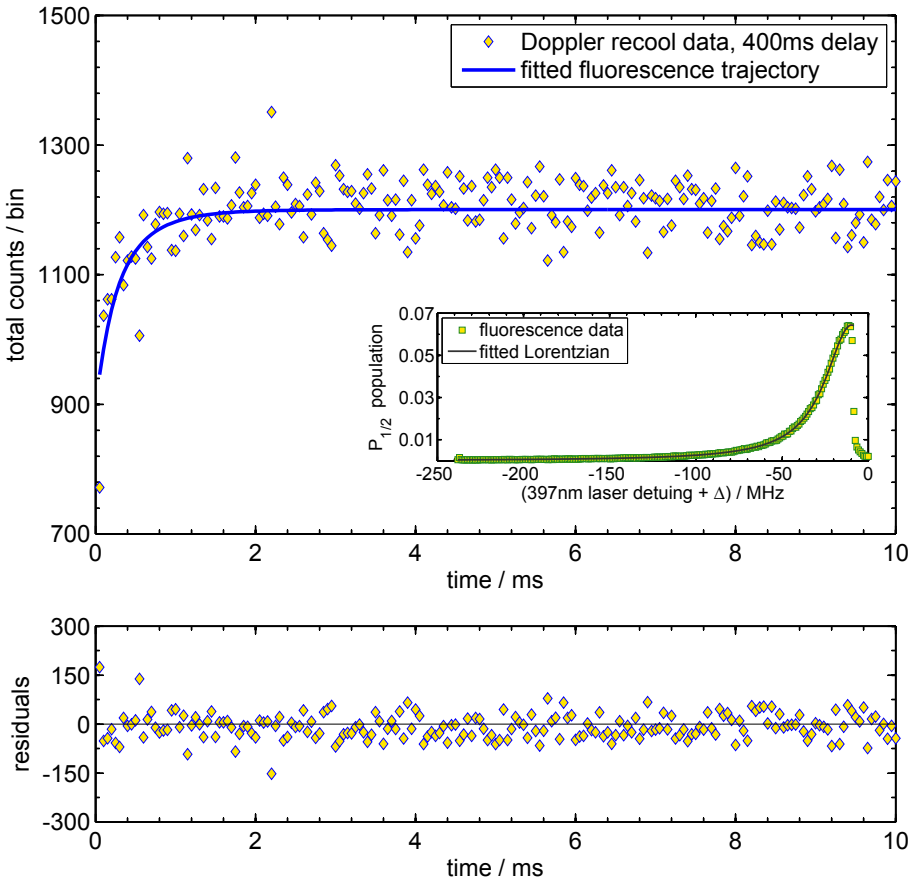

Figure 2.29: Top: A typical Doppler recool measurement with 400 ms delay time and the fitted fluorescence trajectory. The bottom graph shows the residuals. The fit gives a heating rate of $6.97 \cdot 10^4$ quanta/s. The inset shows a Lorentzian fit to a scan of the 397 nm laser which yields the detuning $\Delta_{397} = -13.0$ MHz and the intensity $I_{397} = 0.15\, I_{sat}$ used for the fit of the fluorescence trajectory.

laser parameters is calculated, each with a different starting energy. Then, a weighted sum of these is obtained with weighting factors based on the Maxwell-Boltzmann distribution. The distribution centre is then changed during the fit to give a mean energy which is in agreement with the data. From this energy and the duration of the delay time during which the cooling was turned off, the heating rate is deduced. The model assumes a two-level atom which is closely approximated in Ca^+ when the two lasers at 850 and 854 nm are used to repump the ion from the low-lying $D_{3/2}$ state since it avoids interconnecting multiple levels in the cooling cycle[43]. To interrupt the cooling, the laser at 850 nm was switched off during the delay time trapping the ion in $D_{3/2}$ and thus removing it from the cooling cycle. To analyze the measurement, we have developed a program in Matlab which performs the operations described above. Apart from the Doppler recool data, it takes values for the 397 nm saturation parameter $s = I/I_{sat}$ and the line width Γ, both

[43] for details on different repumping schemes, see chapter 3

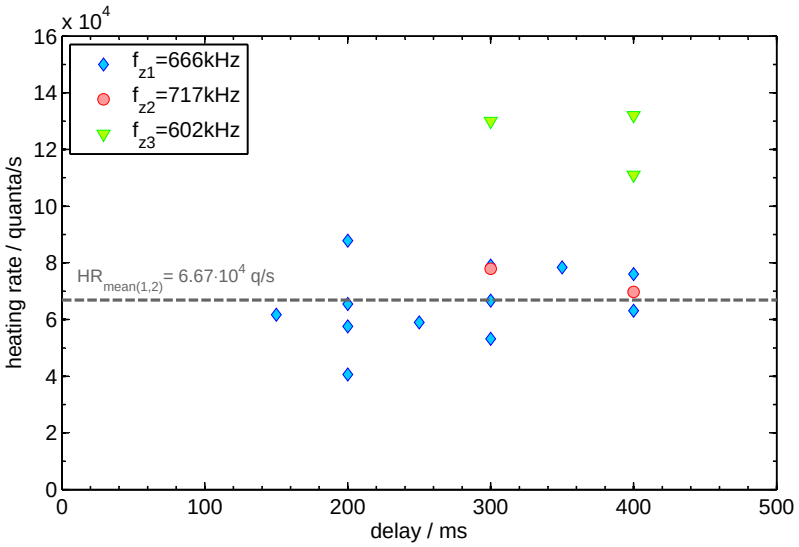

Figure 2.30: Results of heating rate data taken for different delay (heating) times and axial trap frequencies. Due to imperfect compensation, the values for f_{z3} are systematically higher and were excluded from the averaging. The mean is $H_R = (6.67 \pm 1.24) \cdot 10^4$ quanta/s.

of which can be found by fitting a half-Lorentzian profile to a scan of the 397 nm cooling laser. Please refer to appendix A.1 for details. A typical fit for a 400 ms delay time is shown in figure 2.29.

The measurement was repeated for a number of different delay times at our typical axial frequency of $f_{z1} = 666$ kHz (DC voltage 0.8 V). The data is shown in figure 2.30. The top graph shows the heating rates measured in motional quanta ($\hbar\omega_z$) per second. For comparison, two different axial trap frequencies were also used, $f_{z2} = 717$ kHz and $f_{z3} = 602$ kHz at voltage configurations of 0.9 V and 0.7V respectively. For the frequency f_{z3}, the trap was not well compensated and subsequently, the heating rates obtained are higher than the other measurements (see fig. 2.30). They were not included in the averaging to find the overall result. An electric field noise density is obtained from the heating rate H_R by $S_E = (H_R \cdot 4m\hbar f_z)/(e^2)$ where m and e are the ion's mass and charge. This gives a measure of the heating in the trap independent of individual trap parameters. However, an $f_z^{-\alpha}$ dependence with $\alpha \sim 1$ of this quantity has also been reported [105] and so the figure $f_z \cdot S_E(f_z)$ or $\omega_z \cdot S_E(\omega_z)$ is commonly used to compare heating rates between traps. Figure 2.31 shows a plot of various traps used by groups around the world with the Microtrap included as a data point at its ion-to-electrode distance of 140 μm with $\omega_z \cdot S_E(\omega_z) = (1.3 \pm 0.3) \cdot 10^{-3}$ (V/m)^2.

It is apparent that the Microtrap has an above average heating rate. This is not unexpected since the surface quality of the metalization near the ion was very bad (see section 2.3.1.1). Another factor contributing to the high heating rate is positioning of the DC filters. They are outside the vacuum system (compare section 2.4.2.2) which means that the

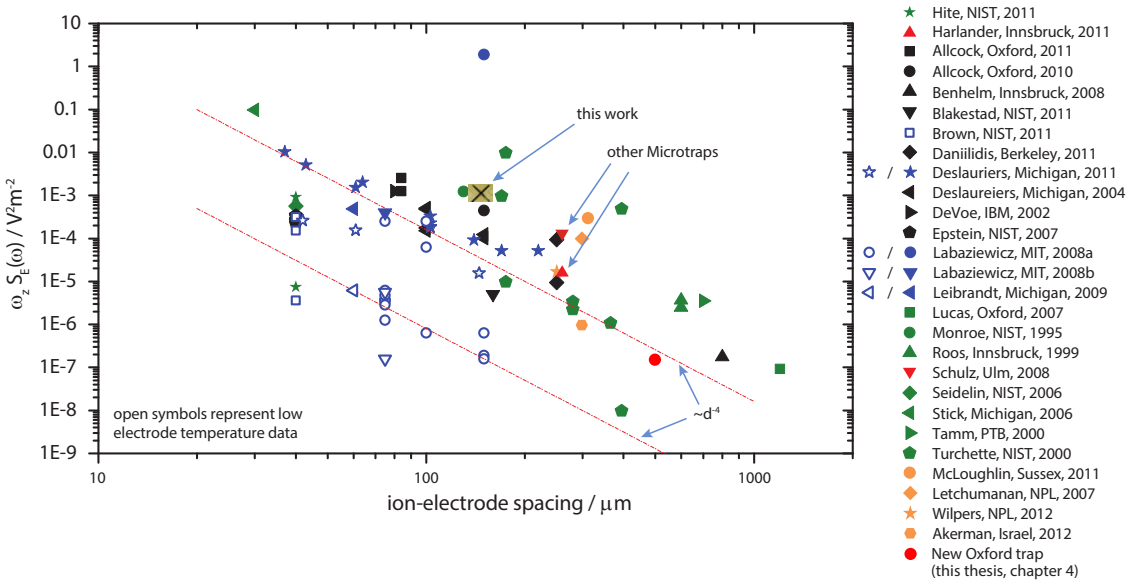

Figure 2.31: Trap frequency times electric field noise density (both in rad/s) versus ion-to-surface distance for a range of traps evaluated in different ion trap groups (modified from [88]). Two dashed lines indicate the d^{-4} dependence for cryogenic (open symbols) and room temperature (closed symbols) traps. Data from this work as well as two other Microtraps ([106],[71]) are pointed out.

inductance of the long ribbon cable connecting the feedthrough to the trap arm is lowering filter performance by blocking any noise and RF picked up from reaching the capacitive grounding the filters provide. This means that the voltages on the DC electrodes are subject to electrical noise which can cause heating. RF pick-up can lead to uncompensatable micromotion due to phase differences but this effect appears to be small in our trap (see 2.6.2).

It is of interest to compare our results to the two other traps from the Microtrap project from which heating rate data has been reported. The linear trap used in Ulm [106] has a wide region (width $500\ \mu$m) and a narrow region (width $250\ \mu$m) connected by a tapered section. Its gold layer is evaporated and does not show the surface quality problems described here. Additionally, the DC electrode filters were placed on the chip carrier close to the trap. The results were obtained in the wide region at an ion-to-electrode distance of $d = 258\ \mu$m and the heating rate reported is 2100 quanta/s at a trap frequency of 1.2 MHz. This gives $\omega_z \cdot S_E(\omega_z) = 1.3(2) \cdot 10^{-4}\ (\mathrm{V/m})^2$. If scaled up to our ion-to-electrode distance using d^{-4}, this gives $1.5(2) \cdot 10^{-3}\ (\mathrm{V/m})^2$ which is perfectly consistent with the findings in our trap despite the disadvantages mentioned in our experiment.

The same linear trap design as the Ulm trap but with our electroplated gold surface has been used in the Innsbruck group [71]. The ions were also trapped in the wide region ($d = 258\ \mu$m) at an axial frequency of $f_z = 537$ kHz and a heating rate of 1300 quanta/s

was measured. This gives $\omega_z \cdot S_E(\omega_z) = 1.6(9) \cdot 10^{-5}(\mathrm{V/m})^2$, an order of magnitude better than ours and the Ulm trap.

In both cases, the heating rate was measured by the more careful method of comparing Rabi oscillations on the red and blue sidebands (see chapter 7). Still, the error figure reported by Innsbruck allows for nearly a factor of two. The fact that the Innsbruck trap achieves such a low heating rate when compared to the one used in Ulm suggests that the surface quality issues are overcompensated by the better conductivity and larger grain size of the electroplated gold. Optical flatness of the surface can be misleading as to the electrical properties as recently shown in a surface trap experiment our own laboratory [16]. A possible idea is that the larger grain size in the electroplated gold might lead to a reduction in patch potential fluctuations compared to the more finely grained evaporated gold surface.

As to the performance of our own trap, several explanations are possible. The Doppler recool method is less precise than the sideband asymmetry comparison since the latter measures the vibrational occupation number directly [105]. Additionally, the position of the DC filters can contribute significantly to the heating, depending on electrical noise sources. A change of filter position would be the next step in investigating this further which would mean a modification to the chip carrier and additional wirebonding.

However, as figure 2.31 shows, variations over several orders of magnitude between different labs are regularly observed. Recent data from our group as well as NIST strongly points at surface adsorbates as a contributing cause for heating [87, 88]. The NIST group achieved a reduction in heating rate of two orders of magnitude after cleaning of their trap by Ar^+-ion bombardment. Since the environment under which the traps are assembled and set up are bound to vary widely between different laboratories, so will the surface contaminants that get adsorbed on the electrode surfaces. This reduces the significance of the differences observed between the traps used in different groups.

2.7 Summary

The project achieved the multi-step preparation and complete assembly of a microfabricated multi-zone Paul trap with micron precision. Ion crystals were successfully trapped, the micromotion effectively compensated and the trap extensively characterized. The results agree reasonably well with a simplified simulation of the trap and a complete computer model (see appendix A.5) is ready for use if more advanced operations are to be made in the trap. Further experimental steps would include trapping of ions in other trap arms and the development of shuttling inside one arm and across the junction. As mentioned, an improvement to the experiment could be made by placing the filter capacitors in close proximity to the trap on the chip carrier rather than on the feedthrough.

However, the numerous problems with the trap chips which resulted in shorts and possibly a relatively high heating rate draw into doubt its usefulness in the long term. The electro-plated gold which was intended to give a thick metal layer and hence better conductivity has produced a bad surface finish and shorted electrodes. The large "nuggets", bumps and depressions might cause problems but the findings in the Innsbruck group suggests their effect on the heating rate to be small.

For shuttling ions around a junction, other approaches have been demonstrated with low ion heating during transport in a 3D trap involving conductive "bridges" across the corner electrodes [73, 107] as well as surface traps with $60°$ rather than $90°$ junctions [83] by the ion trap group at NIST. It would be advantageous for further experiments in our group concerned with shuttling to follow these recent advances and incorporate them in a new trap design. The modular setup of the experiment presented here which allows the fast turnaround of traps mounted on a standard CPGA chipcarrier is conducive to this approach.

Chapter 3

Background-free detection and readout

As explained in chapter 1, scalability is one of the key elements to advance quantum computing experiments. It is one driving factor behind a significant trend towards ever-smaller two- and three-dimensional trap geometries. It is by no means the only one, however. Miniaturization and the close proximity between ions and engineered structures opens new possibilities, for example in quantum state control by coupling to the near-field of a microwave-guide ([103, 108]). There have also been studies of the interaction of trapped ions with a thin conducting wire [109] and proposals to extend this to nano-fibres [110] in order to couple ions to the fibre's evanescent light field (as previously implemented with neutral atoms [111, 112]). Other experiments pursue the entanglement of the internal state of a trapped ion with the vibrational mode of a cantilever in order to study quantum effects in meso- and macroscopic objects [113]. Furthermore, trapped ions are used in sensor applications by employing them as field probes in specifically designed traps [114, 115].

All of these new experimental applications rely on ions being trapped close to surfaces and they depend on laser cooling [116] as the standard technique to reduce the ions' motion, and fluorescence detection as a means to observe the ions. For its large velocity capture range and high cooling efficiency, Doppler cooling is often the first stage in the cooling process and the competing demands between a low final temperature (see chapter 7) and high cooling efficiency mean that laser intensities of around one saturation intensity $\left(I_{sat} = 2\pi hc\Gamma/\lambda^3\right)$ are typically used. Maintaining a high cooling efficiency is particularly important in surface-electrode ion traps, where the shallower trap depth can lead to ion loss after background gas collisions if the cooling rate is low and where anomalous heating effects are more prevalent than in three dimensional traps due to the proximity of the ion to the trap electrodes.

However, one major problem exists with irradiating ions in miniaturized trap structures with laser beams. When detecting a fluorescence signal S from ions trapped in close proximity on the order of $100\ \mu$m or less to surfaces (the trap electrodes, integrated optics

or other objects of study), light scattered off the surroundings is picked up by the imaging or detection optics and can significantly increase the background signal B. The signal is usually shot-noise limited, so the signal-to-noise ratio is given by $S/\sqrt{S+B}$ and reducing the background is clearly advantageous (see [117] for a more detailed study of discrimination of single-ion fluorescence from background performed in our group). Additionally, a low background level is important not only for ion detection, but also for accurate compensation of ion micromotion (for example, by the standard technique of rf/photon arrival time correlation [102] which is used in chapters 2 and 4), or for thermometry as recently described in [118].

Previous work done in the Aarhus group achieved negligible background by driving the narrow dipole-forbidden $S_{1/2} \leftrightarrow D_{5/2}$ transition in $^{40}Ca^{+}$ with 250 mW of laser intensity and collecting fluorescence on allowed decay transitions [119]. This had the disadvantages of reducing both the cooling and fluorescence rates significantly, requiring a complex laser system and relatively high laser power.

This chapter describes two methods that achieve ion detection and readout respectively at essentially zero background in $^{40}Ca^{+}$, but only use dipole-allowed transitions. The first is based on continuous repumping and frequency-selective detection. Whilst maintaining a high cooling rate and being useful for observing ions, the technique is not applicable to detection of the internal state of the ion by the electron-shelving technique because the $D_{5/2}$ "shelf" is part of the cooling cycle (see chapter 6). The second method overcomes this drawback using pulsed excitation and detection, separating signal and background in time rather than in frequency. The methods are readily applicable to other ion species with similar level structure.

3.1 Background-free detection of trapped ions

After a brief outline of the experimental setup, four different repumping schemes are described in the following in order to compare the gains made by the background suppression and alternate repumping paths over the standard scheme. A similar method has previously been used in magneto-optical trapping of neutral ^{85}Rb [120].

3.1.1 Repumping schemes

Our Doppler cooling schemes are based on the standard $S_{1/2} \leftrightarrow P_{1/2}$ cooling transition which in $^{40}Ca^{+}$ is at 397nm (see figure 1.1, chapter 1). The ion has a 5% chance of decaying from the $P_{1/2}$ level into the low-lying $D_{3/2}$ level which is long-lived because the direct transition to the ground state is dipole-forbidden. To repump the ion, an infra-red laser is usually applied to the $D_{3/2} \leftrightarrow P_{1/2}$ transition at 866 nm. This will be referred to as scheme I (see fig. 3.1, inset I).

We can instead repump via the $P_{3/2}$ level using a laser at 850 nm. This state decays quickly to the ground state by emitting a photon at 393 nm. There is also a 5% chance of decay into the $D_{5/2}$ level from which we repump using a laser at 854 nm. This repumping technique which we refer to as scheme II (see fig. 3.1, inset II) makes the system into a quasi-two-level atom because the $S_{1/2}-P_{1/2}$ cooling transition is only weakly coupled by spontaneous decay to the $D_{3/2}-P_{3/2}-D_{5/2}$ manifold. It can add about 10% of 393 nm fluorescence to the signal and can increase the emitted 397 nm light by about 70%, raising the overall signal by a substantial factor (see [82]) without increase in background.

We now consider suppression of scattered laser light background in scheme FII (see fig. 3.2, inset FII). Detected light at 393 nm originates exclusively from the ion which can be discriminated from the cooling light at 397 nm and all the infra-red repumping lasers. The pair of interference filters is placed in front of the PMT to block selectively the cooling light while transmitting the 393 nm light emitted by the ion. This reduces background scatter from the cooling light by more than two orders of magnitude. We then only detect the ion's fluorescence, on a background level which is dominated by the dark counts of the PMT. All the advantages of standard Doppler cooling such as the cooling rate and the velocity capture range are maintained. The overall count rate is reduced however since 397 nm light scattered by the ion is also discarded.

The detected fluorescence at 393 nm is limited by the $P_{1/2} \rightarrow D_{3/2}$ branching ratio (6.0%) since only the population decaying to $D_{3/2}$ can contribute. Scheme FIII addresses this disadvantage and achieves a higher fluorescence rate by actively pumping down more population from the $P_{1/2}$ state with the usual repumping laser at 866 nm. This increases the fluorescence rate at the cost of interconnecting several states which creates more possibilities for two-photon dark resonances [121]. In the experimental implementation we varied the intensities and detunings of the infra-red lasers to maximize empirically the fluorescence. The detunings are not critical because at the optimum intensities the fluorescence peak is relatively broad. We achieved a count rate within a factor of two of the standard 397 nm+866 nm cooling scheme I.

In order to account quantitatively for the experimental values, Derek Stacey and Hugo Janacek have compared them to simulations based on the optical Bloch equations [122, 123]. The agreement between the predicted and measured rates is at the 5% level. This is very satisfactory given that the empirical optimization procedure for the measured rates was only approximate. The detailed results can be found in [124].

As mentioned in chapter 2, scheme II can also be used in conjunction with heating rate measurements by Doppler recooling [104] because repumping with the 850 nm and 854 nm lasers gives a close approximation to a two-level system [82], which allows simple interpretation of the Doppler recooling data to extract the heating rate. In cases where there is high background scatter, scheme FII can be employed.

It would be possible to implement a similar set of schemes by cooling on the 393 nm

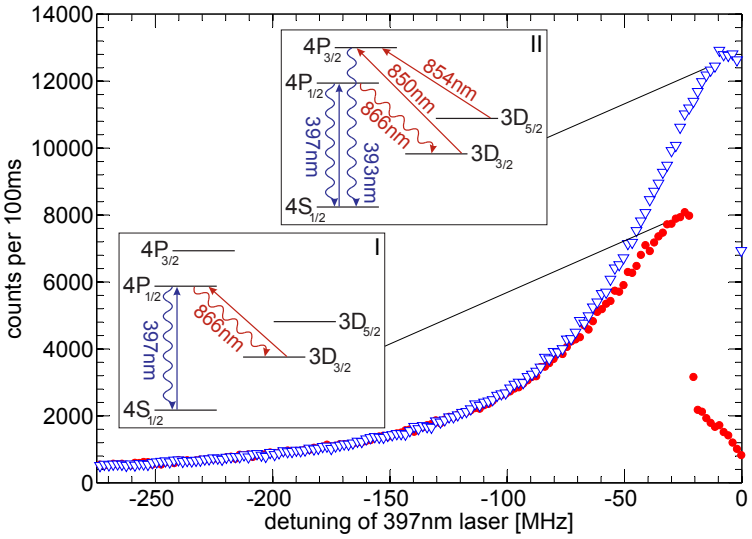

Figure 3.1: PMT count rate versus detuning of the laser at 397 nm, for repumping schemes I and II. Both violet scattered wavelengths are detected. The 397 nm laser power was 22 μW. Zero detuning was inferred from the point at which the signal drops down sharply due to Doppler heating on the blue side of the resonance peak, in scheme II (in scheme I, this point occurs earlier because of a 397 nm/866 nm dark resonance). The insets show the two different repumping schemes. **I:** repumping with a single infra-red laser at 866 nm. **II:** repumping with two lasers at 850 nm and 854 nm.

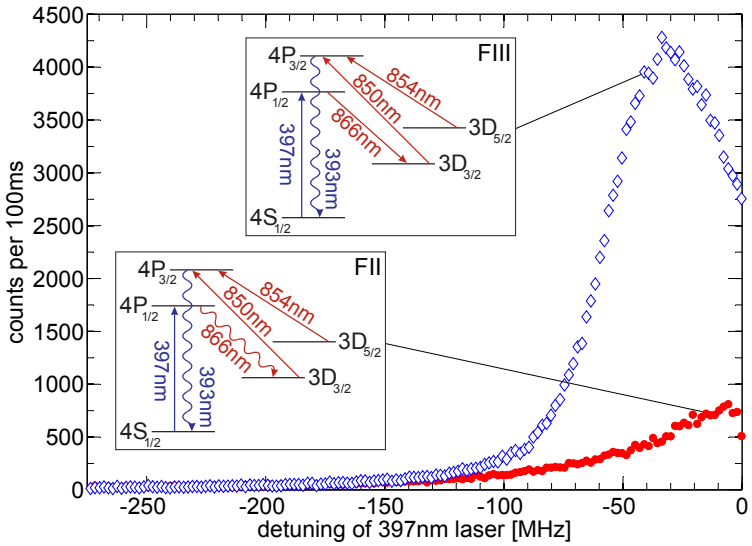

Figure 3.2: PMT count rate versus detuning of the laser at 397 nm, for repumping schemes FII and FIII. The interference filters are placed in front of the PMT so that only scattered light at 393nm is detected. The 397 nm laser power was 22 μW. The insets show the two different repumping schemes. **FII:** repumping with two lasers at 850 nm and 854 nm. **FIII:** repumping with all three infra-red lasers to increase the fluorescing population in $P_{3/2}$. As in scheme I, the fluorescence peaks earlier in FIII because of a 397 nm/866 nm dark resonance.

transition and repumping to the $P_{1/2}$ level via the 866nm transition. Fluorescence at 397nm could then be collected and discriminated in a similar way. However, in the limit of full saturation of all transitions only the two states in $P_{1/2}$ contribute to the fluorescence, compared with the four $P_{3/2}$ states in our scheme, leading to a lower signal.

3.1.2 Experimental setup overview

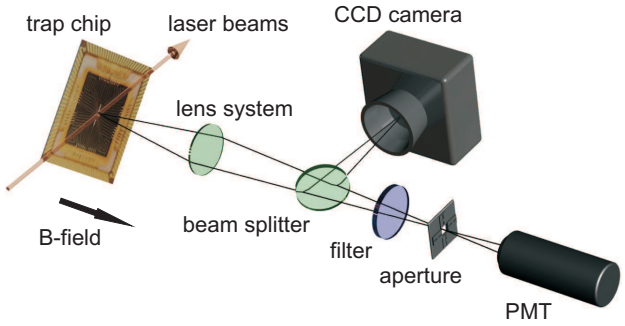

Figure 3.3: Schematic image of the experimental setup. The ion is trapped in a surface trap (left). All laser beams are superimposed and propagate at $45°$ to the trap axis; they are linearly polarized parallel to the chip surface and perpendicular to the magnetic field ($\sigma^{\pm}$ polarization). The ion is imaged through a lens system onto an adjustable aperture and a PMT, or optionally via a beam splitter onto a CCD camera. The 393 nm filters (see text) can be placed in front of the PMT.

At the time of the experiments described in the following, the Microtrap (see chapter 2) was not yet operational. So the experiments for this section were performed in a linear surface-electrode microchip Paul trap set up in the laboratory[1] adjacent to the one used for the other experiments in this thesis. Figure 3.3 shows a sketch of the trap and detection system. The trap was fabricated at Sandia National Laboratories (for details see [80] and [125]). The electrode surfaces are aluminium, supported above the silicon substrate by silicon dioxide insulating pillars, and the electrodes overhang the pillars to shield trapped ions from the insulating surfaces. The ion is trapped 84 μm above the plane of the electrodes. The radial confinement is provided by a harmonic RF pseudo-potential driven at 33MHz with an amplitude of $200\,V_{pp}$, which gives a radial trap frequency of 3.2MHz. Further electrodes carry DC potentials to provide for axial confinement (axial trap frequency 1.0 MHz), tilting of the radial principal axes, and micromotion compensation. The trap is enclosed in an ultra-high vacuum chamber with a residual pressure of $< 1\times10^{-11}$ Torr. An ion is loaded isotope-selectively by photo-ionization [126] from a beam of neutral calcium atoms provided by a thermal oven. The oven is mounted behind the trap chip, sending the atoms through a slit (width 100 μm) in the trap centre. The applied magnetic field is approximately 2.4 G and aligned perpendicular to the chip.

[1] see David Allcock's thesis [103] for more details on the overall setup

Extended-cavity diode lasers at 397 nm, 850 nm, 854 nm and 866 nm are available to Doppler-cool and repump the ion. They are locked to low-finesse optical cavities (drift rates < 0.5 MHz/hour, laser linewidths ≈ 0.5 MHz). All the laser beams are superimposed and polarized linearly perpendicular to the applied magnetic field. They are sent across the chip parallel to the surface at an angle of 45° to the trap axis. The principal axes of the pseudo potential are tilted using a static quadrupole field (for details see [82]) to allow cooling of all motional modes. Spot sizes ($1/e^2$ intensity radius) at the ion of the 397 nm and infra-red beams are (21μm$\times 31\mu$m) and (17μm$\times 22\mu$m) respectively.

The ion is observed with a photomultiplier[2] (PMT) or an electron-multiplying CCD camera[3] through an imaging system with a numerical aperture of 0.25 and a magnification of 8. An image of the ion is formed in a plane in front of the PMT, allowing the use of an adjustable aperture to reduce background scatter. For the new repumping schemes described below, scattered laser light at 397 nm is filtered out using a pair of 393 nm interference filters[4] (with net transmission measured to be 78% and 0.3% at 393.5 nm and 397.0 nm respectively).

3.1.3 Experimental realization

In figure 3.1 fluorescence spectra from a single ion are shown for schemes I and II. No filters were placed in front of the PMT, so both violet wavelengths can contribute to the signal. The maximum signals above background are 77800 $s^{-1}$and 126000 s^{-1}, respectively.

Placing the bandpass filters in front of the detector cuts out almost all light at 397 nm and we only detect 393 nm fluorescence. The results of implementing schemes FII and FIII are presented in figure 3.2. The maximum signals are 7680 $s^{-1}$and 41800 s^{-1} respectively. Scheme FIII thus achieves a signal which is only a factor of two smaller than scheme I, but with the background reduced by two orders of magnitude.

We repeated the four experiments presented in figures 3.1 and 3.2 for a range of different 397 nm laser powers. At each power we took a data set with all infra-red beams turned off to determine the background which is shown in figure 3.4(a). The background is made up of the sum of the constant detector dark count rate and the rate of scatter which is proportional to the laser power. Without the filters the background rises steeply with increasing 397 nm power (slope 44.4(6) s^{-1}/μW) while with the filters it is almost constant with a slope of only 0.16(2) s^{-1}/μW). Straight lines are fitted to the two data sets to use as smooth background data for the signal-to-background comparison. The intercepts are 7(1) s^{-1} and 6.6(4) s^{-1} which corresponds to the PMT dark counts.

We determined the peak fluorescence count for each 397 nm laser power P_{397} and fitted a curve for the signal S as a function of laser power $S = c/(1 + s/P_{397})$, where s and

[2]Electron Tubes P25PC
[3]Andor Luca 285_Mono,USB
[4]Semrock FF01-387/11-25

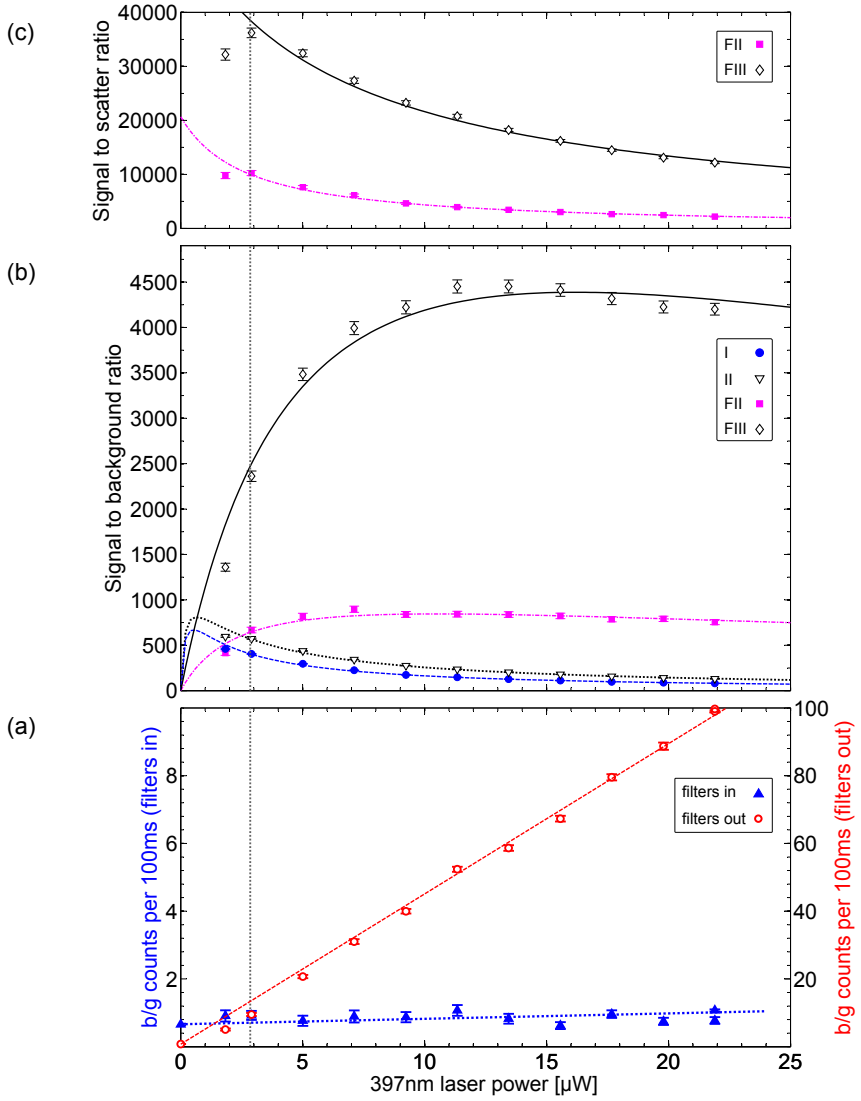

Figure 3.4: **(a)** Background counts versus 397 nm laser power without the filters (open circles, right ordinate) and with the filters (filled triangles, left ordinate) including straight line fits. **(b)** signal-to-background ratio versus 397 nm laser power for the four different repumping schemes, with fitted curves. Data points for the lowest 397 intensity are shifted down which may be due to a systematic reduction in the measured peak signal at very low intensities where the resonance becomes narrow and the peak fluorescence could be dropped, e.g. by finite laser linewidth. **(c)** signal-to-scattered light ratio for the two schemes FII, FIII (for the schemes without the filters, this ratio is very similar to the signal-to-background ratio). The vertical dotted line shows the 397 nm laser power corresponding to the saturation intensity $I_{sat} = 2.8\,\mathrm{mW/mm^2}$.

c are constants. Although strictly appropriate only to a two-level system, we find that this formula is also in good agreement with calculations from the optical Bloch equations model. The signal-to-background ratios for the four datasets are shown in figure 3.4(b) as points. The fitted curves, divided by the respective background slopes, are also shown. The standard scheme I has a peak signal-to-background ratio of 670. This is slightly im-

proved by scheme II to 810. Both maxima are narrow peaks and occur at low laser intensity ($\sim\ 0.2\, I_{sat}$), where the reduced fluorescence leads to a smaller signal-to-(shot noise) ratio and lower cooling efficiency. With the filters in, scheme FII achieves a signal-to-background ratio of 850 which, while only slightly better than the previous results, is maintained over a wide range of 397 nm laser powers and is only gradually reduced in the limit of high laser power. The best performance can be seen in the results for scheme FIII: the signal-to-background ratio achieved is similar to the standard scheme at low intensities but then rises steeply and peaks at 4400. The peak is again very broad which makes the method insensitive to the laser intensity. At typical experimental parameters ($P_{397} \approx 10\,\mu$W) the method surpasses the standard 397 nm+866 nm scheme I by more than an order of magnitude.

Since with the filters the background is dominated by the dark counts, which are highly detector-dependent, it is important to consider also the ratio of signal to scattered laser light. This is shown for the two schemes with the filters in figure 3.4(c), and has a maximum of 36000 for the scheme FIII. This occurs at a 397 nm laser power corresponding to approximately one saturation intensity (2.8 mW/mm^2), which offers a good compromise between high scattering rate and low Doppler cooling temperature. For a different detector, such as a cooled EMCCD camera at the same 100 ms integration time, the dark counts can be negligible and the signal-to-background achievable should be close to this signal-to-scatter ratio.

As mentioned above, the background-free repumping schemes described in this section cannot be combined with qubit readout. However, they could still be useful in the context of ion trap QIP, for example for monitoring fluorescence and maximizing the cooling rate for sympathetic cooling ions [127].

3.2 Background-free readout of trapped ion qubits

In the following we will describe a method that makes background-free qubit readout possible by separating signal and scatter in the time rather than the frequency domain. We use a similar method to determine the imaging system collection efficiency [100].

3.2.1 The pulsed method

The pulsed method is based on separating in time the ion excitation on the fluorescence transition and the spontaneous decay with fluorescence collection. It is a two-step process. First, only the 397 nm laser is turned on exciting the ion on the $S_{1/2} \rightarrow P_{1/2}$ transition until it decays to the $D_{3/2}$ level. During this time, photon detection is turned off and no signal (or scatter) recorded. Then in the second step, the 397 nm laser is turned off and the photon counting is started. Turning on the 866 nm laser will excite the ion to the $P_{1/2}$

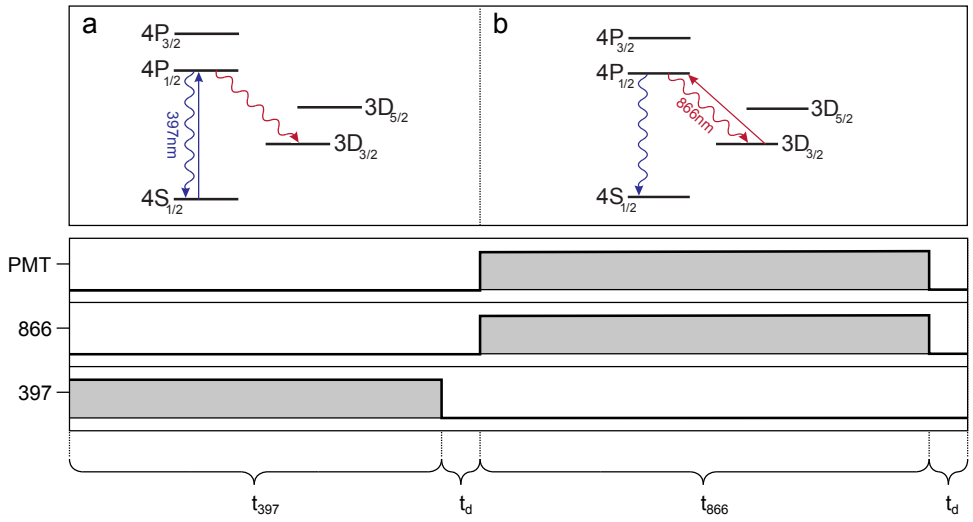

Figure 3.5: Schematic time sequence for the pulsed method (bottom) with corresponding level diagrams (top). Step a: 397 nm pulse of length t_{397} pumping the ion to $D_{3/2}$ while the PMT signal is gated off so that no counts are recorded. Step b: 866 nm pulse of length t_{866} to deshelve the ion, a single 397 nm photon is emitted while the PMT signal is gated on. Dead times t_d are also shown. The readout shelf state $D_{5/2}$ is not involved.

state from where it decays to the ground state emitting a single UV photon. The infrared light is not detected by the PMT (or may be filtered out trivially when other detectors are used), so we obtain the ion signal with no background (except for detector dark counts). The count rate is the product of the imaging system collection efficiency η and the cycle repetition frequency f_c. It will be lower than in the continuous case and so will the cooling efficiency since on average only 20 photons are scattered during the 397 nm excitation step. During the readout stage of an experiment, however, cooling is not the goal and this technique has the great advantage of not involving the $D_{5/2}$ shelf state, so background free-readout is achieved. Figure 3.5 illustrates the sequence including dead time gaps of length t_d between the pulses.

3.2.2 Experimental setup and limitations

The signal that can be achieved with this method is limited technically by the speed with which the laser pulses and PMT gate can be switched. This section describes the experimental setup used to implement the pulsed method and the boundary conditions it imposes.

3.2.2.1 FPGA

The sequence described above is run by an FPGA[5] capable of switching channels with 5 ns resolution. It is connected to the auxiliary Linux computer (see section 4.2.10.2) which is

[5] Digilent Nexys 2

in turn prompted by the experimental control computer to start the cycling of the pulse sequence. The FPGA switches the TTL channels for the two lasers and gates the PMT. If the PMT gate is high, the counts are passed on to the experimental control computer's counter hardware. Conversely, if it is low they are blocked and no counts are registered. This way, the experimental control computer runs as normal during pulsed readout. The parameters for the FPGA are set via the auxiliary Linux computer control program, where start and stop times for the pulses and the PMT gate can be chosen. Different signal delays in the cables need to be taken into account when assembling and optimizing the sequence.

3.2.2.2 AOM switching

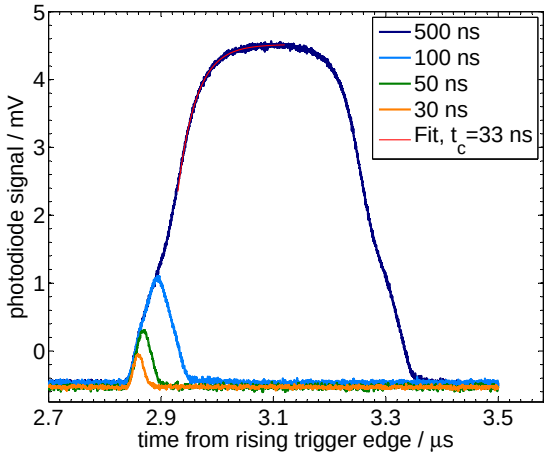

Figure 3.6: Photodiode signal showing the power in the 397 nm beam for different pulse lengths on the AOM. An exponential is included (see text).

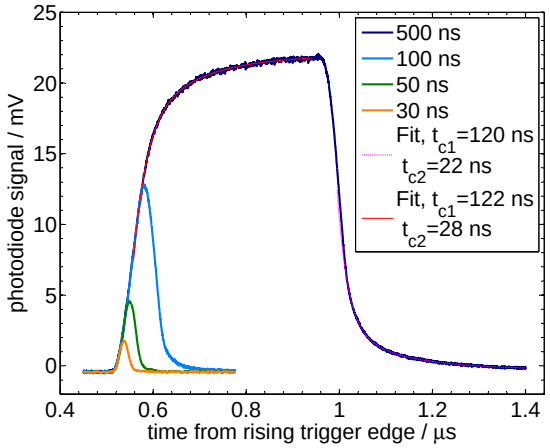

Figure 3.7: Photodiode signal showing the power in the 866 nm beam for different pulse lengths on the AOM. Exponential fits are included (see text).

Even though the FPGA can produce short precise pulses, the AOMs are limited in their switching time by the build-up of the resonant RF signal in the circuit driving the piezo which in turn generates the sound wave within the crystal. The same is true during turn-off where a ring-down effect can be observed. Additionally, the piezo driving the sound wave heats up which also contributes to the time delay before the final intensity is reached. During a very short pulse, the AOM's diffraction efficiency will not have reached its peak before the signal is turned off which leads to a reduced beam intensity.

The signals from the 866 AOM and the 397/40 Master AOM (see chapter 4) were observed on a photodiode[6] for short pulse times. The results are shown in figure 3.6 and 3.7. To get a more realistic simulation (see section 3.2.3), the effect of short pulse times limiting the intensity needs to be included. For this purpose, an exponential function was fitted to the rising edge in fig. 3.6 and gave a time constant of 33 ns. The edge shows a kink which

[6]Hamamatsu S5972, 50 Ω terminated, 500 MHz bandwidth

is due to the second pass of the double-pass setup not being perfectly aligned on top of the first and being switched slightly later. For the 866 nm beam AOM (fig. 3.7), a single exponential decay function resulted in a poor fit, possibly due to the different delay effects mentioned above. The sum of two exponentials was used to model the rising and falling edges. The time constants are very similar for both and are $t_{c1} = 120$, 122 ns and $t_{c2} = 22$, 28 ns respectively. For both AOMs, the rise and fall behaviors are similar. The rising edge functions are used to give the value of the intensity for some of the simulations presented in the following.

3.2.3 Rate equation simulations

Since no two lasers are turned on at the same time during the sequence, the process can be modeled reasonably well (see caveat below) using rate equations. The work presented in this chapter relied on David Szwer's "Transitions" suite of MatLab routines. The basic principle is outlined in appendix B. For more details and a description of the code please see his thesis [21]). The suite was used to simulate the population evolution during the sequence. To find how the photon emission rate depends on the pulse lengths we perform the following steps with the rate equations simulation for each set of the values t_{397}, t_{866}, t_d and the laser intensities:

1. Starting with all the population in the ground state, do 20 simulated sequences to get the steady state populations for the given parameters.

2. Starting from these, do one 397 nm pulse and a t_d pulse (all lasers off) to get the $D_{3/2}$ and $P_{1/2}$ populations after step a (see fig. 3.5). These populations correspond to the probability p_e of being in a state that can emit a photon during step b.

3. Find the probability of emitting a photon during step b.

   a) Set the ground state population to zero and renormalize the $D_{3/2}$ and $P_{1/2}$ populations from step 2.

   b) Perform an 866 nm pulse and record the ground state population which corresponds to the photon emission probability p_{ph}.

4. Calculate the total probability to emit a photon during a cycle: $p = p_e \cdot p_{ph}$

5. Calculate the emission rate $R = p/\left(t_{397} + t_{866} + 2\,t_d\right)$ and the count rate $R_c = \eta R$ where $\eta = 0.003$ is the collection efficiency of our imaging system.

Looking at an idealized situation where we can drive arbitrarily short pulses with infinitely short switching times we get the count rate dependence presented in fig. 3.8. In this regime where the pulses are short compared to the lifetime of the $P_{1/2}$ level, and there

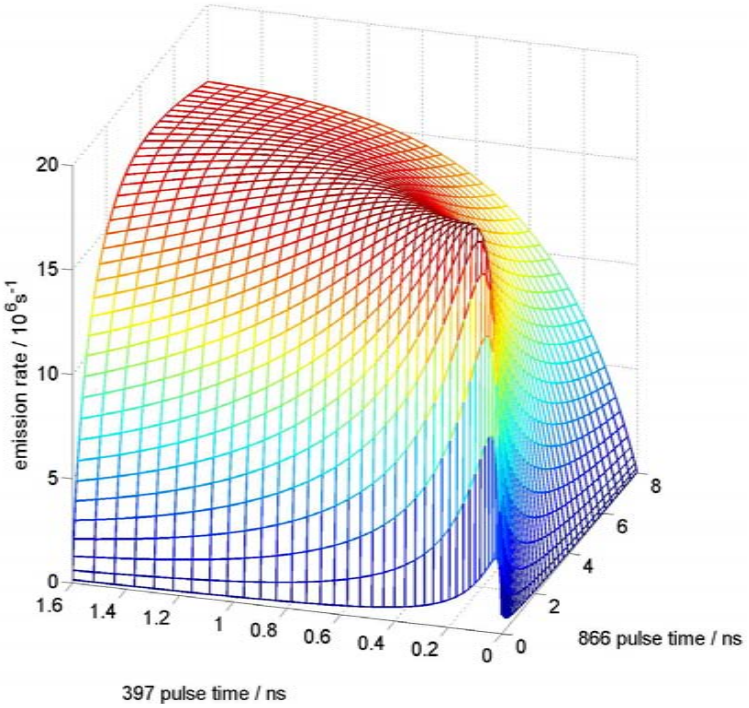

Figure 3.8: Rate equations simulation allowing arbitrarily short pulse times. Fixed parameters: $I_{397} = 10\ I_s$, $I_{866} = 100\ I_s$ and $t_d = 0$. Maximum $R = 1.92 \cdot 10^7$ counts/s occurs at $t_{397} = 0.121$ ns and $t_{866} = 0.245$ ns. The magnetic field was $B = 1.9$ G.

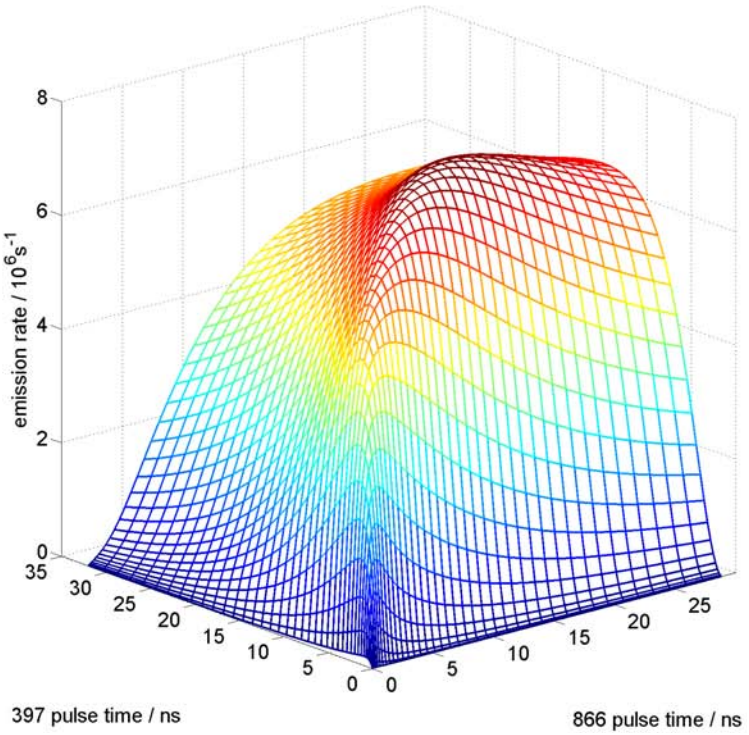

Figure 3.9: Rate equations simulation with pulse-length dependent intensities. Fixed parameters: maximum intensities $I_{397} = 10\ I_s$, $I_{866} = 100\ I_s$ and $t_d = 0$. Maximum $R = 7.70 \cdot 10^6$ counts/s occurs at $t_{397} = 8.82$ ns and $t_{866} = 12.2$ ns. The magnetic field was $B = 1.9$ G.

is no dead time between the 397nm pulse and the detection window, the photons collected originate almost exclusively from population excited to the $P_{1/2}$ level by the 397 nm laser and decaying directly back to the $S_{1/2}$ level. The effect is independent of the $D_{3/2}$ level into which population decays ~ 20 times more slowly than directly back to the ground state. With these hypothetical extremely short pulse times, scatter and fluorescence signal could be separated in time even in a two-level system.

With these parameters, the probability to emit a photon during a sequence is only $p = 0.007$ but this is compensated by the short cycle length. The count rate is $R_c = 53600$ counts/s which is close to the case of continuous excitation where the maximum is $\eta \cdot A = 63000$ counts/s with A being the Einstein coefficient of the $S_{1/2}-P_{1/2}$ transition. From this we see that if we were able to switch laser pulses fast and detect within the $P_{1/2}$ lifetime (7 ns) of the end of the 397 nm pulse, we could get a comparable signal with the pulsed method as we do for continuous excitation. Pulses this short would however have a large frequency spread ($\sim t_p^{-1}$). If this is on the order of the transition linewidth (21 MHz) or larger, the effective pulse intensity would be reduced. This effect is not included in this model.

We now take the switching of the AOMs into account. For each point t_{397}, t_{866}, the intensities used for the rate equation simulations are calculated using the functions fitted in section 3.2.2.2. The result is shown in figure 3.9. The maximum count rate is reduced to $R_c = 23100$ counts/s and the optimal pulse times are longer than in the ideal case, $t_{397} = 8.82$ ns and $t_{866} = 12.2$ ns which raises the probability to scatter a photon in a sequence to $p = 0.031$.

However, the peak is still in an area comparable to the lifetime of the $P_{1/2}$ level (7.1 ns). Since the beams don't turn off instantly and we hence don't want to start counting photons too early, we need to add dead time between the pulses. Figure 3.10 shows the count rate R_c over a range of pulse times $t = t_{397} = t_{866}$ for increasing dead time t_d. The initial peak disappears for dead times large compared to the $P_{1/2}$ lifetime and we are left with a broad maximum just below $R_c = 3000$ counts/s. Here the $P_{1/2}$ population during the PMT gate is negligible and in contrast to the short-pulse regime, the counts come from population excited from the $D_{3/2}$ level by the 866 nm laser. At short pulse times, the count rate shrinks because of the reduced intensity and excitation time and towards long pulse times it gradually rolls off due to the lower repetition rate.

There is a limitation to this rate equation description of the situation. When repumping $D_{3/2}$ population with the 866 nm laser, the lower state has more Zeeman components then the upper $P_{1/2}$ state which means there is a superposition state in the $D_{3/2}$ manifold, that is not addressed by the laser and will not be repumped (for any laser polarization) [128]. The ion will precess out of this "dark state" with a speed depending on the magnetic field which means that a fraction of the population is pumped out at a much slower rate than the rest. Looking at this effect with a rate equations model Hugo Janacek has found that

up to half the population is trapped in $D_{3/2}$ for longer than 100 ns during an 866 nm pulse which means that around half the population will not contribute to the fluorescence counts collected. To repump this population, fast polarization modulation techniques [129] could be employed.

3.2.4 Experimental results

In order to set up the sequence we need to determine the different delays for the pulses due to the signal traveling time in the cables to be able to precisely time them with respect to each other. This is done in the following way.

With an ion (of $^{40}Ca^{+}$) in the trap, we set up a sequence where the 866 nm beam is on permanently and the 397 nm beam is on for 500 ns at a nominal delay time of 0 ns. We then scan the starting time of a 500 ns PMT gate beginning at 0 ns until we observe a fluorescence signal which indicates an overlap of the two. This yields the 397 nm delay time which we measured to be 3480 ns. By repeating the process with the 866 nm beam pulsed and the 397 nm beam permanently on, we determined the 866 nm delay, 685 ns.

Knowing the pulse delays, the sequence for pulsed readout was set up. The sequence chosen for the following data is shown in the inset in figure 3.11. The PMT gate start time t_1 was scanned from the beginning to the end of the sequence. The pulse and gap times are rather large when compared to the ideal cases investigated above. The reason for this choice will be discussed below. In order to demonstrate readout in the presence

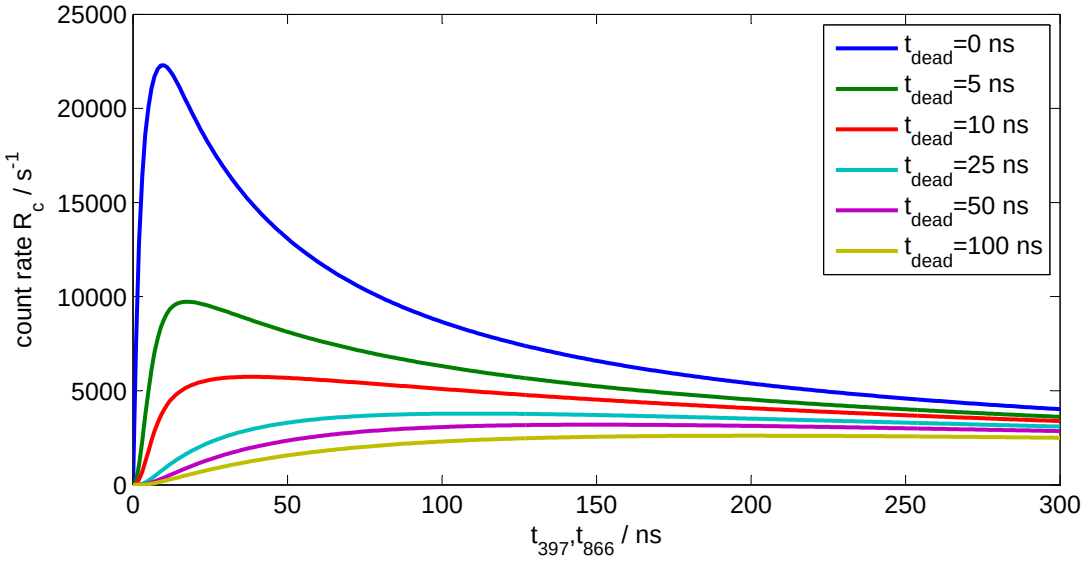

Figure 3.10: Simulated count rate R_c (see text) for different dead times t_d over a range of pulse times for equal pulse length of the two lasers ($t_{397} = t_{866}$). This shows that the initial peak is due to the finite lifetime of the $P_{1/2}$ level (7.1ns), i.e. we detect mainly spontaneous decay from $P_{1/2}$ rather than repumped population from $D_{3/2}$. It disappears for increasing dead time where the majority of the counts are provided by population excited from the $D_{3/2}$ level.

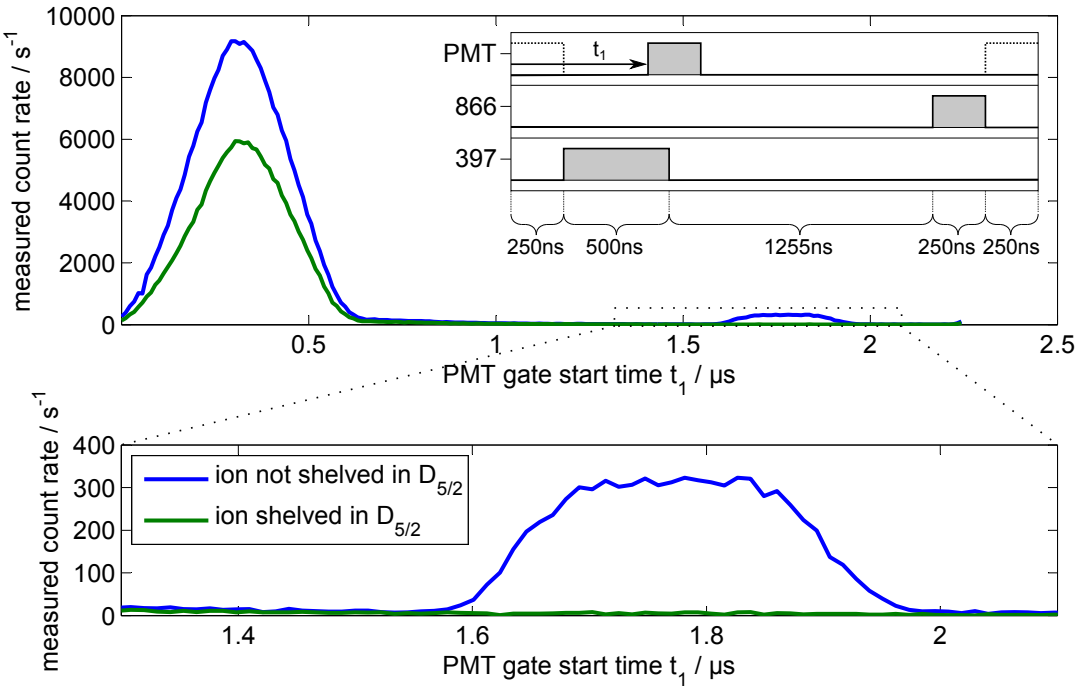

Figure 3.11: *Top:* The curves show the measured count rates during a scan of the PMT gate for the ion being shelved (green) and not shelved (blue) in the $D_{5/2}$ state. The inset shows the pulse sequence used. The first peak is the scatter or scatter-plus-ion signal respectively. The second peak comes purely from single photons generated by depumping the $D_{3/2}$ state for the unshelved ion. *Bottom:* Zoomed in plot of the second peak in the top plot. The signal-to-background ratio is 61 at this PMT gate position. Intensities used: $I_{397} = 4.4\, I_{sat}$, $I_{866} = 77\, I_{sat}$.

of a large amount of scattered light we steered the vertical 397 nm beam onto one of the RF electrodes to deliberately introduce scatter. The data presented below was taken with 59400 counts/s of scatter on top of 56400 counts/s of fluorescence from the ion giving us a signal-to-background ratio of ~ 1.

The fluorescence was sampled for 19.6 ms for each t_1. During this time, the pulse sequence was repeated continuously and the PMT pulses counted. The fluorescence rate is shown in the blue curve in fig. 3.11. Before proceeding to the next t_1 value, we inserted a Doppler cooling pulse during which no fluorescence was recorded. Subsequently, the experiment was repeated with an additional $397 + 850$ nm pulse inserted after the Doppler cooling pulse in order to shelve the ion in the $D_{5/2}$ state. This records the fluorescence rate for a shelved ion as in the case of qubit readout (green curve in fig. 3.11). The data shows a large peak at the start of the sequence where the PMT gate is coincident with the 397 nm pulse. The counts recorded for the shelved ion represent the background scatter. For the unshelved ion this peak is higher since the ion fluoresces (on average up to 20counts/sequence) in absence of the 866 nm laser until pumped to the $D_{3/2}$ state. The fluorescence drops down as the PMT pulse moves between the 397 nm pulse and the 866 nm pulse. As it is scanned onto the 866 nm pulse, we see a signal from the ion of 300counts/s

caused by the single photons that are emitted as the $D_{3/2}$ state is depumped. Since the 397 nm beam is off at this time, the scatter is strongly reduced. The shelved ion does not fluoresce and so we can get a measure of the background which is 15 counts/s giving us a signal to background ratio of 61 which is a substantial improvement over the continuous case. We see that the signal has a flat top even though the PMT gate and the 866 nm pulse have the same length which suggests that the photons arrive mainly at the beginning of the 866 nm pulse which is consistent with the depumping investigated with the Bloch equations. If the sequence as is were used for readout, optimal state discrimination (error $\sim 10^{-2}$) would require a sampling time of ~ 30 ms (~ 12000 cycles).

The background is still larger than expected from the PMT dark counts and it is dominated by the long tail that is trailing the 397 nm scatter pulse. This is the reason why such a long gap between the pulses was chosen. In order to make sure that no pulse sequence or counting hardware error was responsible, we measured the count rate with the PMT for scattered light only (no ion in the trap) and counting the PMT pulses directly with an external pulse counter[7]. The result is shown in a logarithmic plot in figure 3.12. The tail is clearly visible on the photon counts. To show that this effect is not present on the light pulse itself, a photodiode measurement (compare section 3.2.2.2) with long integration time is shown in the same plot for comparison. The initial height of the tail is around 4% of the peak signal which is an order of magnitude larger than the light signal at that point. It then drops off with a time constant of $\sim 0.5\mu$s. These pulses are coming from the PMT after the end of the light pulse. A plausible explanation is a PMT effect called "afterpulsing" (see Hamamatsu PMT manual[8]). Ionized gas atoms (mainly helium) that remain in the tube after the end of the light pulse drift towards the photocathode on timescales of a few hundred nanoseconds (or higher) where they generate electrons upon impact which are amplified and cause false photon signals.

This effect causes the majority of the background counts during our readout pulse (the actual dark count rate of the PMT is ~ 1count/s) and limits the choice of gap time which means a large cycle time and hence a low repetition rate. Even with this limitation, we have achieved a factor of 60 improvement in the signal-to-noise ratio in the presence of high scatter.

The readout fidelity, however, also depends on the signal itself [117]. With the cycle length as presented, the pulsed method would not outperform continuous readout in terms of fidelity. A detector with lower afterpulsing would allow the shortening of the pulses and hence a higher repetition rate which would increase the signal. A factor of 10 is needed to surpass continuous readout (see section 3.3). One possible strategy might be to use a switchable PMT and replace the gated pulse counting with pulsed PMT operation.

[7] Stanford SR400

[8] available at http://sales.hamamatsu.com/assets/pdf/catsandguides/PMT_handbook_v3aE.pdf

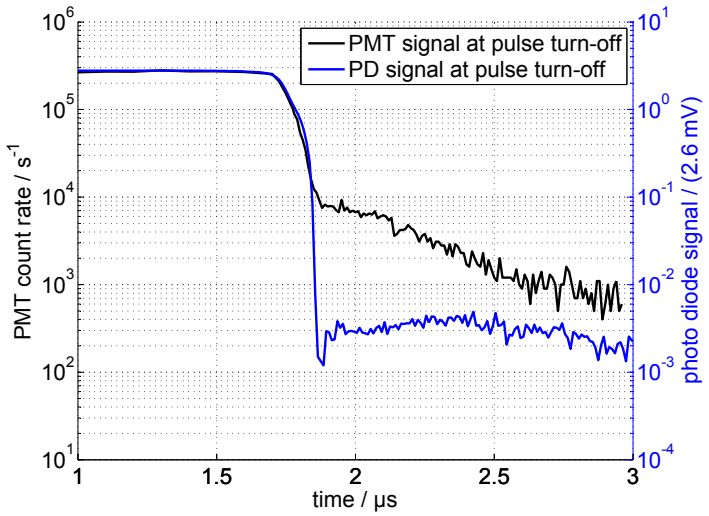

Figure 3.12: *Black curve, left ordinate*: Scan of a 25 ns long PMT gate over the trailing edge of a 1.5 μs pulse of scattered light generated from the 397 nm beam. The signal pulse is tailed by "afterpulsing" of the PMT (see text). *Blue curve, right ordinate*: Photodiode signal of the trailing edge of a 2.5μs pulse from the 397nm beam measured after the double-pass AOM used for switching the beam. The data were divided by 2.6 and aligned along the abscissa for comparison with the PMT curve. A background was subtracted and the smallest voltage recorded on the scope is 10^{-4} mV.

Fast high voltage switches are available[9]. Alternatively, a hybrid photo detector (HPD) could be used[10]. It consists of a single photocathode and instead of a dynode cascade uses a an avalanche photo diode (APD) for detection of the electrons and amplification of the signal. While requiring a high operating voltage (~ 8 kV), its afterpulsing is very low compared to PMTs (see Hamamatsu PMT manual).

3.3 Summary

Wherever ions are trapped close to surfaces and scattered light from the laser cooling beam is an issue for ion detection, the repumping techniques described in section 3.1 can be implemented to increase significantly the signal-to-background ratio. This is the case in miniaturized scalable trap geometries for QIP as well as other recent experiments in ion traps mentioned in the beginning of this chapter. In all these cases, the ease of implementation with only broadly stabilized diode lasers as well as its ready applicability to other ion species with similar level structures make this scheme attractive.

A low background level is important not only for ion detection, but also for accurate compensation of ion micromotion (for example, by the standard technique of rf/photon arrival time correlation [102]), or for thermometry as recently described in [118]. Our scheme can also be used in conjunction with heating rate measurements by Doppler re-

[9] e.g. Behlke HTS 151-02, 50 ns pulses ($\leq$ 10 ns rise time) with 6 MHz repetition rate
[10] e.g. Becker & Hickl HPM-100-40

cooling as described in [104]. The theory given in [104] is based on a two-level system which is not realized exactly in the standard repumping scheme I involving 3 levels connected in a Λ arrangement. Repumping with the 850 nm and 854 nm lasers (scheme II) gives a close approximation to a two-level system, as discussed in [82], which allows simple interpretation of the Doppler recooling data to extract the heating rate. In cases where there is high background scatter, scheme FII can be employed.

The main drawback of suppressing the background in this way is that the $D_{5/2}$ "shelf" level (see section 6.2) is part of the fluorescence cycle which means that the schemes cannot be combined with qubit readout. In order to overcome this we have developed and demonstrated a pulsed method in section 3.2.

We showed that method succeeds in significantly increasing the signal-to-background ratio by separating in time excitation and photon counting with precisely timed pulses and gated PMT signal operation. For the first demonstration presented here, the sequence was not optimized for readout fidelity. The latter is important, however, if the sequence is to be used as part of a QIP protocol and hence must be compared to the performance of the standard method of continuous fluorescence detection. The performance improvement through the pulsed method depends on how much background is present from the 397nm laser. At very low background, the pulsed method brings no advantage since, due to technical constraints, the cycle frequency will always be limited which means a lowered count-rate. At very high background, however, the pulsed method brings an increase in readout fidelity. What constitutes high and low in this context depends on how fast the sequence can be run, i.e. what fluorescence count rate the pulsed method can achieve. In the demonstration presented here we were severely limited by PMT afterpulsing in our cycle speed and hence our signal collection. This means the experiment presented establishes only a proof of principle and does not yet show an improvement in fidelity F over the standard method. The expected state-discrimination error ($\epsilon = 1 - F$) is shown for a number of example parameters in table 3.1.

	method	count rate / s^{-1}	s/b	ϵ
1	cont. (exp)	$5 \cdot 10^4$	$1 \cdot 10^0$	$5 \cdot 10^{-4}$
2	pulsed (exp)	$3 \cdot 10^2$	$6 \cdot 10^1$	$1 \cdot 10^{-2}$
3	pulsed	$5 \cdot 10^3$	10^2	$5 \cdot 10^{-4}$
4	cont.	$5 \cdot 10^4$	10^{-1}	$3 \cdot 10^{-3}$

Table 3.1: Comparison of the pulsed method against continuous fluorescence detection (cont.) in terms of the error ($\epsilon = 1-F$) in state-discrimination by fluorescence threshold [20]. ϵ was estimated using fig. 3.17 in [117]. Lines 1 and 2 show ϵ for the experimental parameters used in this chapter (not optimized for readout). The technically limited pulsed method has a higher error than the standard technique. Line 3 shows the pulsed method with estimated parameters achievable in the absence of afterpulsing (factor 10 speed-up). Here, the pulsed method breaks even which means for higher scatter the standard method will be surpassed (see line 4).

Chapter 4

The "New Old" trap

4.1 Motivation: Why a new trap?

Apart from scalability, achieving fault tolerant quantum operations is the other main challenge in quantum computing (see chapter 1). We are working towards performing a high-fidelity two-ion entangling gate between two different isotopes of calcium. For this purpose we need a reliable ion trap with a low heating rate, a high trap strength and low background scatter. Since we are not trying to focus on scalability in this case, we choose to work in a macroscopic trap. Previously, our group has performed such a gate between two $^{40}Ca^{+}$ ions with 83% fidelity [29] but extending this to higher fidelities and a mixed species crystal did not prove successful. This chapter describes the construction of a new trap and experimental setup towards this goal.

The old linear Paul trap which had been at the heart of our group's experimental success for over ten years consisted of four RF rods and two cylindrical endcaps [130]. The RF electrodes and the endcaps were 1.22 mm and 6 mm away from the trap centre respectively. The RF frequency used was $\omega_{RF} = 2\pi \cdot 6.4$ MHz with voltages up to 170 V_{p-p} and allowed for a maximum radial trap frequency of $\omega_r = 2\pi \cdot 900$ kHz. Typical axial trap frequencies were around 500 kHz at ~ 220 V_{DC}.

Given the limitations imposed by the breakdown voltages of the vacuum feedthroughs, the trap strength could not be easily increased beyond these values. The low trap frequency created difficulties in ground state cooling, since a slow continuous Raman cooling step had to be inserted between Doppler- and pulsed sideband cooling (see chapter 7). The experiments with mixed species ion crystals also ran into problems. The ions would frequently swap places or decrystallize. Often, irregular crystal shapes with radial alignment components as well as unexplained ion ejection from the trap were observed [21]. Increasing the trap strength as well as the aspect ratio should overcome these difficulties but was not possible with the existing trap setup. Finally, the vacuum chamber had a hexagonal shape and did not allow laser beams to be aligned perpendicular to the magnetic field which meant that pure π polarized light was not available on the ion. As a result the $^{43}Ca^{+}$ clock state preparation by optical pumping (see chapter 6) was poor.

In order to advance our experiments, we decided to construct a new ion trap. It is around 40% smaller in size making stronger confinement possible and is housed in an octagonal vacuum chamber to give the previously missing angles of optical accesss. The trap was nicknamed the "New Old trap" and its geometry as well as the experimental apparatus necessary for its operation is described in this chapter.

Apart from the direct scientific advantages, it was felt that after the continuous operation of the laboratory for over a decade, replacing the trap was a good opportunity to undertake renovations including the introduction of a new optical table, improved laser setups and an upgrade of the general laboratory infrastructure.

4.2 Experimental apparatus

The experiment was set up in two stages. First, a provisional setup with the minimum capabilities for trapping was arranged to test and characterize the trap. After the trap was established, the lab rebuild was undertaken and a number of modifications to the trap drive and the experimental setup implemented. Another change was that the beam height and correspondingly the height of the trap centre above the table top was raised from 75 mm to 100 mm.

Where the apparatus or results concerned with the first phase are described in the following, it will be referred to as being part of the "initial setup".

4.2.1 The trap

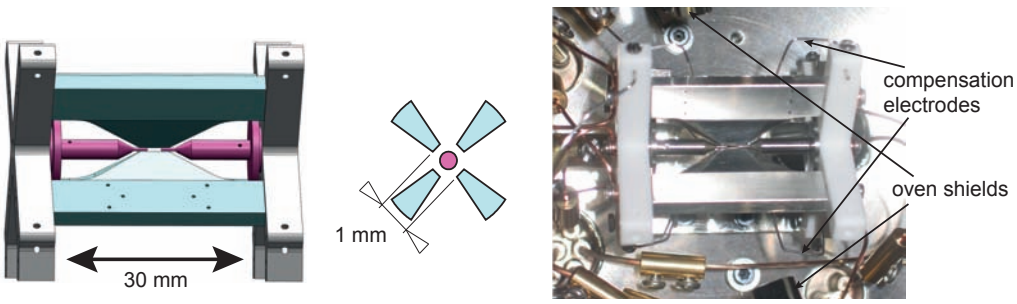

Figure 4.1: *Left:* Construction drawing of the trap. The Macor holders are shown in white, the RF electrodes in turquoise and the endcaps in purple. *Centre:* A cross-section view showing the electrode separation. *Right:* A photograph of the trap mounted on the base flange of the vacuum chamber. The compensation electrodes and the shields hiding the two calcium ovens are indicated.

Figure 4.1 shows the new ion trap. It consists of four tapered RF electrodes ("blades") and two cylindrical endcaps. The electrodes are machined out of stainless steel[1]. The concept is based on a smaller version of the established Innsbruck ion trap design [34]. The ion-to-electrode distance is 0.5 mm for the RF blades and 1 mm for the endcaps. The

[1] differing from the specifications, the electrodes are not made out of 316 and hence are weakly magnetic

trap is held together by two $\times$-shaped Macor supports which are themselves mounted on an aluminium holder. There are three compensation electrodes (designated "left", "right" and "bottom") which are stainless steel wire attached to the Macor supports and bent in towards the trapping region. They can be seen in the photo in fig. 4.1 and their nominal locations are marked in the technical drawing in appendix C, fig. C.1. The front edges of the blades facing the ion were rounded by manual polishing before assembly.

4.2.2 Vacuum setup

The trap is housed in a 316 stainless steel octagonal vacuum chamber[2] with two CF100 flanges on the top and bottom, and eight CF35 flanges around the side. The top flange is closed by a viewport[3] which has an AR coating for 397 nm light. This main viewport allows optical access for imaging the ions (see section 4.2.7) and to introduce the photo ionization beam (see section 4.2.8.1). The CF100 bottom flange is sealed by a custom base plate[4] in the centre of which the aluminium trap mounting block is attached. A technical drawing of this flange can be seen in the appendix, fig. C.3. It has three sets of feedthroughs built in. One 8-pin set is used to connect the three compensation electrodes, the two endcaps and the connections for the left oven (see section 4.2.3). Two 2-pin sets of feedthroughs are used to connect the two grounded RF blades on both ends. This allows the flexible application of microwaves for single qubit operations in $^{43}Ca^{+}$ (see chapter 6) since there is an output as well as an input. We can apply the signal on one side and choose the termination on the other. For the experiments in this thesis the output end was grounded. The third set has four pins, two of which are used to connect the right oven (see section 4.2.3). The base flange additionally features a CF16 flange which is welded partly sunk to allow clearance to the table surface. It is placed and angled such that it allows the photo-ionization beam that is introduced through the top viewport to exit the chamber avoiding scatter. It is sealed by an AR coated viewport[5].

The trap axis is aligned along one of the symmetry axes of the octagon. Optical access to the ion along the trap axis is blocked by the endcaps. The two flanges along this direction are hence chosen for the RF feedthrough and vacuum pumping respectively (see below). Five of the other six flanges have viewports attached and allow optical access perpendicular to and at $\pm 45^{\circ}$ to the trap axis.

The sixth leads to a T-piece with a viewport at the end maintaining optical access in this direction and a chemical getter pump[6] on the top housed in a 4.5" CF60 tube[7] connected to

[2] Kimball spherical octagon MCF600-SO20080
[3] TSL VPZ100QBBAR-LN
[4] LewVac ZFH-OXSW-100CF
[5] TSL VPZ16QBBAR-LN
[6] SEAS Sorb-AC GP 50 with C50-ST101 cartridge
[7] Kurt J Lesker CF Full Nipple FN-0450

the T by an adapter flange[8]. It is one of two pumps maintaining vacuum at $2.0 \cdot 10^{-11}$Torr. The other is an ion pump[9] connected to one of the flanges along the trap axis via another T-piece. The second connector is attached to a final T-piece which holds an ion gauge[10] and two all-metal valves[11] in series.

4.2.3 Ca ovens

Two calcium ovens are placed either side of the trap facing each other at about 35° from the trap axis. This angle was chosen to avoid blocking optical access from the viewports at 90° to the trap axis while retaining the ability to send the photoionization beams through at right angles to the atomic beam.

The ovens are made from 0.2 mm thick steel tube[12] which is filled with small flakes of metallic calcium. The tube is crimped together and spot-welded at both ends and has a small hole ($0.3 - 0.5$ mm) pointing towards the trap centre. As with the oven described in chapter 2, the calcium is heated up by an electrical current passed through the tube. A stream of evaporated calcium atoms leaves the opening and passes through the trap. Since the beam is less collimated than in the design presented in chapter 2, a steel foil[13] shield is placed in front of the oven to limit the output angle and avoid unnecessary calcium deposition on the electrodes (see photograph in figure 4.1).

While ^{40}Ca is the most prevalent isotope, ^{43}Ca only has a natural abundance of 0.135%. Loading $^{43}Ca^+$ by photoionization from a naturally abundant source was done in the old trap [126] but requires a high atom flux. Therefore we filled one of the two ovens with enriched material[14] containing 10% ^{43}Ca and $\sim 90\%$ ^{40}Ca. We have used this oven exclusively for the work presented here[15]. To start the calcium evaporation we had to increase the current to 6.6 A (see section 4.4.1). During normal ion loading operation, it is run[16] at 4.5 A and turned off once the desired number of ions is trapped.

4.2.4 Trap voltage supplies

4.2.4.1 RF resonators

A synthesized function generator[17] provides the radio frequency signal for the radial confinement. For initial trapping, we used a toroidal transformer similar to the one shown

[8] Kurt J Lesker zero length reducer RF 450X275
[9] Varian Vacion Plus 20
[10] Varian UHV-24P with x-ray limit of $5 \cdot 10^{12}$ Torr
[11] VG Scienta ZCR40R
[12] 316L stainless steel, inner diameter 1.8 mm
[13] 316 stainless steel, FE240265
[14] Oak Ridge National Laboratory, Q2010-0137-1
[15] the oven used is seen on the top in the photo, fig. 4.1
[16] power supply: TTi CPX 200
[17] SRS DS 345

in fig. 2.15 (chapter 2). The toroid[18] has an outer diameter of 33 mm and 28 turns on the high and 2 on the low voltage side. When loaded with the trap capacitance, the resonant frequency is 11.35 MHz and the quality factor is $Q = 22$.

The transformer was replaced with a helical resonator (can dimensions: length $B = 133$ mm, diameter: $D = 98.5$ mm; helix dimensions: 8 turns, wire diameter $d_0 = 4.76$ mm, diameter 4.5 cm, length $b = 90$ mm, winding pitch $\tau = 12$ mm; symbols from [131]). It has a loaded quality factor of $Q = 385$, a voltage step-up factor of $Q_{stepup} = 35$ and a resonant frequency of 29.72 MHz. Before the resonator, the signal is sent through a 44 dB amplifier[19]. We apply 30 dB of attenuation[20] after the frequency generator. This means that we get 14 dB overall signal amplification which even at maximum output settings of the frequency generator (24 dB) is safe to use with our feedthrough.

4.2.4.2 DC supplies

To provide the axial potential for initial trapping we used the DAC supply that was still in place from the old trap. It is set by the experimental control computer and can provide up to 700 V. For the smaller new trap, we only need tens of Volts for trapping and the high voltage supplies were found to be unstable at these voltages which is why they were replaced by a new set of DAC boards designed by Chris Ballance. The boards are controlled via the auxiliary Linux computer (see section 4.2.10.2) and provide voltages between -240 and $+240$ V. They are filtered by 2-pole CRCLC[21] filters and provide the endcap as well as the compensation voltages. The a.c. "tickle" voltages for the secular frequency measurements (see section 4.4.3) are applied through a capacitive tap-off after the filter.

4.2.5 Magnetic field coils

Coil	no.	N	diam. [mm]	dist. [mm]	B [G/A]
main	2	171	95	119.5	5.45
vertical	2	30	165	95	1.49
horizontal	1	92	84	115	1.40
initial	1	500	100	135	2.63

Table 4.1: Details of the magnetic field coils showing the number of coils used in each direction (no.), the number of turns N, the diameter $2R$ and distance d from the trap centre. The nominal magnetic field for each set in G/A was calculated using $B/I = \mu_0 N R^2/[2(R^2 + d^2)^{3/2}]$. The initial coil was replaced by the other three sets for the main experimental phase.

[18] Micrometals T94-6
[19] Frankonia FLL-25
[20] MW Devices MA-50 (10 dB) and Mini-Circuits BW-S20W2+ (20 dB)
[21] $C = 100$ nF, $R = 100$ kΩ, $L = 22$ μH

Five coils are used to set the direction and strength of the magnetic field at the ion position, two main field coils[22] along the set field direction (see fig. 4.5), a pair of vertical trim coils[22] around the base flange and the top window, and a single trim coil[23] arranged perpendicular to the main field for horizontal trimming. The field strength used for the main experiments is 2.05G which gives us a $^{40}Ca^{+}$ Zeeman splitting of 5.7MHz. For initial trapping, only a single coil along the main field direction was used (see section 4.4.4).

Table 4.1 summarizes the coil properties and the nominal fields they generate at the ion position.

4.2.6 RF and MW

Single qubit transitions can be driven by applying oscillating magnetic fields at the qubit splitting frequency, which is in the radiofrequency range at 5.7 MHz in $^{40}Ca^{+}$ and in the microwave range 3.2 GHz in $^{43}Ca^{+}$ (see section 6.3, chapter 6).

The radiofrequency is generated by a synthesized function generator[24], amplified[25] and matched into a 30-turn coil placed on the top viewport around the imaging optics tube. The coil forms a stable low Q resonator ($Q = 12$). The function generator settings are controlled by the experimental control computer.

The microwave fields are applied either directly to one of the DC-grounded blades or one of the endcaps via a bias tee. The two options give a different polarization for the MW field (see chapter 6). The signal is generated by a synthesizer[26] and goes to an amplifier[27]. The synthesizer is controlled by the experimental control computer via an analog DAC output. This setup will be replaced by a DDS board channel (compare section 5.5.2) which will allow more stable phase control.

4.2.7 Imaging system

We observe the ions with an EMCCD camera[28] or a photomultiplier tube[29] (PMT). The former is used to confirm the number of ions we have in the trap while all the quantitative measurements are performed with the latter. The imaging system is mounted vertically above the main viewport. Figure 4.2 shows the present state. Its history is illustrated in David Szwer's thesis, [21], chapter 2.6. The objective lens[30] has a focal length of 70mm and images the ion onto a pinhole directly in front of the PMT or via a movable beamsplitter onto the camera. One modification was made with the introduction of the new trap. Since

[22] power supply: TTi QL355TP
[23] power supply: TTi QL355P
[24] SRS DS 345
[25] Frankonia FLL-25, 44 dB amplifier
[26] Agilent E4422B
[27] MiniCircuits ZVE-8G
[28] Andor iXON DU437-BU2
[29] Hamamatsu H6180-01
[30] Nikon ED PLAN 1.5x SM2-U

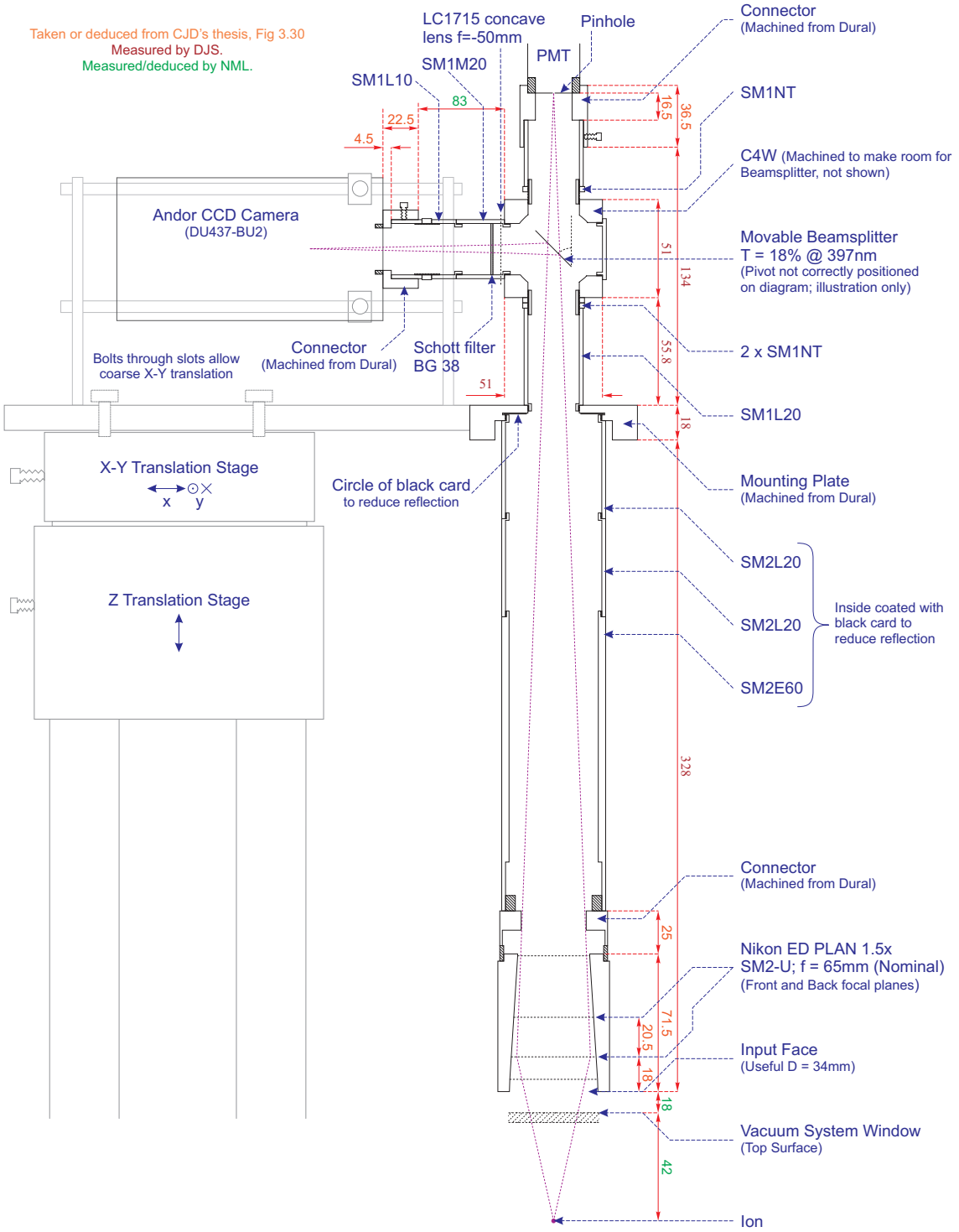

Figure 4.2: Imaging system as used for the majority of the experiments with the new trap. For the version used with the old trap and the initial setup see [21]. The main change is the addition of the concave lens in front of the camera to resolve the ions in the tighter trap.

the ions are now confined in a tighter trap, their distance shrinks to $\sim 5\ \mu$m. With the previous magnification ($M \simeq 5$), they could not be well resolved on the camera (pixel size $16\,\mu\text{m}\times 16\,\mu\text{m}$) anymore. We therefore added a secondary imaging stage in the CCD imaging path by placing a concave lens $f = -50$ mm in front of the camera. This increased the magnification by a factor ~ 4 so that it now stands at $M = 19.5$ allowing us to again clearly distinguish the ions on the camera. The lens position is chosen to give a simultaneously focused image at the camera and on the pinhole so that the PMT can still be used with the beam splitter in. Between the two settings, the imaging system needs to be moved by $\Delta x = 0.165$ mm (along the trap axis) and the focus adjusted by $\Delta z = 0.035$ mm[31].

The second change is that the spherical octagon is lower in height than the old vacuum system which brings the ion about 6 mm closer to the imaging lens. Together with the new AR coated main viewport, this has increased our collection efficiency significantly, from $\eta = 0.18\%$ previously [132] to 0.28% now. This value is measured by a pulsed method [100] related to the technique described in chapter 3. A combination of a 397 nm shelving pulse and an 866 nm deshelving pulse causes the ion to emit a single photon and the number of detected photons in a series of many such pulse cycles yields the collection efficiency η.

4.2.8 Lasers

Laser light is the main tool we use to create, cool, initialize, manipulate and read out our trapped ions and the quantum information they carry. This section gives an overview of the different laser systems used with the exception of the injection-locked frequency-doubled Raman laser system which is covered in chapter 5.

4.2.8.1 Photoionization

The ions are generated by photoionization (PI) from a beam of calcium atoms (see section 4.2.3). Figure 4.3 shows the energy level structure for exciting an electron in neutral calcium. The photoionization scheme[32] we use is highlighted in blue. A laser at 423 nm resonantly excites the atoms to the $4s4p\,^1\mathrm{P}_1$ state. The isotope shift between ^{40}Ca and ^{43}Ca is 612 MHz on this transition so the process can be driven isotope-selectively. Ionizing and loading the different calcium isotopes has been investigated previously in our group [126].

In our experiment, we drive the 423 nm transition with a Toptica DL100 extended cavity diode laser. The laser frequency is not locked to an external cavity but can changed over a small range via the experimental control computer through the laser controller's scan input for the grating piezo.

[31] this corresponds to a 0.07 mm change in micrometer setting
[32] another scheme is based on the 272 nm transition [134]

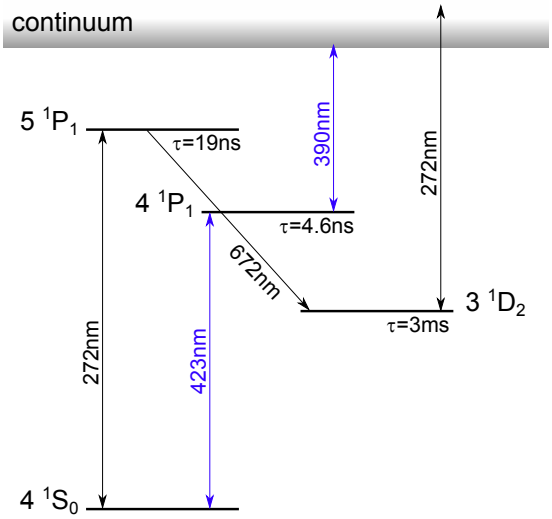

Figure 4.3: Transitions used for the photo-ionization of calcium with the transition wavelengths and state lifetimes. The scheme used in our group is highlighted in blue [133].

The ionization step from the excited state to the continuum requires light at wavelengths shorter than 389.81 nm. We use a free-running diode laser at 389 nm on a home-made mount. The two PI lasers are superimposed on a dichroic filter[33] and coupled into a single mode fibre[34]. A mechanical shutter in front of the fibre switches the beam. The PI lasers are shared between the group's two laboratories.

4.2.8.2 Lasers for Ca^+

The five transitions we need to address in singly-ionized calcium are indicated in fig. 1.1. The lasers at 866, 850 and 854 nm will be referred to collectively as the infrared (IR), 397 and 393 nm as the ultraviolet (UV) lasers. This section first describes the features common to all of the laser systems and then gives additional details specific to individual systems where appropriate.

Common features

All lasers described in the following are extended cavity diode lasers protected from back reflections by optical isolators ($\geq$ 30 dB isolation). With the exception of the 854 nm laser, they are Toptica DL100 systems frequency locked to reference cavities using the Pound-Drever-Hall (PDH) method [135]. On the 397/40 and 393 nm lasers, the modulation is achieved with EOMs[35] in the cavity beam path to avoid sidebands on the experimental beams. The other lasers are current-modulated. The PDH error signals are generated by

[33] Semrock FF409-Di02
[34] Thorlabs S405
[35] Leysop EOMs $\sim$ 80 MHz

electronic modules developed in our group [136] and fed into the laser's PID controller. The reference cavities used are commercial low-drift (≤ 500 kHz/hr) etalons produced by NPL. Their length can be adjusted by an integrated piezo mirror. The experimental control computer is set up to scan the piezo voltage of each cavity and thereby also the frequency of the respective laser locked to it.

All lasers except the 854nm laser have a blazed diffraction grating as one of the first optical elements to prevent amplified spontaneous emission from reaching the ion. The first order is used for the experiment while the weaker zeroth and minus first orders are used for the diagnostic and stabilization beams. The diagnostic beams are coupled into multimode fibres[36] and sent to a fibre switcher[37] which selects them in turn for analysis with our laser diagnostic system [137]. It uses a wavemeter[38] to display the laser frequencies and a pair of optical spectrum analyzers[39] to show the laser mode via their transmission signals.

All lasers go through AOMs[40] so they can be switched by the experimental control computer via the TTL input on the AOM controllers. To improve extinction, the AOMs are used in double-pass configuration. For the IR lasers, we separate the incoming from the outgoing beam by rotating the polarization after the first pass. For the UV AOMs, the diffraction efficiency depends more strongly on the polarization direction so we use vertical displacement with a lens and prism arrangement instead which allows us to pick off the second pass with an edge mirror. To further improve the extinction, we use the AOM driver's FM input to take the drive frequency off resonance when the AOM is off. This way, RF leakage is less likely to diffract photons and any photons still diffracted are less likely to be absorbed by the ion (extinction $< 10^{-6}$ after the fibre).

All laser systems with the exception of the 393 nm laser and the Raman system are located on a separate optical table from the experiment. After the switching AOMs, they are sent to the experimental table via single-mode fibres[41]. Since the fibres add intensity noise and polarization drift, we use an FPGA-based noise-eater system to stabilize the beam powers at each fibre output (see section 4.2.10.3).

397 nm lasers

There are two 397 nm lasers, designated $397/40$ and $397/43$ for each of the two calcium isotopes. In order to address both hyperfine levels in $^{43}Ca^{+}$, the $397/43$ laser goes through an EOM[42] before the fibre. We typically set the carrier on the $S^3_{1/2} \rightarrow P^4_{1/2}$ and the first

[36] UV: Thorlabs AFS 50/1257; IR: Corning J-VH IG5V/125 or Thorlabs AFS 50/50/1254
[37] High-Finesse MC-8
[38] High Finesse WS-7 with 10 MHz resolution and 60 MHz absolute accuracy
[39] IR: Technical Optics SA-7.5; UV: Toptica FPI100
[40] UV: IntraAction ASM-85(200)1.588 at 85 or 200 MHz; IR: Crystal Technology 3200-121 200 MHz
[41] fibre for 850 nm laser: HB 800-125P; other fibres see 4.2.8.2-4.2.8.2 footnotes
[42] New Focus 443 Visible Phase Modulator, centre freq. 3.226 GHz

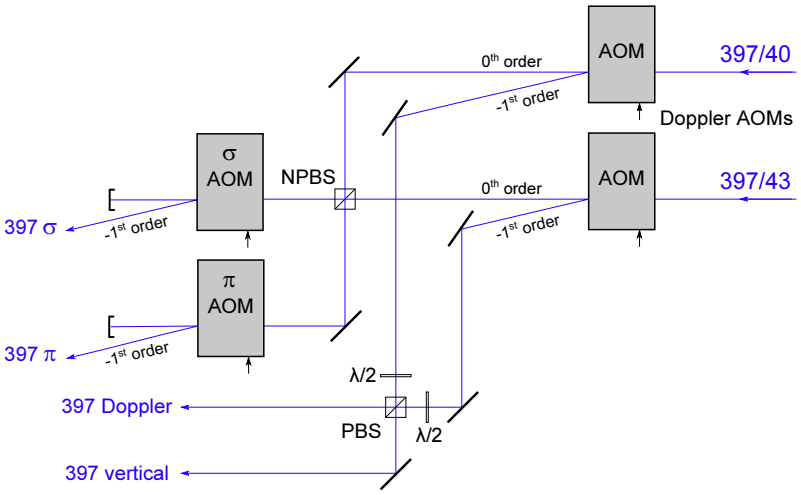

Figure 4.4: Schematic layout of the beam paths of the two 397 nm lasers on the experimental table after the noise eaters. The beams are superimposed to generate the Doppler cooling beam, the σ and π polarized state preparation beams as well as the vertical Doppler cooling beam used for micromotion compensation.

sideband on the $S^4_{1/2} \rightarrow P^4_{1/2}$ transition (see appendix D.2.1). We adjust the EOM frequency to empirically find the setting for maximum fluorescence (typical value 3.273 GHz).

To avoid feedback in the lasers from back reflections off the fibre ends which can be a problem even with the isolators [103], the fibres used for the two lasers are angle-polished (APC) single mode fibres[43]. The double-pass switching AOMs (at 85 MHz) on the laser table are called "Master" AOMs to distinguish them from the AOMs (at 200 MHz) on the experimental table.

After the noise-eater photodiode pick-offs (see section 4.2.10.3), the beams are superimposed to form the four experimental beams. The layout is sketched in figure 4.4. The Doppler beam, and the σ- and π-polarized state preparation beams can be independently switched with 200 MHz AOMs while power is distributed between the vertical and regular Doppler beam with a half waveplate and PBS. The vertical beam is only used for micromotion compensation (see section 4.4.5 and 2.6.2).

393 nm laser

The 393 nm laser is located on the experimental table. A beam splitter[44] picks off part of the main beam for the noise-eater photodiode. The beam also goes through an EOM[45]. The frequency is set so that we shelve $^{40}Ca^+$ with the carrier and $^{43}Ca^+$ by addressing the $S^4_{1/2} \rightarrow P^5_{3/2}$ transition (see Appendix D.2.2) with the first sideband, 1940 MHz to the blue. The beam is switched with a 200 MHz AOM.

[43] Schäfter+Kirchhoff PMC-360Si-2,3-NA012-3-APC-1000-P
[44] Thorlabs BSW10
[45] New Focus 4421 Visible Phase Modulator, centre freq. 1.938 GHz

866 nm laser

Similar to the 393, the 866nm laser is used to address both isotopes using an EOM[46]. In this case, we don't just want to address a single transition between two hyperfine states, but repump the entire $D_{3/2}$ manifold. This is accomplished by setting the main (carrier) frequency in the centre of the various narrowly spaced frequency components (see appendix D.2.3), so all are repumped sufficiently by off-resonant excitation. The first EOM sideband is set to be in resonance with $^{40}Ca^{+}$, 3.464 GHz to the blue of the carrier. The beam is sent to the experimental table by an APC fibre[47].

854 nm laser

The 854 nm laser is home built[48] and was used at 850 nm before the reorganization following the commissioning of the New Old trap. The frequency is not locked since the passive stability is enough to hold the laser close enough to resonance to provide reliable deshelving from the $D_{5/2}$ state for several hours. For mixed species work, we set the laser between the two resonances (1.7 GHz away from each (see appendix D.1) and increase the intensity so we are able to deshelve both isotopes. While this is workable, it was sometimes difficult to get enough power through the fibre[49] for this application, since the mode shape of this laser is particularly poor. In the medium term, replacing this laser will be a useful improvement. The laser was also not intensity-stabilized during the experiments presented here.

4.2.9 Optical setup

Figure 4.5 shows a sketch of all the beams going through the trap. The 866 and 854 lasers are superimposed on a PBS. Their polarizations are rotated by 45° with a $\lambda/2$ waveplate, so at the trap they are 50% $\sigma^{\pm}$ and 50% π polarized. They are superimposed with the 397 Doppler cooling beam on a mirror coated for the UV and then focussed through the trap.

The state preparation and readout beams 397σ, 393 and 850 come in through the same viewport at small angles to each other. The 850 nm beam is parallel to the magnetic field direction for optimal $^{40}Ca^{+}$ readout. By changing the trim coil fields, the field can instead be aligned with the 397σ beam for optimal state preparation. All three beams are linearly polarized with crystal polarizers[50] and then pass $\lambda/4$ plates making them either left- or right circularly polarized so they are σ^{+} or σ^{-} at the ion. The 397π beam for preparing the

[46] New Focus 4431 Visible Phase Modulator, centre freq. 3.266 GHz
[47] Diamond HB 800
[48] diode: SDL 5422-H1 SN=AN361
[49] Schäfter+Kirchhoff PMC-780-4,7-NA013-3-APC-1000-P
[50] UV: Thorlabs GT10-A; IR: Thorlabs GT10-B

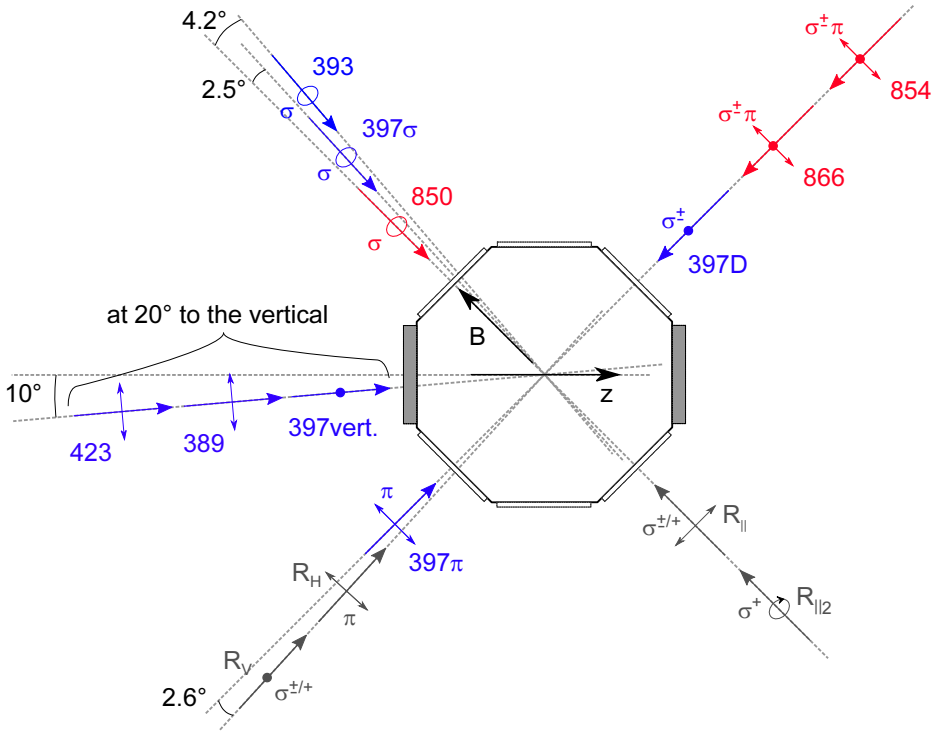

Figure 4.5: Layout of the different beams going through the trap with polarization directions and angles. 397D is the 397 nm Doppler cooling beam superimposed with the two IR repumpers. The viewport for this beam is mounted at the end of a T-piece connected to the chemical getter pump (not shown). The Raman beams R, indicated in dark grey, are described in chapter 5. The magnetic field direction B and the trap axis z are also shown. The on-axis ports of the chamber do not have viewports but hold the RF feedthrough (left) and vacuum components (right, see section 4.2.2).

$m_F = 0$ clock state in $^{43}Ca^+$ (see chapter 6, section 6.1) is sent in perpendicular to the B field direction.

As described at the start of section 4.2.8.1, the PI lasers are sent in through the top window. They are superimposed with the vertical 397 nm beam on a PBS. The optics for this beam path are mounted on a platform above the helical resonator which is connected to the RF feedthrough on the flange below. For completeness, the Raman beams (see chapter 5) are also included in the drawing.

4.2.10 Experimental control

The experiment is controlled by several computers. Apart from the main experimental control and an interfaced auxiliary computer which are described below, there is one computer running the laser diagnostic system and displaying its output and one used for the EMCCD camera acquisition program.

4.2.10.1 Experimental control computer

The experimental control computer has three main purposes. Firstly it is used to define and run timed experimental sequences. During these, lasers and RF/MW signals are switched by TTL outputs on a PCI card[51] connected to AOM controllers or RF switches respectively. The pulses are hardware-timed by the laser control unit (LCU) designed by Ben Keitch [136] and have 0.1 μs resolution.

Secondly, it records fluorescence data from the PMT. The number of photons arriving in a set time interval are counted with the help of a pulse stretcher[52] by counting hardware integrated on the PCI card. Additionally, photon arrival times with respect to the RF cycle can be recorded with a time-to-amplitude converter[53] (see [117] for details). These RF correlation measurements are needed for micromotion compensation (see section 4.4.5 and chapter 2).

Thirdly, the program interprets and presents the recorded data in an accessible way. It displays the photon count rate during continuous operation or a laser frequency scan. Timed sequences are repeated many times (typically 500 to 2000) before a parameter is changed. Here, the fluorescence data is interpreted by discriminating between a "bright" and a "dark" state of the ion with a threshold method (see chapter 6) and the relevant fraction displayed. Finally, the program saves the data including the raw photon counts and relevant analogue signals such as photo diode signals for beam power measurements or DAC voltages used during a scan. It also records a log of the experiments performed in a session including the parameters and pulse sequences used for each data file.

The Turbo Pascal program performing all these tasks with ineffable reliability is called "PC"[54] and runs under MS-DOS. For more details on the experimental control computer, please refer to [136, 138, 139].

4.2.10.2 Auxiliary Linux computer

The auxiliary computer runs Linux (Ubuntu) and is used to control the DC electrode voltages for axial confinement trap and micromotion compensation by serial port. It also manages the DDS boards for the Raman beams, sets magnetic field coil currents, the frequencies on the RF and MW synthesizers as well as on the synthesizer[55] driving the injection AOM, and the PMT power supply via GPIB.

The control program was written by Chris Ballance and Thomas Harty in C++ and has a graphical user interface on which the different values can be changed manually. The program can also take inputs from the main experimental control program via a serial link.

[51] Advatech PCI 1200 A
[52] Oxford central electronics (the ~ 8 ns PMT pulses are stretched to 50 ns)
[53] ORTEC TAC 566
[54] "Politically Correct Photon Counting"
[55] Marconi Instruments 2019A

This makes it possible for the main program to prompt parameter changes on the systems controlled by the auxiliary computer. In this way, the main program can for example have the Raman beam detuning changed between sequences which means this parameter can be scanned similarly to the experimental control computer's own DAC outputs.

4.2.10.3 Noise eater FPGA

In order to stabilize the laser intensity at the ion, we use an FPGA-based digital PID feedback circuit controlled by a LabView program to stabilize the beam powers. This is running on a third, independent computer. A polarizer and a pick-off leading to a photo diode are placed after the fibres bringing the beams from the laser table to the experimental table. The polarizer translates any polarization change caused by thermal or mechanical fluctuations in the fibre into intensity noise. Together with any additional noise coming from the fibre input coupling, this noise is reduced to $\leq 1\%$ by the feedback circuit which modulates the AOM RF power via the AOM controller's AM input (see [140, 103] for details). The system also takes the laser switching TTL signals as a digital input, pausing the feedback when the beam is off. In the LabView program, the setpoint of the feedback loop can be adjusted to change the power in the experimental beams.

4.3 Trap model

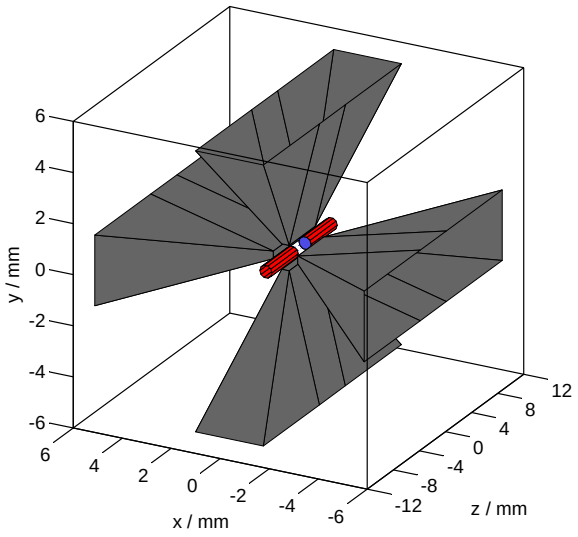

Figure 4.6: Model used for the CPO simulation of the trap (by Chris Ballance). The RF electrodes are in gray, the endcaps in red and purple.

As for the Microtrap described in chapter 2, we constructed a simple CPO model of the trap to calculate the potentials and find suitable initial trap voltages. A graphical representation is shown in figure 4.6. Second-order polynomial fits to the potentials are

shown in figures 4.7 and 4.8. The quadrupole amplitudes (see chapter 2, eq. 2,3) we obtain from the fits are:

$$Q_z/V_{DC} = 0.286\,\mathrm{mm}^{-2} \tag{4.1}$$

$$Q_r/V_{RF} = 1.98\,\mathrm{mm}^{-2} \text{ and } 1.84\,\mathrm{mm}^{-2} \text{ (for the two radial directions)} \tag{4.2}$$

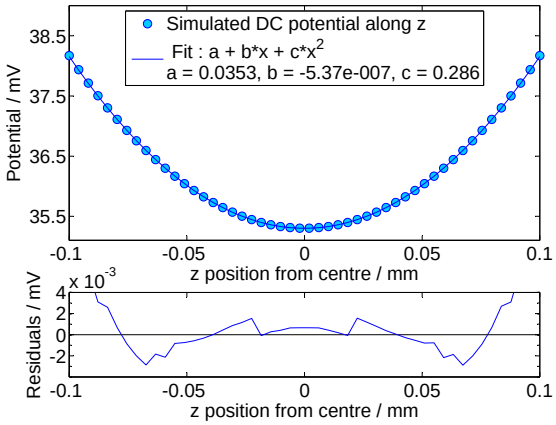

Figure 4.7: Second order polynomial fit along the axial direction of the simulated DC endcap potential (1 V applied). From the parameter c we get $Q_z/V_{DC} = 0.286\,\mathrm{mm}^{-2}$.

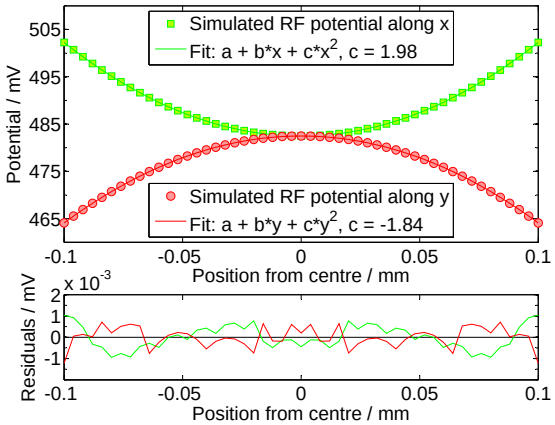

Figure 4.8: Fits along the radial directions of the simulated RF potential (1 V applied). We get $Q_r/V_{RF} = 1.98$ and $1.84\,\mathrm{mm}^{-2}$. The other parameters are $a = 0.482$ and $b = 0\,\mathrm{mm}^{-1}$ for both.

4.4 Trap characterization

Most of the results presented in this section were part of the early characterization of the trap and obtained with the initial experimental setup as described in section 4.2.

4.4.1 Loading both isotopes

In order to load mixed species crystals, we need to ionize the two isotopes selectively (see section 4.2.8.1). Figure 4.9 shows the neutral fluorescence signal from the enriched calcium oven recorded with the PMT during a scan of the 423 nm laser. Since the 423 nm laser is not locked, this scan was taken by scanning the grating piezo which means the ramp was not entirely linear. Additionally, the beam is not intensity-stabilized and so the beam has fluctuations introduced by the fibre and is subject to a nominally linear power change with detuning. A sloped baseline was subtracted from the data but the fit quality is still not high. However, we find the peaks 603 MHz apart which is close to the expected value for the isotope shift of 612 MHz [126] for the 423 transition. Comparing the peak

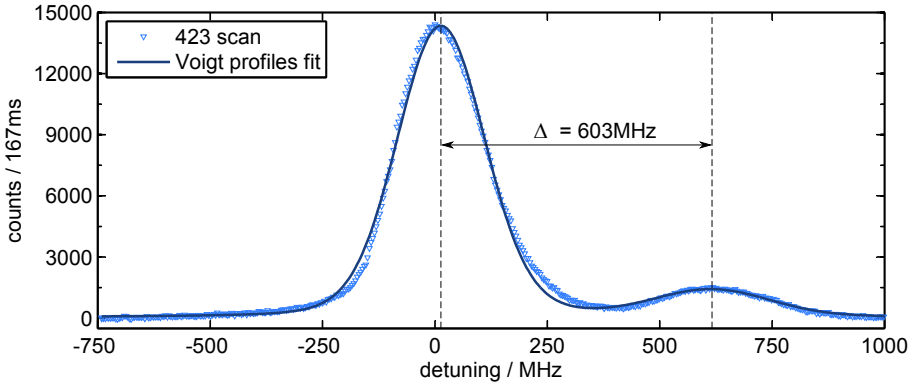

Figure 4.9: Background-corrected neutral fluorescence signal during a scan of the 423 nm laser (intensity $\simeq 4.8 \cdot 10^3$ W/m^2, oven current 5.5 A). A sum of two Voigt profiles was fitted to the data which gives the peaks to be 603 MHz apart and the peak height ratio yields 10.7% ^{43}Ca. The fit quality is limited because of intensity and frequency drifts during scan (see text).

heights relative to each other we get 10.7% ^{43}Ca and 89.3% ^{40}Ca which agrees closely with the nominal isotope ratio in the enriched calcium (10% : 90%).

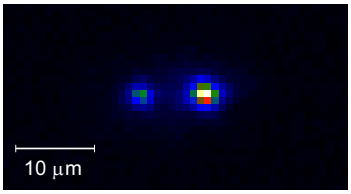

Figure 4.10: Two-ion crystal (^{40}Ca$^+$ right, ^{43}Ca$^+$ left) in a 0.67 MHz axial trap.

With our enriched calcium oven, we are able to easily add single ions of either isotope to our trap. Figure 4.10 shows an EMCCD camera image of a mixed species two-ion crystal. The ^{43}Ca$^+$ ion is dimmer since the $P_{1/2}$ states constitute a smaller fraction of the Doppler cooling manifold compared to ^{40}Ca$^+$. In the initial setup, only ^{40}Ca$^+$ ions were loaded because the laser setup for ^{43}Ca$^+$ was not in place. The image was taken after the lab rebuild. Typical single-ion fluorescence signals for a near-resonance beam saturating the 397 nm transition are 60000 counts/s in ^{40}Ca$^+$ and 24000 counts/s in ^{43}Ca$^+$.

4.4.2 Background gas collision rate

Apart from heating through electrical noise, a more drastic heating mechanism is collisions with background gas atoms in the vacuum chamber. In the old trap, about one fluorescence drop-out per hour due to collisions of the ion with the background gas was observed [117]. To compare this to our trap, ion fluorescence over several hours was recorded. One such data set is shown in figure 4.11. The 866 nm laser jumped out of lock after three and a half hours. Until then, we see on average one dropout every 40 mins which is consistent with the old trap given the pressure in our system is $2.0 \cdot 10^{-11}$ mBar compared with $1.3 \cdot 10^{-11}$ mBar in the old system [117]. The experiment was repeated with higher time resolution and for longer recording time and a consistent drop-out rate found.

4.4.3 Secular frequencies

We measured the trap frequencies using the tickle method (see section 2.6.3). We applied an AC excitation voltage to one of the endcaps and varied the frequency observing the fluorescence. This allows us to determine the trap frequencies to within a couple of kHz in most cases except for weak trapping potentials where the accuracy is decreased by the broad resonance and it is easy to kick the ion out of the trap.

Axial trap frequency

Figure 4.12 shows a plot of the axial trap frequency for different endcap voltages. A fit of the axial frequency (see eqn. 2.5) shows that there is an offset on our axial field so that we were able to trap even with negative voltages, which means applying an anti-trapping field. The first two points in the plot are very unreliable and were ignored for the fit since they were taken with a very weak trap (see above).

The feature we want to deduce from this is the parameter C from which we can get Q_z using the equations stated in section 2.5.2, $Q_z/V_{DC} = (2\pi\ C)^2\ m/e^2$. From the fitted parameter $C = 189\,\mathrm{kHz}/\sqrt{\mathrm{V}}$ we get: $Q_z/V_{DC} = 0.292\,\mathrm{mm}^{-2}$. This value is very close to the one we expected from the CPO simulations ($Q_z/V_{DC} = 0.286\,\mathrm{mm}^{-2}$, see section 4.3).

The axial frequency does slightly depend on the RF voltage. This effect is not part of our linear trap model and is due to the finite length of the RF electrodes, the edges of which give an axial field contribution. When making the measurements of the radial trap

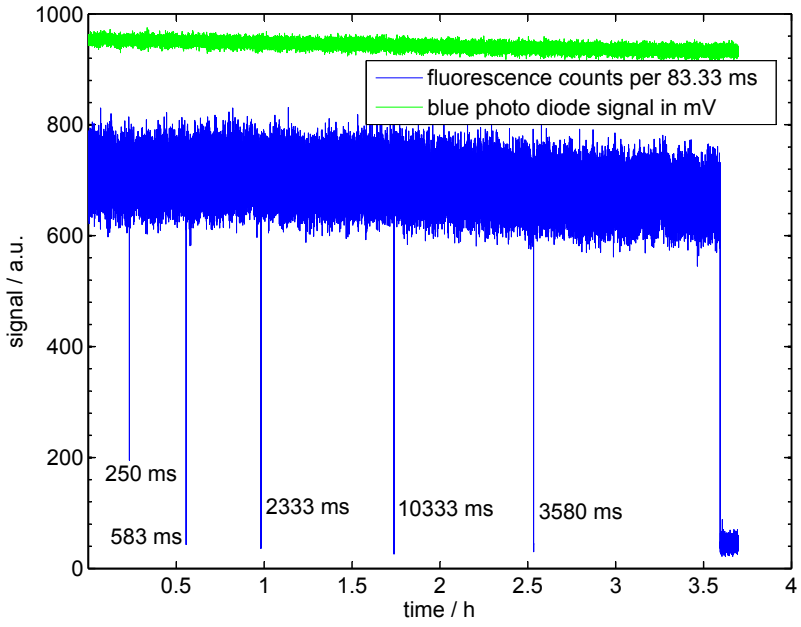

Figure 4.11: Fluorescence signal of a single $^{40}Ca^{+}$ ion with dropouts. The labels show the duration of each dropout. The photo diode signal monitoring the 397 nm laser intensity is also shown.

frequency (see 4.4.3), we recorded this change. It can be seen in figure 4.13, including a second order polynomial fit. The axial frequency only changes by a few percent over the entire range of RF drive voltages.

Radial trap frequency

Figure 4.14 shows a plot of the radial trap frequency for different driving voltages set at the RF generator. The fit follows equation 2.4.

We get $q/V_{pp} = 0.0267$ which means $Q_r \cdot Q_{stepup}/V_{RF} = 27.7\,\mathrm{mm}^{-2}$ (see eq. 2.9). Since the axial model matches the data closely, we can use the radial quadrupole amplitude from the trap model to get a better estimate of the voltage step-up Q_{stepup}. Taking $Q_r/V_{RF} = 1.9\,\mathrm{mm}^{-2}$ (see section 4.3), this gives $Q_{stepup} = 14.6$ which is a very reasonable value given that it is only about two thirds of what we estimated from the reflected power ($Q_{stepup} = 22$), a value that does not include losses.

Typical trap parameters

The above results were obtained with the toroid in the initial setup. Now we are using the helical resonator to amplify the trap RF voltage. Here we give typical parameters used for trapping in the experiments described in chapters 6 and 7. Our standard axial trap strength is $f_z = 1.98$ MHz with 104 V on the near and 109 V on the far endcap. Other typical values are $f_z = 1.50$ MHz (endcap voltages: 60.0 V and 62.5 V respectively) and $f_z = 0.99$ MHz (endcap voltages: 25.0 V and 26.2 V respectively).

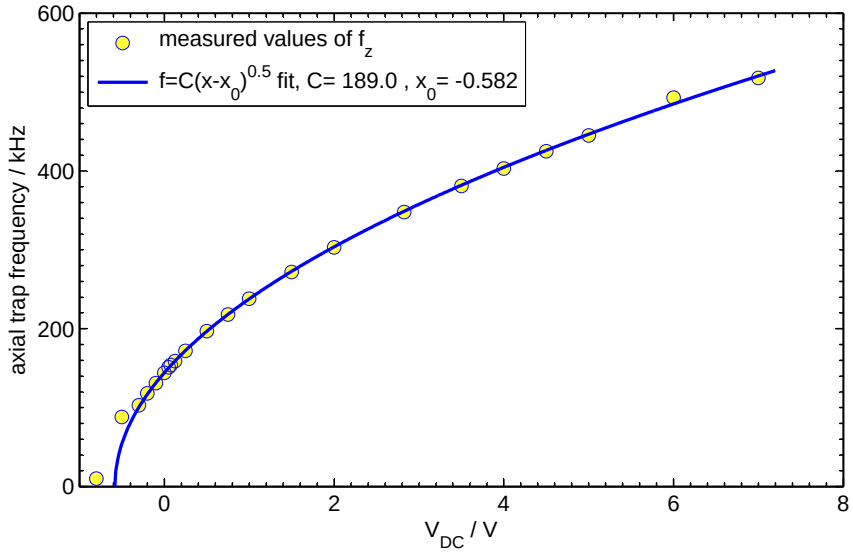

Figure 4.12: Tickle measurement, axial trap frequency for different endcap voltages

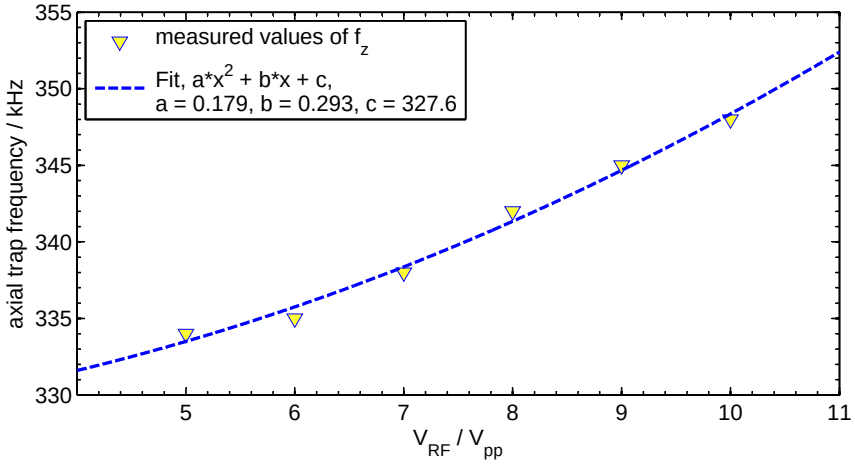

Figure 4.13: Tickle measurement, axial trap frequency for different RF voltages, 10/02/2011

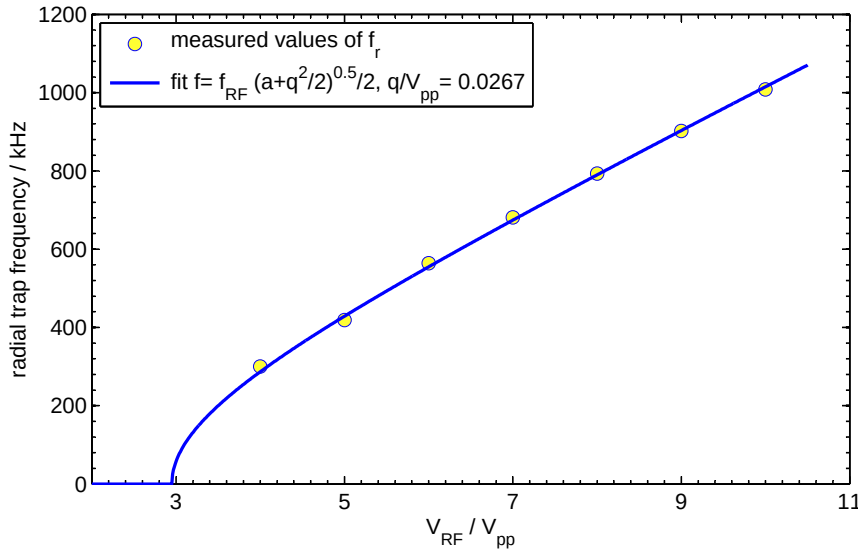

Figure 4.14: Tickle measurement of the radial trap frequency for different voltage settings at the RF synthesizer. The fitted value is $q/V_{pp} = 0.0267$.

For the radial confinement, we typically use a frequency-generator setting of 18.0 dBm which is equivalent to 1.5 W of input power at the feedthrough. At the standard 1.98 MHz axial trap this gives a radial trap frequency of $f_r = 3.1$ MHz. For the 1.49 MHz and the 0.99 MHz axial trap settings, this rises to $f_r = 3.2$ MHz and $f_r = 3.3$ MHz respectively.

The standard setting was used for the majority of the experiments presented in chapters 6 and 7. The maximum radial trap strength we have tested is $f_r = 4.1$ MHz at a setting of 20 dBm.

4.4.4 Magnetic field

In the initial setup, there was only a single field coil and the cooling beams at 397 and 866 nm were $\sigma^{\pm}$ polarized. The direction of polarization was adjusted by temporarily

placing a polarizing beam splitter directly in front of the window and maximizing reflection by changing the appropriate $\lambda/2$ plate in each beam.

The coil gives us a nominal field at the trap centre of 2.6 G/A (see section 4.2.5). We took a series of scans with the 866 nm laser at different coil currents. Derek Stacey fitted them with a Bloch equations simulation [122, 123] to infer the B field experienced by the ion. The results are shown in figure 4.15 with negative values of the applied field meaning an inversion of the field direction.

The overall magnetic field at the ion's position is the sum of the applied field $\vec{B}_a$ and the laboratory field $\vec{B}_0$:

$$\vec{B} = \alpha\, \vec{B}_a + \vec{B}_0 \tag{4.3}$$

where α is a scaling factor that includes screening of the applied field by the vacuum system. This means the magnitude of the field can be written as:

$$B = |\vec{B}| = \sqrt{\alpha^2 B_a^2 + 2\alpha B_a B_0 \cos(\theta) + B_0^2} \tag{4.4}$$

where θ is the angle between $\vec{B}_a$ and $\vec{B}_0$. A fit of this function to the data is included in figure 4.15. The parameters indicate that the field magnitude is 76% of the nominally applied field and the laboratory field has a magnitude of 1.2 G, at an angle of 109° to the applied field.

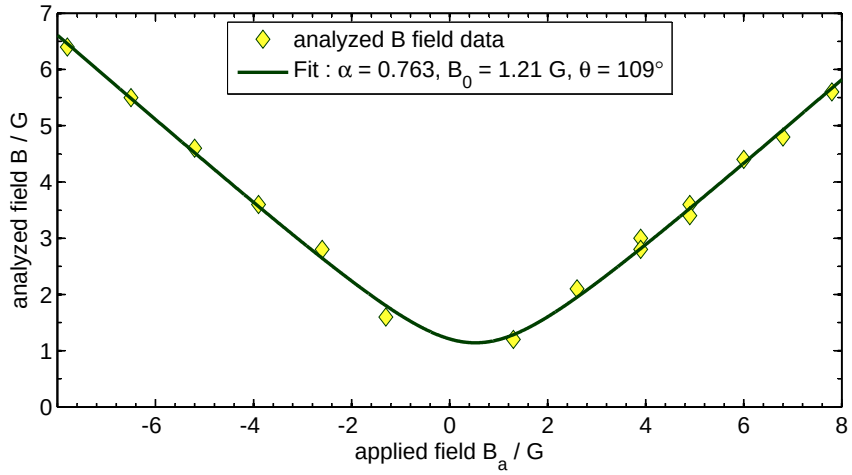

Figure 4.15: B field values analyzed from 866 scans versus nominal values of the applied field. The parameters from a fit of eq. 4.4 are shown.

4.4.5 Micromotion compensation

The compensation system described here was realized in the current version of the experiment with all the beams in place (see fig.4.5). In order to detect and compensate the ion's micromotion, we use photon arrival-time RF correlation measurements [102]. The amplitude of the RF correlation histograms is minimized when the ion is moved into the

centre of the RF potential by adjusting the compensation voltages. Only the micromotion along the direction of the cooling beam used during the measurement can be observed. So in order to find the global minimum we use three independent beam directions, the "Doppler", "sigma" and "vertical" beams, and minimize the RF correlation signal along each. The "Doppler" direction designates the usual Doppler cooling beam. The "sigma" beam is normally used for state preparation by optical pumping with σ^+ polarized light. For the compensation measurements, it is set to linear polarization so fluorescence can be observed. The "vertical" beam is introduced through the imaging viewport (see fig. 4.5).

The trap has three compensation electrodes (see diagram C.2 in appendix C), labeled "left comp", "right comp" and "bottom comp". The voltage on each of these will introduce a different field at the ion's position, both in direction and strength. Therefore in general all three voltages will need to be modified to minimize micromotion along one beam direction without affecting the other two.

We need a compensation voltage basis set that allows us to change the compensation fields along the three beam directions independently. To obtain it, we measured the relative change in correlation signal along each direction under variation of each voltage. We fit sine curves to the normalized correlation signals to get the amplitudes for each voltage (compare figure 2.26, chapter 2). Fitting a straight line to this data for each combination of beam and voltage gives us a set of nine slopes (see table 4.2) which are the coefficients in a system of three linear equations. Solving this system numerically yields three vectors (see equation 4.5), one for each beam direction. The vector entries are ordered from the top to give a left, right and bottom comp value. The values give the amount by which each compensation voltage has to be altered in order to achieve a change in the correlation amplitude of 1% in the beam direction in question.

	vertical	Doppler	sigma
left comp	53.3	6.0	3.84
right comp	-14.6	-1.2	-1.19
bottom comp	0	9.71	9.53

Table 4.2: Fitted slopes in units of %/V for the change in correlation signal for the three different beam directions with each different compensation electrode.

$$\vec{x}_v = \begin{pmatrix} 0.0004 \\ -0.0670 \\ -0.0085 \end{pmatrix} \quad \vec{x}_D = \begin{pmatrix} 0.4688 \\ 1.7115 \\ 0.0248 \end{pmatrix} \quad \vec{x}_\sigma = \begin{pmatrix} -0.4777 \\ -1.7438 \\ 0.07965 \end{pmatrix} \tag{4.5}$$

In our auxiliary experimental control program, we implement this basis set so that we have three compensation parameters (Doppler, sigma, vertical) to change during compensation which get converted into applied voltages on the electrodes automatically. Using this system, only one compensation round is necessary. The largest residual cross-

coupling can be observed between the Doppler and vertical directions where a change in the Doppler parameter has an effect on the compensation histogram observed with the vertical beam that is only about a factor of 5 lower than the influence exerted by the vertical parameter. We therefore adjust the vertical direction last when compensating our trap.

4.4.6 Recrystallization

As described at the beginning of this chapter (see section 4.1), keeping mixed species crystals stable was a major problem in the old trap. In our new trap, we found that we could "crystallize" a $^{40}Ca^{+}-^{43}Ca^{+}$ pair at axial trap frequencies up to 1 MHz quite easily both when loading the second ion and when the crystal had heated up (by a background gas collision, see section 4.4.2, or if one of the 397 nm lasers had been taken to the blue of resonance). At higher trap strengths, such as our standard operating trap at 2 MHz, however, we could not get the pair to crystallize even by trying a range of different detunings of both 397 nm beams as well as increasing the beam powers.

To solve this we reduce the endcap voltages, crystallize the ions and then take the trap strength back up to normal levels. Once the ions are crystallized, they remain so reliably unless they are heated by a background gas collision or by a cooling laser going out of lock and jumping to the blue of resonance. In order to simplify and automate the recrystallization process, we have set up the following very reliable[56] recipe. It is implemented in the experimental control program code (see section 4.2.10.1). It involves cooling the crystal with the $397/40$ laser only.

1. Detune the $397/40$ laser 150 MHz red of resonance.
2. Lower endcap voltages to give a $f_z = 500$ kHz trap.
3. Wait a short period of time (typically 3 s).
4. Raise endcap voltages back to their previous value.
5. Retune $397/40$ frequency to its previous value.

During experimental runs, the program can be set to perform this sequence automatically if the fluorescence level detected on the PMT during a "check" observation time at the end of an experimental sequence falls below a certain threshold indicating decrystallization. This way, data acquisition during long runs does not need to be restarted even when a background gas collision occurs.

[56] in ~ 100 tests, we observed only one instance where two attempts were necessary to crystallize the ions

4.5 Summary

We have successfully set up a new ion trap experiment for the performance of high-fidelity laser gates. A new macroscopic trap was constructed and ions subsequently trapped. We have characterized the trapping potentials including a comparison with a computer model which gave good agreement. The trap was well-compensated using an adapted basis set of compensation voltages. The experimental apparatus in the laboratory was almost entirely rebuilt and updated and the relevant details were presented. The main purpose of this trap is to allow us to perform coherent manipulations in mixed-species two-ion crystals of $^{40}Ca^{+}$ and $^{43}Ca^{+}$ and the data presented in this chapter establishes it as the required experimental tool. We have demonstrated reliable isotope-selective loading of mixed-species crystals and were able to reliably maintain them in our trap for up to one day. A robust technique to automatically recrystallize the ion-pair after background gas collision was also developed and implemented.

Readout and coherent manipulation of both $^{40}Ca^{+}$ and $^{43}Ca^{+}$ in this trap are described in chapter 6 of this thesis. The trap is also used for the ground-state cooling of single ions and mixes-species crystals presented in chapter 7.

Chapter 5

The Raman laser system

Double your gun, double your fun.
Serious Sam

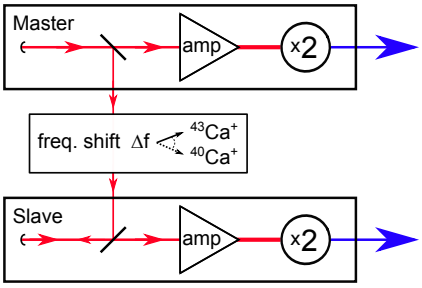

Figure 5.1: Principle behind the injection lock setup (see text).

As mentioned in chapter 1, using far-detuned Raman lasers to drive one- and two-qubit gates is an established technique. This chapter describes a pair of frequency-doubled lasers to provide Raman beams in our experiment. Since they are used far off-resonance, there are no stringent requirements for absolute frequency stability. Instead, relative interferometric stability is needed which we achieve by injection-locking the two systems. In order to address both isotopes with the same setup, the injection beam is switchable in frequency using an AOM. In this way an offset between the lasers corresponding to the qubit splitting of either of the calcium isotopes used in our experiments is available.

The lasers themselves, the locking scheme as well as stability measurements are presented in this chapter. This is followed by a description of the required operations on our qubits as well as the beam layout and alignment procedure to provide the necessary combinations of beam directions an polarizations. The fidelity of laser gates is limited fundamentally by errors introduced through off-resonant scattering. In the final part of the chapter a study of off-resonant Raman scattering shows the expected scaling of this error source for future gate operations.

5.1 Laser systems

The two lasers used to provide the Raman beams for the experiment are commercial semiconductor diode laser systems[1]. The lasers share the same basic layout which is exemplified in figure 5.2. The laser diode at 794 nm wavelength is set up in Littrow configuration using an adjustable diffraction grating for frequency selection. The grating can be coarsely

[1] Toptica, models TA/DL-SHG 110 Pro and TA/DL-SHG 110

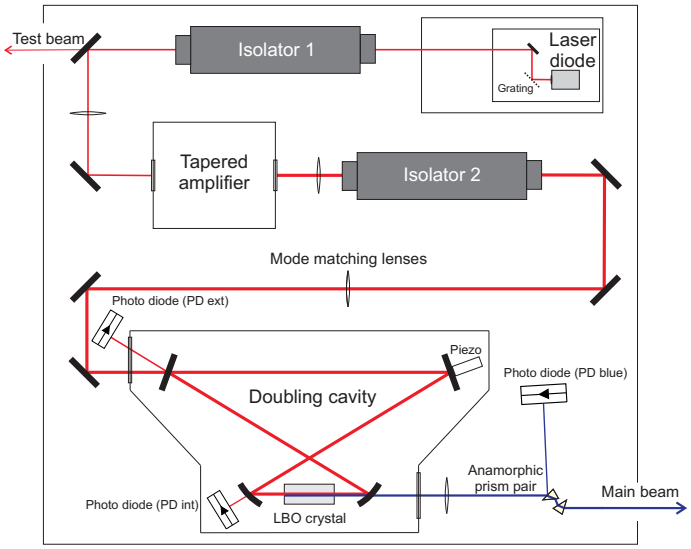

Figure 5.2: Basic layout of laser system 1 (TA/DL-SHG 110 Pro). The diffraction grating is adjustable by means of a screw and a piezo actuator (not shown). The light passes a Tapered Amplifier and is then frequency doubled. Two photodiodes (PD ext, PD int) are used for locking the cavity and a third one for intensity stabilization (PD blue). System 2 follows the same basic layout but has a removable grating and isolator 1 is split in two smaller units allowing access for the injection beam (see inset b, fig.5.4).

tuned by a screw and fine tuned with a piezo actuator. The diode is protected from back reflections by a 30dB Faraday isolator. After that, a weak test beam is split off at a 90%-reflective mirror. The main beam is sent into a Tapered Amplifier (TA) which is seeded at powers over 20 mW. The amplifier increases the power to about 450 mW and is protected by a second optical isolator. The next stage is the second harmonic generation (SHG) using a Lithium Triborate (LBO) crystal in an optical ring cavity. The cavity is enclosed in a monolithic Aluminium casing. The cavity length is locked to the laser frequency to maximize transmission and hence conversion to the second harmonic for that frequency by employing the Pound-Drever-Hall scheme [135] using current modulation of the laser diode (see section 5.3). This gives frequency-doubled light at a wavelength of 397 nm with 100 mW of output power. It passes an anamorphic prism pair to improve the symmetry of the beam shape before leaving the system.

There are two differences between the systems. The setup of the diode in system 1 (DL100-Pro) features a closed setup. The diffraction grating and mirror rotate on a common disk which is encapsulated in a metal casing for increased stability. On system 2 with its standard DL100 diode on the other hand, the grating is more accessible and can be removed for use as a slave system in an injection scheme. For that purpose the diode is also AR-coated. This design was necessary for the injection but made for slightly lower output power and decreased stability of the grating-stabilized system. The second difference is the Faraday isolator protecting the diode. In system 2 this is split into two smaller units.

The outward pointing polarizing beam splitter cube on the first isolator is accessible from the side (see inset b, fig.5.4). This allows for the injection beam to be sent in while the diode is still protected from back reflections. The scheme is described in the following section.

5.2 The injection

In a master-slave system a small portion of the light emitted by a stabilized master diode is injected into one or more free running slave diodes. By tuning the current and operating temperature of the slave diode to the right values the slave frequency can be locked to the master's resulting in the slave light being emitted into the mode set by the master. The slave diode is thus stabilized by the injected light [141].

5.2.1 Injection through an optical isolator

In our case the slave diode was delivered stabilized by a diffraction grating. The grating was removed and the diode moved over to retain the same beam path. The laser diode is protected by two polarization sensitive Faraday isolators. They consist of two polarizing beam splitters (PBS) set at $45°$ to one another and placed on either side of a Faraday rotator. The latter is a magneto-optic device, where light is transmitted through a transparent medium which is exposed to a magnetic field. Here, the medium is a Terbium Gallium Garnet (TGG) crystal and the magnetic field is provided by a strong permanent magnet inside which the crystal is placed such that the field lines are approximately parallel to the beam direction. Light passing through the medium is subjected to a continuous rotation of its polarization direction. The total rotation angle is given by $\beta = V \cdot B \cdot L$, where V is the Verdet constant of the material[2], B is the magnetic flux density and L is the length of the medium [143]. The rotator is designed to turn the polarization of light passing through by a total of $45°$. All light coming from the diode and passing through the first PBS is therefore turned to pass also the second one. The direction of rotation depends on the direction of the magnetic field relative to direction of light propagation[3]. Light traveling in the opposite direction back towards the diode passing the second PBS, is rotated by a further $45°$, which makes it perpendicular to the light coming from the diode so that it gets reflected at the first PBS. In this way the diode is protected from all back reflections.

In order to inject a beam into the diode while still maintaining this protection, one has to send the injection beam in from the side onto the first PBS at an angle of $45°$ so that it is reflected into the rotator. Its polarization direction when entering the rotator is then $-45°$ with respect to the light coming out of the diode and is subsequently rotated to be parallel

[2] for TGG at 794 nm, $V = 82.4\,\mathrm{rad\,T^{-1}\,m^{-1}}$, [142]

[3] as opposed to the action of a wave plate

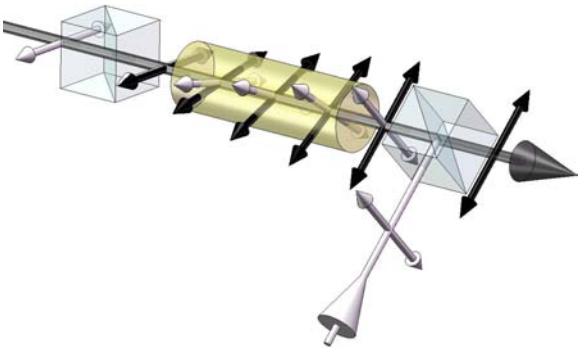

Figure 5.3: Injection through a Faraday isolator. The black beam coming from the left represents the light from the diode. The white beam coming at an angle of $45°$ from below is the injected light. The double pointed arrows indicate the direction of polarization. The cylindrical zone in between the PBS cubes is the Faraday rotator which turns the polarization axis of both beams in the same direction.

to it. It therefore passes the first PBS and is injected into the diode. Figure 5.3 illustrates the situation.

The light coming from the diode might not be exactly p-polarized and the Faraday rotation is not precisely $45°$ because of its wavelength dependence. Since the isolator is turned to maximize extinction of reflected light under these circumstances, the injection angle required in the present setup is not $45°$ but rather $54°$ with respect to the vertical. An adjustable mirror holder (see inset b, fig.5.4) using a turnable $45°$ mount[4] allows us to provide the beam at injection angles between $35°$ and $60°$.

5.2.2 The Master-Slave setup

Figure 5.4 shows the complete injection setup. The test beam from the master laser is split between a diagnostic beam which is sent to the wavemeter, and an injection beam using a PBS and half wave plate. The injection beam is sent through an AOM[5] in a dual double-pass arrangement which can be switched between the zeroth and first diffraction order to be used for injection by a computer-controlled TTL signal. The beam is then coupled into the slave diode via the injection mirrors as described in the previous section using the weak leakage beam that exits the isolator's side port as a tracer for alignment. Since the injection beam is linearly polarized, a half wave plate has to be used before the tilted mirror to turn the polarization direction to avoid making the light elliptically polarized on the injection mirrors.

The dual double-pass setup works in the following way. The TTL signal simultaneously controls an RF switch in the AOM's drive signal path and a shutter blocking the zeroth order beam. The AOM is driven at 806 MHz, so when the first diffraction order is

[4]Thorlabs H45B2
[5]Brimrose TEF-800-300-.794

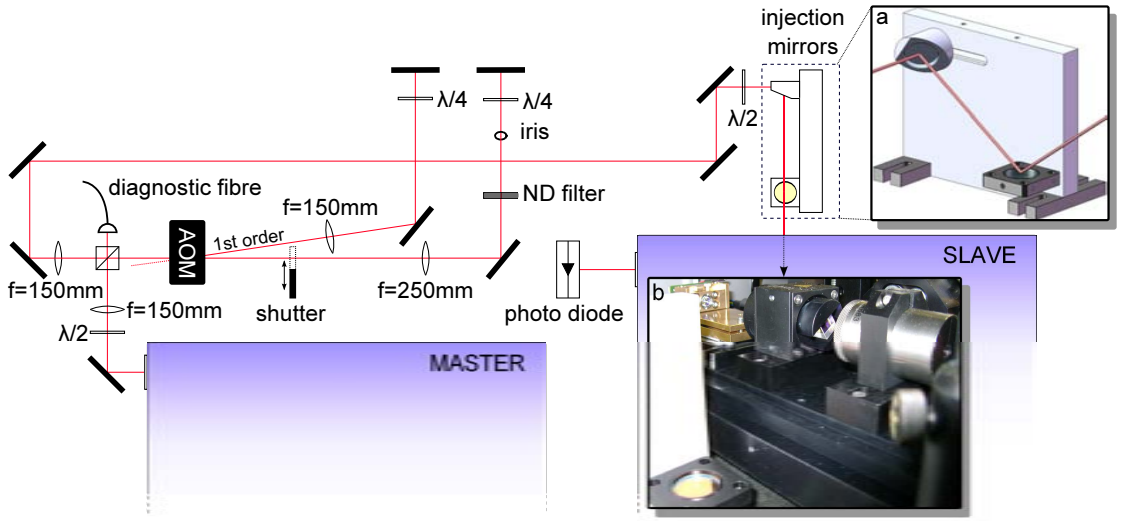

Figure 5.4: The injection setup. The red test beam coming out of the master laser is split between a diagnostic and an injection beam. The latter sent through a double-passed 800 MHz AOM. A computer controlled TTL signal switches between injecting the first and zeroth order. Inset **a** shows the injection mirrors. Inset **b** is a photograph of the optical isolator on the slave system through which the beam is injected into the diode which can be seen in the background.

used, this is doubled in the second pass and then doubled again in the SHG to correspond to the ground state hyperfine splitting in $^{43}Ca^{+}$ of 3.22 GHz. When the AOM is switched off, no shift is applied and the zeroth order is unblocked. The same double-pass layout as for the first order is used so that the beam follows the exact same path as the first order after passing the AOM for the second time. Master and slave then have the same frequency which makes the setup able to drive transitions in $^{40}Ca^{+}$ using AOMs in the blue beam paths (see section 5.5.2). The first order light is sent through an iris and an ND filter to give a similar intensity and beam shape as the first order beam. The ND filter also serves a second purpose. When well-aligned, the zeroth order double-pass setup forms an extended cavity for light that exits the slave laser via the injection path. This causes unwanted reinjection of slave light which amplifies the diode's ASE background and reduces the gain available for the injected beam. The ND filter introduces loss into this cavity-like beam path and reduces this feedback.

In order to align and monitor the injection, and its dependence on the slave diode current and temperature (see following section 5.2.3) the slave diode's power is observed by sending the test beam onto a photo diode.

When switching between the first and zeroth order of the injection AOM, the system takes around 100ms to relock the doubling cavity. This makes it too slow to be used in an experimental sequence but convenient to switch between experiments.

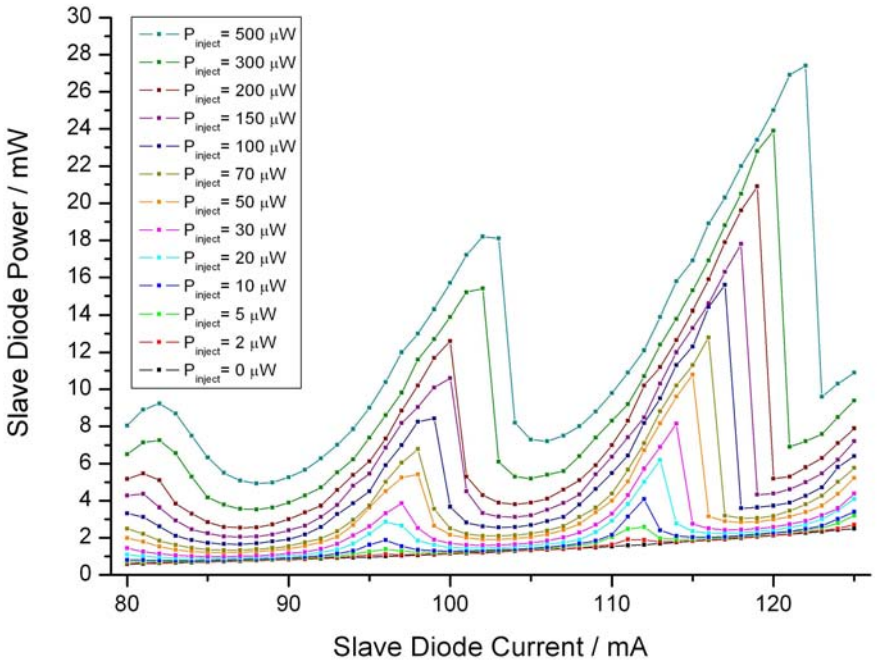

Figure 5.5: Scans of the slave current at different injection powers. The diode temperature was $T_{LD} = 20°\mathrm{C}$. The peaks are asymmetric due to the mode hysteresis.

5.2.3 Injection measurement

For alignment, the injection beam is superimposed with the tracer beam coming out through the injection path. Scanning the diode current reveals points of good injection as emission peaks which the final alignment aims to maximize. Figure 5.5 shows the output power of the slave diode for different slave currents and different injection powers. Three peaks can be seen over a range of 40 mA. They are highly asymmetric since the position of the peak shows some hysteresis with respect to the current. With rising current, the injected mode gains more and more power. This power is retained even beyond the point where the conditions make the injected mode the dominant one. The system is unstable and the power drops suddenly down as the lasing power is redistributed among the different possible modes. A backwards scan shows similar peak shapes but mirrored with the steep drop at the lower current side. The scans in figure 5.5 however were taken by setting the current manually at each point making this characteristic very prominent. The power was measured after the isolators and the 90% mirror which picks off the test beam.

The second parameter which influences the injection is the slave diode temperature. By changing this parameter, the spectrum of emission peaks can be shifted with respect to the current axis at a rate of $-10\,\mathrm{mA}/°\mathrm{C}$. For a given injection power the peaks are all on a straight line and shrink or grow accordingly when moved back and forth with

temperature. With the double-passed injection beam, we have about $275\ \mu$W available. During normal operation, the diode temperature is $20.4°$C. which gives us around 22 mW at 128 mA, enough to seed the tapered amplifier.

5.3 Dual Second Harmonic Generation

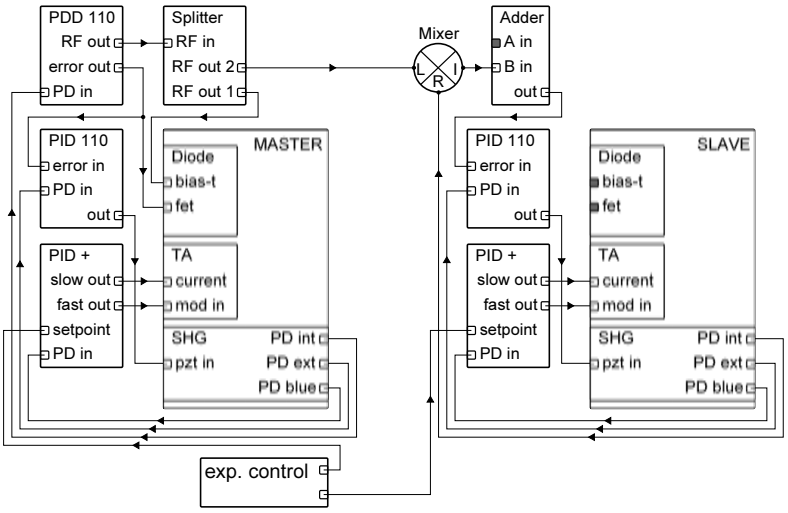

Figure 5.6: The electronic setup to lock both doubling cavities and stabilize the output powers (see text). Terminals on the left indicate inputs, those on the right outputs. Dark gray terminals are $50\,\Omega$ terminated. Abbreviations: PDD stands for "Pound Drever Detector", TA for "Tapered Amplifier", SHG for "Second Harmonic Generation" and PID for "Proportional, Integral, Differential".

Just as in the master, the doubling cavity on the slave laser needs to be locked to the diode's frequency in order to generate the second harmonic. The sidebands generated by the local oscillator used to lock the master are inherited by slave via the injection. Therefore its signal can be used to generate the slave error signal. For this purpose, Toptica supplied us with a Dual PDD box which comes with a second output with a separately adjustable phase and gain. Unfortunately, a design flaw caused strong electronic cross-talk at the 30% level between the channels and large gain-dependant pick-up of the 20 MHz modulation signal. We therefore generate the error signal as shown in figure 5.6.

The 20MHz RF signal generated in the Toptica PDD110 box is split into two paths using a power splitter[6]. The first of these is used to modulate the master diode current. The signal from the photo diode measuring the light reflected off the master doubling cavity (PDext) is sent back to the PDD110 and mixed internally. Phase and gain are adjustable to give the error signal. This error signal is then used in two ways. Firstly, it is sent directly onto the Diode current via the FET channel to provide a fast lock of the laser frequency to the cavity length. And secondly, it is used for a slower feedback path using a Toptica PID

[6]Mini Circuits ZSC-2-1W+

110 to lock the cavity length to the laser wavelength using the cavity piezo. The PID box also has an input for the second photo diode (PDext) which is used to relock the cavity if it comes out of lock by scanning the cavity piezo until a peak on the cavity transmission signal picked up by PDext is found.

In in order to lock the slave laser, the second RF branch from the splitter is sent onto the local oscillator port of an RF mixer[7] where it is combined with the photo diode signal from the light reflected off the slave cavity (PDext) to give the slave error signal. The phase has to be adjusted by choosing appropriate cable lengths before the mixer. The error signal is processed by sending it through an Analog Adder box[8] which allows offset and gain adjustment as well as a sign flip. With its bandwidth of about 500 kHz it also filters out any 20MHz drive signal still present after the mixer. As on the master lock, the error signal is processed by a PID 110 box and applied to the doubling cavity piezo. The PID box also uses the PDext signal to relock itself. On short timescales, the slave inherits the frequency stability provided by the master's fast lock to its own doubling cavity.

5.3.1 Intensity stabilisation

The intensity stabilization electronics are also included in figure 5.6. The intensity of the frequency-doubled light is monitored on a fast reverse-biased photo-diode[9] (PDblue). The signal is processed by a home-built (by Chris Ballance) PID box with a fast and a slow output ("PID+"). The slow signal is used to cancel drifts in the output power caused for example by cavity misalignment by changing the TA current via the modulation input on the control module. The fast signal is applied to the amplifier's own modulation input which has a high bandwidth (100 MHz). The goal is to take out fast intensity noise caused by vibrations in the cavity or injection path which are either too fast or too large to be corrected for by the slow cavity lock. To control the power level of the lasers, the set-points of the PID circuits can be adjusted by an analog signal from the experimental control system. The main bottleneck for the feedback speed is the cavity transfer function. Any power change before the cavity is only translated into a power change in the blue after a delay on the order of the cavity ring-down time (0.22 μs from $10\% - 90\%$). For the experiments presented in the following chapters, the full system was not yet in place. The setpoints on both intensity locks were adjusted manually and for most experiments, the fast feedback loop was used on the slave laser only while the master was stabilized with a Toptica PID box connected to the TA modulation input. This stabilized the intensity to $\sim 1\%$ with ~ 100 kHz bandwidth.

[7] Mini Circuits ZAD-3
[8] Oxford central electronics group EW1258
[9] Hamamatsu S6775, bandwidth 20 MHz

5.4 Beat measurements

This section presents beat measurements of the two laser systems both free-running and injection-locked. The former gives a measure of the (passive) absolute frequency stability on short timescales while the latter characterizes the relative linewidth which is important for the interferometric stability needed between the two Raman beams.

5.4.1 Absolute linewidth: independent lasers

Before the injection scheme was realized, both free-running grating-stabilized lasers were set about 35 MHz apart using an optical spectrum analyzer and beat against each other. This measurement was not done in the setup shown in figure 5.4, but instead by coupling both lasers into the same single mode fiber and sending the fiber output onto a fast photo diode[10]. Figure 5.7 shows a typical signal trace taken with a sweep time of 50 ms. The signal was not stable and suffered jumps of about 10 MHz roughly every second. Coupling the test beams of both systems into an optical spectrum analyzer showed that this behaviour was only present on the diode of system 2 and therefore relayed down to the beat signal. This might be due to the fact that the diode is AR coated for optimal injection and therefore jumps between several modes resonating on the grating. The behaviour disappeared when the grating was removed and the diode injection-locked.

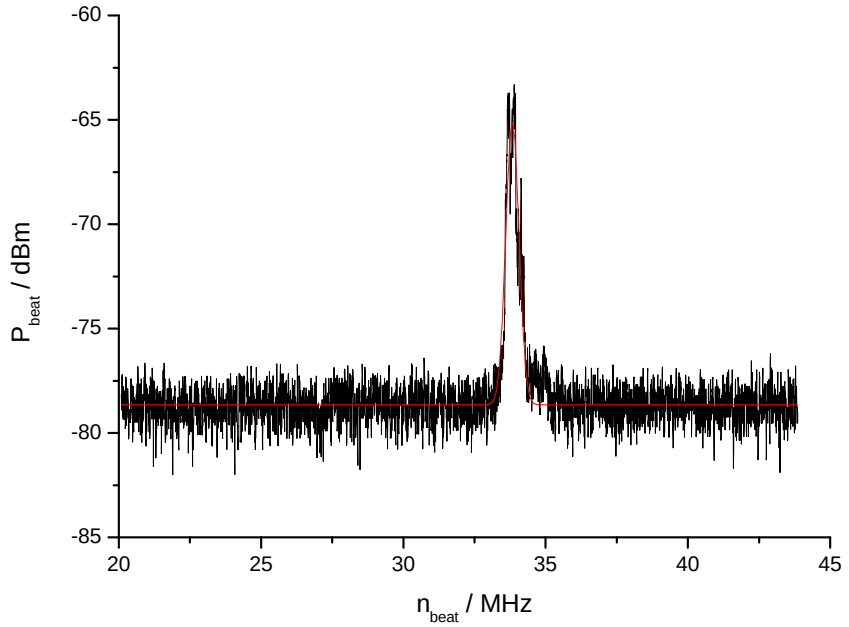

Figure 5.7: Typical spectrum of the beat signal of the free-running frequency-doubled systems. The red curve is a Lorentzian fit with a linewidth of 460 kHz. The spectrum analyzer scan resolution was 20 Hz, sweep time 50 ms, and the data was taken without intensity stabilization.

[10] NewFocus 1437

The mean width of the beat signal is 420 kHz which corresponds to the combined linewidth (in quadrature) of the two free-running systems. Assuming the two lasers contribute equally to the beat signal having similar configurations, the linewidth observed is $\sqrt{2}$ times the linewidth of an individual laser. This assumption is not exactly valid however, since system 1 with its "'Pro"' diode and grating design is supposed to be more stable than the open design of system 2. Nevertheless, this gives a good upper limit to the linewidth of system 1 of $\Delta\nu_1 \approx 300$ kHz. The system is stable enough for the far-detuned (~ 500GHz) qubit operations required. This is however subject to the slave laser inheriting the master's stability, which is why a measurement of the relative linewidth of the injected system is also crucial.

5.4.2 Relative linewidth: injected lasers

The lasers were beat against each other near the trap to include both the effects of the injection, second-harmonic generation and blue beam paths in the observation. These stages can all have an effect on the interferometric stability between the two beams needed to get a narrow beat signal. This measures the relative stability which will limit the fidelity of Raman operations performed on the ion. The light was picked off from the R_H and R_V beams using a PBS and waveplate set to give equal reflection of the two initially perpendicularly-polarized beams (see fig.5.15). The injection was set to zero-order to give no frequency offset between the beams and the two blue AOMs were set 10 kHz apart to have a signal easily observable on a photodiode[11] with ~ 1 MHz bandwidth.

The photo diode signal was recorded on an oscilloscope[12] at sampling rate of 50kS/s for 40 s to give a spectral resolution of 25 mHz. The data was Fourier-transformed (FFT) to show the signal in the frequency domain. The result is shown in figures 5.8 and 5.9. Both show the same data set. Figure 5.8 has a linear scale and gives the area close to the central peak. Despite the high resolution, the highest peak is only represented by a single data point. We can safely give an upper limit of the relative linewidth of 100 mHz. There are other raised points visible on either side which suggests that the peak experienced a small amount of jitter (< 0.25 Hz) during the 40 s recording time.

Figure 5.9 has a logarithmic scale and shows a wider range around the peak. At around ± 700Hz, there are two servo-bumps which indicate the bandwidth-limit of the cavity lock.

There are also other peaks visible at a few hundred Hz around the peak which probably correspond to acoustic vibrations being picked up in either the injection or the blue beam path. In order to reduce this noise, we enclosed both lasers and the injection path in an MDF box clad with lead-lined foam[13]. This material consists of a lead sheet with a layer of foam on either side and has good sound-damping qualities. The metal sheet lids on the

[11] Thorlabs PDA 36A-EC
[12] Tektronix TDS 5104
[13] noisekiller.co.uk "Lead Sandwich"

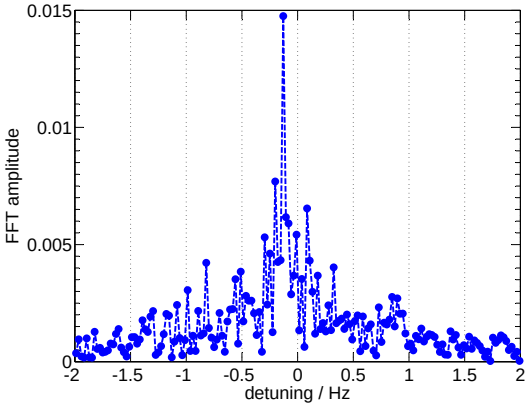

Figure 5.8: Beat signal between master and slave on a linear scale. Centre frequency 10 kHz.

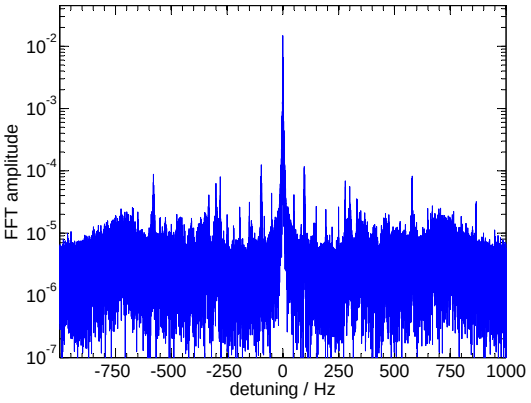

Figure 5.9: Beat signal on a logarithmic scale. Centre frequency 10 kHz. Servo bumps and acoustic noise is visible.

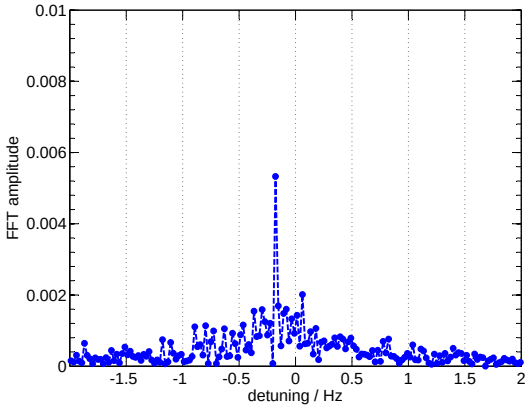

Figure 5.10: Beat signal between master and slave on a linear scale with the noise insulation box. Centre frequency 10 kHz. The noise near the peak has been reduced relative to the peak which appears lower and is clearly undersampled.

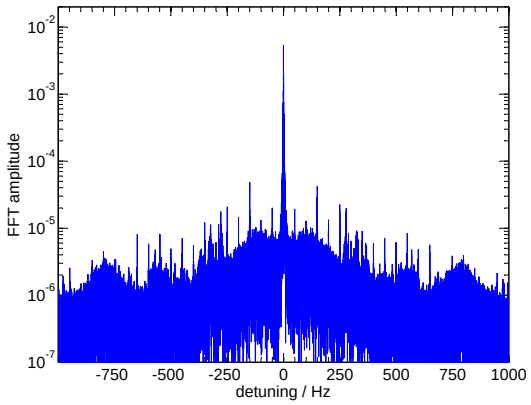

Figure 5.11: Beat signal on a logarithmic scale with the noise insulation box. Centre frequency 10 kHz. The peak is narrower and at frequencies above 100Hz, a noise reduction of up to an order of magnitude can be observed.

lasers were removed at that stage since it has been suggested that their flexible material can cause vibrations. Another beat signal data set was taken using the same setup and parameters as before. It is presented in figure 5.10 and 5.11. The linear plot shows that the noise floor relative to the peak is lower. The resolution of 25 mHz is not enough to resolve the peak which might be lowered due to undersampling. To resolve the peak better, a longer data set would need to be taken which was not possible on the oscilloscope used. On the logarithmic plot, we see that the box is effective in suppressing the noise > 150 Hz by about an order of magnitude and making the central peak narrower. Several of the main noise peaks while getting narrower were still present and there is a plateau at < 150 Hz. It is possible that these represent acoustic vibrations picked up in the blue beam path outside

the box. Overall however, the relative linewidth of ≤ 100 mHz is not expected to limit the fidelity of laser-driven qubit operations (on timescales of typically $< 100\,\mu$s), compared to other noise sources such as magnetic field fluctuations in our system.

5.5 Raman beam setup

5.5.1 Experimental requirements

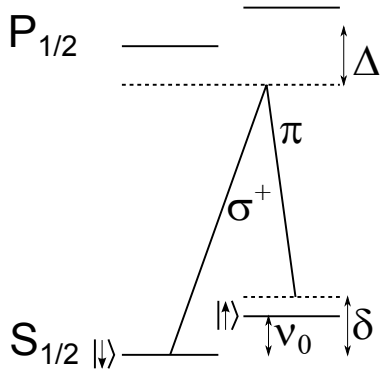

Figure 5.12: Raman transitions with polarizations and relevant detunings to drive qubit transitions: The global Raman detuning Δ, qubit splitting ν_0 and detuning δ.

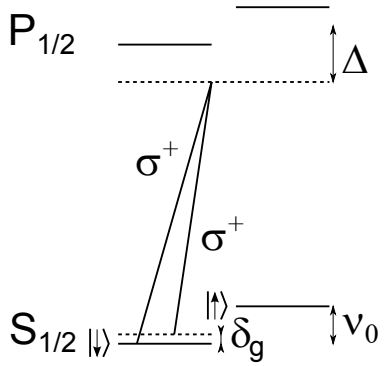

Figure 5.13: Raman transitions with polarizations and relevant detunings for the wobble gate: The global Raman detuning Δ, qubit splitting ν_0 and gate detuning δ_g.

The Raman beam setup allows us to drive a range of transitions on single qubits ($^{40}Ca^+$ Zeeman, $^{43}Ca^+$ stretch and clock state) as well as a specific two-qubit entangling gate called the "wobble" gate (see [29] for details). The polarizations needed are shown in figures 5.12 and 5.13. All Raman beams have a global detuning Δ from the 397nm resonance. They are also detuned with respect to each other by δ. Overall, we want to perform four different types of operation on both $^{43}Ca^+$ and $^{40}Ca^+$:

1. Single qubit gates (Rabi flops and phase shifts)
To drive single qubit gates, we need δ to be equal to the qubit frequency ν_0 (either around 5 MHz for $^{40}Ca^+$ or 3.2 GHz for $^{43}Ca^+$). Since we don't want to couple to the motion, the beams have to be collinear. We need one beam to be π and the other to be $\sigma^{\pm}$. Although only one σ beam is necessary for the transition, we need the two σ beams to balance out the different light shifts on the qubit states. To drive phase gates, we apply a phase offset to the drive field (AOM signal).

2. Sideband transitions and sideband spectroscopy
To drive sideband transitions, we have to couple to the ions' motion and hence require the beams to propagate at $90°$ to each other with the resultant k-vector ($\Delta\vec{k} = \vec{k}_1 - \vec{k}_1$) along the trap axis. We need the same polarizations as before, but δ now needs to be ν_0 plus or

minus the axial trap frequency ν_z ($1 - 2$ MHz) on the COM mode or $\sqrt{3}\,\nu_z$ on the stretch mode (see chapter 7). For sideband spectroscopy, δ needs to be scanable over several ν_z.

3. Motional 2-ion gate (see [29])

We again drive the ions' motion with perpendicular beams but the detuning has to additionally include a gate offset δ_g. The polarization has to vary spatially along the z-axis. This is achieved in the "traveling standing" wave of two σ beams. The ion-to-ion distance has to be aligned to be exactly an integer number of wavelengths of the traveling standing wave, so that both ions experience identical forces when they are in the same qubit state and opposite when they are in different states.

4. Clock state single qubit gates

These operations are similar to application 1 in $^{43}Ca^{+}$ but instead of the usual stretch-state qubit, we perform them on the clock state. In order to connect the $F = 4, m_F = 0$ and $F = 3, m_F = 0$ states, we need both Raman beams to be either σ^+ or σ^- since beams containing both circular polarization would have the two beam pairs cancel each other out and a pure π transition is forbidden. To achieve the polarization we need, we superimpose the $R_{||}$ and $R_{||2}$ beams on a removable NPBS and have a rotatable quarter waveplate before the trap to set the polarization to circular for clock state experiments.

5.5.2 Optical setup and control

The beam arrangement shown in figure 5.15 allows the flexibility to perform all four applications as summarized in table 5.1.

application	detuning δ	beams
single qubit	ν_0	R_H & R_V
sidebands	$\nu_0 + \nu_z$	$R_{||}$ & R_H
wobble gate	δ_g	$R_{||}$ & R_V
clock state	ν_0	$R_{||}$ & $R_{||2}$

Table 5.1: Raman beam detunings

The AOM setup shown in fig. 5.14 provides the necessary beams. To apply the different AOM drive frequencies and phases in sequence, two 4-channel DDS boards are used. Each channel provides one frequency-phase offset to the synthesizer setting. The injection AOM and the R_H-path AOM are powered directly by synthesizers[14] and remain at a constant frequency and phase. All synthesizers used are referenced to a 10 MHz rubidium frequency standard[15]. One of the boards is connected to the $R_V/R_{||2}$ AOM to switch the phase to different values for single-ion phase gates. The other drives the $R_{||}$ AOM allowing us to switch between COM and stretch mode frequencies, as well as the frequency of

[14] Marconi Instruments 2019A
[15] SRS FS725

the stretch mode plus the gate detuning. Since frequency changes at the AOM also affect the angular beam pointing, the centre of the $R_{||}$ AOM is imaged onto the trap, reducing this beam movement at the ion to $\sim 4\,\mu$m/MHz.

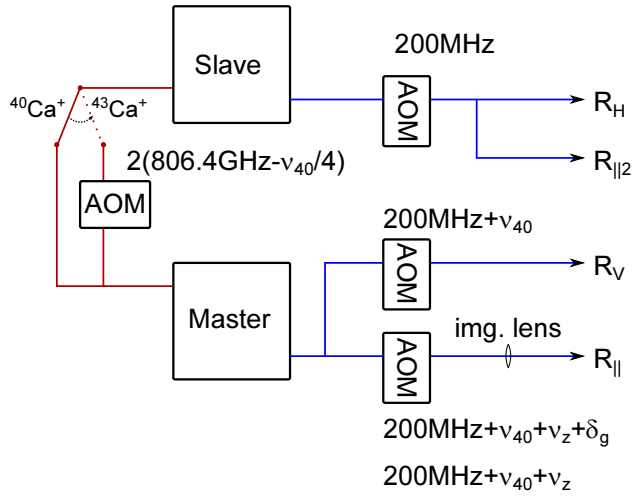

Figure 5.14: The beam setup providing the four different Raman beams with the switchable injection path between the SHG laser systems and the AOMs to provide the different detunings.

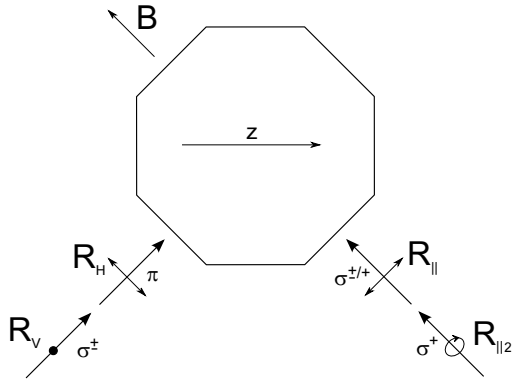

Figure 5.15: The vacuum chamber with the four Raman beams. R_V and R_H are superimposed on a PBS while $R_{||}$ and $R_{||2}$ are superimposed on a removable NPBS (see text). The magnetic field direction B and the trap axis z are also indicated.

5.6 Raman beam alignment

When detuning the Raman lasers far from resonance, the doubling cavity needs to be peaked up to maintain the blue power output. This causes small shifts in the beam direction which moves the beam off the ion. When the Raman beams are far-detuned from the $S_{1/2} \rightarrow P_{1/2}$ resonance, we cannot use the ion's fluorescence to align the beam. For the measurements in section 5.7 we installed two beam splitters, one behind the trap and one

close to the laser and sent the picked-off light onto a pair of rigidly mounted cameras [16]. On these, the beam position was recorded and saved with the laser tuned to resonance. The laser was then detuned and walked back to the original positions on the cameras. This method was time consuming and unreliable however, which is why with the new trap we developed a different technique.

5.6.1 Light shift method

Even when off-resonant with the transition, the Raman beams can still cause a light shift. The two Zeeman states in $^{40}Ca^{+}$ are addressed by different polarization components, which means the qubit will acquire a differential light shift of the following form [144]:

$$\Delta_D = \frac{\Omega_{\sigma^-}^2 - \Omega_{\sigma^+}^2}{4\Delta} \tag{5.1}$$

If the beam is on for a time τ, the phase acquired through this shift is $\phi_{LS} = \Delta_D \cdot \tau$ which can be thought of as a rotation around the z axis of the Bloch sphere. We can use this effect to align the R_{para} beam. We first align it roughly by superimposing it by eye onto the 397σ beam. Then, with its polarization set to circular (e.g. σ^+) in order to maximize the differential light shift, we use a spin-echo sequence to measure the light shift it induces on the ion. By scanning the pulse length τ we get Ramsey fringes, whose frequency is given by the differential light shift. This in turn depends linearly on the intensity. By choosing τ to be half way up the flank of a Ramsey fringe and repeating the sequence, we are maximally sensitive to changes in the intensity between sequences (see fig.5.16). The beam can then be aligned by observing the shelving probability on the screen. If the beam centre is moved towards the ion, the frequency of the Ramsey fringes increases and the shelving probability rises towards the high readout level. At the high point, we do another time scan and choose a reduced τ to again give a shelving probability around 50%. The process is repeated until no further increase can be made.

After alignment, the beam's polarization is set to linear ($\sigma^{\pm}$) by rotating the quarter waveplate before the trap. To optimize the linear polarization, we use the same technique as for the alignment, but this time minimizing the 50% signal and increasing τ at every step. We are able to reduce the light shift by more than two orders of magnitude. The sensitivity is limited by the fact that we were unable to observe flopping long on timescales ($\sim$ms) due to beam pointing fluctuations (see section 6.3.4). In the $^{43}Ca^{+}$ stretch state qubit, the lights shifts do not cancel out due to the asymmetry of Zeeman states. For the power we are using ($10\,$mW) we are left with $\sim 30\,$kHz of differential light shift, which can be taken out by an additional Ramsey sequence, driven either with the Raman beams or microwaves during future gate operations.

[16] Maplin bare board CCD

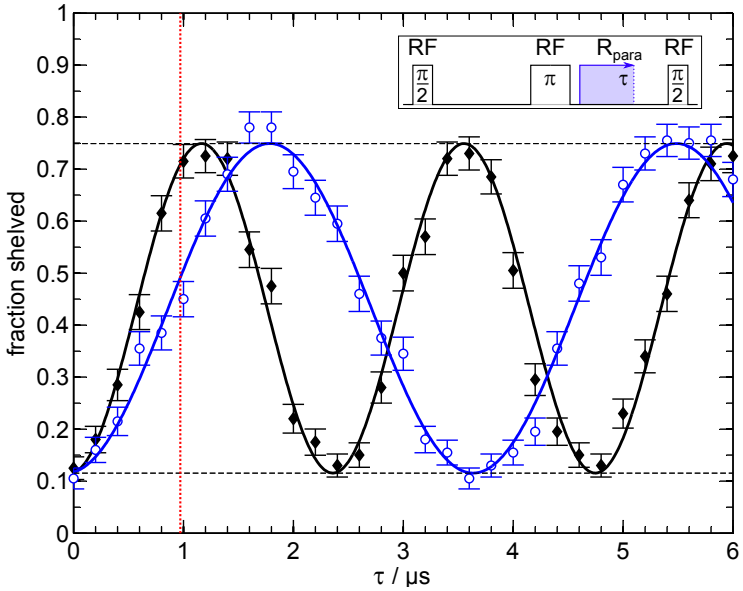

Figure 5.16: Ramsey fringes during alignment of the R_{para} beam ($P = 10$ mW) with fitted sine curves. The inset shows the spin-echo sequence. The blue curve is the signal with the misaligned beam. If the sequence is repeated with τ set on first flank (red dotted line), moving the beam onto the ion (black curve) will increase the flopping rate which at a constant τ is visible as a rise in the shelved fraction. The black dashed lines are the readout levels.

The alignment of the two other Raman beams, R_V and R_H, cannot be accomplished using the light shift. Since they propagate perpendicular to the magnetic field direction, their polarization can only be a superposition of π and $\sigma^{\pm}$, both of which have canceling light shifts ($\Delta_D = 0$) in $^{40}Ca^+$. In $^{43}Ca^+$ the shift is prohibitively small for alignment as mentioned above. Instead, we align them by driving Raman transitions in combination with R_{para}. This means that R_{para} has to be aligned first. R_V and R_H are superimposed with each other and then with the Doppler cooling beam propagating in the opposite direction. After that, we drive Rabi flops with R_V and R_{para}, this time increasing the Rabi frequency by aligning R_V and using the same technique on the Rabi flops as described for the Ramsey fringes. The Rabi frequency only depends on the square root of the intensity, but the sensitivity can be increased by sitting on the second or consecutive flops. In practice, we find it sufficient to use the first slope since we are limited by the smallest steps we were able to make with the mirror mount micrometers. The frequency and polarization of R_V have to be set to those of R_H temporarily during alignment to be able to drive Rabi flops (see fig.5.12). The frequency change in the R_V-AOM causes a shift in beam position which we correct for by recording the aligned beams position on a camera[17] and repositioning it after changing back the frequency. Finally, the procedure is repeated for R_H using the last two mirrors that are independent of R_V.

[17] Pulnix PE2015

5.6.2 Alignment measurement

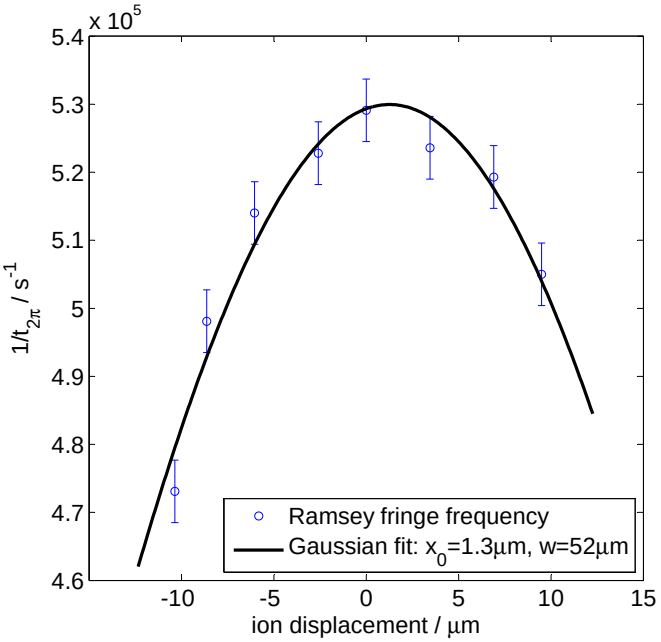

Figure 5.17: Ramsey fringe frequency at different ion positions across the R_{para} beam. The ion was moved along the trap axis and its position relative the standard value measured using the camera. The values are corrected for the $45°$ angle between trap axis and beam. A Gaussian fit shows the standard position to be close to the beam centre and the e^{-2}-radius w to be $52\ \mu$m.

In order to estimate how close to the ion's position we can align the beam centre, we performed a measurement of the beam intensity profile of R_{para} at the ion position by moving the ion along the trap axis using the endcap voltages. At each point, we measured the light shift with the spin-echo technique described above, and the polarization set to circular for maximal light shift. Since the light shift is proportional to the intensity, we can fit a Gaussian to the data to give an estimate of the beam centre position relative to the ion and the beam waist. The ion's position at each point was observed on the EMCCD-camera and converted into a position relative to the starting point ($1.22\,\mu$m/pixel). Since the beam propagates at a $45°$ angle to the trap axis, the positions were scaled by $1/\sqrt{2}$. The data is presented in fig. 5.17 with a fitted Gaussian curve. The centre at $0\ \mu$m corresponds to the original ion position. The $1/e^2$ radius of $52\ \mu$m is consistent with our independent measurement of the beam waist using a pick-off and beam profiler before the vacuum system, which yielded 54μm. The peak of the fitted Gaussian is only $1.3\ \mu$m from the centre position of the ion. The Doppler cooling beams were aligned onto the ion at every position. We did not compensate the trap at the new ion positions because this causes displacement perpendicular to the trap axis. As a result, we could not take data further away from the centre since the Doppler broadening associated with the ion's micromotion reduced the readout level contrast.

5.7 Photon scattering experiment

As described above, we want to use our two injection locked frequency doubled lasers at 397 nm to drive Raman gates. The advantage of the lasers is that they allow us to detune far from resonance, thereby reducing photon scattering errors, while still being able to drive Rabi flops fast due to their high output power. There are two types of photon scattering processes that can occur when the ion is off-resonantly excited by one of the Raman beams, Rayleigh scattering and Raman scattering. Rayleigh scattering leaves the ion ground state population unaffected and therefore does not necessarily lead to decoherence [145]. Raman scattering on the other hand changes the ground level population and leads to decoherence by qubit amplitude decay [146].

Before the injection or the new trap was set up, we performed a preliminary experiment to see the different scaling of Rabi frequency and Raman scattering error with respect to Raman detuning. The experiment was performed in the old trap (see [21] and references therein for a complete description of the setup) in the $^{40}Ca^{+}$ qubit. Therefore, the Raman beam setup used here is different from the one described earlier in this chapter. In order provide the two Raman beams, the main beam of the Master laser is split and each path sent through an AOM driven at 200 MHz, and 200 MHz plus the qubit splitting (~ 5 MHz) respectively. They are recombined at a PBS cube and remain linearly polarized as they are sent onto the ion at an angle of 60° with respect to the magnetic field direction. The vertically polarized beam is referred to as RperpV and has an intensity ratio for the different polarization directions, $(\sigma^{+} : \pi : \sigma^{-})$, of $(1/2 : 0 : 1/2)$. The horizontally polarized beam, RperpH, has a ratio of $(1/8 : 3/4 : 1/8)$.

5.7.1 Estimating beam intensities

Since we were exploring a wide range of detunings $\Delta = -100$ to -1000 GHz, the doubling cavity had to be realigned after each detuning step to keep a constant output beam direction and power. In order to maintain the same beam path, two cameras were used to realign the beam back to its original position, one near the laser and one on the far side of the trap.

In order to measure the beam intensity at the ion after each beam alignment step we performed a qubit depumping experiment: we prepare the ion through optical pumping in one of the Zeeman qubit states and then apply a depumping pulse from one Raman laser. We read out the state by our usual shelving method and through repetition of this process (typically 200 times) infer the population in the two states. Increasing the pulse length we can see the level decay away from the initial readout level. This is done for both states and repeated for the second Raman laser. The effect the $D_{3/2}$ level has on this process is only relevant for very long depumping times since the ion will depump about ten times faster than it will scatter into $D_{3/2}$.

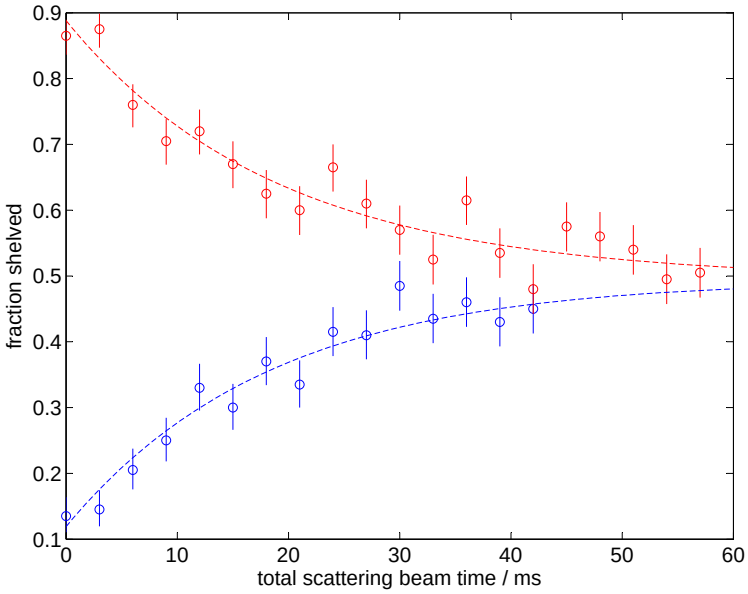

Figure 5.18: Depumping experiment with RperpH with fitted exponential decay. The resulting intensity is $(2140 \pm 100)\ I_0$ where $I_0 = 934\,\mathrm{W/m^2}$ is the saturation intensity, $\Delta = -503\,\mathrm{GHz}$.

The experiment is repeated for the other qubit state. For each laser we simultaneously fit the decay to both data sets using David Szwer's Rate equations suite [21] using the known detuning to determine the beam intensity. The simulation includes the effects of the $D_{3/2}$ state as well as the read-out process. Plot 5.18 shows such a combined dataset for R_H and the fitted curves. These experiments yield a measure of the individual beam powers with a fitting error of $5 - 10\%$. There is also the systematic effect of the beam charging up the electrodes during the long depumping pulses and so moving the ion position, making the alignment worse. We observed this as a change in the voltages needed to compensate the micromotion in our trap. Comparing the intensity values we obtain by this method with estimates from spot-size and beam power measurements as well as the Rabi frequency (which gives a measure of $\sqrt{I_H I_V}$), we found agreement at the 25% level. We subsequently developed the light shift technique (described in section 5.6.1 above) for alignment and measuring beam intensities.

5.7.2 CPMG sequences

Following the method outlined in [145], we employed a spin echo scheme to study the decohering effect of photon scattering. In a Rabi flopping experiment we measured the length of a Raman π- and $\pi/2$-pulse. These were used to drive a spin-echo sequence consisting of a Ramsey $\pi/2$-pulse, a series of π-pulses and another $\pi/2$-pulse, the phase of which was scanned from $-3/2\pi$ to $3/2\pi$ to create fringes. The purpose of the sequence is to cancel out phase shifts, mainly caused by fluctuations in the magnetic field since our qubit splitting is strongly magnetic field dependent.

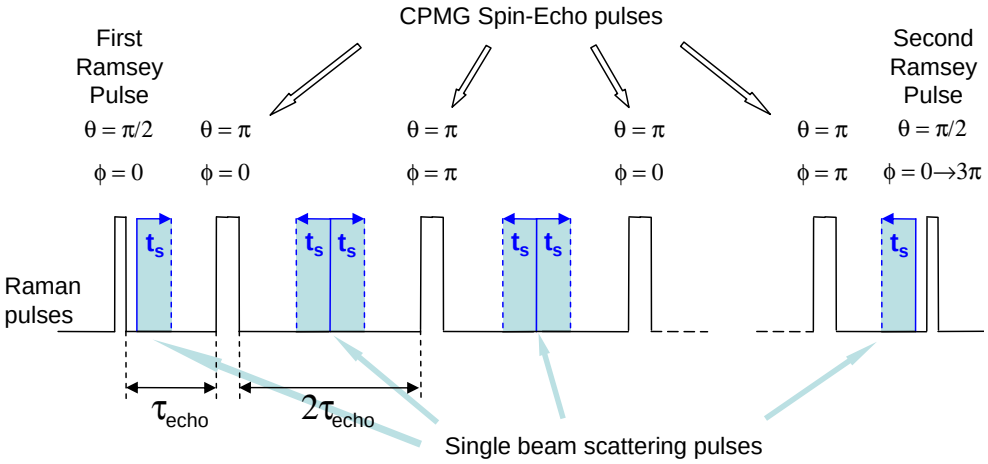

Figure 5.19: CPMG sequence consisting of typically 16 π-pulses of alternating phase ϕ, framed by two Ramsey $\pi/2$-pulses ($\theta = \Omega_R \cdot t_{pulse}$ gives the pulse area). We chose $\tau_{echo} = -500$ μs for our experiment (see text). The phase of the last Ramsey pulse is scanned from $-3\pi/2$ to $+3\pi/2$ to generate the fringes. One of the Raman beams is turned on in the gaps for a scattering pulse of length t_s which is varied for different experimental runs.

During the gaps between the sequence pulses we applied one of the Raman lasers to the ion for a time $2t_s$ (t_s for the first and last pulse, see figure 5.19) to introduce photon scattering. The longer these pulses are, the more the fringe contrast is reduced by the decohering effect of photon scattering.

We line-triggered the experiment to minimize the effect of magnetic field oscillations at the mains frequency which limits the length of a sequence to 20 ms. This means the choice of τ_{echo} is a trade-off between the number of π-pulses in the sequence and the possible scattering time. The more π-pulses the sequence contains, the higher the noise frequencies it can correct for, but increasing the number of pulses will reduce the time available for the scattering pulses. We chose to use a gap time $\tau_{echo} = 500$ μs.

Slow drifts in the ambient field will also cause our π- and $\pi/2$-pulse times to be incorrect. We employed two mechanisms to reduce the error caused by this problem. Firstly, the phase of the π-pulses was changed back and forth between 0 and π making our scheme a full CPMG[18] sequence [147, 148]. This phase alternation corrects for errors in the pulse lengths (see [149]) and we found it improved the fringe contrast by about 20% and reduced systematic noise in the scans resulting in better fits. Secondly, we checked the resonance frequency after every experimental run by using a simple 2-pulse Ramsey sequence, and adjusted the AOM difference frequency as necessary. The atomic resonance typically drifted by about 1 kHz over ten minutes[19].

For a typical experiment, we ran the sequence for a number of different scattering pulse lengths and for each laser beam independently. The contrast is determined by fitting a sine

[18] the acronym refers to the authors: H. Y. Carr, E. M. Purcell, S. Meiboom and D. Gill

[19] drift not observed in the new system (possibly due to the use of a non-magnetic steel vacuum chamber)

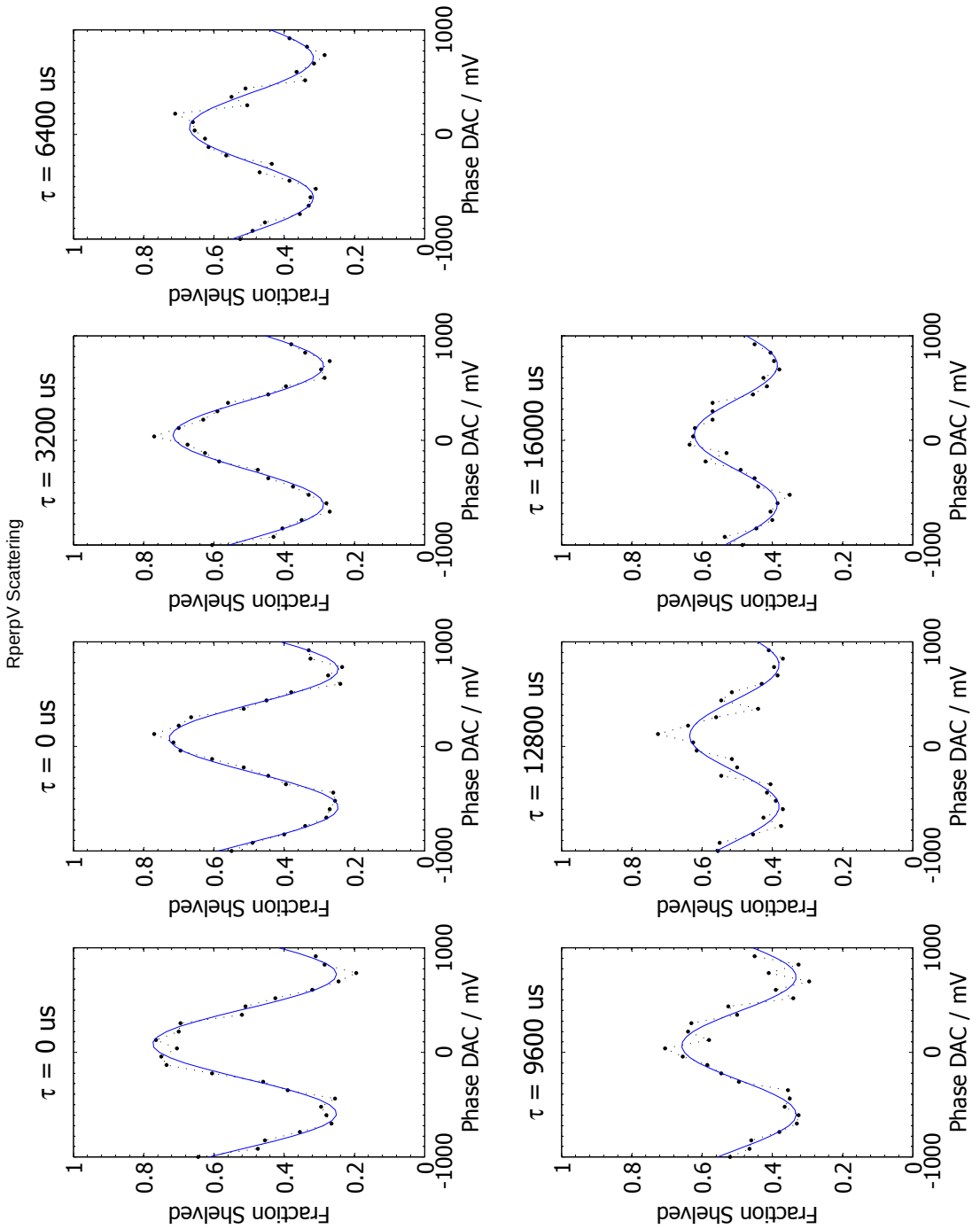

Figure 5.20: Data from a series of CPMG experiments with increasing total scattering pulse length τ of the R_V beam at a detuning of $\Delta = -504$ GHz. τ represents the sum of all individual pulse times t_s (see fig. 5.19). A DAC scan from -1 V to -1 V corresponds to a phase scan from $-3/2\pi$ to $3/2\pi$. Sine curves are fitted to determine the contrast. Each point consists of 200 experimental sequences.

curve to each of them to find the amplitude. Figure 5.20 shows the results of an experiment with scattering pulses from the R_V beam at a detuning of $\Delta = 504$GHz including the fitted sine curves.

The contrast values thus found are plotted against the scattering time and an exponential decay curve is fitted to them (see figure 5.21). The time constant of this decay corresponds to the coherence time of the superposition state under the influence of the scattering beam. The inverse of this value is the Raman scattering rate.

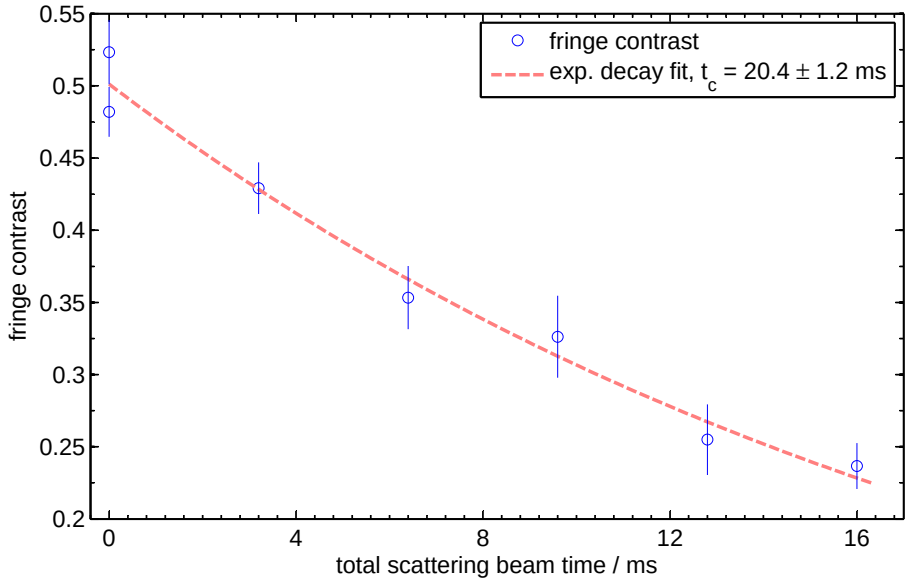

Figure 5.21: Contrast data from the sine fits to the series of CPMG experiments shown in figure 5.20. An exponential decay fit yields a coherence time of (20.4 ± 1.2) ms.

5.7.3 Analysis

5.7.3.1 Scattering rate vs detuning

When plotting the Raman scattering rates $\Gamma_{Raman} = 1/\tau_{decay}$ versus the detuning Δ we expect the following dependency [150]:

$$\Gamma = \frac{1}{2\hbar^2} \sum_{\substack{i,j \\ i \neq j}} \sum_{\lambda} \sum_{J} \gamma_J p_i \frac{\left(\langle \mathrm{S}_{1/2,i} | \vec{d} \cdot \vec{E}_{\lambda+i-j} | J, \lambda + i \rangle \langle J, \lambda + i | \vec{d} \cdot \vec{\epsilon}_\lambda | \mathrm{S}_{1/2,j} \rangle \right)^2}{\Delta_{J\lambda}^2} \tag{5.2}$$

$i, j \in \{-1/2, +1/2\}$ and p_i is the probability of starting in each of the two qubit states $|S_{1/2,i}\rangle = |\uparrow\rangle, |\downarrow\rangle$. In accordance with [146], we have only included matrix elements in the equation that change the qubit state. $|J\rangle = |\mathrm{P}_{1/2}\rangle, |\mathrm{P}_{3/2}\rangle$ are the different upper state manifolds by which a photon can be scattered, and γ_J and $\Delta_{J\lambda}$ are the scattering rate and detuning respectively of state $|J, j\rangle$. We assume the Zeeman splitting (≈ 5 MHz) is small compared to the detuning (many GHz in our case), so Δ does not depend on i. $\vec{E}_\lambda = E b_\lambda \vec{\epsilon}_\lambda$

is the electric field amplitude vector for the polarization component b_λ and $\vec{d}$ is the electric dipole operator. $\lambda = (-1, 0, 1)$ is the polarization index for $(\sigma^-, \pi, \sigma^+)$ respectively. The second matrix element contains only $\vec{\epsilon}_\lambda$, which is the polarization direction of the vacuum mode through which the scattering process occurs.

We can neglect the effect of the $P_{3/2}$ state if the detuning is small compared to the fine structure splitting $\omega_f = 2\pi \cdot 6.7\,\text{THz}$. The detunings used were all smaller than $2\pi \cdot 1\,\text{THz}$ so this effect gives corrections at the few percent level and should not be relevant given the precision of our data. This means we only have one upper level, $|J\rangle = |J_0\rangle = |P_{1/2}\rangle$, to consider, which means $\Delta_{J\lambda} = \Delta$ and $\gamma_J = \gamma = 2\pi \cdot 22.3\,\text{MHz}$, which corresponds to the Einstein A coefficient of the $P_{1/2}$ state. The value for the matrix elements are summarized in table 5.2. We have an equal superposition of the two qubit states giving $p_m = 1/2$ which combined with the symmetry of the matrix elements further simplifies the expression:

$$\Gamma = \frac{\gamma E}{2\hbar^2\Delta^2} \sum_\lambda \left(b_\lambda \langle \downarrow | \vec{d} \cdot \vec{\epsilon}_{\lambda + i_0 - j_0} | J_0, \lambda + i_0 \rangle \langle J_0, \lambda + i_0 | \vec{d} \cdot \vec{\epsilon}_\lambda | \uparrow \rangle \right)^2 \tag{5.3}$$

The beam RperpV only contains $\sigma^\pm$ light, $\vec{E} = E_V(\sqrt{1/2}, 0, \sqrt{1/2})^T$ which means there is only one combination of polarization components and the sum reduces to a single term:

$$\begin{aligned} \Gamma_V &= \frac{\gamma E_V^2}{2\hbar^2\Delta^2} \left(\frac{1}{\sqrt{2}} \langle S_{1/2,-1/2} | d | P_{1/2,+1/2} \rangle \langle P_{1/2,+1/2} | d | S_{1/2,+1/2} \rangle \right)^2 \\ &= \frac{\gamma I_V}{\epsilon_0 c\, \hbar^2\Delta^2} \frac{1}{2} |\langle S_{1/2,-1/2} | d | P_{1/2,+1/2} \rangle|^2 \\ &= \frac{I_V}{I_{sat}\Delta^2}\, 3.82757 \cdot 10^{21}\ \text{Hz}^{-3} \end{aligned} \tag{5.4}$$

We have used $E = \sqrt{2I/\epsilon_0 c}$ to write E in terms of the intensity I. To obtain the number in the last line, the saturation intensity $I_{sat} = 934\,\text{W/m}^2$ and the value for the matrix element from table 5.2 has been inserted, and Δ is linear frequency (Hz).

For RperpH with $\vec{E} = E_V(\sqrt{1/8}, \sqrt{3/4}, \sqrt{1/8})^T$, we have an analogous expression with an extra term for the π polarization component:

$$\begin{aligned} \Gamma_H &= \frac{\gamma I_H}{\epsilon_0 c \hbar^2 \Delta^2} \left(\frac{3}{4} |\langle S_{1/2,-1/2} | d | P_{1/2,-1/2} \rangle|^2 + \frac{1}{8} |\langle S_{1/2,-1/2} | d | P_{1/2,1/2} \rangle|^2 \right) \\ &= \frac{I_H}{I_{sat}\Delta^2}\, 6.70 \cdot 10^{21}\ \text{Hz}^{-3} \end{aligned} \tag{5.5}$$

Again, I_{sat} has been inserted and Δ is linear frequency. Figures 5.22 and 5.23 show the scattering rates of Γ_V and Γ_H versus the detuning. All detunings are to the red of the $S_{1/2}$–$P_{1/2}$ resonance. The rates were divided by the intensities in units of the saturation intensity to account for the fact that we did not use the same beam intensities for all runs. A weighted fit was performed which matches the data plausibly for both beams. We attribute discrepancies (e.g. for the $\Delta = -600\,\text{GHz}$ points) to uncertainties in the beam intensity measurements.

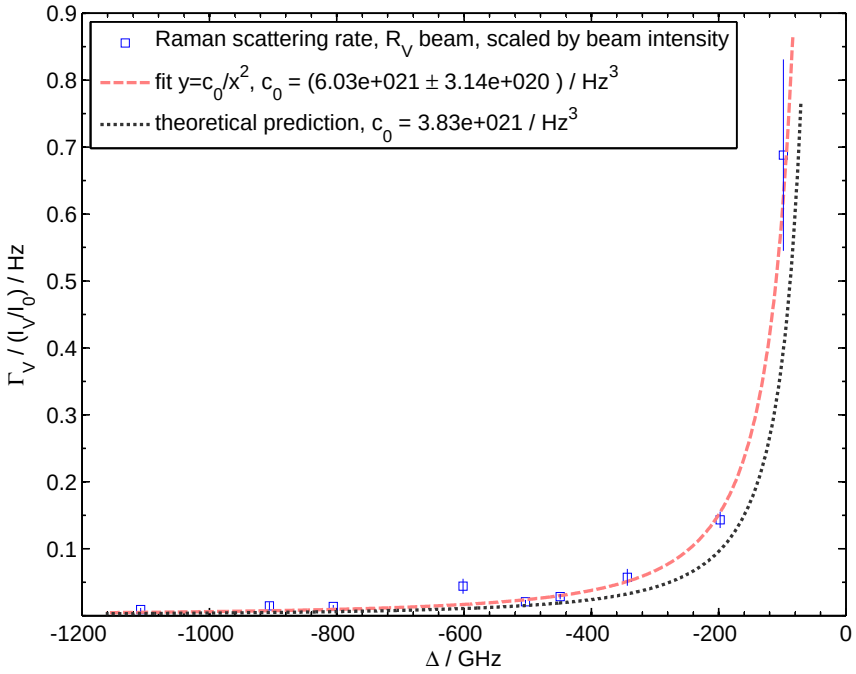

Figure 5.22: Scattering rate Γ_V for the beam RperpV divided by the intensity in units of the saturation intensity versus the detuning in absolute frequency with a weighted-fitted c/x^2 curve. The curve for the theoretical value calculated in equation 5.4 is also shown.

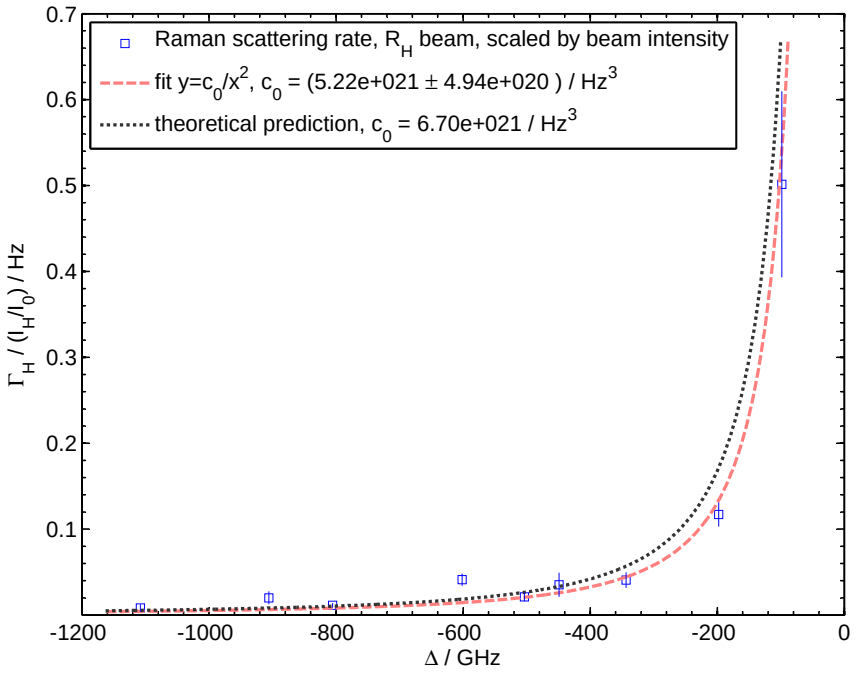

Figure 5.23: Scattering rate with Γ_H for the beam RperpH divided by the intensity (in units of the saturation intensity) versus the detuning in absolute frequency with a weighted-fitted c/x^2 curve. The curve for the theoretical value calculated in equation 5.5 is also shown.

The graphs also show the curves for the theoretical values from equations 5.4 and 5.5. The agreement is at the $20\% - 30\%$ level respectively which is reasonable given the uncertainties in the measurement mentioned above.

	$m = -1/2$	$m = 1/2$
$m' = -1/2$	$1/3$	$-\sqrt{2}/3$
$m' = 1/2$	$\sqrt{2}/3$	$-1/3$

Table 5.2: Transition matrix elements $\langle S_{1/2,m}|d|P_{1/2,m'}\rangle$ between the two Zeeman states in $S_{1/2}$ and $P_{1/2}$. Values are in units of the reduced matrix element $\langle L = 0||d||L = 1\rangle$ which for the $4S_{1/2} \rightarrow P_{1/2}$ transition in $^{40}Ca^{+}$ has a value of $3.4965\ ea_0$ where e is the unit charge and a_0 is the Bohr radius (see [151]).

5.7.3.2 Rabi frequency vs detuning

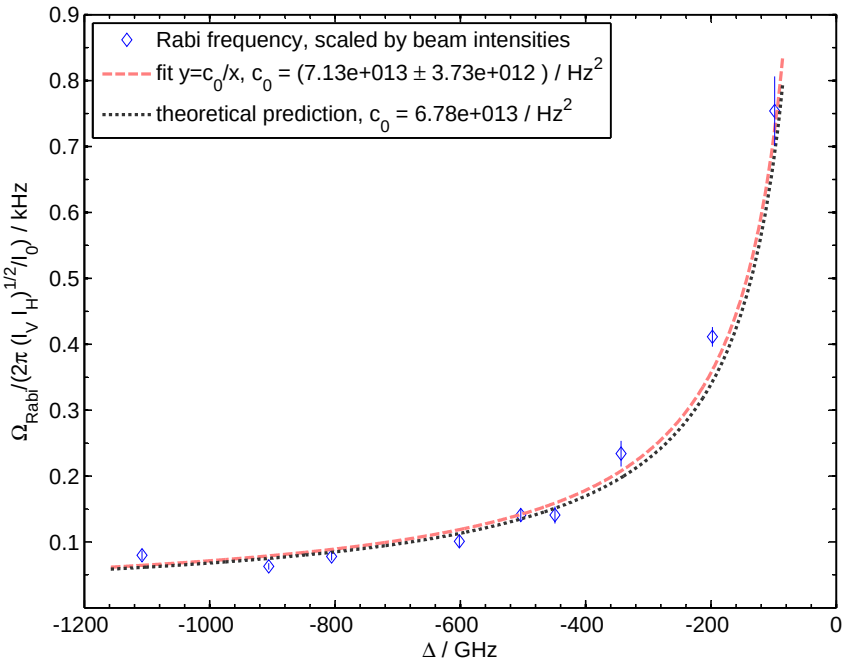

Figure 5.24: Rabi frequency divided by the geometric mean of the intensities of the two beams versus the detuning with a weighted-fitted c/x curve. The curve for the theoretically predicted value (see equation 5.9 is also shown.

The Rabi frequency has the following detuning dependence for $\Delta \ll \omega_f$ [146]:

$$\Omega_{Rabi} \sim \left(\frac{\omega_f}{\Delta\,(\Delta + \omega_f)}\right) \approx \frac{c_0}{\Delta} \tag{5.6}$$

To find a theoretical value for the constant of proportionality c_0, we evaluate [152][20]:

$$\Omega_R = \frac{1}{2\hbar^2} \sum_i \frac{\langle \downarrow |\vec{d} \cdot E_2\vec{\epsilon}_2|i\rangle\langle i|\vec{d} \cdot E_1\vec{\epsilon}_1| \uparrow\rangle}{\Delta_i} \tag{5.7}$$

[20] eq. in [152] differs by a factor of 2 because we define Ω_R such that $\Omega_R t = \pi$ corresponds to a full bit-flip.

Neglecting again the effect of the $P_{3/2}$ state, we have only one upper state $|i_0\rangle$ through which Rabi flops between the two Zeeman qubit states can be driven and the sum reduces to a single term:

$$\Omega_R = \frac{1}{2\hbar^2}\frac{1}{\Delta}\epsilon_V\langle\downarrow|d|i_0\rangle\langle i_0|d|\uparrow\rangle\epsilon_H\,\frac{2\sqrt{I_V I_H}}{\epsilon_0 c} \tag{5.8}$$

The electric fields have again been converted into intensities. Which one of the two $P_{1/2,m}$ states is $|i_0\rangle$ depends on the choice of relative detuning between RperpV and RperpH but has no influence on the value of Ω_R due to the symmetry in the matrix elements (as long as the detuning Δ is large compared to the Zeeman splitting). The polarization components are $\epsilon_H = \sqrt{3/4}$ and $\epsilon_V = \sqrt{1/2}$ (see section 5.7). Since the data points were taken at different intensities, we divide by $\sqrt{I_H I_V}/I_{sat}$. Then, the constant of proportionality is:

$$\begin{aligned} c_0 &= \frac{\sqrt{3}\,I_{sat}}{2\sqrt{2}\hbar^2\epsilon_0 c}\langle S_{1/2,-1/2}|d|P_{1/2,+1/2}\rangle\langle P_{1/2,+1/2}|d|S_{1/2,+1/2}\rangle \\ &= 6.78\cdot 10^{13}\ \mathrm{Hz}^2 \end{aligned} \tag{5.9}$$

Figure 5.24 presents the Rabi frequency divided by the geometric mean of the intensities of both beams in units of the saturation intensity, plotted versus the detuning. The fit shows that the data agrees very well with the model. The fitted value for c_0 is $7.1(4)\cdot 10^{13}$ Hz^2 which is an exact match to the theoretical value obtained in equation 5.9, the curve for which is also shown. A possible reason for the better agreement than in figs. 5.22 and 5.23 is that the Rabi frequency is less sensitive to errors in the intensities than the scattering rates, since they only enter by the geometric mean.

5.8 Summary

The first part of the chapter described a Raman laser system consisting of two injection-locked frequency-doubled diode lasers which can be used to address either isotope of calcium by use of a switchable AOM in the injection path. The injection was characterized and the use of a dual locking scheme to achieve SHG in both systems presented. The relative linewidth which is critical for coherent Raman transitions was measured to be sub-Hz with some slow acoustic components. These were reduced by an order of magnitude using a specially built isolation box.

With the system established, the beam arrangement to drive all the necessary transitions for single qubit rotations in each of the isotopes including the clock state qubit in $^{43}Ca^+$ as well as motional transitions for cooling and the wobble was laid out. This included the development of the light shift method which allows the accurate (to within a few μm) manual alignment of the the far-detuned beams onto the ion. The application of the experimental capabilities provided in this chapter for Rabi flopping and sideband cooling will be presented in chapters 6 and 7 respectively.

The second part of the chapter presented a study of Raman scattering with one of the laser systems as a key source of decoherence when driving coherent manipulations. In their paper from July 2010 [150], Uys et al. report that contrary to their predictions in [145, 146], Rayleigh rather than Raman scattering can be the dominant source of decoherence. They develop a theoretical model that calculates scattering amplitudes for different states ($P_{1/2}$ and $P_{3/2}$) through which the scattering event can take place. These can interfere constructively which causes dephasing (rather than depolarizing as in the Raman scattering case) and leads to higher rates of decoherence than previously expected. They show this experimentally by choosing a detuning Δ between two Zeeman states (splitting ~ 80 GHz) of the $P_{3/2}$ manifold in $^9Be^+$ which maximizes this effect. We expect it to be much smaller than Raman scattering decoherence in our system because of the choice of detuning and the larger fine structure splitting.

The results presented here show that the error introduced by photon scattering from the Raman lasers is consistent with the theory. It rules out the presence of other spectral components in the laser light which can greatly increase the scattering rate even when the central frequency is far detuned. In the Raman system previously used in our group for example (see [136]), peaks of the laser ASE at $\pm n \cdot 60$ GHz were present which corresponds to the diode's internal free spectral range [153]. The doubling cavity in our system acts as a spectral filter that removes any such effects.

As to the uncertainties in the data, our new setup (presented in section 5.5) has much reduced beam power uncertainty since it is more repeatable in terms of beam positioning using the light shift (see section 5.6.1). Additionally, pointing noise will be minimized since each beam will eventually go through a single-mode fiber[21] with a piece of glass spliced onto the fibre end protecting it from damage by the high beam intensities used.

[21] Schäfter+Kirchhoff PMC-360Si

Chapter 6

The Ca^+-qubits

In $^{40}Ca^+$, we use the two ground state Zeeman components $S_{1/2,M_J=\pm 1/2}$ as qubit states. In $^{43}Ca^+$ the qubit is encoded in the ground state hyperfine manifolds $S_{1/2}^{F=4}$ and $S_{1/2}^{F=3}$. Within these we choose either one of the two "stretch" state pairs $S_{1/2}^{4,M_F=+4}$–$S_{1/2}^{3,M_F=+3}$ and $S_{1/2}^{4,M_F=-4}$–$S_{1/2}^{3,M_F=-3}$ at the edges of the manifolds, or the $M_F = 0$ states $S_{1/2}^{4,0}$–$S_{1/2}^{3,0}$. The latter have no first-order Zeeman-shift at zero magnetic field and are hence known as "atomic clock" states. This chapter outlines how we prepare and read out our qubits and presents experimental data taken in the "New Old" trap (see chapter 4) on driving single qubit operations with radiofrequency or microwave fields as well as by Raman transitions with laser light.

6.1 State preparation

Every quantum computing operation requires the initialization of the qubits involved. In our case, this means preparing the ion in a known state by optical pumping. The principle is to excite population from all but one Zeeman component from $S_{1/2}$ to $P_{1/2}$. From here it decays either to the $D_{3/2}$ from which it is repumped with the 866 nm laser, or back to the ground state where it eventually reaches the required state.

For the stretch state qubits in $^{43}Ca^+$ and the Zeeman qubit in $^{40}Ca^+$, we apply a circularly polarized 397 nm beam. This pumps population to either edge of the respective manifold (see figs. 6.1 and 6.2). In $^{40}Ca^+$, the choice in polarization direction, σ^+ or σ^-, determines which qubit state is prepared, $M_J = +1/2$ or $M_J = -1/2$. In $^{43}Ca^+$, we always prepare the ion in $F = 4$ because of the asymmetry in Zeeman state number. We set the 397 nm laser to drive $S_{1/2}^4 \rightarrow P_{1/2}^4$ and its first EOM sideband $S_{1/2}^3 \rightarrow P_{1/2}^4$. The choice in polarization direction selects whether $M_F = +4$ (fig. 6.2) or $M_F = -4$ is initialized.

In order to prepare the clock state in $^{43}Ca^+$, we exploit the selection rule that forbids $M_F = 0 \rightarrow 0$ for $\Delta F = 0$. By using a π polarized 397 nm beam to drive transitions with $\Delta M_F = 0$ only and the EOM as described, we connect all ground state Zeeman components to their $P_{1/2}$ counterparts except $S_{1/2}^{4,0}$ where all the population will be pumped as a result.

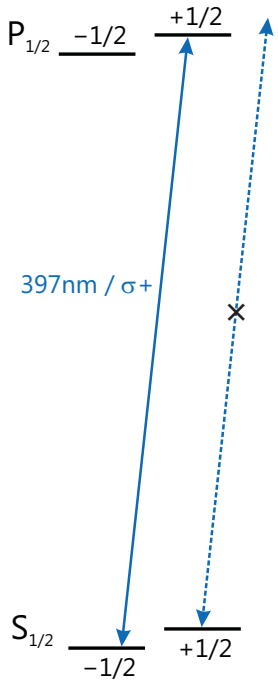

Figure 6.1: State preparation by optical pumping with σ^+ light in $^{40}Ca^+$.

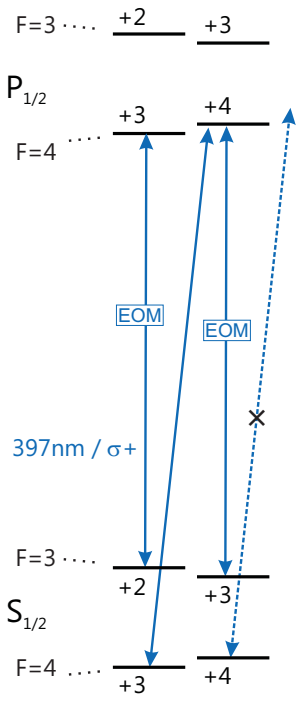

Figure 6.2: Stretch state preparation in $^{43}Ca^+$ by optical pumping with σ^+ light.

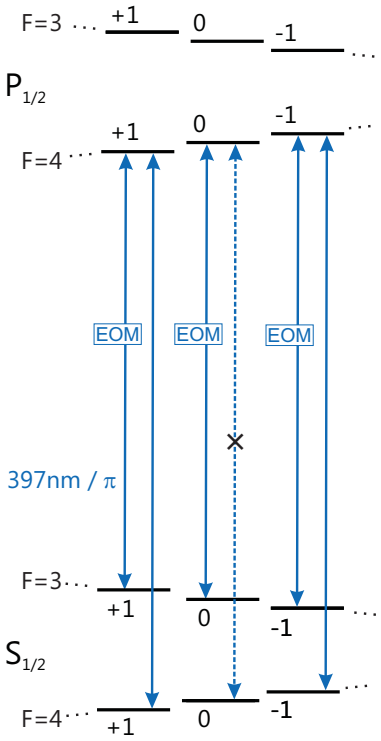

Figure 6.3: Clock state preparation by optical pumping with π light in $^{43}Ca^+$ using the selection rule $M_F = 0 \nrightarrow 0$ for $\Delta F = 0$.

The state preparation fidelity in $^{40}Ca^+$ and in the stretch state in $^{43}Ca^+$ is limited by polarization impurities. Preparation of the clock state in $^{43}Ca^+$ is additionally limited by off-resonant excitation of the $S^{4,0}_{1/2} \rightarrow P^{3,0}_{1/2}$ transition to $\leq 99\%$ even for perfect polarization. As described in section 4.2.9, we use crystal polarizers to clean up the polarization in the 397σ beam and a PBS cube for the π beam. However, since our 397σ beam propagates at a slight angle to the magnetic field and we did not study in detail the possible birefringence of our vacuum viewports, our typical preparation fidelity is $95 - 98\%$, measured by comparing the residual fluorescence observed with the state preparation beam to the fluorescence we get when setting the polarization to repump all states. State preparation studies to optimize these techniques have been done in our group by Simon Webster [154] in $^{40}Ca^+$, and David Szwer [155] and Thomas Harty in $^{43}Ca^+$.

6.2 Qubit readout

Reading out a qubit means performing a projective measurement of its quantum state in the computational basis. On our trapped ion qubit, we accomplish this by making the ion fluoresce if it is in one qubit state and remain dark if it is in the other. The two states are

then discriminated by observing the light (or lack thereof) from the ion on the PMT or camera. Discrimination between bright and dark state are achieved by counting photons for a certain time and setting a threshold for the signal below which the ion is counted as "dark". If the photon count is above the threshold, it is counted as "bright". The accuracy of this method as well as improvements on it, e.g. by counting the photons in a time-resolved way, have been studied in detail in our group [20, 117].

Since we are using ground state qubits in $^{40/43}Ca^+$ which do not have one of the states inherently bright or dark [1], we need to add a step which state-selectively removes the ion from the $397/866$ cycling transition and places it in the $D_{5/2}$ level (which is also called "shelf" in this context). This level has a lifetime of 1.17 s which is large compared to the time it takes to do the fluorescence detection (< 1 ms).

The shelving can be accomplished using a narrow-linewidth high-power laser on the $S_{1/2} \rightarrow D_{5/2}$ quadrupole transition as implemented by the Innsbruck group [157, 158]. To avoid the technological challenges involved with such a laser system, our group uses the laser at 393 nm instead which drives the $S_{1/2} \rightarrow P_{3/2}$ transition. Cycling on this transition will pump the ion into the shelf as there is a decay from the $P_{3/2}$ to the shelf with a branching ratio of 5.87%. The state-selectivity of this process is achieved differently for the two calcium isotopes.

6.2.1 Shelving in $^{40}Ca^+$

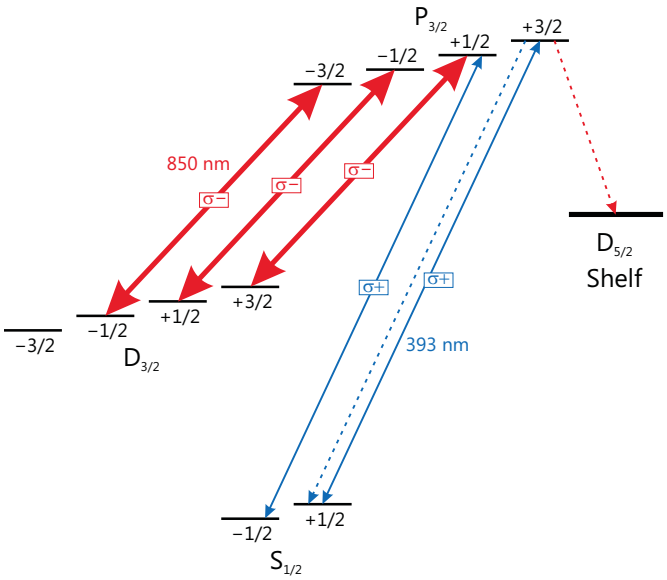

Figure 6.4: State selective shelving in $^{40}Ca^+$ using the dark resonance (EIT) between the 393 nm and the 850 nm laser. The $S_{1/2}^{-1/2} \rightarrow P_{3/2}^{+1/2}$ and $D_{3/2}^{+3/2} \rightarrow P_{3/2}^{+1/2}$ transitions are driven resonantly while the others are slightly off-resonant due to the differences in g_J factors between the levels (not shown). Figure from [21].

[1] as opposed to the optical qubit in Ca^+ [28] or the hyperfine qubits in Be^+ [76] or Yb^+ [156]

In $^{40}Ca^+$ the shelving process is made state-selective by the use of the EIT shelving method which was developed in our group [51]. Fig.6.4 illustrates the situation. The 393 nm beam is σ^+ polarized and can excite the two qubit states $S_{1/2,-1/2}$ and $S_{1/2,+1/2}$ to the $P_{3/2,+1/2}$ and the $P_{3/2,+3/2}$ state respectively. Adding an intense σ^- polarized 850 nm beam at the correct detuning creates a dark resonance or electromagnetically induced transparency (EIT) with the 393 nm beam and suppresses excitation of the $S_{1/2,-1/2}$ state. Therefore only $S_{1/2,+1/2}$ is cycled and pumped to the $D_{5/2}$ shelf. This cycling process preserves the quantum state since the decay from $P_{3/2,+3/2}$ to $S_{1/2,-1/2}$ is forbidden. Up to 90% shelving fidelity can be achieved (limited by $P_{3/2} \rightarrow D_{3/2}$ decay). In practice, this is limited further by laser linewidths and polarization impurity. By swapping the polarizations to σ^- on the 393nm and σ^+ on the 850nm laser, the other qubit state can be shelved. Fig. 6.5 shows shelving during a scan of the 393 nm laser for the two qubit states. The state-selective dark resonance for the $S_{1/2,-1/2}$ is visible.

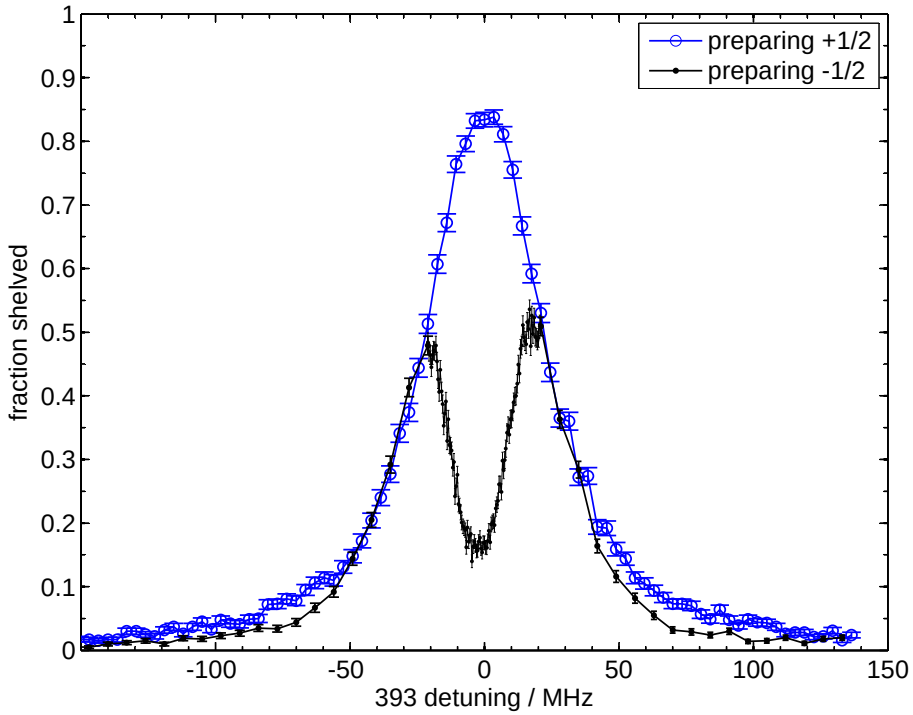

Figure 6.5: Shelving with the 393 nm laser for the two different qubit states in $^{40}Ca^+$. Shelving pulse length: 30 μs. The $S_{1/2,-1/2}$ scan consists of two data sets. The number shelved for the two curves at the centre correspond to the upper and lower readout level, here 83% and 16%, giving an average fidelity of 83.5% (limited by the laser linewidths which reduce the depth of the dark resonance).

The choice of shelving pulse length is a trade-off between reliably shelving $S_{1/2,+1/2}$ which improves with long pulses, and erroneously shelving $S_{1/2,-1/2}$ which worsens with long pulses but at a different time constant. Figure 6.6 shows a shelving pulse length scan for the two different qubit states with fitted exponential curves. Shelving of the intended

state $S_{1/2,+1/2}$ improves to a maximum fraction of experiments of $a = 0.848$ with a time constant of $\tau_s = 10.7\mu$s. The unshelved state $S_{1/2,-1/2}$ rises much more slowly ($\tau_u = 415\mu$s) to the same level. For the fit, the parameter a obtained from the shelved state fit was used and not varied. The data also has a short, fast rising contribution in the beginning which is residual $S_{1/2,+1/2}$ population being shelved which exists due to state preparation error. This is included in the model curve by the addition of a term rising with τ_s with a weighting parameter η.

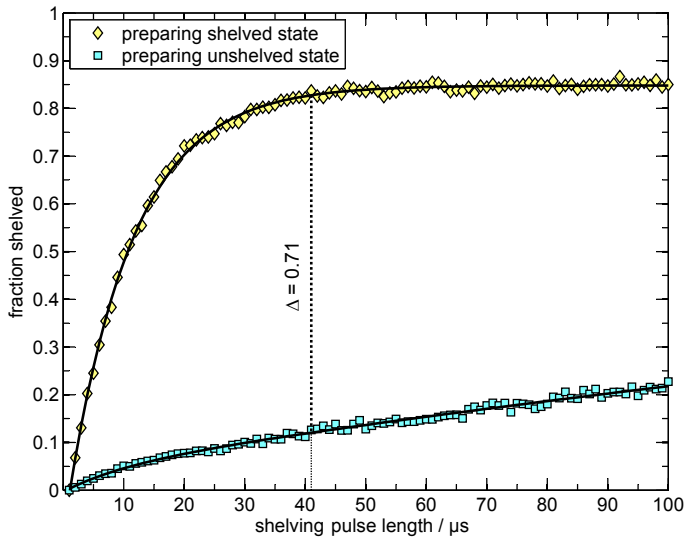

Figure 6.6: Scan of the shelving pulse length in $^{40}Ca^+$ (393 nm + 850 nm lasers). The shelved state was prepared in the same sequence using an RF π pulse. Fitted curve to the shelved level data: $y(a, \tau_s, t_s; t) = a\left(1 - e^{-(t-t_s)/\tau_s}\right)$, $a = 0.848$, $\tau_s = 10.7$ μs, $t_s = 1.12$ μs.
Fitted curve to the unshelved level data: $y_u(\eta, \tau_u, t_u; t) = \eta\ y(a, \tau_s, t_u; t) + (1 - \eta)\ y(a, \tau_u, t_u; t)$, $\eta = 0.055$, $\tau_u = 415$ μs, $t_u = 1.12$ μs. The optimal readout level contrast (0.71) which occurs at a shelving pulse length of 41 μs is also indicated. Each point corresponds to 4096 experimental runs.

6.2.2 Shelving in $^{43}Ca^+$

Fig. 6.7 shows the principle of shelving in the stretch state qubit in $^{43}Ca^+$. The qubit states are $S_{1/2}^{4,+4}$ and $S_{1/2}^{3,+3}$. The hyperfine splitting of the ground state of 3.2 GHz allows state selective cycling with the 393 nm laser. The ion is excited to the $P_{3/2}^{5,+5}$ state using σ^+ polarized light from where it cannot decay to the other qubit state. It is therefore pumped either to the shelf with 89.9% probability or to one of three states in $D_{3/2}$ with 10.1% probabiliy. The latter can be recovered using the 850 nm laser. It is also possible to prepare and shelve out the other stretch state $S_{1/2}^{4,-4}$ and $S_{1/2}^{3,-3}$. In this case, shelving is performed with the 393 nm and the 850 nm laser σ^- polarized.

David Szwer has optimized pulsed shelving sequences and beam arrangements to perfect readout in this system (see [21] for details). In our experiments we only use a single shelving pulse with the 850 nm polarization being σ^+ only which gives us a readout fi-

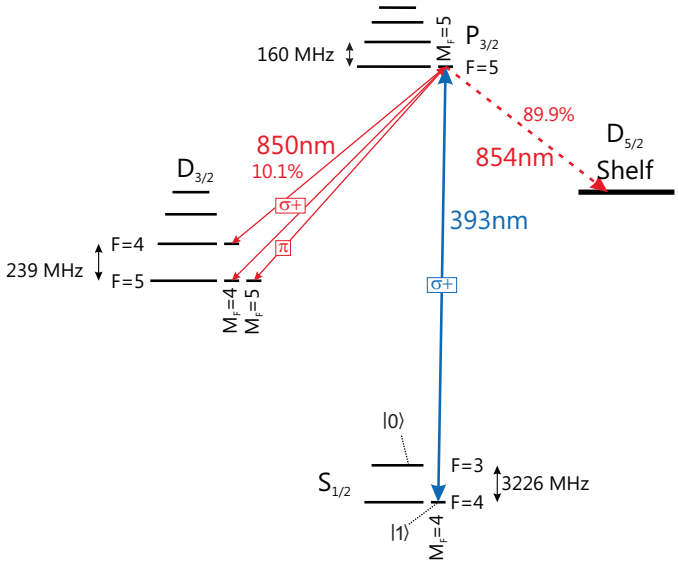

Figure 6.7: State-selective shelving in $^{43}Ca^+$ with the 393 nm laser tuned to the $4 \rightarrow 5$ resonance. The 850 nm laser recovers population that decays to $D_{3/2}$ (figure from [21]).

delity of up to 99%. A pulse length scan can be seen in fig. 6.8. The off-resonant excitation by the 393 nm laser is negligible and the error is dominated by population preparation imperfection (which was not fully optimized in this experiment). The absence of σ^- light is crucial for this scheme since it can pump population from $D_{3/2}$ to states in $P_{3/2}$ that can decay to the other hyperfine ground state (F= 3) where it will be interpreted as being in the other qubit state.

For clock-state readout, we are using the same shelving beams as for the stretch state. The additional decay paths to the $D_{3/2}$ state that are available when operating away from the maximum $|m_F|$ states mean that more population is lost during the shelving process.

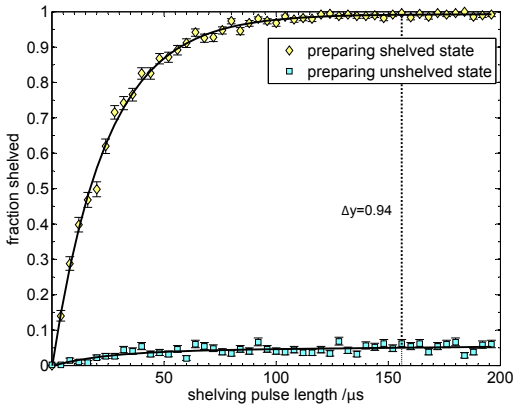

Figure 6.8: Shelving the stretch state $S_{1/2}^{4,-4}$ in $^{43}Ca^+$. Fitted curves as in fig. 6.6: $a = 0.993$, $\tau_s = 24.0$ μs, $t_s = 0.161$ μs, $\eta = 0.041$, $\tau_u = 15200$ μs and $t_u = 1.10$ μs

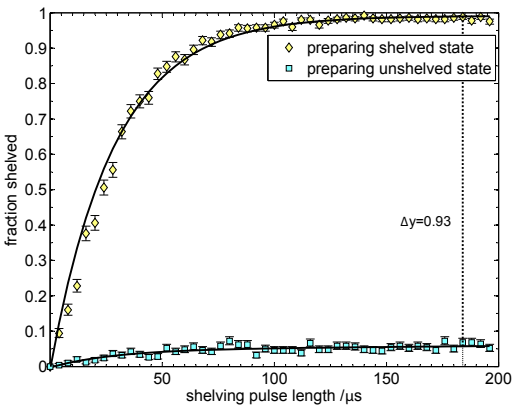

Figure 6.9: Shelving the clock state $S_{1/2}^{4,0}$ in $^{43}Ca^+$. Fitted curves as in fig. 6.6: $a = 0.991$, $\tau_s = 28.6$ μs, $t_s = 0.219$ μs, $\eta = 0.048$, $\tau_u = 18400$ μs and $t_u = 1.59$ μs.

A pulse length scan is shown in figure 6.9 in which a combined preparation and readout fidelity of 97.5% is indicated. Note from these data that the 90% shelved level is already achieved after about $60\ \mu$s which is a normal shelving pulse time for $^{40}Ca^{+}$ (see fig. 6.6). This is important for simultaneous readout of both isotopes (see next section).

6.2.3 Mixed species readout

For experiments with a $^{40}Ca^{+}-^{43}Ca^{+}$ crystal, we need to be able to prepare and read out both qubits in the same experimental sequence. This means we will have to use the same polarization for state preparation and shelving in both isotopes. Following the situation outlined in figures 6.4 and 6.7, we prepare $S_{1/2,+1/2}$ and $S_{1/2}^{4,+4}$ with $397\sigma^{+}$, and shelve with $393\sigma^{+}$. The 850 nm detuning and polarization is set for $^{40}Ca^{+}$ shelving since it is a critical parameter for the scheme to work, whereas in $^{43}Ca^{+}$ we still get nearly 90% readout fidelity without it. We are thus able to shelve both ions with a single pulse. The 850 nm beam is σ^{-} polarized but the isotope shift (-3464 MHz) means that it is far off resonance in $^{43}Ca^{+}$.

In order to differentiate the fluorescence signals from the two individual ions, we need to be able to drive the cycling transitions independently. Again, the isotope shift between the two ions allows us to do this. For the 397 nm transition it is 688 MHz [154] which is large compared to the 20 MHz linewidth.

Fig. 6.10 shows simultaneous Rabi flopping in a $^{40}Ca^{+}-^{43}Ca^{+}$ crystal. Both qubits are prepared and transitions are driven with a simultaneous RF and a MW pulse (see section 6.3) the length of which is increased during the scan. After a shelving pulse, fluorescence is detected in $^{40}Ca^{+}$ first and then in $^{43}Ca^{+}$. Individual addressing and sympathetic sideband cooling with mixed-species crystals has been reported [159, 127, 160, 161]. This is however, as far as we know, the first demonstration of simultaneous two-qubit manipulation and readout in a mixed-species ion crystal.

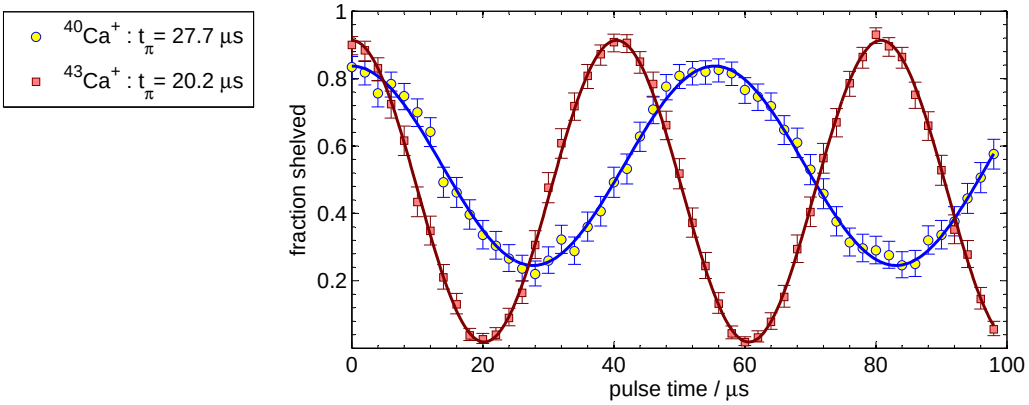

Figure 6.10: Simultaneous Rabi flopping in a $^{40}Ca^{+}-^{43}Ca^{+}$ crystal with RF and MW, using a single 70μs shelving pulse.

6.3 Single qubit operations

Being able to drive single qubit gates with high fidelity is a crucial ingredient for quantum computing. In our experiment, we can do this in two ways. We either expose the ions to radiation at the qubit frequency, ~ 5 MHz radiofrequency in $^{40}Ca^+$ and ~ 3.2 GHz microwaves in $^{43}Ca^+$ or we drive Raman transitions with our injection-locked laser systems (see chapter 5). This section demonstrates Rabi flops using these two different techniques during which the population of the one of the qubit states is given by the following expression:

$$\frac{\Omega_R^2}{\Omega_R^2+\Delta^2}\sin^2\left(\frac{\sqrt{\Omega_R^2+\Delta^2}}{2}t_{pulse}\right) \tag{6.1}$$

where Δ is the detuning from resonance, t_{pulse} is the pulse length, and Ω_R is the Rabi frequency. The term $\sqrt{\Omega_R^2+\Delta^2}$ is also called the effective or off-resonant Rabi frequency. For resonant driving ($\Delta = 0$), the population simply oscillates with Ω_R. No rescaling was applied to the data shown in the following sections which means the oscillations occur between the two readout levels.

6.3.1 Rabi flopping with radiofrequency in $^{40}Ca^+$

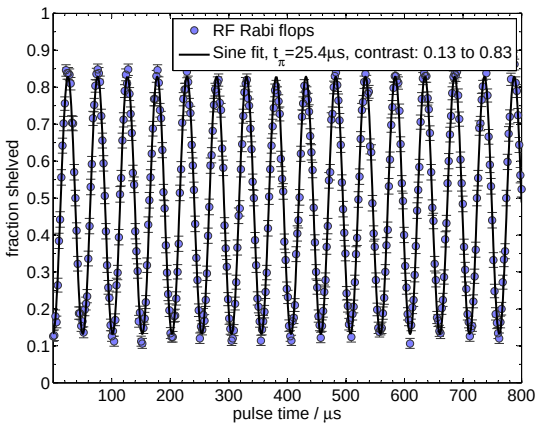

Figure 6.11: Rabi flops in $^{40}Ca^+$ driven with radiofrequency. The fitted sine curve shows the π time to be 25.4 μs. The contrast levels are 0.13 and 0.83. For short pulse times, this corresponds to the readout levels.

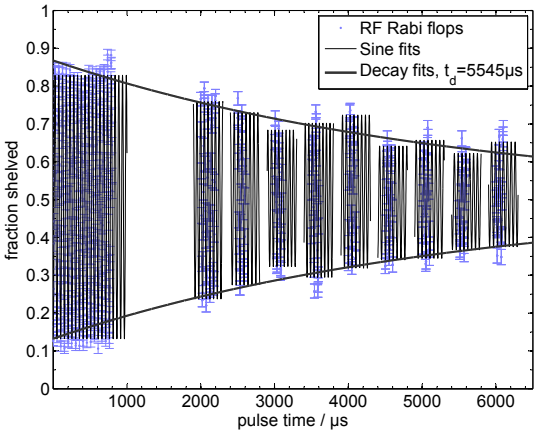

Figure 6.12: Rabi flops in $^{40}Ca^+$ driven with radiofrequency for long pulse times including fig. 6.11 data. Each experiment was fitted with a sine curve to get the upper and lower contrast level. Both were fitted simultaneously to obtain the decay time of 5.5 ms.

The ion can be exposed to a magnetic field oscillating at radiofrequency from the coil near the main viewport (see section 4.2.5). We first scan the drive frequency to find the qubit resonance. Since it depends on the magnetic field it is subject to small ambient field drifts on the order of 10 mG over the course of a day (see [136]). Figure 6.11 shows

readout after an RF pulse of increasing length. The maximum Rabi frequency we achieve is $\omega_{\text{Rabi}} = 2\pi \cdot 39.4$ kHz with the synthesizer set to -3 dBm. With extended pulse lengths, the qubit is subject to decoherence which becomes apparent as a reduction in contrast. This is shown in figure 6.12 on a series of experiments for extended pulse times. At each stage, several flops were recorded in order to be able to obtain the contrast through a Sine fit. The decay of the upper and the lower level towards 0.5 was fitted simultaneously and gave a coherence time of 5.5 ms. Since the qubit state energies depend on the magnetic field, the decay is dominated by magnetic field fluctuations, some of which are related to the 50 Hz mains cycle ($t_{\text{mains}} = 20$ ms) and our coherence time corresponds to a quarter cycle. The experiment was not line-triggered.

6.3.2 Rabi flopping with microwaves in $^{43}Ca^{+}$

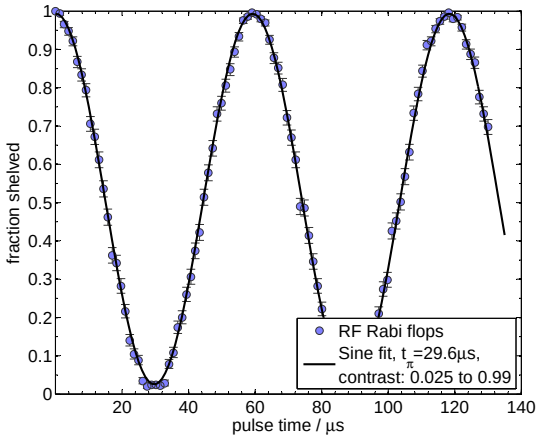

Figure 6.13: Rabi flops on the stretch-state qubit in $^{43}Ca^{+}$ driven with microwaves. The fitted sine curve shows the π time to be $29.6\,\mu$s and the contrast, which for short pulse lengths corresponds to the readout levels to be 0.025 and 0.99.

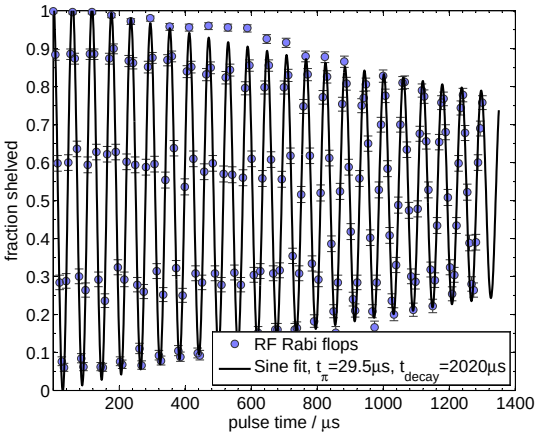

Figure 6.14: Rabi flops on the stretch-state in $^{43}Ca^{+}$ driven with microwaves for longer pulse times. The fitted decaying sine curve yields a decay time of $2020\,\mu$s. The experiment was not line-triggered.

Similar transitions can be driven in our $^{43}Ca^{+}$ qubits using microwaves. The amplified signal (see section 4.2.6) is applied either to one of the grounded trap RF electrodes or to an endcap. Figure 6.13 shows Rabi flops driven in this way on the stretch state qubit with a Rabi frequency of $\omega_{\text{Rabi}} = 2\pi \cdot 16.9$ kHz. The signal was applied to an RF electrode and the synth was set to $+3$ dBm. Figure 6.14 shows an extended scan for the same situation to estimate the decay. The scan was taken without line trigger and the decoherence time is 2.0 ms.

The magnetic field dependence of the two qubit states is very similar, $\Delta E_{40}/\mu_{\text{B}} = 2B$ and $\Delta E_{43}/\mu_{\text{B}} = -7/4\ B$, but we find them only in agreement within a factor of 2 which is possibly due to the magnetic field variations not being the same from day to day and the

volume of data taken for the stretch state being smaller than for the $^{40}Ca^+$ qubit where the decay rate is not yet apparent for short timescales (compare figure 6.12). Additionally, all data in this section suffers from readout level drift due to an unreliable lock of the 393 nm laser which reduces the quality of the exponential decay fits.

This dependence is zero to first order in the $m_F = 0$ states of the clock state qubit at zero magnetic field. In order to lift the m_F degeneracy, we operate at a finite magnetic field (typically $B = 2.0$ G) which means there is still a small dependence of the clock state qubit splitting on the magnetic field. When preparing the clock state and using the same microwave setup as for the stretch state, we initially observed a reduced π time of 80 μs of the Rabi flops. Applying the microwaves to one of the endcaps instead, we recover the flopping speed. This is shown in figure 6.15. The change is due to difference in polarization of the microwave field required to drive $\Delta m_F = 0$ rather than $\Delta m_F = 1$ in the stretch state. The readout contrast is reduced since there are more decay channels from the centre of the $P_{3/2}$ manifold and we cannot use the 850 nm laser to block population decay from the $D_{3/2}$ state (see section 6.2.2).

The decay is estimated in figure 6.16 where the contrast decays with a time constant of $t_d = 110$ ms, which is about 50 times longer than in the stretch state. To see if this is due to the residual magnetic field dependence or the drive field, we estimate the magnetic field sensitivity using the Breit-Rabi formula. For $m_F = 0$, it reduces to [103]:

$$\Delta E\ (B) = \frac{E_{hfs}}{2}\sqrt{1+\chi^2 B^2} \tag{6.2}$$

where $E_{hfs}/h = -3.2256$ GHz is the ground state hyperfine splitting and $\chi = (g_I\mu_N + g_J\mu_B)$ with μ_N and μ_B the nuclear and Bohr magneton and the nuclear g factor $g_I = -1.3176$ [103] and $g_J = 2$ as above. In order to estimate the sensitivity, we differentiate the expression and evaluate it at $B = 2$ G which yields

$$\delta\left(\Delta E_{\text{clock}}\right)/\mu_{\text{B}} = \frac{\partial \Delta E\,(B=2)}{\partial B} B = 0.00177B \tag{6.3}$$

This suggests the coherence time for clock state flopping should be $7/4/0.00177 = 989$ times longer than in the stretch state. Therefore the effect of magnetic field noise modifying the energy levels can be neglected in the clock state in our experiment and the decay time we observe is predominantly caused amplitude fluctuations of our microwave drive field and photon scattering from imperfectly extinguished laser beams which removes population from the qubit states. Despite these limitations, the ratio of decay time to Rabi π-time implies a single flop fidelity of 99.97% on the clock state compared to 98.5% on the stretch state and 99.5% for the $^{40}Ca^+$ qubit.

6.3.3 Rabi flopping with Raman lasers

As described in chapter 5, we can use our injection locked laser system to drive Raman transitions between the qubit states. Figure 6.17 shows Rabi flops in $^{40}Ca^+$ using the

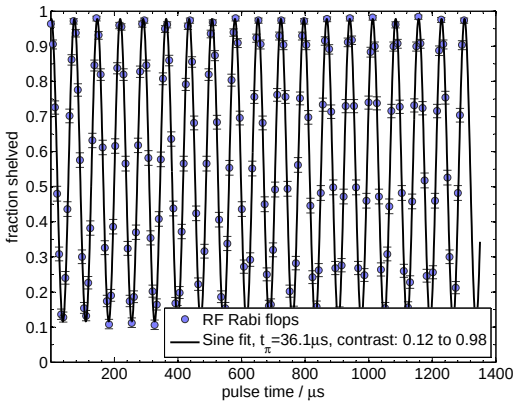

Figure 6.15: Rabi flops on the clock-state in $^{43}Ca^{+}$ driven with microwaves. The fitted sine curve shows the π time to be $29.6\,\mu$s and the contrast, which for short pulse lengths corresponds to the readout levels to be 0.12 and 0.98.

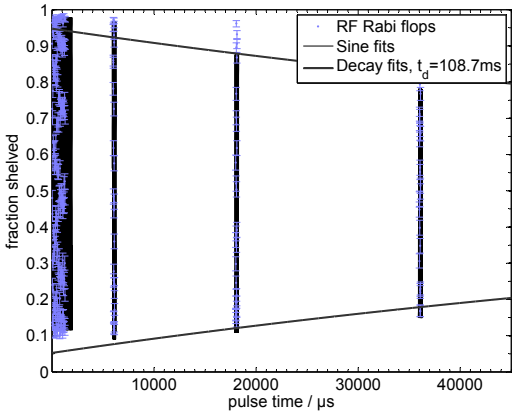

Figure 6.16: Rabi flops on the clock-state in $^{43}Ca^{+}$ driven with MW for longer pulse times including fig. 6.15 data. Each experiment was fitted with a sine curve to get the contrast levels. Both were fitted simultaneously to obtain the decay time of 109ms. The experiment was not line-triggered.

motionally-insensitive beam pair R_V and R_H (see fig. 5.15). With 5 mW in each beam and at a Raman detuning of $\Delta \approx +300$ GHz, we get a π time of $t_\pi = 2.28\,\mu$s. At the start of the scan, there is a $1.1\,\mu$s dead time due to a relative offset in the turn-on times of the two AOMs. After about $32\,\mu$s or 13π worth of flopping, the signal shows a spiky behavior very

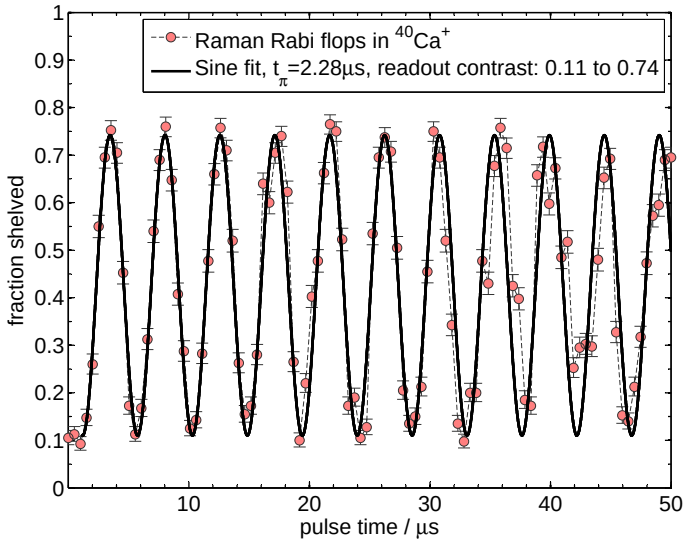

Figure 6.17: Rabi flopping in $^{40}Ca^{+}$ using the Raman beams R_V and R_H (see fig. 5.15) for motionally-insensitive driving. There is a dead time of $1.1\,\mu$s due to the different turn-on times of the two AOMs. The fit takes this delay into account and ignores the last 30 data points where irregularities due to intensity fluctuations at the ion position start occurring (see text). Beam powers: 5 mW in each beam, detuning $\Delta \approx +300$ GHz.

unlike contrast decay. Our analysis in section 6.3.4 implies this to be beam pointing noise which occurs on a timescale of ~ 0.5 s. This causes the intensity at the ion to vary causing fluctuations in Rabi frequency from one experimental point to the next which explains the fluctuations in fig. 6.17. The last 30 points were not included in the fit to get a better estimate of the Rabi frequency. Due to this issue, a reliable measurement of the fidelity of our single qubit Raman pulses cannot be presented yet in this work.

Figures 6.18 and 6.19 show Rabi flops in ^{43}Ca$^+$ on the stretch and clock state respectively. Here, the injection path through the AOM (see chapter 5) was used to set the two lasers by the ground state hyperfine splitting of 3.22 GHz apart. The difference in readout level contrast is larger than described in section 6.2 because clock state preparation was not at its optimum.

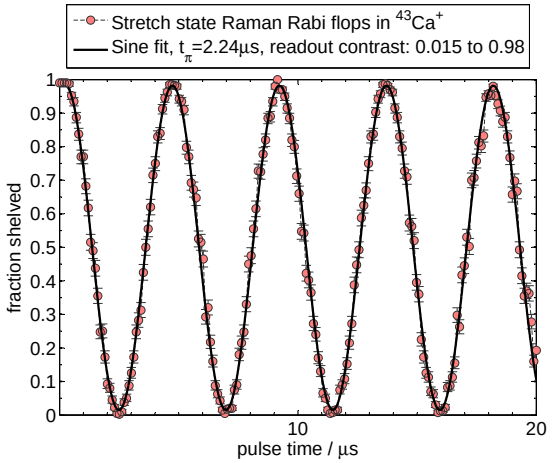

Figure 6.18: Rabi flops on the stretch state in ^{43}Ca$^+$ using $R_{||}$ and R_H.

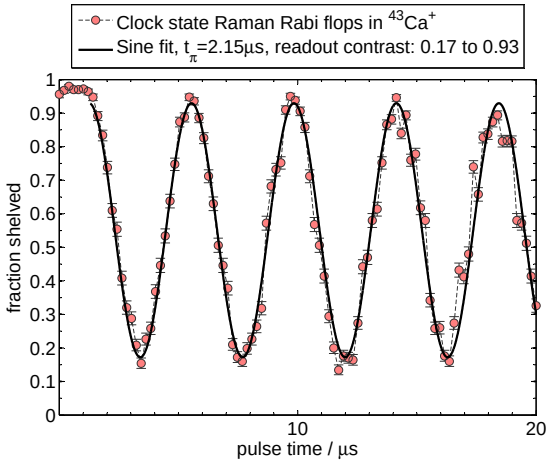

Figure 6.19: Rabi flops on the clock state in ^{43}Ca$^+$ using $R_{||}$ and $R_{||2}$.

6.3.4 Beam pointing noise

In order to measure beam pointing fluctuations we use a knife-edge technique. A Gaussian beam has the rotationally symmetric intensity profile $I(r) = I_0 \mathrm{e}^{-2r^2/w^2}$ where I_0 is the intensity at the centre and w is the $1/\mathrm{e}^2$ radius. The power transmitted when the beam is partly obstructed by a sharp edge can be found by integrating this function (see Appendix E). The result is:

$$P(x) = \frac{P_0}{2}\left(1 - \mathrm{erf}\left(\frac{x\sqrt{2}}{w}\right)\right) \tag{6.4}$$

where $P_0 = I_0 \pi w^2/2$ is the power of the open beam. The error function has its steepest gradient when 50% of the beam is cut off. At this position a power measurement behind the knife-edge is most sensitive to beam pointing changes perpendicular to the knife edge. For our measurement, we first determine the beam radius w at the knife edge position

using a beam profiler[2]. For the given w, we plot $P(x)$ for $P_0 = 1$ and find the gradient in the centre through a linear fit. The resultant slope is the conversion from percentage intensity change to absolute beam pointing change. We then measure the beam intensity using a photodiode[3] in a time-resolved fashion. We perform the measurement twice. Once with the beam uncovered and again with 50% obstructed by the knife edge. The first measurement gives an estimate of pure intensity fluctuations and cannot be differentiated from beam pointing noise with the knife-edge in place. If these are negligible, the second measurement can be directly converted into beam pointing changes perpendicular to the knife edge.

Using the Gaussian beam profile equation, we can convert the beam pointing into intensity fluctuations at the ion position. Data from the R_V beam that has been converted in this way is shown in figure 6.20. The data assumes the ion to be nominally at a distance of $x_0 = 2$ μm from the beam centre in accordance with our measurement in section 5.6.

Figure 6.21 shows a simulation that uses this data to estimate the effect on the Rabi flops. Rabi frequency and readout levels were chosen to be the same as for the data in figure 6.17. The experiment was simulated in the following way: For each point on the curve an intensity value from the data in fig. 6.20 was randomly chosen. The value of the Rabi flops at this time consists of an average of 500 shots for different intensities starting at the random point and moving forward in 200μs steps and modifying the intensity as given by the data. This corresponds to the many fast repetitions of the experimental sequence. The random choice for different steps in time simulates the longer waiting time between sequences (hundreds of ms) as experimental parameters are changed. This shows that the spiky behavior we observe is consistent with the beam fluctuations. Faster intensity or pointing noise would instead lead to a decrease in contrast.

The observed pointing noise originates from the laser's doubling cavity. The feedback loop that moves one of the mirrors to keep the cavity on resonance with the light frequency introduces jitter on the beam. As mentioned in section 5.8, we are working on overcoming this by coupling the beam into a single mode fibre right after the laser (within the soundproof box) and then stabilizing the intensity on the output. Our previous attempts at fiberizing the Raman lasers have been unsuccessful since their 100 mW output power means a very high intensity at the fibre input end where the beam is focused by the collimation lens. This causes damage to the fibre end due to dust being dipole-trapped by the light and charred on the surface. The fibres we are planning to use have a short length of glass spliced onto the fibre end sealing it off from the environment and allowing a much smaller intensity at the glass surface where the beam is not collimated.

[2]Thorlabs BP 2150
[3]Thorlabs PDA36A-EC

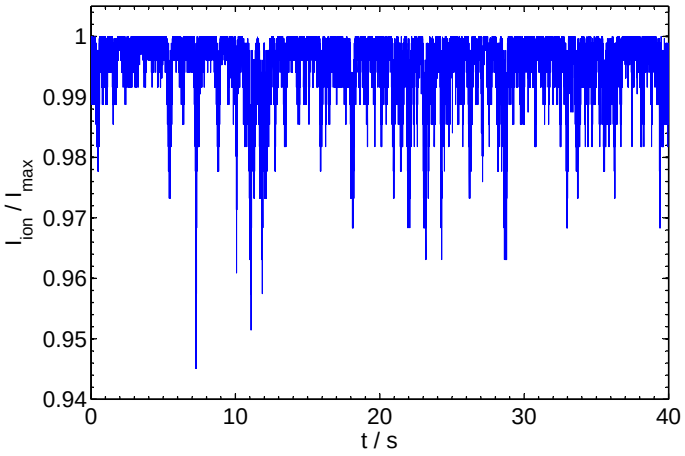

Figure 6.20: Relative intensity fluctuations at the ion's position as a result of beam pointing noise measured with the knife-edge technique on the R_V beam (see text).

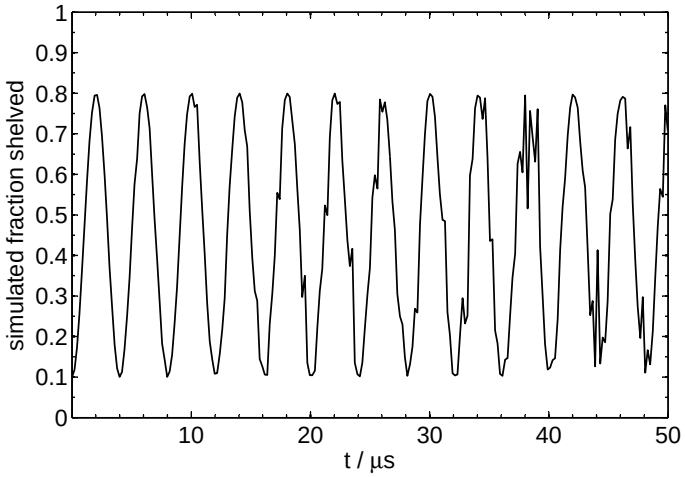

Figure 6.21: Simulated Rabi flops based on the intensity fluctuations shown in fig. 6.20. Choosing similar parameters, spiky features like those seen in the data arise (compare fig. 6.17).

6.3.5 Summary

In this chapter we have demonstrated the experimental capabilities of our ion trap and Raman laser setup in terms of the manipulation and readout of the three different qubits we work with. This is a crucial step towards more advanced experiments since the coherent driving of single qubits as well as their readout by projective measurement are prerequisites for any quantum computing operation (see chapter 1).

The limiting factor on the readout fidelity in our system is the state-selective shelving process since the subsequent step of discriminating $S_{1/2}$ from $D_{5/2}$ has previously been performed with $99.9913(11)\%$ fidelity in our group [20]. The chapter explained the prin-

ciple behind the state-selective shelving methods in the $^{40}Ca^{+}$ qubit as well as the clock and stretch qubits in $^{43}Ca^{+}$. In $^{40}Ca^{+}$ we experimentally achieve a shelving fidelity of 85% which is lower than previously reported in our group (90%, [51]) due to problems with the 393 nm laser which we are currently addressing. In $^{43}Ca^{+}$ we achieve up to 98.5% and 99% shelving fidelity in the clock and stretch state respectively. The latter is an improvement over the single-pulse result by David Szwer [21] in the old trap and is due to the higher polarization purity and intensity stability of the relevant laser beams in our setup. His multi-pulse sequences (on which he reported 99.7% fidelity) could be employed to increase this further. Other groups use the optical qubit which removes this shelving step at the cost of having to address the $S_{1/2} \rightarrow D_{5/2}$ quadrupole transition with stringent requirements on the laser system. This transition can also be used for shelving of ground state qubits as reported by the Innsbruck group who achieved 99.8% shelving fidelity for the $^{43}Ca^{+}$ clock state [157]. The Mainz group has reported shelving and readout in $^{40}Ca^{+}$ with 99.5% fidelity by using a rapid adiabatic passage method on the quadrupole transition which places less stress on the laser linewidth but introduces the need for chirping [162]. While our method achieves lower overall readout fidelities compared to other approaches, it presents no limit to our ability to implement a high-fidelity entangling gate. It is the fidelity of the gate that this experiment aims to optimize and the performance of this process will be gauged independently of these small differences in readout fidelity. For these reasons we have chosen to invest our efforts and resources in the Raman laser system described in chapter 5.

A first application of the Raman beams was given in this chapter by showing coherent manipulations of all three qubits. This proves on the one hand the flexibility of the difference frequency injection system which can be used on both isotopes. On the other hand it shows the value of the high power generated by the use of frequency doubling as Rabi flopping π-times as short as 2 μs were achieved at a detuning of $\Delta = 500$ GHz. Similar parameters ($t_\pi = 3$ μs, $\Delta = 500$ GHz) were implemented in the group of C. Monroe to drive entangling gates in $^{171}Yb^{+}$. The Innsbruck group reported the use of a Raman beam pair at $\Delta = 10$ GHz and $t_\pi = 65$ μs [28]. Our first application of the new laser system has also brought to light the technical issue of beam pointing noise solutions to which have been proposed and are currently being implemented.

A final degree of control over our qubits was described by showing coherent manipulations with microwaves and radio frequency in $^{43}Ca^{+}$ and $^{40}Ca^{+}$ respectively. Similar measurements were published by J. Benhelm [163] reporting negligible amplitude decay on the clock state after 150 state transfers which is matched by our results. However, our coherence time is clearly lower since we see the amplitude decay after 100 ms; the limitation is possibly amplitude stability. In terms of single flop fidelity, our setup achieves 99.97% on the clock state compared to 98.5% on the stretch state and 99.5% for the $^{40}Ca^{+}$ qubit which is enough to provide the spin-flip operations needed for future experiments.

Using a mixed-species crystal of trapped ions is one of the main features of our experiment. The new possibilities of using such a system are demonstrated by implementing for the first time the use of radiofrequency and microwave radiation to simultaneously drive coherent transitions in two ions in the same trap followed by independent readout with a single shelving pulse. This shows the ease of implementation of a two qubit system with individual addressing by use of two different isotopes.

Chapter 7

Cooling

As described in section 1.3.1, the geometric phase gate does not have very stringent ion-temperature requirements. However, in order to diagnose our experiment and take the next steps towards the gate such as motional coherence experiments [164], we need to cool the mixed species two-ion crystal close to the motional ground state. In previous experiments in our group, this was achieved in three steps, using Doppler cooling, continuous sideband cooling and pulsed sideband cooling. The new trap with its stronger confinement allows us to forgo the second stage and implement pulsed sideband cooling directly after Doppler cooling. To make this possible, the Doppler cooling procedure needs to yield a thermal state with low occupation number $\bar{n} < 10$ for $f_z = 2\,\text{MHz}$. This chapter presents the concepts and experimental results of the two cooling stages implemented in the "New Old" trap (see chapter 4). We first briefly introduce the theory of Raman transitions which couple to motional states of the ion as they are used both for characterizing the Doppler cooling and for implementing and analyzing the sideband cooling.

7.1 Raman transitions and motional states

Assuming canceling single beam light shifts (see chapter 5), the Hamiltonian for Raman transitions between $|\downarrow\rangle$ and $|\uparrow\rangle$ in the interaction picture is [30][1]:

$$\hat{H}_{R,I} = -\frac{\hbar\Omega_R}{2} e^{i(\Delta\vec{k}\cdot\vec{r}-\delta t+\Delta\phi)} |\downarrow\rangle\langle\uparrow| - \text{h.c.} \tag{7.1}$$

with $\Delta\vec{k} = \vec{k}_1 - \vec{k}_2$ and $\Delta\phi = \phi_1 - \phi_2$ the wave vector and phase difference respectively between the two Raman beams, and the detuning from Raman resonance $\delta = \omega_1 - \omega_2 - \omega_0$ (see figure 7.1).

Since the ions are trapped in a harmonic potential, each of the spin states is associated with a ladder of Fock states $|n\rangle$ with energy $\hbar\omega_m\,(n + 1/2)$ where ω_m is the frequency of the motional mode ($= \omega_z$ for a single ion). When driving transitions that can change the motional state of the ion from $|n\rangle$ to $|n'\rangle$, the Rabi frequency of each of the Fock states is

[1] Please note that we define the Rabi frequency such that $\Omega t = \pi$ constitutes a single spin-flip which differs from parts of the standard literature [165] by a factor of 2.

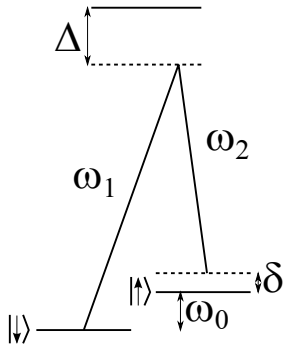

Figure 7.1: Raman transitions with polarizations and relevant detunings to drive qubit transitions: The global Raman detuning Δ, qubit splitting ω_0 and detuning from Raman resonance δ.

different which can be expressed as a modification factor to give $\hat{H}'_{R,I} = \hat{H}_{R,I}\, M_{n',n}$ where M has the following form [165]:

$$M_{n',n} = \langle n'|e^{i\eta\left(\hat{a}+\hat{a}^\dagger\right)}|n\rangle = (i\eta)^{|n-n'|}\sqrt{\frac{n_<!}{n_>!}}\, e^{-\eta^2/2} L_{n_<}^{|n-n'|}\left(\eta^2\right) \tag{7.2}$$

Here $n_<$ and $n_>$ denote the larger and smaller values of n for the two states respectively and the function $L_{n_<}^{|n-n'|}$ is the generalized Laguerre polynomial of order $|n-n'|$. The Lamb-Dicke parameter η is defined as:

$$\eta = \Delta k \cos(\theta)\sqrt{\hbar/2m\omega_m} \tag{7.3}$$

where $\Delta k = |\Delta\vec{k}|$ is the wave number of the Raman beam frequency difference and θ is the angle between $\Delta\vec{k}$ and the trap axis. The Lamb-Dicke parameter is the ratio between size of wave-function of the motional ground state and the light wavelength. If it is small, the wave function stretches over an area much smaller than the wavelength and experiences only a single light wave phase. In this approximation, the ion is said to be in the Lamb-Dicke regime. For Fock states with $n > 0$, the wave function extends further and the Lamb-Dicke condition becomes $\eta^2\,(2n+1) \ll 1$ since the extent of the wavefunction scales as $\sqrt{2n+1}$[2]. In our experiment, the beams are aligned such that $\Delta\vec{k}$ is parallel to the trap axis, so $\theta = 0$. For our typical trap frequency $\omega_z = 2\pi \cdot 1.98\,\text{MHz}$, we have $\eta = 0.179$ which justifies using the Lamb-Dicke approximation.

Under this approximation $\hat{H}'_{R,I}$ simplifies to:

$$\hat{H}'_{R,I} = \frac{\hbar\Omega_R}{2}\left(1 + i\eta\left(\hat{a}e^{i\omega_z t} + \hat{a}^\dagger e^{-i\omega_z t}\right)\right) e^{-i(\delta t - \Delta\phi)}|\downarrow\rangle\langle\uparrow| + \text{h.c.} \tag{7.4}$$

We can now differentiate three regimes: the carrier at $\delta \simeq 0$ where we only drive transitions between the qubit states, and the first red and blue sidebands at $\delta \simeq \pm\omega_m$ where a transition changes the motional state by $\Delta n = \pm 1$ as well. Applying the rotating

[2] $E_n = 1/2\, m\omega^2 a_n^2$ with amplitude a_n. Since E_n scales $\sim (n+1/2)$, a_n scales $\sim \sqrt{2n+1}$.

wave approximation in each of these regimes yields three Hamiltonians [30]:

$$\begin{aligned}\hat{H}_{carrier} &= \frac{\hbar\Omega_R}{2} \mid\downarrow\rangle\langle\uparrow \mid e^{-i(\delta t-\Delta\phi)} + \text{h.c.} \\ \hat{H}_{bsb} &= i\hbar\eta\sqrt{n+1}\frac{\hbar\Omega_R}{2} \mid\downarrow,n\rangle\langle\uparrow,n+1\mid e^{-i(\epsilon_b t-\Delta\phi)} + \text{h.c.} \\ \hat{H}_{rsb} &= i\hbar\eta\sqrt{n}\frac{\hbar\Omega_R}{2} \mid\downarrow,n\rangle\langle\uparrow,n-1\mid e^{-i(\epsilon_r t-\Delta\phi)} + \text{h.c.}\end{aligned} \tag{7.5}$$

Where $\epsilon_{r/b}$ is the detuning around the sidebands, $\epsilon_{r/b} = |\delta \pm \omega_z|$. The dynamics of each of these Hamiltonians give Rabi flopping between the two respective states involved. The probability of finding the ion in the final state after a pulse of duration t_p and local detuning $\delta' = \delta$ for the carrier, or $\delta' = \epsilon_{r/b}$ for the sidebands, is given by:

$$p_f(\delta', t_p) = \frac{\Omega^2}{\Omega^2+\delta'^2}\left(\frac{1}{2} - \frac{1}{2}\cos\left(\sqrt{\Omega^2+\delta'^2}\, t_p\right)\right) \tag{7.6}$$

where $\Omega = \Omega_R$ for the carrier, and $\Omega = \eta\sqrt{n+1}\,\Omega_R$ and $\eta\sqrt{n}\,\Omega_R$ for the blue and red sideband respectively. Summing several terms of this form is used to analyze scans of the Raman detuning over the carrier and sidebands in section 7.3.

This model assumes that the off-resonant carrier excitations are small when driving a sideband. Since the carrier transition is a factor $1/\eta$ stronger than the sidebands, this is only well obeyed if $(\Omega_R/\omega_z)^2 \ll 1$. In our experiment (see below), this value is typically only $\sim 2-3\%$ and the effect can usually be neglected (see section 7.3.2).

7.2 Doppler cooling

The ions are Doppler cooled with a single 397 nm laser at 45° to the trap axis (see figure 4.5). The transition at 397 nm allows a high cycling rate and hence efficient cooling [166]. For the experiments presented here, we repump population from the $D_{3/2}$ level using the 866 nm laser. As described in chapter 3, repumping can also be achieved via the $P_{3/2}$ level using the lasers at 850 nm and 854 nm which gives a higher cooling and fluorescence rate. At the moment our setup only contains one 850 nm beam which has to be circularly polarized for readout and therefore cannot be used for repumping. As will be seen below however, the repumping scheme used is not limiting us in terms of cooling.

7.2.1 The Doppler limit

The optimal detuning Δ to reach the minimal Doppler cooling temperature is at the half-fluorescence point $\Delta = 1/2\,\Gamma\sqrt{1+s}$ [167], where s is the saturation parameter $s = I/I_0 = 2\Omega_R^2/\Gamma^2$. I_0 is the saturation intensity, Ω_R the Rabi frequency and Γ the natural linewidth ($2\pi \cdot 22.3$ MHz for the 397 nm cooling transition). Near this point, the gradient of the absorption profile is steepest and hence most sensitive to Doppler shifts. The achievable

minimum Doppler energy under these conditions is given by [167][3]:

$$E_D/\hbar = \frac{\Gamma\sqrt{1+s}}{4}\left(1+\frac{1}{3\cos^2(\theta)}\right) \tag{7.7}$$

where θ is the angle between the cooling beam and the motional mode of interest. In our case this is the axial mode with the trap frequency ω_z and $\theta = 45°$. Expressing the Doppler limit energy E_D in terms of the minimal $\bar{n} = \bar{n}_D$ gives $E_D = \bar{n}_D\hbar\omega_z$ and hence:

$$\bar{n}_D = \frac{5}{12}\frac{\Gamma\sqrt{1+s}}{\omega_z} \tag{7.8}$$

In order to observe ion fluorescence for state discrimination, a large signal is beneficial which is why we typically choose our 397 nm laser intensity I to saturate the transition, $s \simeq 2$. This limits the minimum temperature we can achieve. So in order to minimize the ion temperature at the start of an experimental sequence, we reduce the intensity by lowering the AOM drive power using the driver's AM input and do a Doppler cooling pulse of 1 ms at $s \simeq 0.1$. To determine the ion's temperature, we analyze carrier flops after Doppler cooling, as described next.

7.2.2 Carrier flops of a thermal state

For carrier transitions ($n' = n$), the Rabi frequency modification factor (eq. 7.2) reduces to:

$$M_c(n) = e^{-\eta^2/2}L_n^0\left(\eta^2\right) \tag{7.9}$$

If the ion is in a thermal state, the Rabi flops between $|\downarrow\rangle$ and $|\uparrow\rangle$ which it undergoes are a thermally weighted superposition of oscillations at the Rabi frequencies of its constituent Fock states:

$$p(|\uparrow\rangle) = \sum_{n=0}^{\infty}\frac{e^{-n/\bar{n}}}{Z}\left[\frac{1}{2}-\frac{1}{2}\cos(\Omega_R M_c(n)\,t)\right] \tag{7.10}$$

As above, Ω_R is the unmodified Rabi frequency in the absence of motional states and the partition function Z normalizes the weighting factors: $Z = \sum_{n=0}^{\infty} e^{-n/\bar{n}}$.

Figure 7.2 shows simulations of the resulting Rabi flops for two different Lamb-Dicke parameters and a number of different $\bar{n}$, each for an arbitrary Rabi frequency. The weighting of Fock states was truncated at $n = 100$. The truncation error is below 10^{-3} for $\bar{n} < 15$. The decay of the flops happens faster for higher $\bar{n}$ and η. The top graph corresponds to our standard experimental settings. The bottom graph at 1 MHz axial trapping frequency shows rephasing of the different Fock state components at around 35π of Rabi flopping. We did not attempt to observe this in our experiments since we could not drive flopping long enough (see section 6.3.4).

Knowing the trap frequency and hence the Lamb-Dicke parameter, we can fit this curve to experimental data after Doppler cooling and extract the $\bar{n}$ we achieve. This is

[3] for a beam that cools all directions symmetrically, $\cos(\theta) = 1/\sqrt{3}$ which yields the standard form

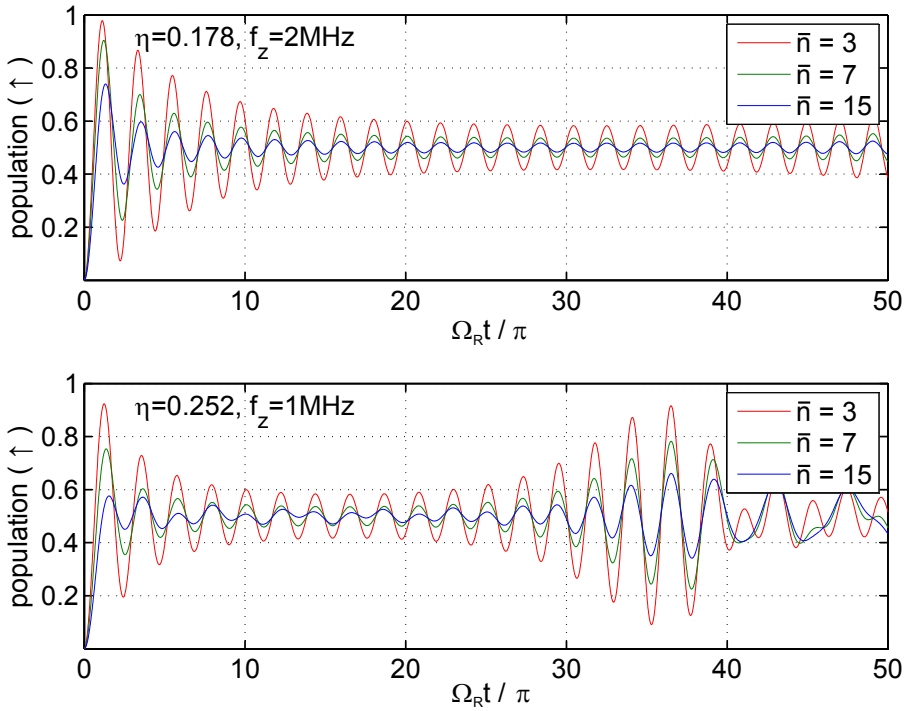

Figure 7.2: Simulation of carrier flops for thermal states with different $\bar{n}$ and for two different Lamb-Dicke parameters η. The trap frequencies f_z are the axial frequencies we have to set in our trap to achieve the respective η. The bottom graph shows "rephasing" of the different Fock state components around $\Omega_R t = 35\pi$.

shown in figure 7.3. The Doppler limit at zero saturation is $\bar{n}_D = 4.6$ and for our estimated saturation parameter of $s = 0.1$ we get $\bar{n} = 4.8$. The fit has four free parameters: $\bar{n}$, the Rabi frequency, an amplitude offset and a phase offset to take the dead time for the AOMs switching the Raman lasers into account. The readout levels were determined independently by fitting a short RF flopping experiment taken just before this scan. Our value $\bar{n} = 5.3$ is very close to the Doppler limit and a good starting point for pulsed sideband cooling.

The measurement was repeated for a series of different trap frequencies for comparison with equation 7.8. The results are shown in figure 7.4 and the fit gives a constant of $\Gamma_{eff} = 5/12\Gamma\sqrt{1+s} = 2\pi\cdot 11.8$MHz. This corresponds to $s = 0.67$ assuming correct detuning. The absolute and achievable Doppler limits are also indicated on the plot. We see that we consistently cool to within 20% of the achievable Doppler limit (dashed line). There are several possible reasons for the offset. Firstly our estimate of s is based on setting the laser to peak fluorescence during an experimental sequence and observing the measured count rate. A direct measurement of the beam intensity is very unreliable, since heating effects in the AOM cause its diffraction efficiency and angle to change between continuous operation and a pulsed experimental sequence. Using the collection efficiency of the imaging system (0.3%), the fluorescence is transfered into an excited state population

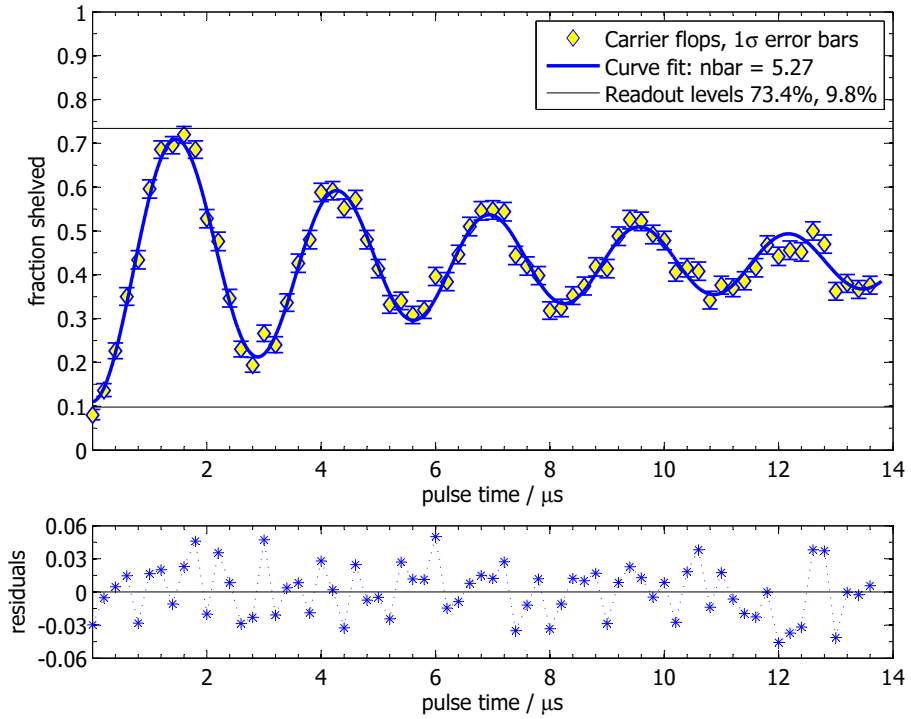

Figure 7.3: Carrier flops with R_H and R_{para} on a $^{40}Ca^+$ ion after Doppler cooling. The fitted function is eq. 7.10 with an additional phase and baseline offset. The readout levels were determined by RF flopping and are fixed for this fit. The resulting $\bar{n}$ is 5.27 which is close to the Doppler limit of $\bar{n}_D = 4.8$

and compared to a Lorentzian profile to obtain s (see eq. A.1). Since we are also cooling on the transition we are observing, peak fluorescence will occur to the red of resonance. This effect is increased by the fact that we are repumping with the 866 nm laser which introduces a dark resonance into the spectrum which, even when detuned to the blue, can shift the observed fluorescence peak to the red (see fig. 3.1). This means that we are most likely somewhat underestimating s. A second systematic error is that the detuning of the 397 nm laser was only set approximately and will not be exactly at the half fluorescence point assumed for the analysis. This will increase the minimum achievable temperature. A detuning error of only 3 MHz and $s = 0.35$ would give a result consistent with our experiment. Additionally, the 397 nm laser has a finite linewidth of ~ 1 MHz which increases the effective Γ and also gives a higher minimum temperature.

The data clearly shows that our system is able to cool ions very close to the Doppler limit which is an excellent starting point for sideband cooling to the ground state.

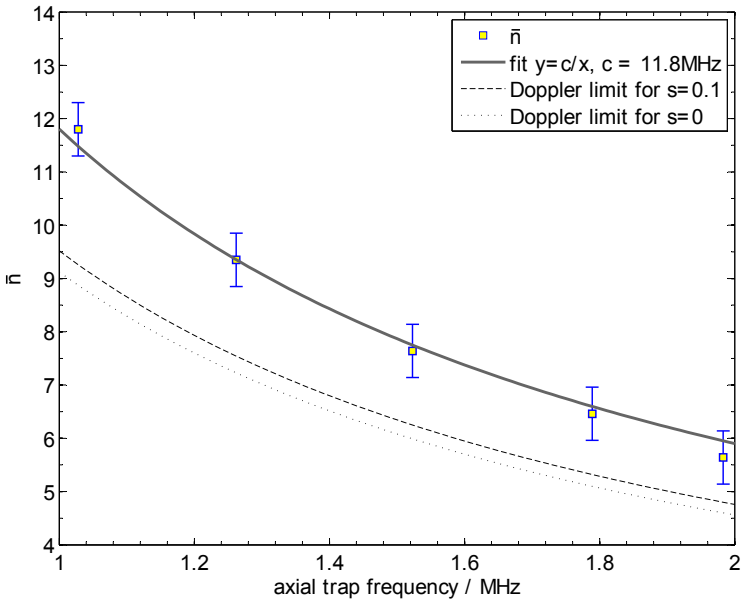

Figure 7.4: Measurements of $\bar{n}$ for different axial trap frequencies. The fit gives an effective linewidth of $\Gamma_{eff} = 2\pi \cdot 11.8$ MHz. The measured $\bar{n}$ values are only 20% above than the Doppler limit which is also indicated on the plot, both the absolute minimum value and the one for our estimated saturation parameter $s = 0.1$. The errors on the data points were determined by the relative precision between scans at nominally identical parameters we observed over several days.

7.3 Pulsed sideband cooling

7.3.1 Cooling principle

Pulsed sideband cooling uses a coherent transition between the Fock states and a repumping step to reduce the ion's motion. Figure 7.5 shows one cooling cycle. The ion is prepared in $|\downarrow\rangle$, but is spread thermally over a number of different motional states. A single red-sideband pulse driven with the Raman lasers transfers the population to $|\uparrow\rangle$ and lowers the motional quantum number by 1. Only the motional ground state is unaffected. A repumping pulse transfers the population back to the $|\downarrow\rangle$ state. Since decays predominantly happen on the carrier, the population is shifted down on average nearly one step. In our experiment, we repump via the $P_{1/2}$ state with the circularly polarized 397 nm and the 866 nm repump beams. This second phase cannot be driven coherently since any cooling scheme requires a dissipative process. During the decay, the emitted photon carries away some of the ion's motional energy. The cycle is repeated to accumulate population in the motional ground state. The minimum temperature achievable with this method is limited by off-resonant excitation of the carrier and the blue sidebands during the red sideband pulse.

In order to perform sideband cooling, the transition must be narrow enough to be able to resolve the sidebands ($\Gamma \ll \omega_z$). For this reason, driving sideband transitions with

Raman lasers is advantageous since the linewidth of the Raman transition is given by the relative linewidth of the two lasers which can be made extremely small by deriving both beams from a single laser source or as in our case by using injection locking (see chapter 5). Raman sideband cooling is a standard technique in ion trap work [168].

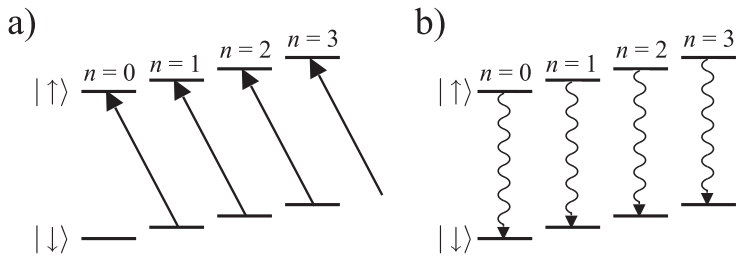

Figure 7.5: The two stages of an operational cycle of pulsed sideband cooling. The Fock states $n = 0$ to $n = 3$ are shown for the two qubit states. a) A Raman laser pulse on the red sideband transfers population to the excited state, lowering the vibrational quantum number by 1. b) The ion is repumped to the ground state using a circularly polarized 397 nm pulse. Since decay mostly happens on the carrier, the population of each motional state is shifted down on average nearly one step. The cycle is repeated until all the population accumulates in $n = 0$ (figure from [30]).

Sideband Rabi flopping on a thermal distribution of Fock states can be used to get a measure of the temperature [169]. Comparing the population transfered from $|\downarrow\rangle$ to $|\uparrow\rangle$ using the same length pulse on the red and blue sideband yields a sideband height ratio (blue/red) of R. By dividing two thermally-weighted sums of Rabi-flopping terms of the form shown in eq. 7.6 for the same pulse time $t = t_p$, this can be related to $\bar{n}$ in the following way (see [154] for derivation):

$$\bar{n} = \frac{R}{1 - R} \tag{7.11}$$

So long as off-resonant carrier excitations can be neglected, this is a straightforward way to determine the ion temperature. Preparing $|\downarrow\rangle$ after cooling, we scan the Raman detuning δ over the red and blue sidebands with equal pulse time t_p and determine the amplitude ratio by a simultaneous fit to the following function for the probability $P_\uparrow$ of being in the $|\uparrow\rangle$:

$$P_\uparrow(\delta) = b + a\left[p_f(\delta - \omega_m, t_p) + R\, p_f(\delta + \omega_m, t_p)\right] \tag{7.12}$$

where a and b are amplitude and baseline b, the p_f are the Rabi flopping terms from eq. 7.6, and ω_m is again the mode frequency. Alternatively, knowing the sideband frequency ω_m we can take data at each of the peaks to determine the height as well as with $t_p = 0$ to record the baseline. This corresponds to a direct measurement of a and $a \cdot R$. Both methods were used to analyze data in the following section.

7.3.2 Single ion ground state cooling

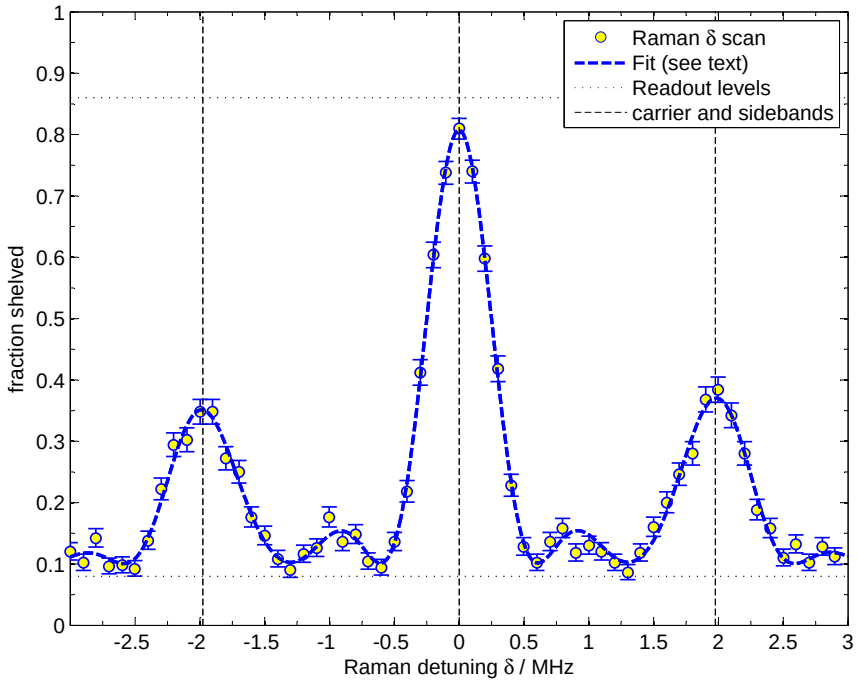

Figure 7.6: Raman detuning scan over the carrier and the first red and blue sideband after Doppler cooling. The fit follows eq. 7.12 with an extra term for the carrier. The Rabi frequency was determined by a carrier flopping scan (compare fig. 7.3), $\Omega_R = 2\pi \cdot 396.6$ kHz, and fixed for the fit. The free parameters were the pulse length ($t_p = 1.575$ μs), the sideband Rabi frequency ($\Omega_s = 2\pi \cdot 217.3$ kHz), the trap frequency ($f_z = 1.98$ MHz), the sideband height ratio ($R = 0.93$) as well as the offset and scale factors.

Figure 7.6 shows a sideband spectrum of a single $^{40}Ca^+$ ion after Doppler cooling. It was taken by applying a fixed length pulse of $t_p = 2$ μs of R_H and $R_{||}$ to the ion corresponding to a carrier π pulse (which included the turn-on dead time of the AOMs). This is repeated for different $R_{||}$ detunings in order to scan the relative Raman detuning δ from -3 to 3 MHz. The carrier, and the first blue and red sideband are visible. Equation 7.12 including an additional term for the carrier was fitted to the data. The fit is good, even though the formula is strictly only valid for a single Fock state. The trap frequency, which determines the sideband positions, is 1.98 MHz which coincides with the value measured by the tickling method (see section 2.6.3).

Resolving the carrier and the sidebands well in a single scan is difficult because of the difference in Rabi frequency. Since the sidebands are very similar in height and the short pulse time means that they are underdriven, the ratio obtained gives an unreliable temperature measurement under the shot noise compared to the carrier flopping method described in section 7.2.2. The latter yields $\bar{n} = 5.9$ in this case while $R = 0.93$ from the fit in fig. 7.6 suggests $\bar{n} = 13.3$. For better results, we only scan over the sidebands and

choose the pulse length to be that of a blue sideband π pulse. At very low temperatures, the carrier flops are not a sensitive measure anymore while the difference in sideband height has high sensitivity.

Figure 7.7 shows fitted sideband scans for different stages of sideband cooling. Starting from just after Doppler pre-cooling where R yields a result consistent with the carrier flopping data, $\bar{n} = 5.25$ we reach $\bar{n} = 0.27$ after ten sideband cooling pulses of length $t_\pi = 3.6\,\mu$s. After that, we performed a time scan on the blue sideband to determine a new approximate sideband π time for the now colder ion, $t_\pi = 8.0\,\mu$s. We then added another ten red sideband pulses of $t_\pi = 8.0\,\mu$s resulting in successful ground state cooling with a final mean occupation number of $\bar{n} = 0.058$, see fig. 7.7d.

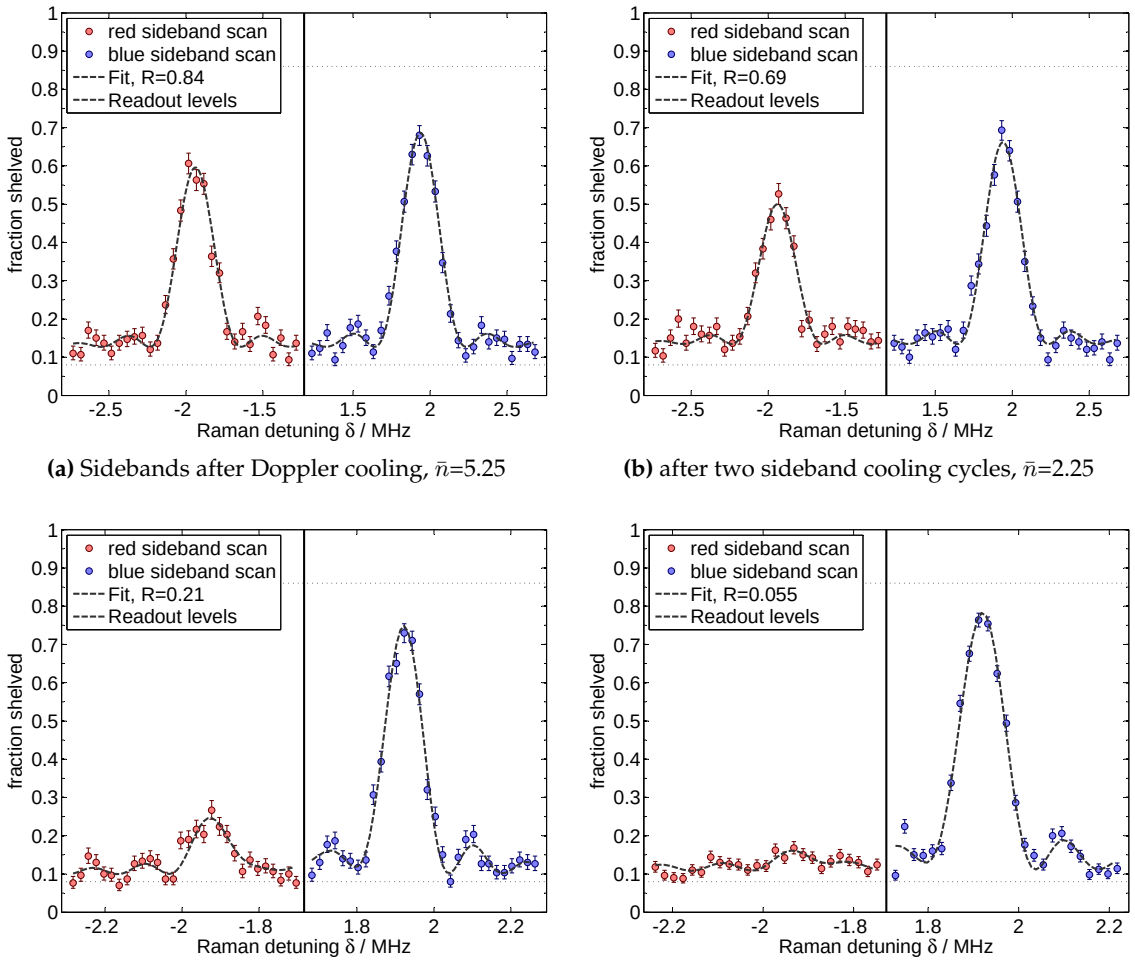

(a) Sidebands after Doppler cooling, $\bar{n}$=5.25

(b) after two sideband cooling cycles, $\bar{n}$=2.25

(c) after ten sideband cooling cycles, $\bar{n}$=0.27

(d) after twenty sideband cooling cycles, $\bar{n}$=0.058

Figure 7.7: Four sideband scans showing the sideband cooling process. (a) shows a sideband scan after Doppler cooling. Both sidebands are simultaneously fitted with eq. 7.12. Figures (b) to (d) are repeats of the scan for an increasing number of sideband cooling pulses. The captions show the mean Fock state occupation number $\bar{n}$ calculated from the fitted R by eq. 7.11. For (c) and (d) the carrier term was included since it was found to improve the fits. This demonstrates cooling very close to the ground state.

7.3.3 Trap heating rate

We performed temperature measurements by sideband height comparison for a series of different delay times after sideband cooling. From the increasing temperature, the trap heating rate can be inferred through a linear fit. This is shown in figure 7.8 where fit gives a heating rate of about one motional quantum per second, $H_R = 0.97\,\mathrm{s}^{-1}$. With our trap frequency of $\omega_z = 2\pi \cdot 1.98$ MHz, this corresponds to a product of spectral noise density (see section 2.6.4) and trap frequency of $\omega_z S_E(\omega_z) = 1.65 \cdot 10^{-7}$ V/m. The international comparison in figure 2.31 shows this value to be below average for our ion-to-electrode distance of $500\ \mu$m. Given the smaller size, the trap also outperforms the previous trap (see section 4.1) in terms of the heating rate. As opposed to the fits in fig. 7.7, this data was taken by recording a series of low shot-noise points (typically 2000 experiments each) on both sidebands together with a zero length pulse $t_p = 0$ to measure the baseline. The levels are then compared to give R.

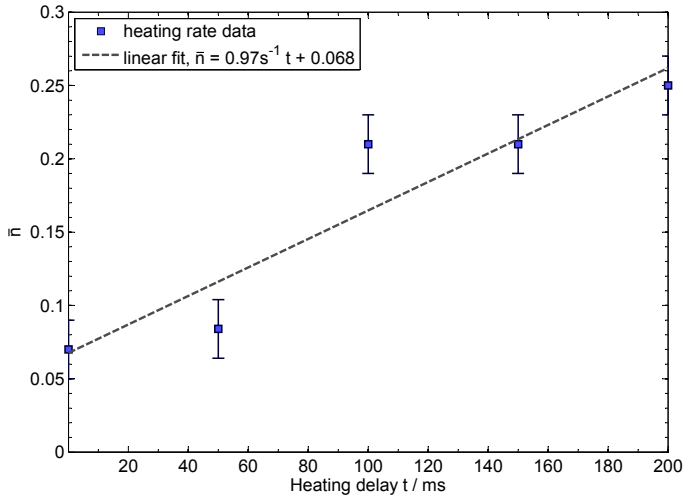

Figure 7.8: Temperature data measured after sideband cooling followed by a variable heating delay time. $\bar{n}$ was determined by comparing the height of the red and blue sideband (see eq. 7.11). A straight line fit shows the heating rate to be ~ 1 quantum per second.

7.3.4 Mixed species crystal ground state cooling

We apply the same cooling method to a crystal consisting of one $^{40}Ca^+$ and one $^{43}Ca^+$ ion. In the cooling experiments presented here we only drive transitions on $^{40}Ca^+$ to cool the crystal. The $^{43}Ca^+$ ion acts as a spectator without having coherent manipulations applied. There are two axial modes, the centre of mass (COM) and the stretch mode (str). The cooling procedure is set up analogously to the one-ion case but with each of the modes being cooled in turn during a cycle. After Doppler cooling we find the times for a π-pulse on the red sideband to be $5\ \mu$s for the COM mode and $9\ \mu$s for the stretch mode. After ten sideband cooling pulses, we repeat the procedure (this time on the blue sideband, see

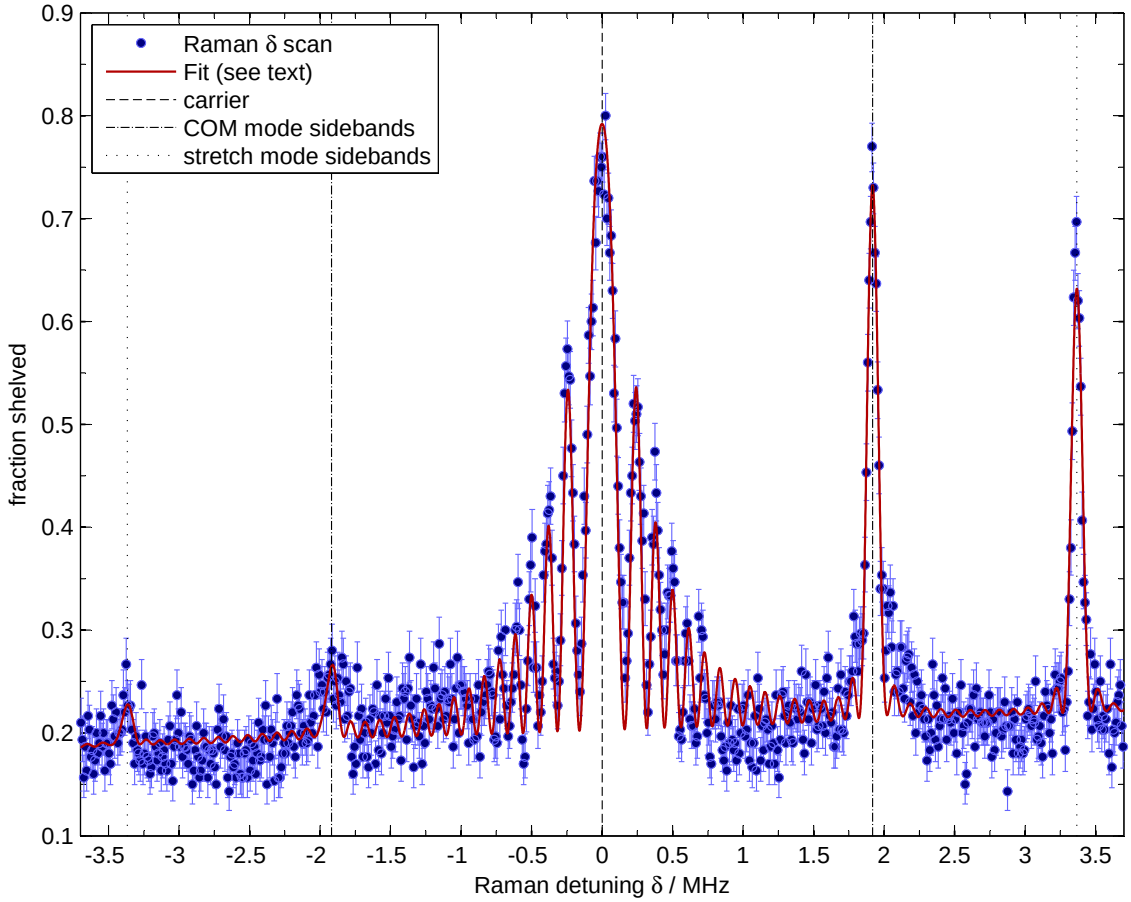

Figure 7.9: Raman detuning scan over the first sidebands of each mode of a $^{40}Ca^{+}$-$^{43}Ca^{+}$ crystal. The data was taken with a probe pulse length of $11.4\,\mu$s, strongly overdriving the carrier. The data was fitted with a five-term version of eq. 7.12 with an additional parameter to take the baseline drift into account. The resulting sideband frequencies are $f_{z,COM} = 1.919$ MHz and $f_{z,str} = 3.37$ MHz.

above) and find $t_\pi = 11.5\,\mu$s and $16\,\mu$s for the COM and stretch mode respectively. We then extend the sequence by another 5 pulses on each mode.

A full Raman detuning scan over the first sidebands on each mode is shown in figure 7.9. The chosen probe pulse time $11.4\,\mu$s is a compromise which resolves the sidebands but overdrives the carrier. The plot also shows the fit of a five-term version of eq. 7.12. It gives the sideband frequencies as $f_{z,COM} = 1.919$ MHz and $f_{z,str} = 3.37$ MHz.

The frequency of the two modes is different from a single species crystal where we would expect $f_{z,COM} = f_z$ and $f_{z,str} = \sqrt{3} f_z$ because of the different charge-to-mass ratio of the $^{43}Ca^{+}$ ion. For a crystal consisting of two ions with a mass ratio $\mu = m_1/m_2$, the mode frequencies are [167]:

$$f_{z,COM} = \sqrt{\frac{1+\mu-\sqrt{1-\mu+\mu^2}}{\mu}}\, f_z$$
$$f_{z,str} = \sqrt{\frac{1+\mu+\sqrt{1-\mu+\mu^2}}{\mu}}\, f_z \tag{7.13}$$

In our case, with $\mu = 43/40$ and $f_z = 1.98$ MHz, we get:

$$f_{z,COM} = 1.943\,\text{MHz} \qquad f_{z,str} = 3.370\,\text{MHz} \tag{7.14}$$

which agrees well with our fitted peaks from fig.7.9. The sideband ratios obtained suggest $\bar{n} \simeq 0.1$ on both modes, but the data quality is not very good and the pulse time was not optimized for each of the modes. In order to get a better estimate, we performed sideband scans in the same way as shown in fig. 7.7 on the two modes. The data and fits are presented in figure 7.10. The fits show that we can cool the two modes of a $^{40}Ca^{+}$-$^{43}Ca^{+}$ crystal close to the ground state with similar $\bar{n}$ than was a achieved for a single $^{40}Ca^{+}$ ion. Since the modes have different frequencies, it is also interesting to compare the equivalent temperatures, $T = (\bar{n}\,\hbar\,2\pi f_m)\,/k_B$. They are $6.9\,\mu$K for the COM and $5.2\,\mu$K for the stretch mode. We do not expect these to be exactly the same since the modes do not couple to each other and each is cooled by its own tailored pulse sequence, but we reach similar final values for both. Performing the twenty cooling cycles necessary to achieve our results takes ~ 0.5 ms per mode.

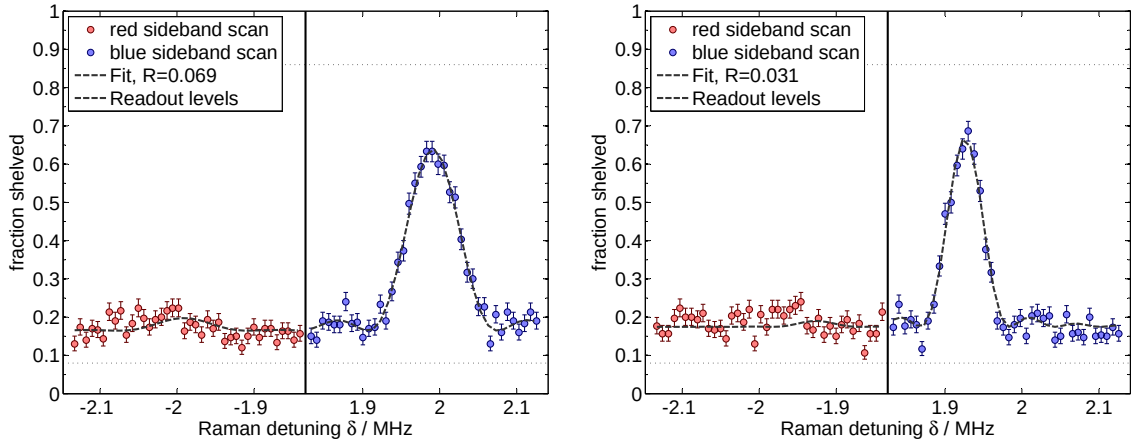

(a) COM mode after sideband cooling, $\bar{n}$=0.074 **(b)** stretch mode after sideband cooling, $\bar{n}$=0.032

Figure 7.10: Two sideband scans showing the COM (a) and stretch (b) modes of a $^{40}Ca^{+}$-$^{43}Ca^{+}$ crystal. Both modes were cooled with 15 interleaved sideband cooling cycles (see text). The captions show the mean Fock state occupation number $\bar{n}$ calculated by eq. 7.11 from the fitted R (using eq. 7.12 for the fit). This demonstrates cooling of both axial modes very close to the ground state.

7.4 Summary

This chapter presented ground state cooling of single ions as well as a mixed species crystal. This is achieved by Doppler cooling followed by pulsed sideband cooling. By analyzing thermal state carrier flops, the Doppler cooling step was shown to achieve temperatures close to the Doppler limit. Using this as a starting point, pulsed sideband cooling was implemented with the Raman laser system presented in chapter 5 to cool the axial motion of a single ion to the ground state. We achieved a final mean occupation number of $\bar{n} = 0.058$. This result is a typical value for trapped calcium experiments. J. Benhelm et al. report cooling the axial mode ($f_z = 1.2$ MHz) of a single $^{43}Ca^+$ ion to $\bar{n} = 0.06$ [157]. The Mainz group has cooled single $^{40}Ca^+$ ions to $\bar{n} < 0.1$ in a 1.4 MHz axial trap [77]. Similar values are achieved with other species such as beryllium ($\bar{n} = 0.06$, $f_z = 3$ MHz [170]) and magnesium ($\bar{n} = 0.03$, $f_z = 2$ MHz [171]).

After sideband cooling, the temperature measurement was used to determine the heating rate of our trap to be 1 motional quantum per second. This value is relatively low for the trap's ion-to-electrode distance as can be seen from the comparison with other results in figure 2.31. It also outperforms the previous macroscopic trap experiment in our group.

Finally, the chapter demonstrated ground state cooling of both axial modes of motion of a mixed-species two-ion crystal of $^{40}Ca^+$ and $^{43}Ca^+$. We reach $\bar{n} = 0.074$ and $\bar{n} = 0.032$ on the COM and stretch mode respectively. Other groups have reported similar results for two-ion crystals. The Innsbruck group reports cooling of same-species two-ion crystals of calcium trapped with $f_z = 1.2$ MHz to $\bar{n}_{COM} = 0.03$ and $\bar{n}_{str} = 0.4$ for $^{43}Ca^+$ [158] and to $\bar{n} < 0.05$ on both modes for $^{40}Ca^+$ [28]. Results from NIST taken with a mixed species crystal of $^{9}Be^+$ and $^{24}Mg^+$ in a 2 MHz axial trap give $\bar{n}_{COM} = 0.03$ and $\bar{n}_{str} = 0.04$ when cooling the beryllium ion, and $\bar{n}_{COM} = 0.2$ and $\bar{n}_{str} = 0.5$ when cooling magnesium [127][4]. They have also cooled crystals of aluminium and beryllium as well as aluminium and magnesium for their atomic clock and quantum logic spectroscopy to $\bar{n} < 0.05$ [160, 161]. All of these results were reached on typical timescales of between 1 and 10 ms of cooling. Here, our system compares well (~ 0.5 ms per mode) due to the short pulse lengths driven with the high power Raman lasers.

The ground state cooling of a mixed species crystal described in this chapter lays the foundation for future experiments in this trap, in particular setting up coherent superpositions of motional states as a next step towards a mixed-species two-qubit entangling gate.

[4] for ion crystals with different masses it is strictly no longer valid to speak of the "COM"/"stretch" mode since the ions don't oscillate exactly in/out-of phase

Chapter 8

Conclusion and Outlook

The first half of this thesis was concerned with scalability which is one of the key requirements for quantum computing. Firstly, we presented the assembly of a microfabricated linear Paul trap with multiple zones. Ions were successfully trapped and the micromotion compensated in one of the zones. The trap was characterized and compared to a numerical model of the electric fields. The heating rate due to electric field noise was found to be consistent with similar traps. While the trap could be used for further studies of ion shuttling, the issues encountered and the developments made in other groups (particularly in the design of junctions [73, 107, 83]) suggest an updated trap design to be the most advantageous next step in this direction. Trap fabrication efforts in our group currently focus on surface traps [103] with the aim of implementing high fidelity gates and individual addressing of ions with microwave fields. The project will soon include the ability to cryogenically cool the trap using liquid nitrogen or helium. This will not only increase the ion lifetime by improving the vacuum but also lower the heating rate (compare fig. 2.31). Additionally, the higher conductivity of the trap electrodes when cold means that higher microwave currents can be used to increase gate speeds without thermally damaging the trap.

Secondly, we introduced and demonstrated two techniques to advance trapped ion experiments in the presence of high background scatter which is a particular issue in miniaturized geometries. We presented several repumping techniques which showed background-free detection of ions by separating in frequency the light used to excite from the light used to observe the ions. As discussed in chapter 3, this is readily extendable to other ions with low-lying D states and will be useful for a number of experiments where ions are trapped in close proximity to surfaces. In addition, this work has opened up an interesting study of a system of multiple interconnected states in $^{40}Ca^{+}$ which we are currently pursuing. Since the filter used allows fluorescence decay on the $393\,$nm transition to be detected exclusively, we have a direct measure of the $P_{3/2}$ population. The top plot in figure 8.1 shows such fluorescence data under variation of the 866 nm and 850 nm detunings. The 854nm and 397nm lasers were held constant. The multiple excitation paths from the ground state to the $P_{3/2}$ state give rise to a rich structure of dark and bright resonances.

Hugo Janacek has started to analyze and model this system using the optical Bloch equations. A preliminary result can be seen in figure 8.1. Even though the data was taken in the old trap without intensity stabilization on the lasers, agreement at the 10% level has been achieved. More data varying the other parameters involved (particularly the beam intensities) will have to be taken and detailed results will be reported shortly [123].

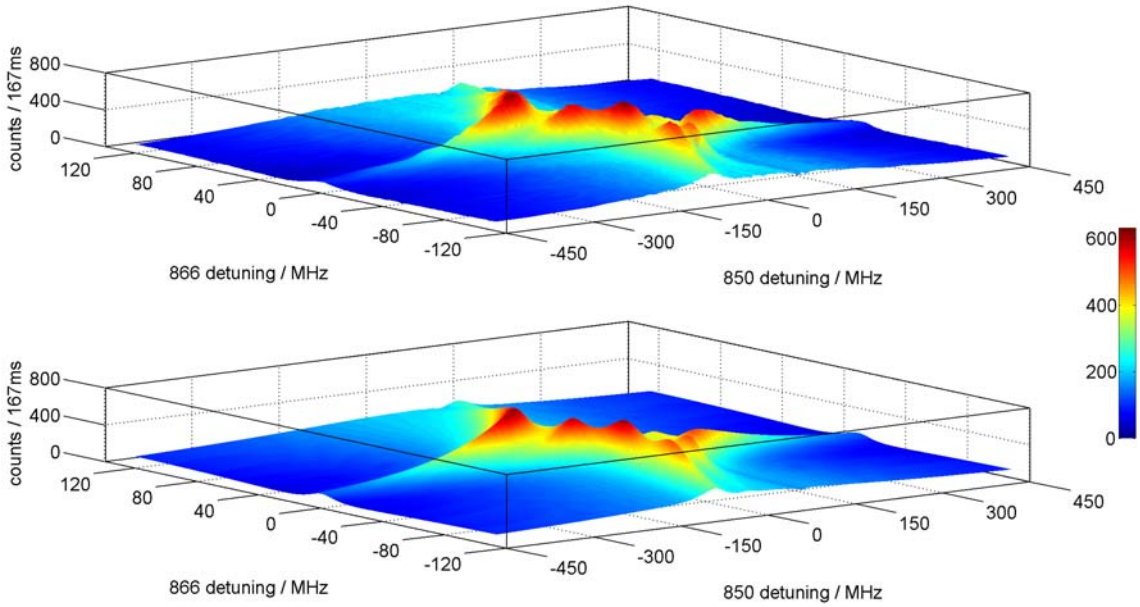

Figure 8.1: *Top*: Experimentally measured fluorescence on the 393 nm transition for different 850 and 866 nm laser detunings. The 854 and 397 nm laser detunings were held constant. *Bottom*: Fit of a Bloch equations model to the data. All dark and bright resonance features are reproduced to a high level of agreement.

The experiments presented on background-free readout of trapped ions have shown that it is possible to perform high-fidelity qubit readout in the presence of large background scatter by again separating excitation and detection but in this case in time rather than frequency. This may be an important technique for quantum computing in scalable miniaturized geometries. The results presented only establish a proof of principle, however. We obtained a high signal-to-noise ratio (much higher than without employing the scheme) but since the repetition rate we could achieve was relatively low, the ion signal obtained was small. This meant that the readout fidelity which depends on both of these parameters was not yet higher than for standard readout. As described in section 3.2.4, the PMT dark count behaviour imposes a limit on the performance. The use of a different detector is being investigated. Making the sequence a factor of ~ 10 faster would allow us to surpass the standard method in the presence of scatter at the levels used for the experiment.

The second half of this thesis described our efforts towards implementing an entangling phase gate between two different isotopes of calcium. We have successfully set up a

new experiment with a macroscopic linear Paul trap. The trap has been characterized and shown to reliably load and crystallize a mixed species pair of calcium ions. We have also demonstrated single-qubit rotations with microwaves and radio frequency respectively as well as the first implementation of independent simultaneous readout of two qubits in a mixed-species ion crystal.

One of the key features of the experimental setup are the new Raman lasers. We have realized an injection-locking scheme that allows us to switch between the relative detunings for $^{40}Ca^{+}$ and $^{43}Ca^{+}$ and provides all the beam directions and polarization combinations needed for the single and two-qubit operations required for sideband cooling and an entangling gate. The relative linewidth was measured to be well in the sub-Hz range which proves the interferometric stability needed to drive Raman transitions. This was subsequently performed on all three qubits we use in the two isotopes. We have also confirmed the correct scaling of the errors introduced by the lasers through off-resonant Raman scattering in a single qubit experiment and shown single qubit rotations with the injected systems on both isotopes, including the clock-state qubit.

Driving motional transitions is crucial for the gate. This has been demonstrated in chapter 7 both for a single ion and for a mixed-species crystal where we were able to cool both axial modes very close to the ground state with a two-stage process consisting of Doppler cooling close to the Doppler limit followed by pulsed sideband cooling with the Raman lasers. We have thereby made a first step towards precisely manipulating the motional state of the ion crystal. The next stage will be to perform experiments on motional coherence by generating motionally entangled states and measuring their coherence time.

One technical issue that has been discovered is beam pointing noise out of the doubling cavities of the Raman lasers. This is being addressed with the introduction of a pair of optical fibres. With these in place we should be able to perform single-qubit gates with fidelities beyond the fault-tolerance threshold based on photon scattering error. Together with the motional manipulations we have started to implement, these will form the basis of the entangling gate on a mixed-species crystal. The characterization will be done by state tomography which can be performed in full since we have the capability to read out each ion separately.

Bibliography

[1] J. Bardeen and W. H. Brattain. The transistor, a semi-conductor triode. *Phys. Rev.*, 74:230–231, Jul 1948. [cited at p. 1]

[2] R. P. Feynman. Simulating physics with computers. *International Journal of Theoretical Physics*, 21(6/7):467–488, 1982. [cited at p. 1]

[3] D. Deutsch. Quantum computational networks. *Proc. Roy. Soc.*, 425(1868):79–90, 1989. [cited at p. 1]

[4] D. P. Vincenzo. The physical implementation of quantum computation. *Fortschritte der Physik*, 48:771–783, 2000. [cited at p. 1, 7]

[5] R. Ursin, F. Tiefenbacher, T. Schmitt-Manderbach, H. Weier, T. Scheidl, M. Lindenthal, B. Blauensteiner, T. Jennewein, J. Perdigues, P. Trojek, B. Ömer, M. Fürst, M. Meyenburg, J. Rarity, Z. Sodnik, C. Barbieri, H. Weinfurter, and A. Zeilinger. Entanglement-based quantum communication over 144 km. *Nature Physics*, 422:481–486, June 2007. [cited at p. 2]

[6] T. D. Ladd, F. Jelezko, R. Laflamme, Y. Nakamura, C. Monroe, and J. L. O'Brien. Quantum computers. *Nature*, 464:45, 2010. [cited at p. 2]

[7] I. Marzoli, P. Tombesi, G. Ciaramicoli, G. Werth, P. Bushev, S. Stahl, F. Schmidt-Kaler, M. Hellwig, C. Henkel, G. Marx, I. Jex, E. Stachowska, G. Szawiola, and A. Walaszyk. Experimental and theoretical challenges for the trapped electron quantum computer. *Journal of Physics B*, 42:154010, 2009. [cited at p. 2]

[8] M. Himsworth, P. Nisbet, J. Dilley, G. Langfahl-Klabes, and A. Kuhn. EIT-based quantum memory for single photons from cavity-QED. *Applied Physics B: Lasers and Optics*, 103:579–589, 2011. 10.1007/s00340-011-4523-2. [cited at p. 2]

[9] Jonathan A. Jones. Quantum computing with NMR. *Progress in Nuclear Magnetic Resonance Spectroscopy*, 59(2):91 – 120, 2011. [cited at p. 2]

[10] M.L. Markham, J.M. Dodson, G.A. Scarsbrook, D.J. Twitchen, G. Balasubramanian, F. Jelezko, and J. Wrachtrup. Cvd diamond for spintronics. *Diamond and Related Materials*, 20(2):134 – 139, 2011. [cited at p. 2]

[11] Søren Stobbe Peter Lodahl. Solid-state quantum optics with quantum dots in photonic nanostructures. *arXiv:1211.7250*, Nov 2012. [cited at p. 2]

[12] L. DiCarlo, M. D. Reed, L. Sun, B. R. Johnson, J. M. Chow, J. M. Gambetta, L. Frunzio, S. M. Girvin, M. H. Devoret, and R. J. Schoelkopf. Preparation and measurement of three-qubit entanglement in a superconducting circuit. *Nature*, 467:574–578, Sept. 2010. [cited at p. 2]

[13] Jerry M. Chow, Jay M. Gambetta, A. D. Córcoles, Seth T. Merkel, John A. Smolin, Chad Rigetti, S. Poletto, George A. Keefe, Mary B. Rothwell, J. R. Rozen, Mark B.

Ketchen, and M. Steffen. Universal quantum gate set approaching fault-tolerant thresholds with superconducting qubits. *Phys. Rev. Lett.*, 109:060501, Aug 2012. [cited at p. 2]

[14] Chad Rigetti, Jay M. Gambetta, Stefano Poletto, B. L. T. Plourde, Jerry M. Chow, A. D. Córcoles, John A. Smolin, Seth T. Merkel, J. R. Rozen, George A. Keefe, Mary B. Rothwell, Mark B. Ketchen, and M. Steffen. Superconducting qubit in a waveguide cavity with a coherence time approaching 0.1 ms. *Phys. Rev. B*, 86:100506, Sep 2012. [cited at p. 2]

[15] H. Häffner, C. F. Roos, and R. Blatt. Quantum computing with trapped ions. *Physics Reports*, 469:155, 2008. [cited at p. 3]

[16] D. T. C. Allcock, T. P. Harty, C. J. Ballance, B. C. Keitch, N. M. Linke, D. N. Stacey, and D. M. Lucas. A microfabricated ion trap with integrated microwave circuitry. *arXiv:1210.3272*, Oct 2012. [cited at p. 3, 5, 47]

[17] C. F. Roos, M. Chwalla, K. Kim, M. Riebe, and R. Blatt. 'Designer atoms' for quantum metrology. *Nature*, 443:316, 2006. [cited at p. 3, 4]

[18] C. Langer, R. Ozeri, J. D. Jost, J. Chiaverini, B. DeMarco, A. Ben-Kish, R. B. Blakestad, J. Britton, D. B. Hume, W. M. Itano, D. Leibfried, R. Reichle, T. Rosenband, T. Schaetz, P. O. Schmidt, and D. J. Wineland. Long-lived qubit memory using atomic ions. *Phys. Rev. Lett.*, 95:060502, Aug 2005. [cited at p. 3]

[19] D. T. C Allcock, T. P. Harty, D. M. Lucas, and et al. publication in preparation. 2013. [cited at p. 3, 5, 6, 9]

[20] A. H. Myerson, D. J. Szwer, S.C. Webster, D. T. C. Allcock, M. J. Curtis, G. Imreh, J. A. Sherman, D. N. Stacey, A. M. Steane, and D. M. Lucas. High-fidelity readout of trapped-ion qubits. *Phys. Rev. Lett.*, 100:200502, May 2008. [cited at p. 3, 66, 121, 132]

[21] D. J. Szwer. *High Fidelity Readout and Protection of a $^{43}Ca^{+}$ Trapped Ion Qubit*. D.Phil. thesis, University of Oxford, 2009. [cited at p. 3, 4, 8, 59, 67, 72, 73, 108, 109, 121, 123, 124, 133, 175, 181]

[22] J. I. Cirac and P. Zoller. Quantum computations with cold trapped ions. *Physical Review Letters*, 74(20):4091, 1995. [cited at p. 3]

[23] F. Schmidt-Kaler, H. Häffner, M. Riebe, S. Gulde, G. P. T. Lancaster, T. Deuschle, C. Becher, C. F. Roos, J. Eschner, and R. Blatt. Realization of the Cirac-Zoller controlled-not quantum gate. *Nature*, 422:408, 2003. [cited at p. 3]

[24] A. Sørensen and K. Mølmer. Quantum computation with ions in thermal motion. *Physical Review Letters*, 8(9):1971, 1999. [cited at p. 3]

[25] A Sørensen and K Mølmer. Entanglement and quantum computation with ions in thermal motion. *Physical Review A*, 62(2), Aug 2000. [cited at p. 3]

[26] C. A. Sackett, D. Kielpinski, B. E. King, C. Langer, V. Meyer, C. J. Myatt, M. Rowe, Q. A. Turchette, W. M. Itano, D. J. Wineland, and C. Monroe. Experimental entanglement of four particles. *Nature*, 404:256, 2000. [cited at p. 3]

[27] D. Leibfried, B. DeMarco, V. Meyer, D. Lucas, M. Barrett, J. Britton, W. M. Itano, B. Jelenkovic, C. Langer, T. Rosenband, and D. J. Wineland. Experimental demonstration of a robust, high-fidelity geometric two ion-qubit phase gate. *Nature*, 422(6930):412–415, MAR 27 2003. [cited at p. 3]

[28] J. Benhelm, G. Kirchmair, C. F. Roos, and R. Blatt. Towards fault-tolerant quantum computing with trapped ions. *Nature Physics*, 4(6):463–466, June 2008. [cited at p. 3, 121, 133, 148]

[29] J P Home, M J McDonnell, D M Lucas, G Imreh, B C Keitch, D J Szwer, N R Thomas, S C Webster, D N Stacey, and A M Steane. Deterministic entanglement and tomography of ion-spin qubits. *New Journal of Physics*, 8(9), 2006. [cited at p. 4, 67, 102, 103]

[30] J. Home. *Entanglement of Two Trapped-Ion Spin Qubits*. D.Phil. thesis, University of Oxford, 2006. [cited at p. 4, 135, 137, 142]

[31] M. Riebe, H. Häffner, C. F. Roos, W. Hänsel, J. Benhelm, G. P. T. Lancaster, T. W. Körber, C. Becher, F. Schmidt-Kaler, D. F. V. James, and R. Blatt. Deterministic quantum teleportation with atoms. *Nature*, 429(6993):734–737, June 2004. [cited at p. 4]

[32] M. D. Barrett, J. Chiaverini, T. Schaetz, J. Britton, W. M. Itano, J. D. Jost, E. Knill, C. Langer, D. Leibfried, R. Ozeri, and D. J. Wineland. Deterministic quantum teleportation of atomic qubits. *Nature*, 429(6993):737–739, June 2004. [cited at p. 4]

[33] M. Riebe, T. Monz, K. Kim, A. S. Villar, P. Schindler, M. Chwalla, M. Hennrich, and R. Blatt. Deterministic entanglement swapping with an ion-trap quantum computer. *Nature Physics*, 4:5.6–842, Oct 2008. [cited at p. 4]

[34] S. Gulde, M. Riebe, G. P. T. Lancaster, C. Becher, J. Eschner, H. Häffner, F. Schmidt-Kaler, I. L. Chuang, and R. Blatt. Implementing the Deutsch-Jozsa algorithm on an ion-trap quantum computer. *Nature*, 422:408, 2003. [cited at p. 4, 6, 68]

[35] J. Chiaverini, J. Britton, D. Leibfried, E. Knill, M. D. Barrett, R. B. Blakestad, W. M. Itano, J. D. Jost, C. Langer, R. Ozeri, T. Schaetz, and D. J. Wineland. Implementation of the semiclassical quantum Fourier transform in a scaleable system. *Science*, 308:997, 2005. [cited at p. 4]

[36] K.-A. Brickman, P. C. Haljan, P. J. Lee, M. Acton, L. Deslauriers, and C. Monroe. Implementation of Grover's quantum search algorithm in a scalable system. *Physical Review A*, 72:050306, 2005. [cited at p. 4]

[37] P. Schindler, J. T. Barreiro, T. Monz, V. Nebendahl, D. Nigg, M. Chwalla, M. Hennrich, and R. Blatt. Experimental repetitive quantum error correction. *Science*, 332(6033):1059–1061, Mar 2011. [cited at p. 4]

[38] J. Chiaverini, D. Leibfried, T. Schaetz, M. D. Barrett, R. B. Blakestad, J. Britton, W. M. Itano, J. D. Jost, E. Knill, C. Langer, R. Ozeri, and D. J. Wineland. Realization of quantum error correction. *Nature*, 432:602, 2004. [cited at p. 4]

[39] R. Islam, E. E. Edwards, K. Kim, S. Korenblit, C. Noh, H. Carmichael, G.-D. Lin, L.-M. Duan, C.-C. Joseph Wang, J. K. Freericks, and C. Monroe. Onset of a quantum phase transition with a trapped ion quantum simulator. *Nature Communications*, 2:377, 2011. [cited at p. 4]

[40] R. Gerritsma, G. Kirchmair, F. Zähringer, E. Solano, R. Blatt, and C. F. Roos. Quantum simulation of the dirac equation. *Nature*, 463:68, 2010. [cited at p. 4]

[41] B. P. Lanyon, C. Hempel, D. Nigg, M. Müller, R. Gerritsma, F. Zähringer, P. Schindler, J. T. Barreiro, M. Rambach, G. Kirchmair, M. Hennrich, P. Zoller, R. Blatt, and C. F. Roos. Universal digital quantum simulation with trapped ions. *Science*, 334:57, 2011. [cited at p. 4]

[42] C. W. Chou, D. B. Hume, J. C. J. Koelemeij, D. J. Wineland, and T. Rosenband. Frequency comparison of two high-accuracy Al^+ optical clocks. *Phys. Rev. Lett.*, 104:070802, Feb 2010. [cited at p. 4]

[43] D. Leibfried, M. D. Barrett, T. Schaetz, J. Britton, J. Chiaverini, W. M. Itano, J. D. Jost, C. Langer, and D. J. Wineland. Toward heisenberg-limited spectroscopy with multiparticle entangled states. *Science*, 304(5676):1476–1478, 2004. [cited at p. 4]

[44] D. J. Wineland and D. Leibfried. Quantum information processing and metrology with trapped ions. *Laser Phys. Lett.*, 8(3):175–188, Jan 2011. [cited at p. 4]

[45] S. Kotler, N. Akerman, Y. Glickman, A. Keselman, and R. Ozeri. Single-ion quantum lock-in amplifier. *Nature*, 473:61–65, May 2011. [cited at p. 4]

[46] B. Hemmerling, F Gebert, Y. Wan, and P. O. Schmidt. A novel, robust quantum detection scheme. *New Journal of Physics*, 14(2):023043, 2012. [cited at p. 4]

[47] R. Blatt and D. J. Wineland. Entanglement, state manipulation and quantum-limited metrology with trapped ions. *available online*, 2008. [cited at p. 4]

[48] Andrew M. Steane. How to build a 300 bit, 1 giga-operation quantum computer. *Quantum Info. Comput.*, 7(3):171–183, March 2007. [cited at p. 4]

[49] A. M. Steane. Overhead and noise threshold of fault-tolerant quantum error correction. *Phys. Rev. A*, 68(4):042322, Oct 2003. [cited at p. 5]

[50] R. Raussendorf. Key ideas in quantum error correction. *Phil. Trans. R. Soc. A*, 370(1975):4541–4565, Sept 2012. [cited at p. 5]

[51] M. J. McDonnell, J.-P. Stacey, S. C. Webster, J. P. Home, A. Ramos, D. M. Lucas, D. N. Stacey, and A. M. Steane. High-efficiency detection of a single quantum of angular momentum by suppression of optical pumping. *Phys. Rev. Lett.*, 93:153601, Oct 2004. [cited at p. 5, 122, 133]

[52] E. Knill, D. Leibfried, R. Reichle, J. Britton, R. B. Blakestad, J. D. Josta, C. Langer, R. Ozeri, S. Seidelin, and D. J. Wineland. Randomized benchmarking of quantum gates. *Physical Review A*, 77:012307, 2008. [cited at p. 5]

[53] D. Hayes, D. N. Matsukevich, P. Maunz, D. Hucul, Q. Quraishi, S. Olmschenk, W. Campbell, J. Mizrahi, C. Senko, and C. Monroe. Entanglement of atomic qubits using an optical frequency comb. *Phys. Rev. Lett.*, 104:140501, Apr 2010. [cited at p. 5]

[54] C. Ospelkaus, C. E. Langer, J. M. Amini, K. R. Brown, D. Leibfried, and D. J. Wineland. Trapped-ion quantum logic gates based on oscillating magnetic fields. *Physical Review Letters*, 101:090502, 2008. [cited at p. 5]

[55] K. R. Brown, A. C. Wilson, Y. Colombe, C. Ospelkaus, A. M. Meier, E. Knill, D. Leibfried, and D. J. Wineland. Single-qubit-gate error below 10^{-4} in a trapped ion. *Physical Review A*, 84:030303, 2011. [cited at p. 5]

[56] W. C. Campbell, J. Mizrahi, Q. Quraishi, C. Senko, D. Hayes, D. Hucul, D. N. Matsukevich, P. Maunz, and C. Monroe. Ultrafast gates for single atomic qubits. *Phys. Rev. Lett.*, 105:090502, Aug 2010. [cited at p. 6]

[57] C. Senko, J. Mizrahi, W. C. Campbell, K. G. Johnson, C. W. S. Conover, and C. Monroe. Ultrafast spin-motion entanglement and interferometry with a single atom. *arXiv:1201.6597v1*, Jan 2012. [cited at p. 6]

[58] T. Monz, K. Kim, A. Villar, P. Schindler, M. Chwalla, M. Riebe, C. F. Roos, H. Häffner, W Hänsel, M. Hennrich, and R. Blatt. Realization of universal ion-trap quantum computation with decoherence-free qubits. *Physical Review Letters*, 103:200503, 2009. [cited at p. 6]

[59] D J Szwer, S C Webster, A M Steane, and D M Lucas. Keeping a single qubit alive by experimental dynamic decoupling. *Journal of Physics B: Atomic, Molecular and Optical Physics*, 44(2):025501, 2011. [cited at p. 6]

[60] Thomas Monz, Philipp Schindler, Julio T. Barreiro, Michael Chwalla, Daniel Nigg, William A. Coish, Maximilian Harlander, Wolfgang Hänsel, Markus Hennrich, and Rainer Blatt. 14-qubit entanglement: Creation and coherence. *Phys. Rev. Lett.*, 106:130506, Mar 2011. [cited at p. 6]

[61] M. Harlander. *Architecture for a scalable ion-trap quantum computer*. PhD thesis, Universität Innsbruck, 2012. [cited at p. 6]

[62] G.-D. Lin, S.-L. Zhu, R. Islam, K. Kim, M.-S. Chang, S. Korenblit, C. Monroe, and L.-M. Duan. Large-scale quantum computation in an anharmonic linear ion trap. *Europhys. Lett.*, 86(6):60004, Jun 2009. [cited at p. 6]

[63] S. X. Wang, J. Labaziewicz, Y. Ge, R. Shewmon, and I. L. Chuang. Individual addressing of ions using magnetic field gradients in a surface-electrode ion trap. *Appl. Phys. Lett.*, 94(9):094103, 2009. [cited at p. 7]

[64] K. Wang, M. Johanning, M. Feng, F. Mintert, and C. Wunderlich. Quantum gates using electronic and nuclear spins of Yb^+ in a magnetic field gradient. *The European Physical Journal D - Atomic, Molecular, Optical and Plasma Physics*, 63:157–164, 2011. 10.1140/epjd/e2011-20108-2. [cited at p. 7]

[65] D. L. Moehring, P. Maunz, S. Olmschenk, K. C. Younge, D. N. Matsukevich, L.M. Duan, and C. Monroe. Entanglement of single-atom quantum bits at a distance. *Nature*, 449:68, 2007. [cited at p. 7]

[66] G. Shu, C.-K. Chou, N. Kurz, M.R. Dietrich, and Blinov B.B. Ultrafast spin-motion entanglement and interferometry with a single atom. *JOSA B*, 28:2865–2870, 2011. [cited at p. 7]

[67] A. Dantan, J. P. Marler, M. Albert, D. Guénot, and M. Drewsen. Noninvasive vibrational mode spectroscopy of ion Coulomb crystals through resonant collective coupling to an optical cavity field. *Physical Review Letters*, 105(10):103001, 2010. [cited at p. 7]

[68] David R. Leibrandt, Jaroslaw Labaziewicz, Vladan Vuletić, and Isaac L. Chuang. Cavity sideband cooling of a single trapped ion. *Phys. Rev. Lett.*, 103(10):103001, Aug 2009. [cited at p. 7]

[69] M. Keller, B. Lange, K. Hayasaka, W. Lange, and H. Walther. Stable long-term coupling of a single ion to a cavity mode. *Jour. Mod. Opt.*, 54(11):1607–1617, Jan 2007. [cited at p. 7]

[70] J. D. Sterk, L. Luo, T. A. Manning, P. Maunz, and C. Monroe. Photon collection from a trapped ion-cavity system. *Phys. Rev. A*, 85:062308, Jun 2012. [cited at p. 7]

[71] M. Harlander, R. Lechner, M. Brownnutt, R. Blatt, and W. Hnsel. Trapped-ion antennae for the transmission of quantum information. *Nature*, 471:200–203, March 2011. [cited at p. 7, 46]

[72] M. D. Barrett, J. Chiaverini, T. Schaetz, J. Britton, W. M. Itano, J. D. Jost, E. Knill, C. Langer, D. Leibfried, R. Ozeri, and D. J. Wineland. Deterministic quantum teleportation of atomic qubits. *Nature*, 429(6993):737, Jun 2004. [cited at p. 7]

[73] R. B. Blakestad, C. Ospelkaus, A. P. VanDevender, J. M. Amini, J. Britton, D. Leibfried, and D. J. Wineland. High-fidelity transport of trapped-ion qubits through an **X**-junction trap array. *Phys. Rev. Lett.*, 102:153002, Apr 2009. [cited at p. 7, 48, 149]

[74] D. L. Moehring, C. Highstrete, D. Stick, K. M. Fortier, R. Haltli, C. Tigges, and M. G. Blain. Design, fabrication and experimental demonstration of junction surface ion traps. *New Journal of Physics*, 13(7), 2011. [cited at p. 7]

[75] F. Splatt, M. Harlander, M. Brownnutt, F. Zhringer, R. Blatt, and W. Hnsel. Deterministic reordering of $^{40}Ca^{+}$ ions in a linear segmented paul trap. *New Journal of Physics*, 11(10), 2009. [cited at p. 7]

[76] J. P. Home, D. Hanneke, J. D. Jost, J. M. Amini, D. Leibfried, and D. J. Wineland. Complete methods set for scalable ion trap quantum information processing. *Science*, 325:1227–1230, 2009. [cited at p. 7, 121]

[77] A. Walther, F. Ziesel, T. Ruster, S. T. Dawkins, K. Ott, M. Hettrich, K. Singer, F. Schmidt-Kaler, and U. Poschinger. Controlling fast transport of cold trapped ions. *Phys. Rev. Lett.*, 109:080501, Aug 2012. [cited at p. 7, 148]

[78] R. Bowler, J. Gaebler, Y. Lin, T. R. Tan, D. Hanneke, J. D. Jost, J. P. Home, D. Leibfried, and D. J. Wineland. Coherent diabatic ion transport and separation in a multizone trap array. *Phys. Rev. Lett.*, 109:080502, Aug 2012. [cited at p. 7]

[79] S. Seidelin, J. Chiaverini, R. Reichle, J. J. Bollinger, D. Leibfried, J. Britton, J. H. Wesenberg, R. B. Blakestad, R. J. Epstein, D. B. Hume, W. M. Itano, J. D. Jost, C. Langer, R. Ozeri, N. Shiga, and D. J. Wineland. Microfabricated surface-electrode ion trap for scalable quantum information processing. *Phys. Rev. Lett.*, 96:253003, Jun 2006. [cited at p. 7]

[80] D. Stick, K. M. Fortier, R. Haltli, C. Highstrete, D. L. Moehring, C. Tigges, and M. G. Blain. Demonstration of a microfabricated surface electrode ion trap. *arXiv*, 1008(0990v2), 2010. [cited at p. 7, 53]

[81] Kenneth R. Brown, Robert J. Clark, Jaroslaw Labaziewicz, Philip Richerme, David R. Leibrandt, and Isaac L. Chuang. Loading and characterization of a printed-circuit-board atomic ion trap. *Phys. Rev. A*, 75:015401, Jan 2007. [cited at p. 7]

[82] D. T. C. Allcock, J. A. Sherman, D. N. Stacey, A. H. Burrell, M. J. Curtis, G. Imreh, N. M. Linke, D. J. Szwer, S. C. Webster, A. M. Steane, and D. M. Lucas. Implementation of a symmetric surface-electrode ion trap with field compensation using a modulated Raman effect. *New Journal of Physics*, 12(5):053026, 2010. [cited at p. 7, 39, 51, 54, 66]

[83] J. M. Amini, H. Uys, J. H. Wesenberg, S. Seidelin, J. Britton, J. J. Bollinger, D. Leibfried, C. Ospelkaus, A. P. VanDevender, and D. J. Wineland. Toward scalable ion traps for quantum information processing. *New Journal of Physics*, 12:033031, 2010. [cited at p. 7, 48, 149]

[84] S. Schulz, U. Poschinger, K. Singer, and F. Schmidt-Kaler. Optimization of segmented linear paul traps and transport of stored particles. *Fortschr. Phys.*, 54:648, 2006. [cited at p. 7]

[85] G. Wilpers, P. See, P. Gill, and A. G. Sinclair. A monolithic array of three-dimensional ion traps fabricated with conventional semiconductor technology. *Nature Nanotechnology*, 7:572–576, Sep 2012. [cited at p. 7, 12]

[86] L. Deslauriers, S. Olmschenk, D. Stick, W. K. Hensinger, J. Sterk, and C. Monroe. Scaling and suppression of anomalous heating in ion traps. *Phys. Rev. Lett.*, 97:103007, Sep 2006. [cited at p. 7]

[87] D T C Allcock, L Guidoni, T P Harty, C J Ballance, M G Blain, A M Steane, and D M Lucas. Reduction of heating rate in a microfabricated ion trap by pulsed-laser cleaning. *N. J. Phys.*, 13(12):123023, 2011. [cited at p. 7, 47]

[88] D. A. Hite, Y. Colombe, A. C. Wilson, K. R. Brown, U. Warring, R. Jördens, J. D. Jost, K. S. McKay, D. P. Pappas, D. Leibfried, and D. J. Wineland. 100-fold reduction of electric-field noise in an ion trap cleaned with *In Situ* argon-ion-beam bombardment. *Phys. Rev. Lett.*, 109:103001, Sep 2012. [cited at p. 7, 46, 47]

[89] Jaroslaw Labaziewicz, Yufei Ge, David R. Leibrandt, Shannon X. Wang, Ruth Shewmon, and Isaac L. Chuang. Temperature dependence of electric field noise above gold surfaces. *Phys. Rev. Lett.*, 101:180602, Oct 2008. [cited at p. 7]

[90] Jaroslaw Labaziewicz, Yufei Ge, Paul Antohi, David Leibrandt, Kenneth R. Brown, and Isaac L. Chuang. Suppression of heating rates in cryogenic surface-electrode ion traps. *Phys. Rev. Lett.*, 100:013001, Jan 2008. [cited at p. 7]

[91] D. M. Lucas, B. C. Keitch, J. P. Home, G. Imreh, M. J. McDonnell, D. N. Stacey, D. J. Szwer, and Steane A. M. A long-lived memory qubit on a low-decoherence quantum bus. *arXiv:0710.4421v1*, Feb 2008. [cited at p. 9]

[92] Daniel F. V. James, Paul G. Kwiat, William J. Munro, and Andrew G. White. Measurement of qubits. *Physical Review A*, 64(5), Oct 2001. [cited at p. 9]

[93] D. Kielpinski, C. Monroe, and D. J. Wineland. Architecture for a large-scale ion-trap quantum computer. *Nature*, 417:709–11, Jun 2002. [cited at p. 11]

[94] W. M. Itano, C. Monroe, D. J. Wineland, D. Meekhof, D. Leibfried, and B. King. Experimental issues in coherent quantum-state manipulation of trapped atomic ions. *J. Res. NIST*, 103(3):259, 1998. [cited at p. 11]

[95] D. Stick, S. Hensinger, W. K. amd Olmschenk, M. J. Madsen, K. Schwab, and C. Monroe. Ion trap in a semiconductor chip. *Nature Physics*, 2:36–39, 2006. [cited at p. 11]

[96] W. K. Hensinger, S. Olmschenk, D. Stick, D. Hucul, M. Yeo, M. Acton, L. Deslauriers, C. Monroe, and J. Rabchuk. T-junction ion trap array for two-dimensional ion shuttling, storage, and manipulation. *Appl. Phys. Lett.*, 88(3):034101, 2006. [cited at p. 11]

[97] M. Brownnutt. Innsbruck Micreon traps in words and pictures. Microtrap meeting report, Universität Innsbruck, 2008. [cited at p. 16, 18]

[98] D. Rotter. Photoionisation von Kalzium. Diplomarbeit, Universität Innsbruck, 2003. [cited at p. 27]

[99] A. H. Myerson. High-precision qubit readout and microfabricated ion traps for quantum information processing. First year report, University of Oxford, 2007. [cited at p. 32]

[100] G. Shu, N. Kurz, M. R. Dietrich, and B. B. Blinov. Efficient fluorescence collection from trapped ions with an integrated spherical mirror. *Phys. Rev. A*, A81:042321, 2010. [cited at p. 32, 56, 74]

[101] D. Leibfried, R. Blatt, C. Monroe, and D. Wineland. Quantum dynamics of single trapped ions. *Rev. of modern Phys.*, 75:281–324, 2003. [cited at p. 33]

[102] D. J. Berkeland, J. D. Miller, J. C. Bergquist, W. M. Itano, and D. J. Wineland. Minimization of ion micromotion in a Paul trap. *Journal of Applied Physics*, 83(10):5025 –5033, may 1998. [cited at p. 38, 50, 65, 87]

[103] D. T. C. Allcock. *Surface-Electrode Ion Traps for Scalable Quantum Computing*. D.Phil. thesis, University of Oxford, 2011. [cited at p. 40, 49, 53, 77, 81, 128, 149]

[104] J. H. Wesenberg, R. J. Epstein, D. Leibfried, R. B. Blakestad, J. Britton, J. P. Home, W. M. Itano, J. D. Jost, E. Knill, C. Langer, R. Ozeri, S. Seidelin, and D. J. Wineland. Fluorescence during doppler cooling of a single trapped atom. *Phys. Rev. A*, 76(5):053416, Nov 2007. [cited at p. 43, 51, 66, 167, 168]

[105] R. J. Epstein, S. Seidelin, D. Leibfried, J. H. Wesenberg, J. J. Bollinger, J. M. Amini, R. B. Blakestad, J. Britton, J. P. Home, W. M. Itano, J. D. Jost, E. Knill, C. Langer, R. Ozeri, N. Shiga, and D. J. Wineland. Simplified motional heating rate measurements of trapped ions. *Phys. Rev. A*, 76(3):033411, Sep 2007. [cited at p. 45, 47]

[106] S. A. Schulz, U. Poschinger, F. Ziesel, and F. Schmidt-Kaler. Sideband cooling and coherent dynamics in a microchip multi-segmented ion trap. *N. J. Phys.*, 10:045007, 2008. [cited at p. 46]

[107] R. B Blakestad, C. Ospelkaus, A. P VanDevender, J. H Wesenberg, M. J Biercuk, D. Leibfried, and D. J Wineland. Near-ground-state transport of trapped-ion qubits through a multidimensional array. *Phys. Rev. A*, 84:032314, Sep 2011. [cited at p. 48, 149]

[108] C. Ospelkaus, U. Warring, Y. Colombe, K. R. Brown, J. M. Amini, D. Leibfried, and D. J. Wineland. Microwave quantum logic gates for trapped ions. *Nature*, 476:181–184, 2011. [cited at p. 49]

[109] N. Daniilidis, T. Lee, R. Clark, S. Narayanan, and H. Häffner. Wiring up trapped ions to study aspects of quantum information. *J. Phys. B: At. Mol. Opt. Phys.*, 42(15):154012, Jul 2009. [cited at p. 49]

[110] M. Brownnutt. *Personal communication*. 2011. [cited at p. 49]

[111] G. Sagué, E. Vetsch, W. Alt, D. Meschede, and A. Rauschenbeutel. Cold-atom physics using ultrathin optical fibers: Light-induced dipole forces and surface interactions. *Phys. Rev. Lett.*, 99(16):163602, Oct 2007. [cited at p. 49]

[112] E. Vetsch, D. Reitz, G. Sagué, R. Schmidt, S. T. Dawkins, and A. Rauschenbeutel. Optical interface created by laser-cooled atoms trapped in the evanescent field surrounding an optical nanofiber. *Phys. Rev. Lett.*, 104(20):203603, May 2010. [cited at p. 49]

[113] W. K. Hensinger, D. W. Utami, H.-S. Goan, K. Schwab, C. Monroe, and G. J. Milburn. Ion trap transducers for quantum electromechanical oscillators. *Phys. Rev. A*, 72(4):041405, Oct 2005. [cited at p. 49]

[114] G. R. Guthöhrlein, M. Keller, K. Hayasaka, W. Lange, and H. Walther. A single ion as a nanoscopic probe of an optical field. *Nature*, 414:49–51, 2001. [cited at p. 49]

[115] R. Maiwald, D. Leibfried, J. Britton, J. C. Bergquist, G. Leuchs, and D. J. Wineland. Stylus ion trap for enhanced access and sensing. *Nature Physics*, 5:551–554, Jun 2009. [cited at p. 49]

[116] Wayne M. Itano and D. J. Wineland. Laser cooling of ions stored in harmonic and penning traps. *Phys. Rev. A*, 25:35–54, Jan 1982. [cited at p. 49]

[117] A. H. Burrell. *High Fidelity Readout of Trapped Ion Qubits*. D.Phil. thesis, University of Oxford, 2010. [cited at p. 50, 64, 66, 80, 83, 121]

[118] B. G. Norton, E. W. Streed, M. J. Petrasiunas, A. Jechow, and D. Kielpinski. Millikelvin spatial thermometry of trapped ions. *arXiv [quant-ph]*, 1106.1708v1, Jun 2011. [cited at p. 50, 65]

[119] R. J. Hendricks, J. L. Sørensen, C. Champenois, M. Knoop, and M. Drewsen. Doppler cooling of calcium ions using a dipole-forbidden transition. *Phys. Rev. A*, 77(2):021401, Feb 2008. [cited at p. 50]

[120] H. Ohadi, M. Himsworth, A. Xuereb, and T. Freegarde. Magneto-optical trapping and background-free imaging for atoms near nanostructured surfaces. *Optics Express*, 17:23003–23009, 2009. [cited at p. 50]

[121] I. Siemers, M. Schubert, R. Blatt, W. Neuhauser, and P. E. Toschek. The "trapped state" of a trapped ion – line shifts and shape. *Eur. Phys. Lett.*, 18(2):139, 1992. [cited at p. 51]

[122] D. N. Stacey, D. M. Lucas, D. T. C. Allcock, D. J. Szwer, and S. C. Webster. Optical Bloch equations with multiply-connected states. *J. Phys. B*, 41:085502, 2008. [cited at p. 51, 87]

[123] H. Janacek. *(in preparation)*. D.Phil. thesis, University of Oxford, 2013. [cited at p. 51, 87, 150]

[124] N. M. Linke, D. Allcock, D. Szwer, C. Ballance, T. Harty, H. Janacek, D. Stacey, A. Steane, and D. Lucas. Background-free detection of trapped ions. *Applied Physics B: Lasers and Optics*, pages 1–6, 2012. 10.1007/s00340-011-4870-z. [cited at p. 51]

[125] D. Allcock, T. Harty, H. Janacek, N. M. Linke, C. Ballance, A. Steane, D. Lucas, R. Jarecki, S. Habermehl, M. Blain, D. Stick, and D. Moehring. Heating rate and electrode charging measurements in a scalable, microfabricated, surface-electrode ion trap. *Applied Physics B: Lasers and Optics*, 107:913–919, 2012. 10.1007/s00340-011-4788-5. [cited at p. 53]

[126] D. M. Lucas, A. Ramos, J. P. Home, M. J. McDonnel, S. Nakayama, J.-P. Stacey, S.C. Webster, D. N. Stacey, and A. M. Steane. Isotope-selective photo-ionization for calcium ion trapping. *Phys. Rev. A*, 69:012711, 2004. [cited at p. 53, 70, 74, 82]

[127] M. D. Barrett, B. DeMarco, T. Schaetz, V. Meyer, D. Leibfried, J. Britton, J. Chiaverini, W. M. Itano, B. Jelenković, J. D. Jost, C. Langer, T. Rosenband, and D. J. Wineland. Sympathetic cooling of $^{9}Be^{+}$ and $^{24}Mg^{+}$ for quantum logic. *Phys. Rev. A*, 68:042302, 2003. [cited at p. 56, 125, 148]

[128] D. J. Berkeland and M. G. Boshier. Destabilization of dark states and optical spectroscopy in zeeman-degenerate atomic systems. *Phys. Rev. A*, 65:033413, Feb 2002. [cited at p. 61]

[129] M.G. Boshier, G.P. Barwood, G. Huang, and H.A. Klein. Polarisation-dependent optical pumping for interrogation of amagnetic-field-independent "clock" transition in laser-cooled trapped $^{87}Sr^{+}$. *Appl. Phys. B*, 71:51–56, 2000. [cited at p. 62]

[130] P. A. Barton, C. J. S. Donald, D. M. Lucas, D. A. Stevens, A. M. Steane, and D. N. Stacey. Measurement of the lifetime of the $3d^2D_{5/2}$ state in $^{40}Ca^{+}$. *Phys. Rev. A*, 62(3):032503, Aug 2000. [cited at p. 67]

[131] J. D. Siverns, L. R. Simkins, S. Weidt, and W. K. Hensinger. On the application of radio frequency voltages to ion traps via helical resonators. *Appl. Phys. B*, 2012. [cited at p. 71]

[132] A. H. Burrell, D. J. Szwer, S.C. Webster, and D. M. Lucas. Scalable simultaneous multi-qubit readout with 99.99% single-shot fidelity. *arXiv:0906.3304v1*, June 2009. [cited at p. 74]

[133] S. Gulde. Simple and efficient photo-ionization loading of ions for precision ion-trapping experiments. *Appl. Phys. B*, 73:861, 2001. [cited at p. 75]

[134] N. Kjærgaard, L. Hornekær, A. M. Thommesen, Z. Videsen, and M. Drewsen. Isotope selective loading of an ion trap using resonance-enhanced two-photon ionization. *Appl. Phys. B*, 71:207–210, 2000. [cited at p. 74]

[135] R.W.P. Drever, J.L. Hall, F.V. Kowalski, J. Hough, G.M. Ford, A.J. Munley, and H. Ward. Laser phase and frequency stabilization using an optical resonator. *Appl. Phys.*, 31:97, 1983. [cited at p. 75, 92]

[136] B. C. Keitch. *A Quantum Memory Qubit in Calcium-43*. D.Phil. thesis, University of Oxford, 2007. [cited at p. 76, 80, 117, 126]

[137] D. T. C. Allcock. A multi-channel laser diagnostic system for trapped-ion quantum computing experiments. Master's thesis, University of Oxford, 2007. [cited at p. 76]

[138] J. P. Stacey. *Stabilization and Control in a Linear Ion Trap*. D.Phil. thesis, University of Oxford, 2003. [cited at p. 80]

[139] M. J. McDonnell. *Two-Photon Readout Methods for an Ion trap quantum information processor*. D.Phil. thesis, University of Oxford, 2003. [cited at p. 80]

[140] J. Robin. Laser intensity stabilization by a PID controller on an FPGA. Master's thesis, University of Oxford, 2010. [cited at p. 81]

[141] P. Spano, S. Piazzolla, and M. Tamburrini. Measurements of the injection-locking influence on the frequency noise spectrum of single-mode semiconductor lasers. *Opt. Let.*, 10(11):556–558, 1985. [cited at p. 93]

[142] A. Balbin Villaverde, D. A. Donatti, and D. G. Bozinis. Terbium gallium garnet verdet constant measurements with pulsed magnetic fields. *J. Phys. C*, 11, 1978. [cited at p. 93]

[143] Rüdiger Paschotta. *Encyclopedia of Laser Physics and Technology*. RP-Photonics online, Zürich, 2008. [cited at p. 93]

[144] Christopher J. Foot. *Atomic Physics*. Oxford Master Series in Atomic, Optical and Laser Physics. Oxford University Press, 2005. [cited at p. 105]

[145] R. Ozeri, C. Langer, D. Jost, B. DeMarco, A. Ben-Kish, B. R. Blakestad, J. Britton, J. Chiaverini, W. M. Itano, D. B. Hume, D. Leibfried, T. Rosenband, P.O. Schmidt, and D. J. Wineland. Hyperfine coherence in the presence of spontaneous photon scattering. *Phys. Rev. Lett.*, 95(3):030403, Jul 2005. [cited at p. 108, 109, 117]

[146] R. Ozeri, W. M. Itano, R. B. Blakestad, J. Britton, J. Chiaverini, J. D. Jost, C. Langer, D. Leibfried, R. Reichle, S. Seidelin, J. H. Wesenberg, and D. J. Wineland. Errors in trapped-ion quantum gates due to spontaneous photon scattering. *Phys. Rev. A*, 75:042329, Nov 2007. [cited at p. 108, 112, 115, 117]

[147] H. Y. Carr and E. M. Purcell. Effects of diffusion on free precession in nuclear magnetic resonance experiments. *Phys. Rev.*, 94:630–638, May 1954. [cited at p. 110]

[148] S. Meiboom and D. Gill. Modified spin-echo method for measuring nuclear relaxation times. *Rev. Sci. Inst.*, 29:688–691, May 1958. [cited at p. 110]

[149] Ray Freeman. *Spin Choreography: Basic Steps in High Resolution NMR*. Oxford University Press, 1998. [cited at p. 110]

[150] H. Uys, M. J. Biercuk, A. P. VanDevender, C. Ospelkaus, D. Meiser, R. Ozeri, and J. J. Bollinger. Decoherence due to elastic rayleigh scattering. *Phys. Rev. Lett.*, 105:200401, Nov 2010. [cited at p. 112, 117]

[151] H. J. Metcalf and P. van der Straten. *Laser cooling and trapping*. Springer, 1999. [cited at p. 115]

[152] D. J. Wineland, M. Barrett, J. Britton, J. Chiaverini, B. DeMarco, W. M. Itano, B. Jelenković, C. Langer, D. Leibfried, V. Meyer, T. Rosenband, and T. Schätz. Quantum information processing with trapped ions. *Phil. Trans. R. Soc. Lond. A*, 361:1349–1361, May 2003. [cited at p. 115]

[153] C. J. S. Donald. *Development of an Ion Trap Quantum Information Processor*. D.Phil. thesis, University of Oxford, 2000. [cited at p. 117]

[154] S. C. Webster. *Raman Sideband Cooling and Coherent Manipulation of Trapped Ions*. D.Phil. thesis, University of Oxford, 2005. [cited at p. 120, 125, 142]

[155] D. J. Szwer. A $^{43}Ca^{+}$ trapped ion qubit. First year report, University of Oxford, 2006. [cited at p. 120]

[156] S. Olmschenk, K. C. Younge, D. L. Moehring, D. N. Matsukevich, P. Maunz, and C. Monroe. Manipulation and detection of a trapped Yb^+ hyperfine qubit. *Physical Review A*, 76(5), November 2007. [cited at p. 121]

[157] J. Benhelm, G. Kirchmair, C. F. Roos, and R. Blatt. Experimental quantum information processing with $^{43}Ca^+$ ions. *Phys. Rev. A*, 77:062306, Jun 2008. [cited at p. 121, 133, 148]

[158] G. Kirchmair, J. Benhelm, F. Zähringer, R. Gerritsma, C. F. Roos, and R. Blatt. High-fidelity entanglement of $^{43}Ca^+$ hyperfine clock states. *Physical Review A*, 79(2), 2009. [cited at p. 121, 148]

[159] B. B. Blinov, L. Deslauriers, P. Lee, M. J. Madsen, R. Miller, and C. Monroe. Sympathetic cooling of trapped Cd^+ isotopes. *Phys. Rev. A*, 65:040304, Apr 2002. [cited at p. 125]

[160] T. Rosenband, P. O. Schmidt, D. B. Hume, W. M. Itano, T. M. Fortier, J. E. Stalnaker, K. Kim, S. A. Diddams, J. C. J. Koelemeij, J. C. Bergquist, and D. J. Wineland. Observation of the $^1S_0 \rightarrow {}^3P_0$ clock transition in $^{27}Al^+$. *Phys. Rev. Lett.*, 98:220801, May 2007. [cited at p. 125, 148]

[161] C. W. Chou, D. B. Hume, J. C. J. Koelemeij, D. J. Wineland, and T. Rosenband. Frequency comparison of two high-accuracy Al^+ optical clocks. *Phys. Rev. Lett.*, 104:070802, Feb 2010. [cited at p. 125, 148]

[162] U. G. Poschinger, G. Huber, F. Ziesel, M. Deiss, M. Hettrich, S. A. Schulz, K. Singer, G. Poulsen, M. Drewsen, R. J. Hendricks, and F. Schmidt-Kaler. Coherent manipulation of a $^{40}ca^+$ spin qubit in a micro ion trap. *J Phys B*, 42(15), 2009. [cited at p. 133]

[163] J. Benhelm. *Precision spectroscopy and quantum information processing with trapped calcium ions*. PhD thesis, University of Innsbruck, 2008. [cited at p. 133]

[164] M. J. McDonnell, J. P. Home, D. M. Lucas, G. Imreh, B. C. Keitch, D. J. Szwer, N. R. Thomas, S. C. Webster, D. N. Stacey, and A. M. Steane. Long-lived mesoscopic entanglement outside the lamb-dicke regime. *Phys. Rev. Lett.*, 98:063603, Feb 2007. [cited at p. 135]

[165] D. J. Wineland, C. Monroe, W. M. Itano, B. E. Leibfried, D. King, and D. M. Meekhof. Experimental issues in coherent quantum-state manipulation of trapped atomic ions. *Res. Natl. Inst. Stand. Technol.*, 103(3), 1998. [cited at p. 135, 136]

[166] J. Eschner, G. Morigi, F. Schmidt-Kaler, and R. Blatt. Laser cooling of trapped ions. *J. Opt. Soc. Am. B*, 20, 2003. [cited at p. 137]

[167] Jannes B. Wübbena, Sana Amairi, Olaf Mandel, and Piet O. Schmidt. Sympathetic cooling of mixed-species two-ion crystals for precision spectroscopy. *Phys. Rev. A*, 85:043412, Apr 2012. [cited at p. 137, 138, 146]

[168] C. Monroe, D. M. Meekhof, B. E. King, S. R. Jefferts, W. M. Itano, D. J. Wineland, and P. Gould. Resolved-sideband Raman cooling of a bound atom to the 3d zero-point energy. *Phys. Rev. Lett.*, 75:4011–4014, Nov 1995. [cited at p. 142]

[169] D. M. Meekhof, C. Monroe, B. E. King, W. M. Itano, and D. J. Wineland. Generation of nonclassical motional states of a trapped atom. *Phys. Rev. Lett.*, 76:1796–1799, Mar 1996. [cited at p. 142]

[170] C. E. Langer. *High fidelity quantum information processing with trapped ions*. PhD thesis, University of Colorado, 2006. [cited at p. 148]

[171] [cited at p. 148]

[172] Kilian Singer, Ulrich Poschinger, Michael Murphy, Peter Ivanov, Frank Ziesel, Tommaso Calarco, and Ferdinand Schmidt-Kaler. *Colloquium* : Trapped ions as quantum bits: Essential numerical tools. *Rev. Mod. Phys.*, 82:2609–2632, Sep 2010. [cited at p. 173]

[173] Robert D. Cowan. *The Theory of Atomic Structure and Spectra*. Los Alamos Series in Basic and Applied Sciences. University of California Press, 1981. [cited at p. 175]

[174] B. W. Shore and D. H. Menzel. *Principles of Atomic Spectra*. John Wiley, 1968. [cited at p. 175]

Appendix A

Microtrap appendices

A.1 Doppler recool program

The program consists of three MatLab files, *recoolfit.m*, *makeTrajects.m* and *recoolfun.m*. It additionally relies on Andrew Steane's *amsfit.m*. The main program is *recoolfit.m* in which the user enters the experimental parameters used during data acquisition: the imaging system efficiency *imgeff*, the axial trap frequency *trapaxial*, the saturation parameter s and the linewidth *Gamma* of the fluorescence transition. The latter two can be obtained from experimental data using *satfit.m*. It fits a half-Lorentzian to the excited state population during a 397 nm scan following equation 2 in [104], where Δ is the 397 nm detuning and $\rho = \Gamma \cdot \mathrm{d}N/\mathrm{d}t$ the excited state population with the photon scattering rate $\mathrm{d}N/\mathrm{d}t$ (see inset, fig. 2.29):

$$\rho\left(\Delta\right) = \frac{s/2}{1 + s + \left(2\,\Delta/\Gamma\right)^2} \tag{A.1}$$

The program also needs the number of runs that the Doppler recool data was averaged over, the time per bin as well as the heating delay time and the number of bins to look at (as a default setting, the cooling is turned back on after the first 100 bins by the experimental control program). From the last 100 bins, the fluorescence level of the cold ion is averaged which gives us the detuning used during the experiment by again making use of equation A.1.

The program then assembles a list of starting energies and time steps for which to calculate the cooling trajectories. By "cooling trajectory" we mean the fluorescence curve of an ion with a given starting energy after the cooling has been turned back following the heating delay. This is done in *makeTrajects.m* by solving the differential equation for the motional energy during recool (see eq. 10a, [104]) with MatLab's *ode45* solver. The function calculates a set of these trajectories, one for each starting energy ϵ interpolated at the required time points, and returns them as a matrix.

The function *recoolfun.m* is a one-parameter function of time which averages these fluorescence trajectories using the weighting factors $w(\epsilon)$ obtained from a Maxwell-Boltzmann

distribution (see appendix B in [104]).

$$w(\epsilon) = 2\,\mathrm{e}^{-\epsilon/\bar{\epsilon}}\,\sinh\left(\frac{\Delta\epsilon}{2\,\bar{\epsilon}}\right) \tag{A.2}$$

$\Delta\epsilon$ is the step size between starting energies and $\bar{\epsilon}$ is the mean energy in the Boltzmann distribution and also the function's free parameter. The matrix of trajectories, and the corresponding starting energies, are accessed as global variables. The function returns the averaged trajectory.

Continuing in *recoolfit.m*, the function *recoolfun.m* is fitted to the data using *amsfit.m* and the resulting mean energy is converted into a heating rate using the heating delay time. The corresponding electric field noise density is also calculated.

A.2 Trap drawing

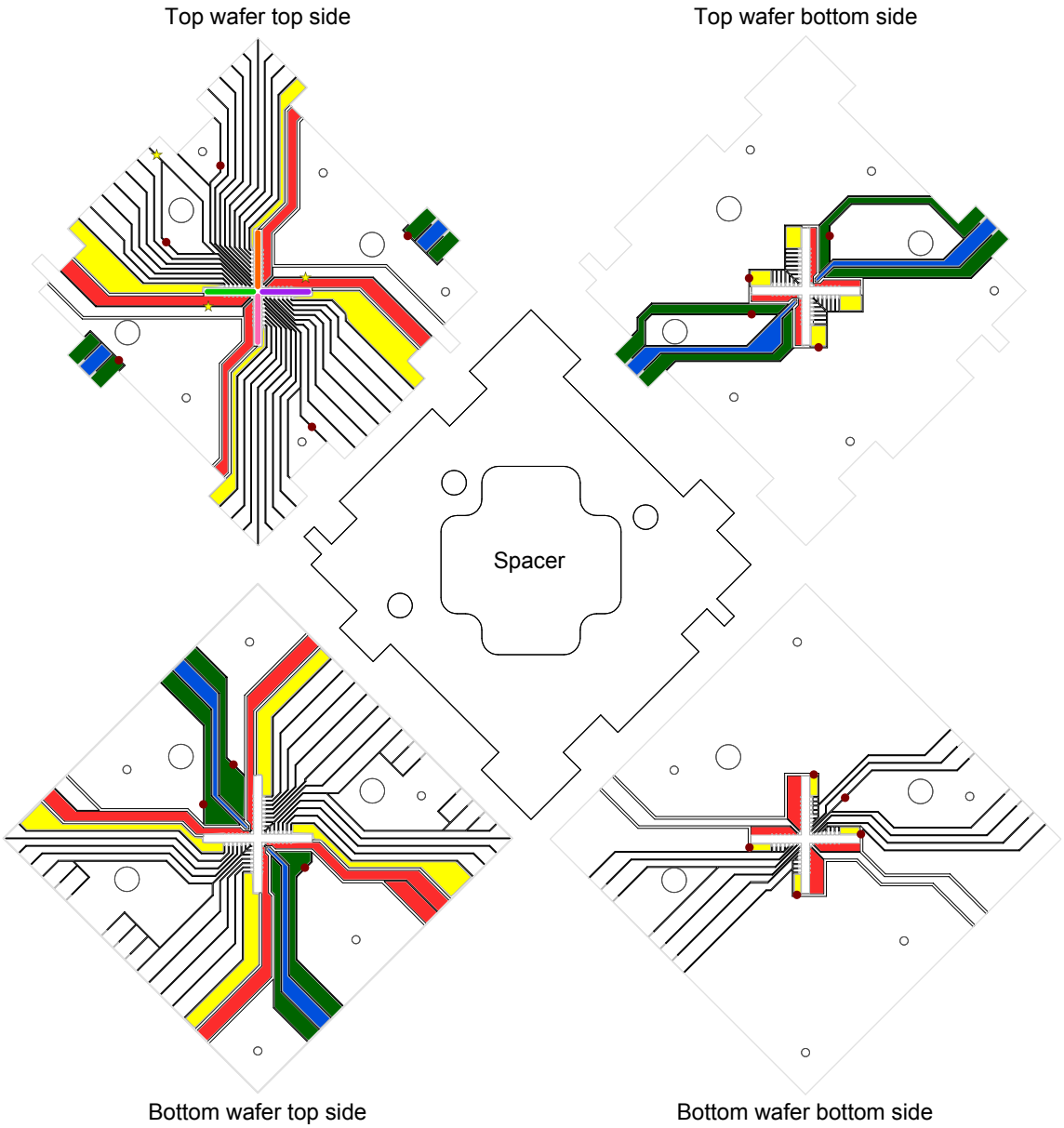

Figure A.1: Complete schematics of both sides of the trap wafers and the spacer. Bond pads that wrap around are indicated by gray separation lines at the edge. The top wafer and the spacer have recesses along the edges to allow bonding to the bottom wafer. Bottom structures are represented in phantom view to show the alignment of the features relative to the top structures. The three alignment holes as well as the smaller glue holes (five per wafer) can be seen. The conductive patches containing these holes are not connected, a problem addressed in section 2.3.1.5. RF electrodes are colored in red, compensation electrodes in green, corner compensation electrodes in blue and the last DC electrode on each trap arm in yellow. The top layer of the top wafer shows the color code for the four different trap arms (orange, purple, pink, green) as well as the three shorts (stars, see section 2.3.1.1). The dark red dots indicate where the connections to the floating patches were made using conductive Epoxy (see section 2.3.1.5).

A.3 Wire bonding

Having been attached to the chip carrier, the bond pads on the chip were connected to the corresponding pads on the carrier. We had them wire bonded in the university photofabrication group. We specified each DC electrode to be connected to its chip carrier pad by two bonds and each RF electrode by four. This was successful on most sites. However, during the bonding process, several bond pads became detached from the substrate. These lift-offs luckily did not result in a connection failure and each pad is connected with at least one bonding wire. Also due to space constraints it was not possible to provide four connections on each RF bond pad. Because of these problems, several wires were only attached on one end. Some were shorting out neighbouring connections or carrying the risk of doing so. Using a high resolution digital optical microscope, a hypodermic needle and a pair of tweezers, all of them could be removed manually. We also made sure that the lift-offs were not touching neighbouring wires. Figure A.2 shows a photograph of the finished trap on which wirebonds and lift-offs can be seen. For a detailed schematic of the wirebonding as well as the corresponding pin-assignment on the chip carrier, please refer to figureA.3.

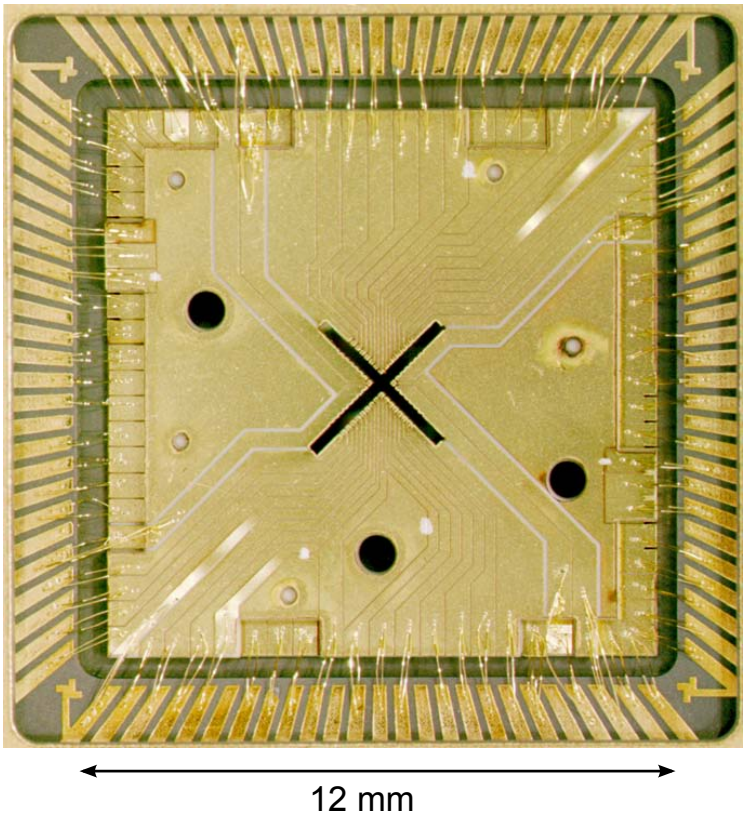

Figure A.2: Photograph of the finished trap. The wire bonding connections around the edge connecting the chip to the carrier are visible. The lift-offs appear as brightly coloured electrode sections which is caused by their angle with respect to the incident illumination. The trap is aligned such that the "orange" trap is on the bottom left.

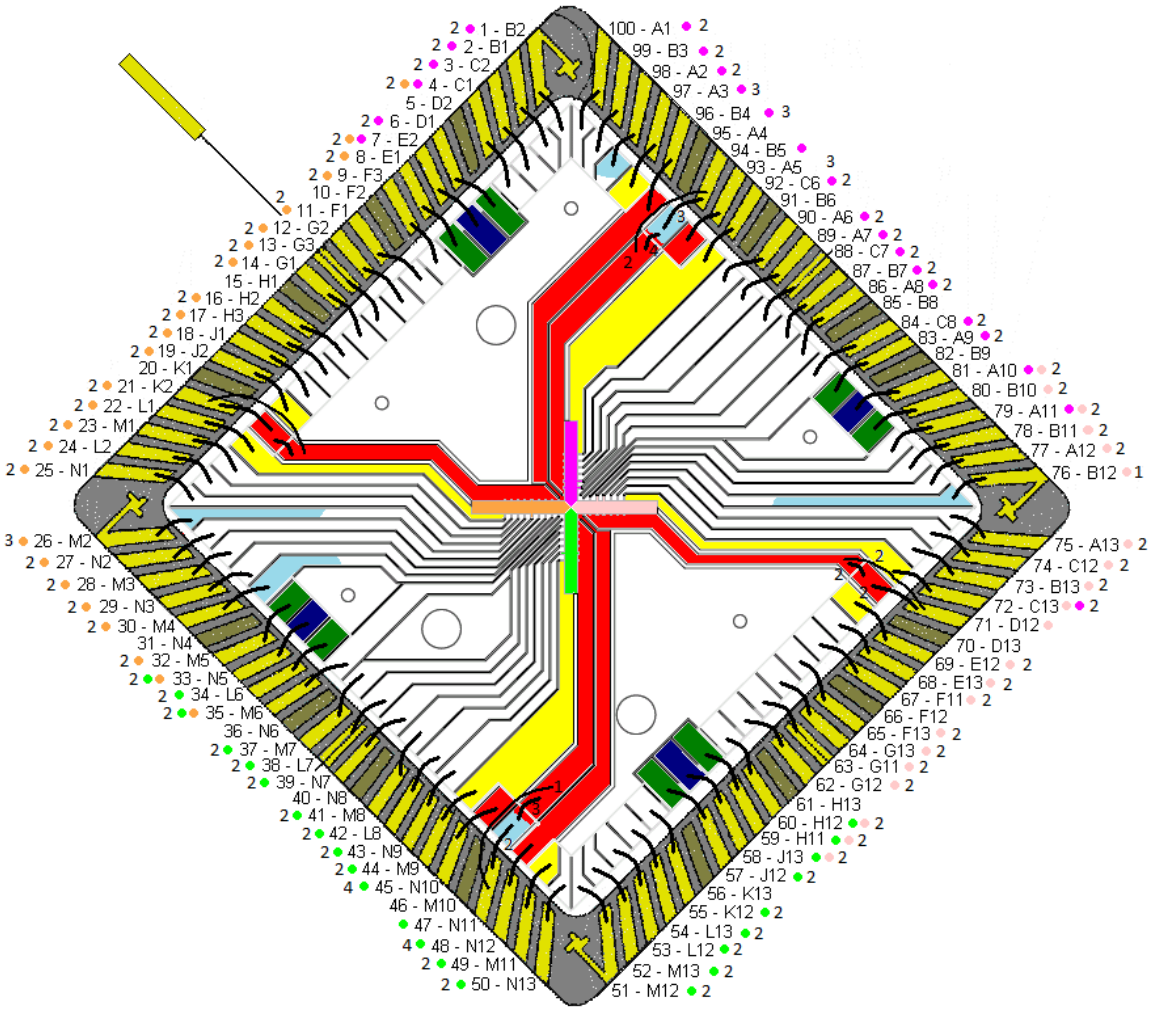

Figure A.3: The drawing shows the trap chip in the chip carrier recess. Each connection pad (shown in yellow) is labeled by its number (1-100) as well as the position of its corresponding pin on the back of the chip carrier (A1-N13). Unconnected pads are dark. The wire bonds are shown as curved black lines. The number of bonding wires are shown on the outside of the labels or, for RF electrodes, next to the connection. The labels also carry a coloured point indicating which trap arm(s) they belong to. The trap arms are coded in the centre by their designated colours, orange, green, pink and purple. RF electrodes are shown in red, compensation electrodes in dark green, corner compensation electrodes in blue, the last DC electrode on each arm in yellow. Lift-offs are shown in light blue, compare section A.3. The view is aligned in the same way as it is placed in the vacuum seen through the main viewport (see section 2.4.1).

A.4 Wiring plans

A.4.1 Orange trap wiring plan

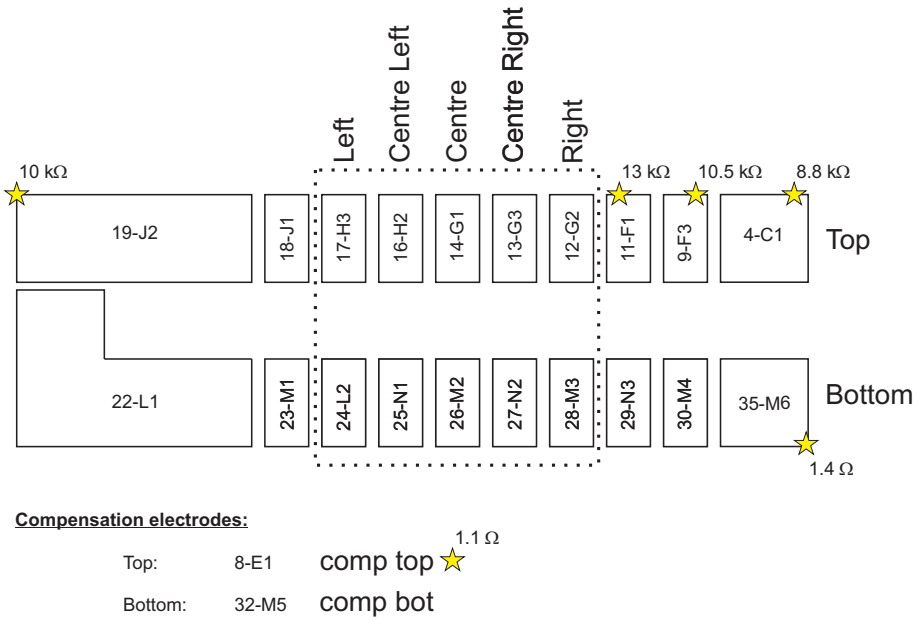

Figure A.4: The labels identify the electrodes as shown in appendix A.3. The dotted line highlights the electrodes used to create the axial trapping potential used in the experiments described in this thesis with the ion being trapped above the "centre" electrode pair. Yellow stars mark shorted electrodes including the measured resistances to ground.

A.4.2 Pink trap wiring plan

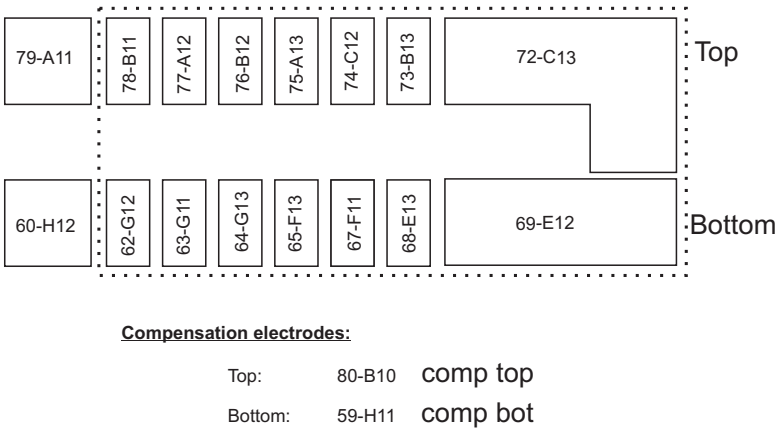

Figure A.5: The labels identify the electrodes as shown in appendix A.3.

A.5 Full trap model

The trap is designed for ion transport and shuttling experiments involving many electrodes and the central junction. The implementation of these operations will require computer simulations across the entire scale of the trap. For this reason, we have built a complete model of the trap cross in AutoCAD[1]. It is shown in figure A.6. It is based on the drawings specifying the design of the trap and in addition to the trap electrodes includes all compensation and corner compensation electrodes. With completed electrode segmentation, the geometry can be read directly into a boundary element program such as the BEM software developed at the Mainz[2] ion trap group [172]. This will allow the optimization of voltage sets at every time step of an ion shuttling operation.

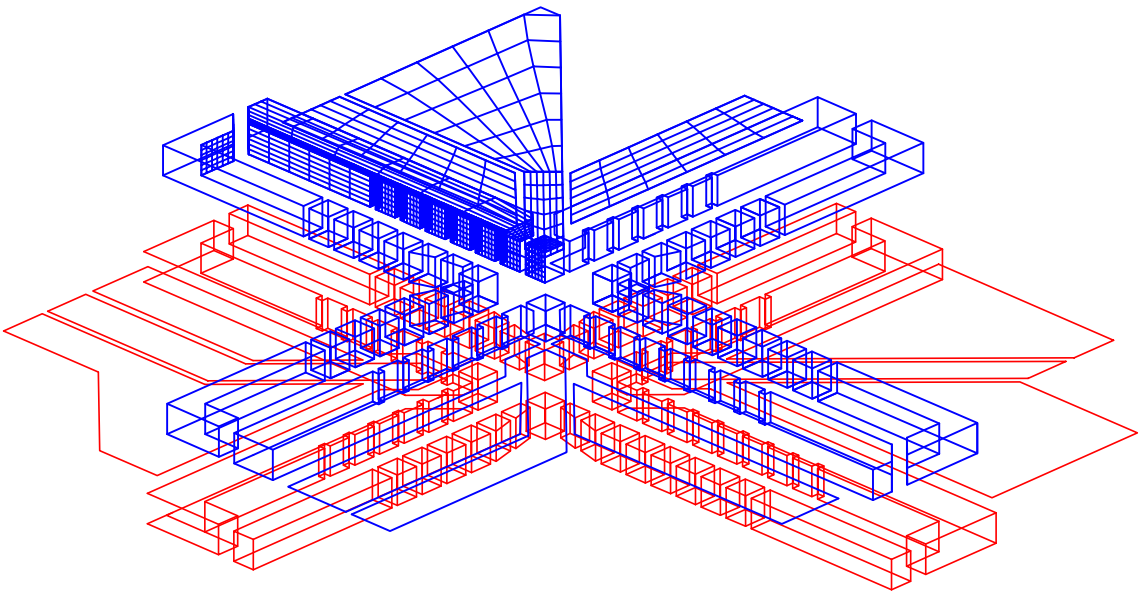

Figure A.6: Model of the entire trap built in AutoCAD. The electrodes on the top chip are shown in blue, the bottom chip in red. The "orange" trap arm is in the foreground on the right hand side. Several electrodes on the far side (top chip) are shown segmented for use in a BEM program.

[1] Autodesk AutoCAD 2010/2011
[2] fomerly Ulm

Appendix B

Rate equations

This explanation is a shortened version of the one given by David Szwer in this D.Phil. thesis [21].

Consider an ion with N energy states interacting with zero or more laser beams. In our case each state is a specific M_J or M_F substate. Let the populations of these states (the probability of the ion being in that state at any one time) be $n_1, n_2, \ldots, n_N$, written as a column vector $\vec{n}$. The rate of change of the populations is given by

$$\dot{\vec{n}} = \vec{\vec{M}}\vec{n} \tag{B.1}$$

where $\vec{\vec{M}}$ is a matrix containing the spontaneous and stimulated transition rates (see below). Equation (B.1) is the matrix form of the rate equations. Note that this model ignores coherent effects and, for instance, cannot model superpositions of states.

For constant $\vec{\vec{M}}$ (i.e. the beams' intensity, polarization and detuning do not vary), and knowing the initial population state $\vec{n}(0)$, equation (B.1) can be solved to find how the state populations $\vec{n}$ change over time, given the additional constraint $\sum_i n_i = 1$.

The matrix $\vec{\vec{M}}$ is formed by decomposing it into two matrices, one for spontaneous decay (which is upper-triangular if the levels are ordered in increasing order of energy) and one for stimulated transitions which is symmetric.

$$\vec{\vec{M}}^{spont}_{ij} = \begin{cases} \Gamma_{j\to i} & j > i \\ -\sum_i \Gamma_{j\to i} = \Gamma_j & j = i \\ 0 & j < i \end{cases} \tag{B.2}$$

$$\vec{\vec{M}}^{stim}_{ij} = \begin{cases} R_{j\to i} = R_{i\to j} & j \neq i \\ -\sum_i R_{j\to k} & j = i \end{cases} \tag{B.3}$$

The transition rates $\Gamma_{i\to j}$ are calculated from atomic theory depending on the kind of transition in question. For details see [173] and [174]. David Szwer's code includes electric dipole and electric quadrupole transitions.

With the laser detuning δ and intensity I the stimulated transition rates are given by

$$R_{i\to j} = \frac{\Gamma_j^2 \Gamma_{j\to i}}{4\delta^2 + \Gamma_j^2} \frac{I}{I_{\text{sat}}}, \tag{B.4}$$

Appendix C

“New Old” trap technical drawings

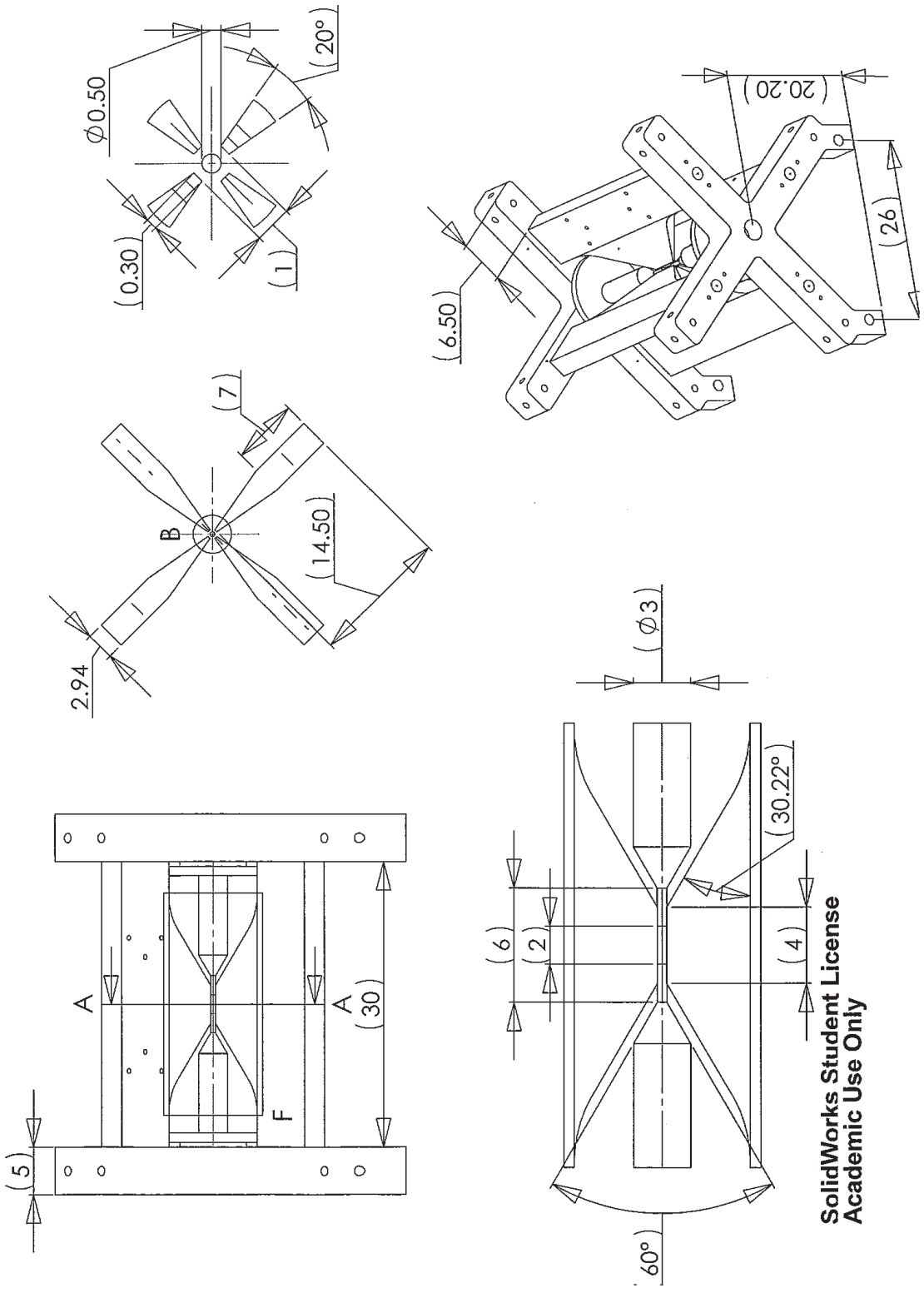

Figure C.1: Technical drawings of the trap. All dimensions in mm.

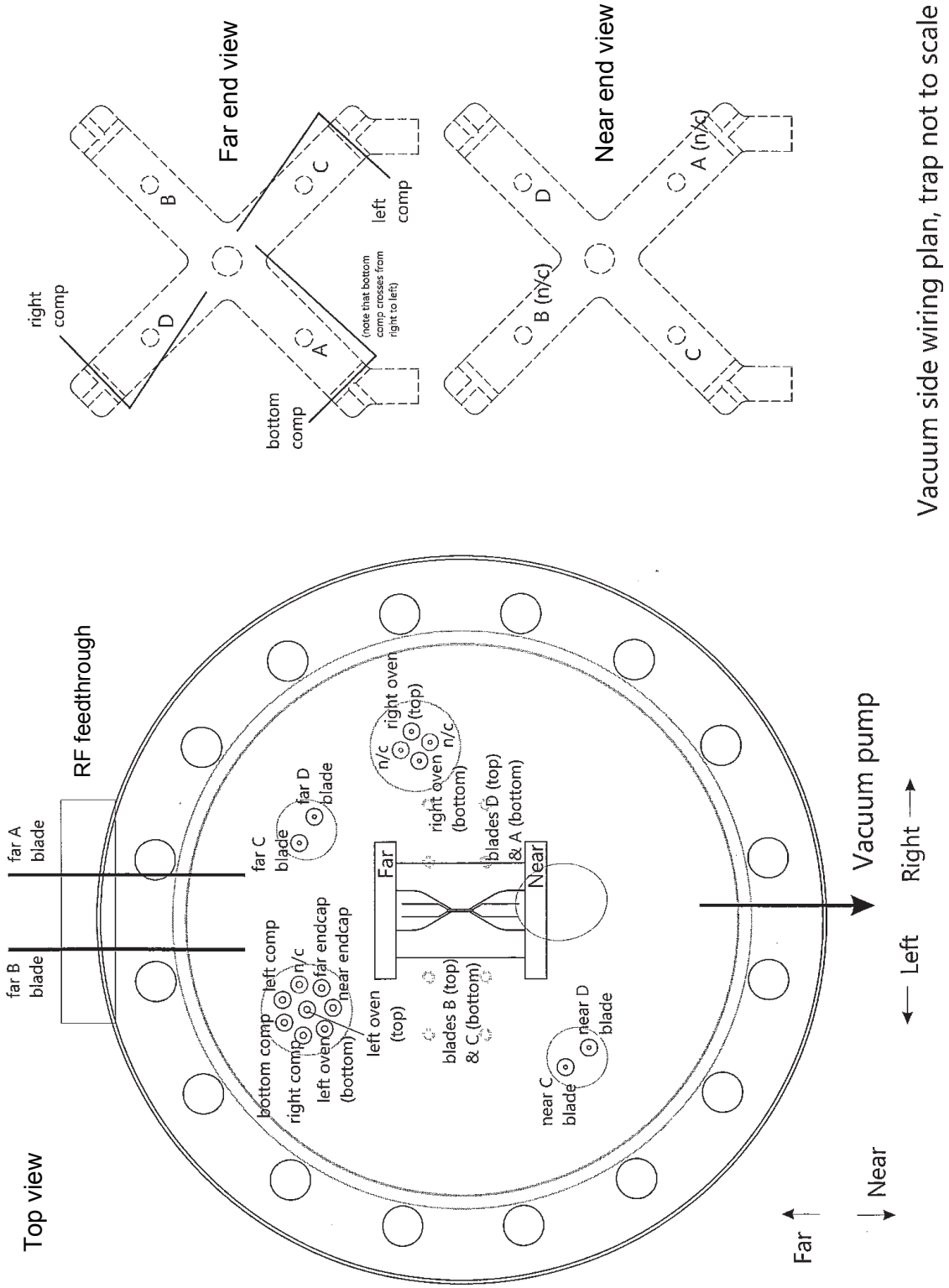

Figure C.2: Technical drawings showing the base flange (see fig. C.3) with the trap in place and the connections identified as well as the trap in end views with compensation electrodes identified.

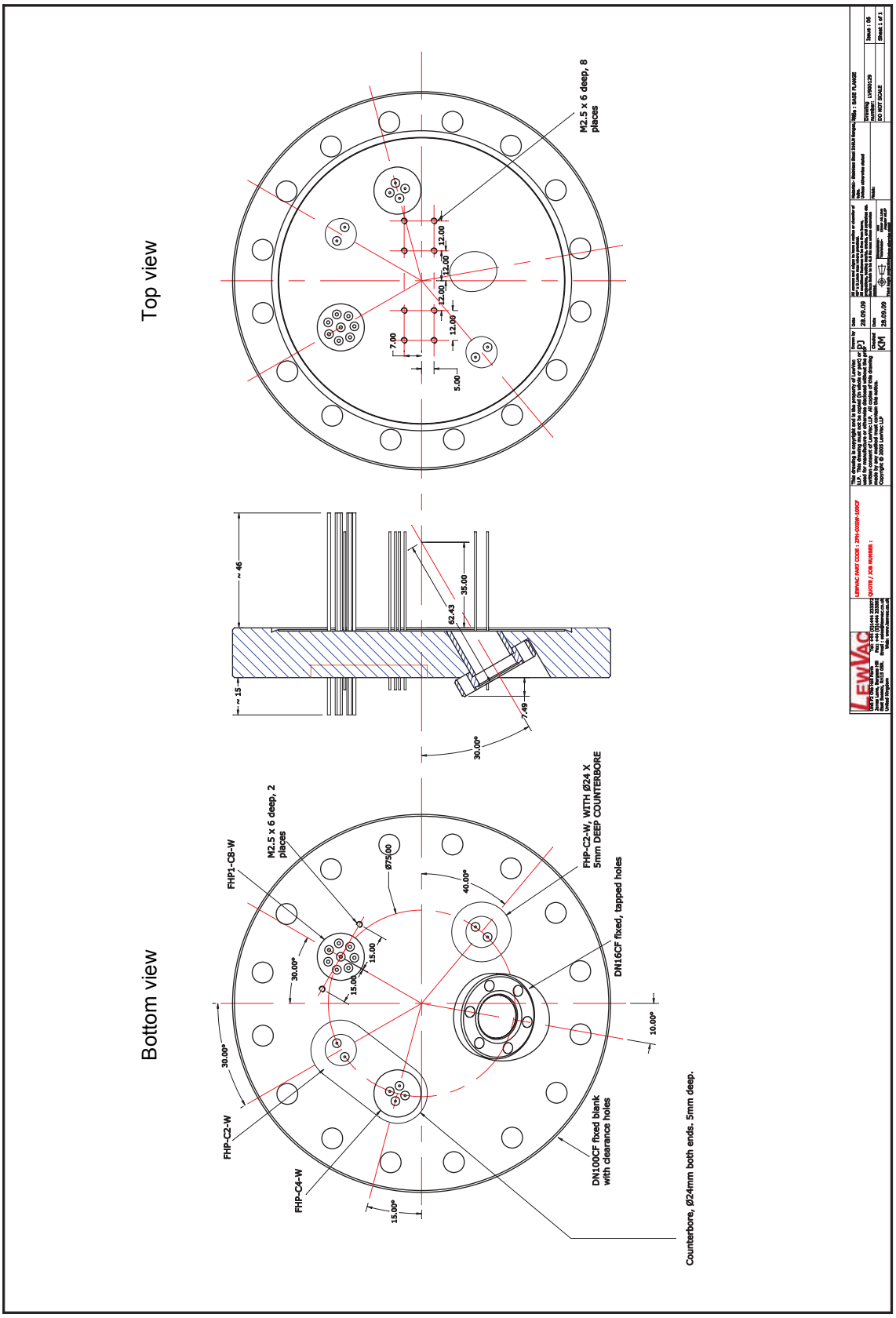

Figure C.3: The custom base flange showing the four groups of feedthroughs, the partly sunk CF16 viewport and the positions of the mounting holes.

Appendix D

Transitions

D.1 Transition properties

Transition	Wavelength / nm	Frequency / THz	$\nu_{43} - \nu_{40}$ / MHz
$4S_{1/2} \rightarrow 4P_{1/2}$	396.9589788(9)	755.2227662(17)	688(17)
$4S_{1/2} \rightarrow 4P_{3/2}$	393.477 471 6(3)	761.9050127(5)	692(19)
$3D_{3/2} \rightarrow 4P_{1/2}$	866.452	346.000	-3464.3(3.0)
$3D_{3/2} \rightarrow 4P_{3/2}$	850.036	352.682	-3462.4(2.6)
$3D_{5/2} \rightarrow 4P_{3/2}$	854.444	350.863	-3465.4(3.7)

Table D.1: Properties of the transitions between energy levels in Ca^+, giving the transition wavelengths and frequencies for $^{40}Ca^+$, and the isotope shifts of $^{43}Ca^+$ (centre-of-gravity) with respect to $^{40}Ca^+$ (from [21]).

Transition	A / s^{-1}	I_{sat} / Wm^{-2}
$4S_{1/2} \rightarrow 4P_{1/2}$	$132 \cdot 10^6$	933.82
$4S_{1/2} \rightarrow 4P_{3/2}$	$135.0(4) \cdot 10^6$	987.58
$3D_{3/2} \rightarrow 4P_{1/2}$	$8.4 \cdot 10^6$	89.798
$3D_{3/2} \rightarrow 4P_{3/2}$	$0.955(6) \cdot 10^6$	97.954
$3D_{5/2} \rightarrow 4P_{3/2}$	$8.48(4) \cdot 10^6$	96.446

Table D.2: Properties of the transitions between energy levels in Ca^+ (continued), giving the Einstein A coefficients and the saturation intensities (from [21]).

D.2 $^{43}Ca^+$ Hyperfine Structure

The following graphs and tables show the hyperfine structure at zero B-field for each of the relevant transitions in $^{43}Ca^+$. Each component is labeled by $F_{lower} \rightarrow F_{upper}$. All frequency shifts are given relative to the centre of gravity, the isotope shift of which from $^{40}Ca^+$ is tabulated above.

D.2.1 $4S_{1/2} \rightarrow 4P_{1/2}$ (397 nm)

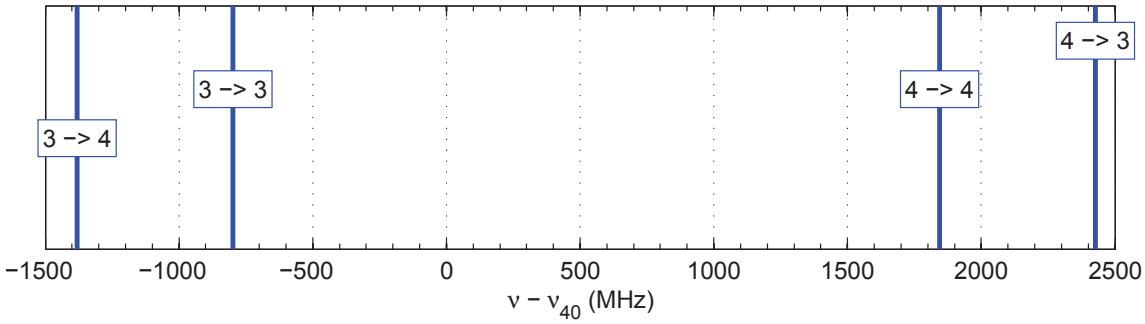

Component	$\nu - \nu_{40}$ / MHz	Component	$\nu - \nu_{40}$ / MHz
$3 \rightarrow 4$	-1381	$4 \rightarrow 4$	1845
$3 \rightarrow 3$	-799	$4 \rightarrow 3$	2426

D.2.2 $4S_{1/2} \rightarrow 4P_{3/2}$ (393 nm)

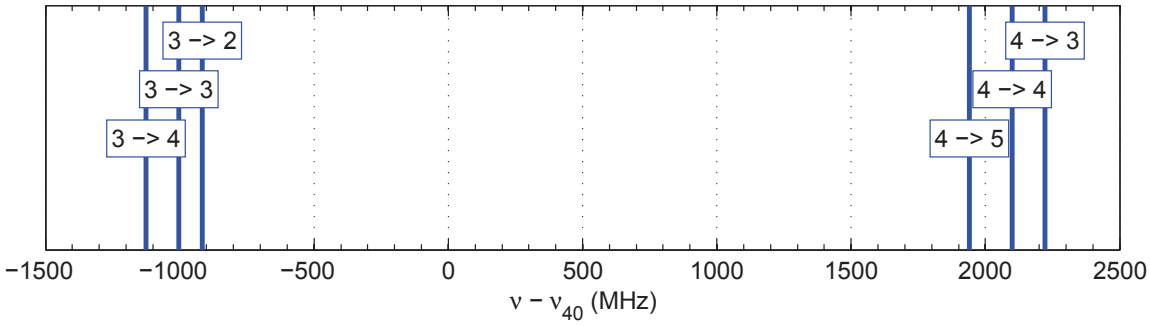

Component	$\nu - \nu_{40}$ MHz	Component	$\nu - \nu_{40}$ MHz
$3 \rightarrow 4$	-1126	$4 \rightarrow 5$	1940
$3 \rightarrow 3$	-1004	$4 \rightarrow 4$	2100
$3 \rightarrow 2$	-916	$4 \rightarrow 3$	2222

D.2.3 $3D_{3/2} \rightarrow 4P_{1/2}$ (866 nm)

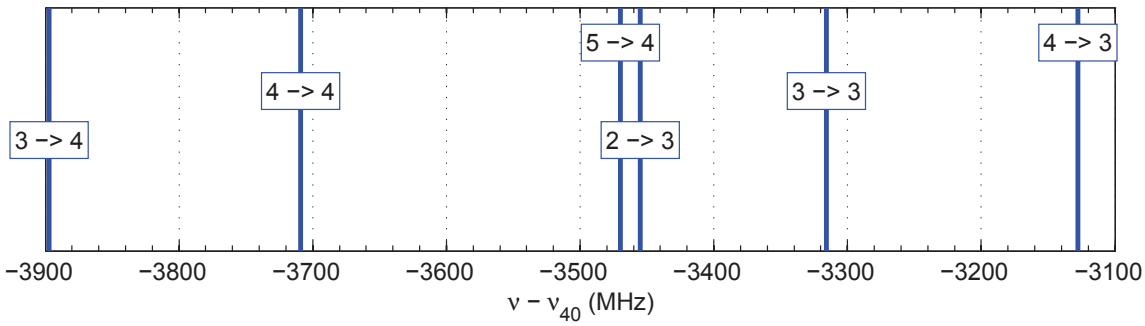

Component	$\nu - \nu_{40}$ / MHz	Component	$\nu - \nu_{40}$ / MHz
$3 \to 4$	-3897	$2 \to 3$	-3455
$4 \to 4$	-3709	$3 \to 3$	-3316
$5 \to 4$	-3470	$4 \to 3$	-3128

D.2.4 $3D_{3/2} \to 4P_{3/2}$ (850 nm)

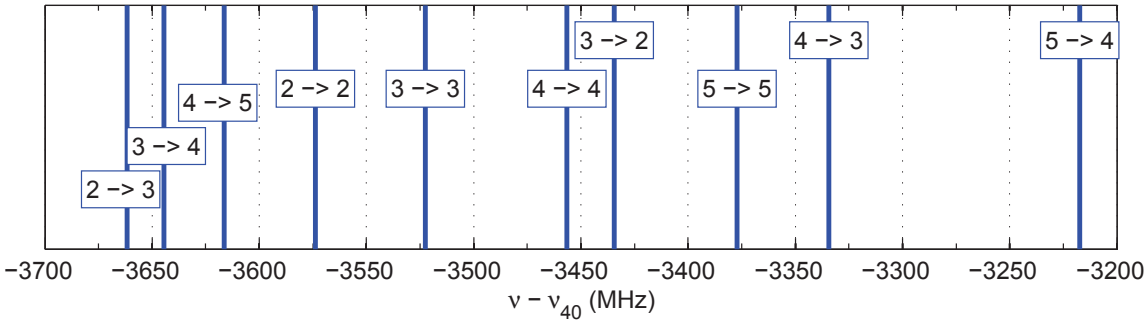

Component	$\nu - \nu_{40}$ / MHz	Component	$\nu - \nu_{40}$ / MHz
$2 \to 3$	-3662	$4 \to 4$	-3456
$3 \to 4$	-3645	$3 \to 2$	-3435
$4 \to 5$	-3616	$5 \to 5$	-3377
$2 \to 2$	-3574	$4 \to 3$	-3334
$3 \to 3$	-3523	$5 \to 4$	-3217

D.2.5 $3D_{5/2} \to 4P_{3/2}$ (854 nm)

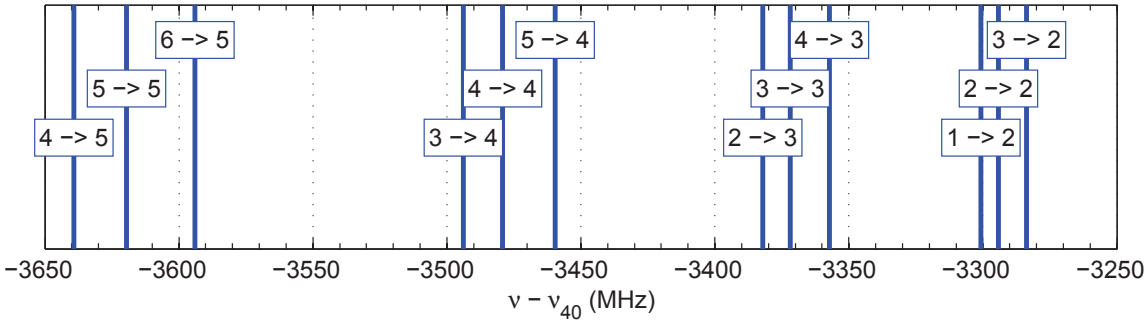

Component	$\nu - \nu_{40}$ / MHz	Component	$\nu - \nu_{40}$ / MHz
$4 \rightarrow 5$	-3639	$2 \rightarrow 3$	-3382
$5 \rightarrow 5$	-3620	$3 \rightarrow 3$	-3372
$6 \rightarrow 5$	-3594	$4 \rightarrow 3$	-3357
$3 \rightarrow 4$	-3494	$1 \rightarrow 2$	-3301
$4 \rightarrow 4$	-3479	$2 \rightarrow 2$	-3294
$5 \rightarrow 4$	-3460	$3 \rightarrow 2$	-3284

Appendix E

Knife-edge calculation

We are placing the knife-edge in the beam perpendicular to the x-direction. To collect the unobstructed part, we integrate $I(r) = I_0 \mathrm{e}^{-2r^2/w^2}$ over the x, y-plane after substituting $r^2 = x^2 + y^2$ from the position x of the edge to infinity and over the entire y range:

$$\begin{aligned} P(x) &= \int_x^\infty dx' \int_{-\infty}^\infty dy' I(r) \\ &= I_0 \underbrace{\int_x^\infty dx' e^{-\frac{2x'^2}{w^2}}}_{\text{substitute: } \tilde{x}=x'\sqrt{2}/w} \underbrace{\int_{-\infty}^\infty dy' e^{-\frac{2y'^2}{w^2}}}_{=\sqrt{\pi}w/\sqrt{2}} \\ &= \frac{w^2\sqrt{\pi}}{2} I_0 \underbrace{\int_{x\sqrt{2}/w}^\infty d\tilde{x}\, e^{-\tilde{x}^2}}_{=\sqrt{\pi}/2\left(1-\mathrm{erf}\left(x\sqrt{2}/w\right)\right)} \end{aligned} \tag{E.1}$$

Inserting $P_0 = I_0 \pi w^2/2$, we get

$$P(x) = \frac{P_0}{2}\left(1 - \mathrm{erf}\left(\frac{x\sqrt{2}}{w}\right)\right) \tag{E.2}$$